

Diss ETH No. 19576

# Sunspot umbra atmospheres

A dissertation submitted to

ETH Zurich

for the degree of  
Doctor of Sciences

presented by

Richard Wenzel  
Dipl. Phys. ETH

born December 24, 1982  
citizen of Germany

accepted on the recommendation of

Prof. Dr. Michael R. Meyer, examiner  
Prof. Dr. Svetlana V. Berdyugina,  
PD Dr. Hans-Martin Schmid and  
Dr. Bruce Lites, co-examiners

2011



---

# Abstract

---

In this thesis we study the atmosphere of sunspot umbra and the umbral substructure.

Sunspots appear as temporary dark features on the solar surface. They are the visible manifestations of the interaction of the solar magnetic fields with the solar atmosphere and the most prominent tracers of solar magnetic activity.

The darkest region of sunspots, the umbra, harbours the strongest magnetic fields in the solar atmosphere. Here, the energy transport by convection is inhibited by the magnetic field which leads to a temperature contrast of about 2000 K with respect to the quiet sun photosphere. But although appearing dark, observations of the umbra show a rich substructure, e.g. bright umbral dots, whose origin and role in the heating process of the umbra is not yet fully understood.

In the thesis at hand we present semi-empirical model atmospheres for different sunspot umbrae. Complementing the horizontal picture we inferred the vertical stratification of the atmosphere at the photospheric level, i.e.  $T = T(\tau)$ ,  $B = B(\tau)$ ,  $p = p(\tau)$  etc.. By including not only temperature but also magnetically sensitive molecular and atomic spectral lines we can use the Zeeman and Paschen-Back effect to effectively probe

the magnetic atmosphere at the different heights within the atmosphere where these lines are formed.

Notably the many molecular absorption lines we include in our analysis distinguish these investigations from former ones. Including temperature and magnetic sensitive absorption features from diatomic molecules like TiO, MgH, and CaH we are able to trace to coolest parts of the umbra with our technique, a state-of-the-art multi line spectral inversion implemented in the code SPINOR.

The observations we rely on were taken at ground based (THEMIS) and space-borne (Hinode) observatories recording not only the intensity but also the polarization state of the light. The analysis of this spectropolarimetric data allows us to evaluate thermodynamic and magnetic atmospheric parameters at once.

In a first study we investigated a big sunspot observed at the THEMIS facility in several spectral wavelengths in the optical. Although the substructure of the umbra was spatially not resolved we could extract its properties through our three component model. This was the first time so many molecular features were successfully included in spectral inversions.

In a second investigation we analyzed and compared the properties of umbrae of different sizes. Based on three sunspot umbrae observed by the Hinode satellite we found that two single component models, hot and cool, describe the differently sized umbrae best. We hope that this is the start of a systematic study of many more sunspots available in the Hinode archive.

In a closing chapter we intercompare our results, elaborate on the sunspot umbra substructure and give an outlook on possible future work.

---

# Zusammenfassung

---

Diese Doktorarbeit befasst sich mit der Atmosphäre innerhalb der Umbra von Sonnenflecken.

Sonnenflecken sind dunkel erscheinende Gebiete auf der sichtbaren Sonnenoberfläche, der Photosphäre. Sie entstehen durch die Interaktion von Magnetfeldern mit der Sonnenatmosphäre. Ihre Anzahl und Eigenschaften sind das einfachste und meistbenutzte quantitative Mass für die periodische Aktivität der Sonne.

Die dunkelsten Regionen der Sonnenflecken werden als Umbra bezeichnet und sind von den stärksten Magnetfeldern, die man auf der Sonne messen kann, durchsetzt. Da die Magnetfelder stark genug sind den Energietransport durch Konvektion zu verhindern ist die Umbra etwa 2000 Kelvin kühler als die sogenannte ruhige Sonne innerhalb der Photosphäre. Genaue Beobachtungen der dunklen Umbra zeigen jedoch eine reiche Struktur die von hellen Punkten, *umbral dots*, geprägt ist. Der physikalische Ursprung und die Bedeutung dieser kleinen, hellen Strukturen für den Energietransport innerhalb der Umbra sind noch nicht endgültig geklärt.

In der vorliegenden Arbeit präsentieren wir semi-empirische Modellatmosphären für die Umbra von verschiedenen Sonnenflecken. Neben der weitgehend bekannten horizontalen Verteilung der atmosphärischen

Größen können wir die vertikale Schichtung der Atmosphäre auf dem Niveau der Photosphäre auflösen, d.h.  $T = T(\tau)$ ,  $B = B(\tau)$ ,  $p = p(\tau)$  etc. bestimmen. Um die Eigenschaften der Atmosphäre in verschiedenen Tiefen zu ermitteln, nutzen wir die spektrale Signatur verschiedener temperaturempfindlicher Atome und Moleküle, die in unterschiedlichen Tiefen vorkommen. Deren Licht wird durch das vorliegende Magnetfeld über den Zeeman- und Paschen-Back Effekt charakteristisch verändert und enthält somit Informationen über die thermodynamischen und magnetischen Eigenschaften der lokalen Umgebung.

Bei den Beobachtungen, auf die wir unsere Rechnungen stützen, wurden nicht nur die Intensität sondern auch der Polarisationszustand des Lichtes aufgezeichnet. Die Analyse dieser spektropolarimetrischen Daten erlaubt uns, die thermodynamischen und magnetischen atmosphärischen Größen gleichzeitig auszuwerten.

Im Unterschied zu vorangegangenen Studien beinhaltet unsere Analyse sehr viele Absorptionslinien von temperaturempfindlichen und magnetisch sensitiven Molekülen. Wir sind in der Lage die dunkelste und kälteste Regionen im Sonnenfleck zu studieren, da diese Moleküle, z.B. TiO, MgH und CaH, nur bei den niedrigeren Temperaturen in der Umbra auf der Sonne existieren können. Aus den beobachteten Spektren berechnen wir unsere Modellatmosphären durch die Methode der spektralen Inversion. Dazu benutzen wir das umfangreiche und erprobte Programm SPINOR.

In einer ersten Studie untersuchten wir einen grossen Sonnenfleck, der am THEMIS Observatorium gleichzeitig in mehreren spektralen Fenstern im optischen Wellenlängenbereich beobachtet wurde. Obwohl in den Beobachtungen die Struktur innerhalb der Umbra räumlich nicht aufgelöst werden konnte, gelang es durch ein Modell bestehend aus drei Atmosphärenkomponenten diese Strukturen und ihre Eigenschaften zu unterscheiden. Mit dieser Arbeit ist uns die erste spektrale Inversion gelungen, bei der zusätzlich zu dominanten atomaren Absorptionslinien eine hohe Anzahl an molekularen Absorptionslinien in die Analyse einbezogen wurde.

In einem zweiten Projekt analysierten und verglichen wir die Eigenschaften der Umbra in Sonnenflecken verschiedener Grösse. Wir wählten drei unterschiedlich grosse Sonnenflecken, die durch den HINODE Satelliten beobachtet wurden, und modellierten ihre Atmosphäre mit einem,

im Unterschied zur vorhergehenden Studie, einfacheren Modell, welches nur aus einer Atmosphäre bestand. Wir konnten zeigen, dass die Eigenschaften der verschieden grossen Umbrae mit nur zwei Modellen klassifiziert werden können: Es gibt warme kleine und grosse heisse Sonnenflecken. Wir hoffen, dass dies der Anfang einer systematischen Untersuchung von verschiedenen Umbrae im HINODE Archiv ist.

Im abschliessenden Kapitel vergleichen wir die gefundenen Resultate, diskutieren die Eigenschaften der Strukturen innerhalb der Umbra und geben einen Ausblick auf mögliche technologische Entwicklungen und weiterführende wissenschaftliche Studien.



---

# Contents

---

<b>Abstract</b> . . . . .	iii
<b>Zusammenfassung</b> . . . . .	v
<b>Abbreviations</b> . . . . .	xiii
<b>1. Introduction</b> . . . . .	1
1.1 Light! - The Sun in astrophysics . . . . .	1
1.2 Why sunspots are interesting . . . . .	3
1.3 Outline of the thesis . . . . .	6
<b>2. The Sun, Stokes profiles' synthesis and inversion techniques</b> . . . . .	9
2.1 The Sun in a nutshell . . . . .	10
2.1.1 Observations of the solar atmosphere . . . . .	11
2.1.2 The Sun as a big dynamo . . . . .	16
2.1.3 Solar activity . . . . .	17
2.1.4 Models of the solar atmosphere . . . . .	18
2.2 Sunspots . . . . .	20
2.2.1 The life of a sunspot . . . . .	21

2.2.2	The sunspot umbra . . . . .	21
2.2.3	Semi-empirical models of the sunspot umbra atmosphere . . . . .	22
2.2.4	Sunspot umbrae finestructure - umbral dots . . . . .	25
2.3	Description of polarized light . . . . .	29
2.3.1	Origin of polarized light . . . . .	29
2.3.2	Stokes formalism . . . . .	31
2.4	Detection and interpretation of polarized light from a magnetized atmosphere . . . . .	32
2.4.1	Zeeman effect in atoms . . . . .	34
2.4.2	Zeeman effect in molecules . . . . .	36
2.4.3	Paschen-Back effect in molecules . . . . .	42
2.4.4	Observational consequences . . . . .	42
2.5	Polarized Radiative transfer in atoms . . . . .	45
2.5.1	The optical depth scale . . . . .	47
2.5.2	Height of line formation . . . . .	47
2.6	The art of inversions . . . . .	49
2.6.1	STOPRO and SPINOR . . . . .	50
2.6.2	Other implementations . . . . .	51
2.6.3	Milne-Eddington inversions . . . . .	52
2.6.4	Model building with SPINOR . . . . .	53
2.6.5	Quality of the models . . . . .	53
2.6.6	On uncertainties in the model . . . . .	55
2.6.7	Plane-parallel models . . . . .	56
2.6.8	Multiple components - magnetic filling factor . . . . .	57
2.6.9	A brief test with simulated observations . . . . .	57
2.6.10	Challenges for inversions . . . . .	61
<b>3.</b>	<b>Sunspot umbra model atmospheres . . . . .</b>	<b>63</b>
3.1	Introduction . . . . .	64
3.2	Observation and data reduction . . . . .	65
3.3	Inversions . . . . .	71
3.3.1	Initial values . . . . .	71
3.3.2	Models with a single magnetic component . . . . .	73
3.3.3	Models with two magnetic components . . . . .	74
3.4	Results . . . . .	75
3.4.1	Maps of umbra model atmospheres . . . . .	76

---

3.4.2	Correlation between magnetic field strength and temperature . . . . .	78
3.4.3	Vertical stratification of temperature and magnetic field strength . . . . .	82
3.4.4	Average umbra model atmospheres . . . . .	87
3.4.5	Umbral dots . . . . .	87
3.5	Conclusions . . . . .	93
<b>4.</b>	<b>Sunspot umbrae: from small to large . . . . .</b>	<b>97</b>
4.1	Introduction . . . . .	98
4.2	Observations and data reduction . . . . .	101
4.3	Inversions . . . . .	104
4.4	Results . . . . .	107
4.4.1	Sunspot umbrae model atmospheres . . . . .	107
4.4.2	Wilson depression and plasma beta . . . . .	113
4.4.3	Vertical stratification of the model atmospheres . . . . .	116
4.5	Discussion and conclusions . . . . .	119
<b>5.</b>	<b>Summary and Outlook . . . . .</b>	<b>125</b>
5.1	Summary: Contribution of this thesis . . . . .	125
5.1.1	THEMIS investigation: multi line inversion of ground based sunspot observations . . . . .	126
5.1.2	Hinode study: a comparison of several sunspot umbrae of different sizes . . . . .	127
5.1.3	Comparing the derived models . . . . .	129
5.1.4	The nature of umbral dots . . . . .	130
5.2	The future is bright . . . . .	135
	References . . . . .	139
	Bibliography . . . . .	139
<b>Appendices . . . . .</b>		<b>151</b>
A	Solar facts . . . . .	151
B	Find Initial Models for SPINOR (FIMS) . . . . .	152
C	Rigid Inversion Control (RIC) package . . . . .	153
D	The coordinate systems on the Sun . . . . .	155
E	Atmospheres of Chapter 3 . . . . .	157
F	Atmospheres of Chapter 4 . . . . .	169

<b>Picture credits</b> . . . . .	183
<b>List of publications</b> . . . . .	185
<b>Curriculum Vitæ</b> . . . . .	188
<b>Acknowledgements</b> . . . . .	189

---

# Abbreviations

---

AR	Active Region
BMR	Bipolar Magnetic Region
CF	Contribution Function
CU	Central Umbra
CUD	Central Umbral Dots
DB	Diffuse Background
DU	Dark Umbra
ETH	Eidgenössische Technische Hochschule (Swiss Federal Institute of Technology)
ff	Filling factor
FORTTRAN	Formula Translating System
GOES	Geostationary Operations Environmental Satellite
HSRA	Harvard-Smith Reference Atmosphere
IDL	Interactive Data Language
LB	Light Bridge
LTE	Local Thermodynamic Equilibrium
ME	Milne-Edington (Inversion scheme)
MHD	MagnetoHydroDynamics
MHS	MagnetoHydroStatics
NASA	National Aeronautics and Space Administration

---

NIR	Near InfraRed part of the spectrum
NOAA	National Oceanic and Atmospheric Administration
NSST	New Swedish Solar Tower
PBE	Paschen-Back Effect
PS	PostScript (document format)
pRTE	Polarized Radiative Transfer Equation
PG	Penumbral Grain
PU	Penumbra
PUD	Peripheral Umbral Dots
QS	Quiet Sun
RF	Response Function
RHESSI	Reuven Ramaty High Energy Solar Spectroscope Imager
RTE	Radiative Transfer Equation
S/N	Signal-to-Noise ratio
SDO	Solar Dynamics Observatory
SOHO	SOLar and Heliospheric Observatory
SOT	Solar Optical Telescope
SP	Spectropolarimeter
SPINOR	Stokes-Profiles-INversion-O-Routines
STEREO	Solar TERrestrial RELations Observatory
STOPRO	STOKes PROfiles
THEMIS	Telescopio Heliografico para el Estudio del Magnetismo y de las Inestabilidades Solares
TSI	Total Solar Irradiance
U	Umbral
UD	Umbral Dots
UV	UltraViolet part of the spectrum
VIS	VISual part of the spectrum
VTT	Vacuum Tower Telescope
ZE	Zeeman Effect

---

# Introduction

---

## 1.1 Light! - The Sun in astrophysics

The Sun is sexy. Being just an ordinary star its close vicinity to Earth makes it the single prime target to study stellar surfaces in detail. Under the best conditions nowadays observatories like the Vacuum Tower Telescope (VTT) on Tenerife in the canary islands can reach spatial resolutions of about 0.1 arsec, close to the theoretical diffraction limit. This corresponds to about 70 km on the solar surface. In no other star we have the opportunity to study surface patterns like granulation, fine structure features as well as atmospheric and plasma processes in such great detail. Often used as the first astronomical target for new astrophysical observational strategies, the Sun is of enormous importance as a prototype for other stars and as a plasma laboratory. An enhanced understanding of both, fundamental physics and the Sun itself, is a necessity to understand not only general stellar processes but also the Sun-Earth relations, i.e. the solar impact on space, Earth's weather, and Earth's climate.

Light is the main source of information for inferring the physical conditions of the solar surface. As classical spectroscopy gives us insight into

scalar thermodynamic quantities like temperature, pressure and magnetic field strength, the simultaneous analysis of the polarization state of the light, called spectropolarimetry, has the power to reveal the geometry or geometrical directions, like anisotropies or the orientation of the magnetic field vector. As polarized light originates from physical settings where the spatial symmetry was broken, e.g. by an external magnetic field, an analysis of type and degree of the polarization signals allows us to trace those asymmetries. Thus, by observing the solar polarization signals, the so-called second solar spectrum, a complementary source of information can be exploited (Stenflo & Keller, 1997).

Magnetic fields are the driver of many distinct phenomena grouped under the term solar activity. Long before the magnetic origin of sunspots was recognized by Hale (1908) via the Zeeman effect, astronomers studied this most dominant signature of solar magnetic activity recognizing the famous 11-year sunspot activity cycle. The Zurich Sunspot Number, introduced by Wolf (1850) is still in use to quantify the number of sunspots and sunspot groups daily present on the surface of the Sun. Archived and combined with other proxies of solar variability like the total solar irradiance (TSI) or  $^{10}\text{Be}$  measurements in arctic ice that go further back in time, they form a trustworthy basis for the nowadays generally accepted notion that Earth's climate is influenced by solar magnetic activity (Solanki, 2003a). A change of the solar irradiance, i.e. a change of the energy reaching the Earth, means a perturbation of the Earth's climate.

At its activity maximum, the Sun can cause rapid eruptions -flares- that trigger extreme X-ray and gamma radiation and particle bombardments in so called solar storms. These solar storms can damage any electronic equipment may it be on a satellite or on Earth, causing shut-downs of electric and telecommunication grids. Strong solar storms really are a major threat to the global economy. Thus, high quality solar activity forecasts based on a coherent model of the solar atmosphere are highly desirable.

Hence, solar physics is not only a field to extend the borders of physical knowledge or pushing observational technology. Since the Sun is the power engine for all life on Earth, of all natural and cultural prosperity, it directly or indirectly affects all aspects of human evolution and culture.

## 1.2 Why sunspots are interesting

Sunspots are visible manifestations of the interaction of solar magnetic fields with the solar surface. As such they are the main traces of solar magnetic activity giving us insight into its internal dynamo processes. Understanding dynamos in stellar plasma is of paramount importance contributing to the explanation of many astrophysical phenomena. As the knowledge of sunspot properties increases they provide us with major insights on how the solar dynamo works and become a convenient laboratory for plasma physics to check, e.g., if the widely used MHD approximation, which excludes electromagnetic waves, is valid in solar plasma.

Statistical approaches use the number and occurrence pattern of sunspots to quantify the solar activity cycle. Based on this historic data predictions are made for the next solar cycle's strength and length. But the short-term forecasts for the current solar cycle 24, which turns out to be the least active of the past century, failed dramatically (Cranmer et al., 2010). Meanwhile long-term analyses point towards the fact that our Sun is about to enter a less active phase extending over the next few cycles (Abreu et al., 2008) with continuously decreasing sunspot magnetic field strengths (Penn & Livingston, 2006).

In addition, many ongoing studies focus on sunspots themselves since their structure and evolution are still not fully understood. Although a general fluxtube geometry of the sunspot is undoubted, two hypotheses compete to explain the magnetic configuration below the surface: the monolithic model proposed by Cowling (1953) and the cluster model (also termed jellyfish or spaghetti model) introduced by Parker (1975).

The parameters of the sunspot fluxtubes such as their typical size, magnetic field vector, temperature and other atmospheric quantities at all height levels characterize the properties of real sunspots. This input is most important for theoretical investigations and MHD simulations of sunspots. These simulations help to explain the energy transport, the heating of sunspot umbra through the atmospheric levels and the role and dynamics of the umbral finestructure. Since sunspots represent the largest inhomogeneities of the solar atmosphere any advance in their understanding might be linked to the understanding of the energy transport throughout the general solar atmosphere tackling the so far unsolved

problem of coronal heating.

Simulations of sunspots dynamics, e.g. waves propagating through a sunspot's umbra, do depend on the proper knowledge of the vertical temperature stratification in the lower photosphere that is obtained through semi-empirical sunspot umbra models as presented in this thesis. When comparing simulations with particular observations, it is advisable to have atmospheric parameter stratifications that are as realistic as possible. It helps reproducing the correct wave propagation speeds, their amplitude increase and cut-off frequency. When changing the stratification, the overall propagation and wave transformation picture remains the same but the simulation results change quantitatively. Thus, the precise locations where, for example, the waves are reflected due to cut-off frequency effects depend on the plasma beta unity border, or where the transformation layer is placed, may change (Felipe et al., 2010).

Recent advances in observational techniques provide an unprecedented opportunity to study sunspot substructure. Ground based instruments like THEMIS on the observatory VTT offer to simultaneously detect the full Stokes vector in several user defined wavelength windows while striving for the highest possible diffraction limited resolution images at the same time. On the other hand, space-borne platforms like the satellites HINODE/SOT or SDO provide seeingless high resolution observations. Inversion techniques, like those used and described in this thesis, are state-of-the-art tools to analyze this wealth of data and to extract the sunspot's atmospheric properties.

The atmospheric conditions at the photospheric level can be monitored through absorption lines in the optical wavelength range. By observing not only the intensity but also the light's polarization state we collect even more information from which we can e.g. infer the orientation of the magnetic field vector. Further, by employing not only one but many spectral lines at once the accuracy of this approach increases, since different lines show different sensitivities to the temperature and other atmospheric parameters. It has been demonstrated that the amount of information present in an observed data set is a monotonically increasing function of the number of available spectral lines (Asensio Ramos et al., 2007). By simultaneous analysis of e.g. the Fe I lines at 525 nm the magnetic field and the filling factor can be decoupled (Stenflo, 1973).

Including not only atomic lines but also absorption features of mole-

cules in our analysis allows us to trace the sunspot atmosphere on a finer grid. This approach is especially useful for investigating the rather cool environment of the umbra and its substructure. At about 4500 K and below umbral spectra show saturating atomic lines and increasingly dominant temperature and magnetically sensitive features of e.g. TiO, MgH, CaH, C<sub>2</sub>, OH, SH, CH, and FeH (Berdyugina, 2010).

With molecular spectropolarimetry we immediately locate the coolest patches of the solar atmosphere where molecules can exist without dissociation. Therefore, molecular lines are also excellent tracers for other cool stellar atmospheres (Berdyugina et al., 2003).

The Sun is the closest star astrophysicists can observe, and it is not the only one presenting spots. It is probable that all late-type stars with external convective envelopes exhibit magnetic activity similar to that of the Sun and show so-called *starspots*. Ranging in age from the pre-main sequence phase up to the asymptotic giant branch it is estimated that 90 % of all stars in the Milky Way exhibit starspots (Berdyugina, 2005; Strassmeier, 2009).

Techniques like (Zeeman-)Doppler imaging reveal a significant coverage of the stellar surface (up to 20 %, according to Strassmeier, 1999). Since sunspots usually cover only about 0.0001 % of the solar surface it may not be appropriate to simply scale up sunspot models in order to explain starspots (Solanki & Unruh, 2004). However, we will have to understand sunspots before we can hope to understand starspots.

Although a vast amount of empirical knowledge has been gathered on sunspots and theoretical descriptions have improved, a number of fundamental questions do persist as observations always focus on singular objects. I may just list some of them (see Solanki, 2003b, chap. 8 for more):

- What is the subsurface structure of sunspots?  
Monolithic vs. Spaghetti model (vs. combination of both)
- Why is there penumbra and umbra?
- Why do sunspots have the observed sizes and lifetimes? Are there intrinsic limits?

- How small are the smallest brightness and magnetic structures in umbrae and what is their nature? Is there a difference between lightbridges and umbral dots and among umbral dots originating from different locations?
- How is the umbra (chromosphere) heated?

Answering these questions not only improves the understanding of sunspots as magnetic and dynamic structures but also places constraints on the solar dynamo at work. This is the bigger context in which this thesis was set up.

The goal of this thesis is to answer the first question, i.e. to discriminate between the monolithic and spaghetti model by constructing semi-empirical atmospheric models of sunspots which include more molecular lines than any comparable former study.

### 1.3 Outline of the thesis

This thesis focuses on the atmosphere of sunspot umbra and umbral substructure at the photospheric level. We create semi-empirical models for umbra subregions that reveal the vertical stratification of the temperature, the magnetic field vector and more physical properties of umbra substructure.

We analyze spectropolarimetric observations of sunspots obtained in the optical at both the ground-based facility THEMIS in Chapter 3 and the spaceborne platform HINODE in Chapter 4. Since diatomic molecules can survive in the cool environment of the umbra we combine their absorption features as temperature tracers with strong and magnetically highly sensitive atomic lines observed simultaneously. These full Stokes observations of a number of blends of many lines are processed simultaneously by spectral inversion using the inversion code SPINOR.

In the following chapter we give a short overview of the Sun and its atmosphere in Sect.2.1 and sunspots in particular in Sect.2.2 where we also review the latest findings from sunspot models. To understand how

---

the observation of polarized light helps us to learn more about the solar atmosphere we have to introduce the Stokes formalism to describe polarization in Sect.2.3 and must understand how the properties of a magnetized atmosphere are imprinted in atomic and molecular spectra via the Zeeman and Paschen-Back effect in Sect.2.4. In addition, the most necessary bit of polarized radiative transfer is covered in Sect.2.5 to understand how we can find not only the order of magnitude of atmospheric parameters but also their vertical stratification using spectral inversions. Finally, we describe the technique of spectral inversions and the implementation SPINOR in Sect.2.6.

The body of this thesis consists of two parts:

In Chapter 3 we create a semi-empirical model for an average sunspot umbra atmosphere. For this project a unique spectropolarimetric dataset was obtained in the optical at the THEMIS facility at Tenerife covering an entire large sunspot. Not only single atomic lines but several spectral windows containing atomic and the strongest known molecular absorption features were observed simultaneously. With these full Stokes observations inversions were carried out simultaneously for the whole Stokes vector containing blends of atomic and molecular absorption lines at different wavelengths. Our method reveals two magnetic components coexisting in each spatial resolution element accounting for unresolved substructures. As a major result and input for further studies a semi-empirical model atmosphere for the sunspot umbra and its subregions is created.

The properties of the umbra atmosphere depend on the size of a sunspot. In Chapter 4 we exploit the huge free archive of sunspot observations obtained by the Spectropolarimeter (SOT/SP) aboard the HINODE satellite. We choose spectropolarimetric observations of several sunspots of different sizes to compare their atmospheres. Full Stokes observations of the blend at 6302 Å including atomic and molecular absorption features are inverted. Similar umbra substructures like umbral dots are located in each sunspot and compared among the sunspots.

A summary compares the results and elaborates on the properties of the umbral substructure. Finally, an outlook on future perspectives of inversion techniques and the science they enable us to do is given at the end of the thesis.

---

# The Sun, Stokes profiles' synthesis and inversion techniques

---

This introductory chapter provides an overview of what we know about the Sun in general and sunspots in particular. After concentrating on the conditions of the light source, the solar photosphere, we focus on the atomic and molecular Zeeman effect that imprints magnetic information on the (polarized) light. Finally, the most necessary bit of polarized radiative transfer theory is reviewed to explain the inversion technique used to infer the atmospheric parameters. A brief summary of the implementation of the inversion code SPINOR and practical information for its hands on use can be found at the end.

The following is based on excellent sources about general solar astrophysics (Stenflo, 1994; Stix, 2002), stellar atmospheres (Mihalas, 1978; Grey, 1976), the theory of atomic (Sobel'man, 1972) and molecular spectroscopy (Herzberg, 1939) and latest reviews on sunspots (Solanki, 2003b), their umbra substructure (Thomas & Weiss, 2004) and solar magnetism (Solanki et al., 2006).

## 2.1 The Sun in a nutshell

The Sun is an ordinary main sequence star of spectral class G2V. A yellow dwarf with an effective surface temperature of about 5575 K. It generates its energy by nuclear fusion of hydrogen nuclei into helium. Being the central star of the Solar system its light travels 8 minutes and 20 seconds to reach the Earth about 149.6 million kilometers (1 AU) away. Table A.1 lists the most important facts about the Sun.

The structure of the Sun, as well as any stellar structure, can be illustrated by a model of spherical shells (see Fig. 2.1).

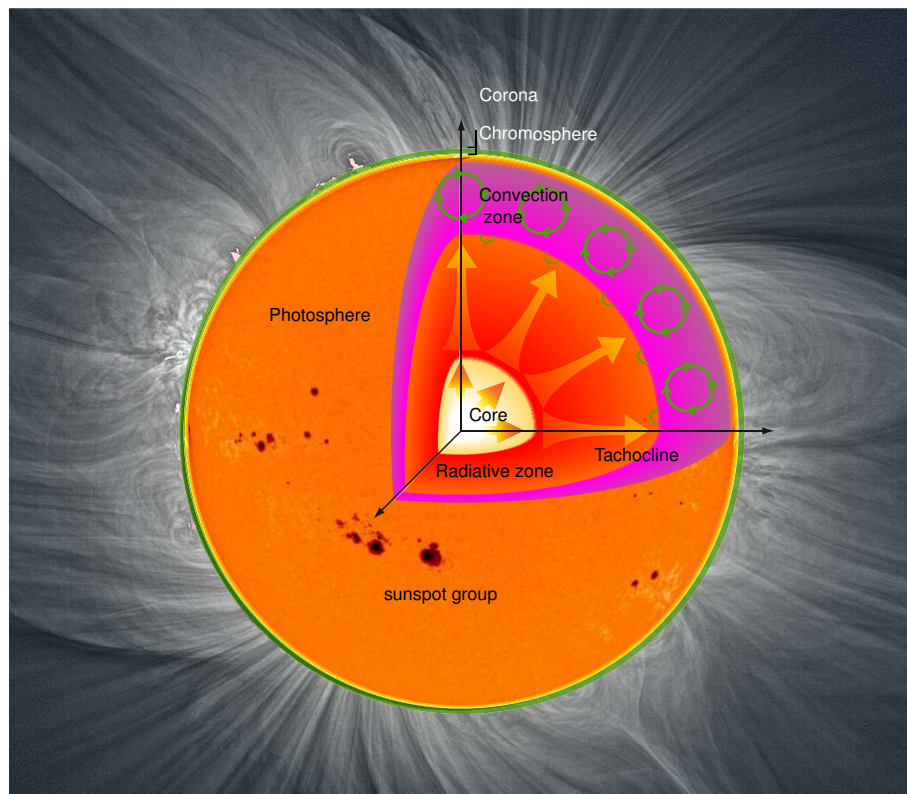


Fig. 2.1 The structure of the Sun. The hot core and the radiative zone reach out to about  $3/4$  of the solar radius where the tachocline marks the transition to the convection zone. The solar atmosphere composed of photosphere, chromosphere, and corona lies above. (Corona image by Miloslav Druckmüller, with kind permission)

In the next sections we will briefly sketch the path of the energy originating from fusion processes in the solar center towards the outer atmospheric layers where it is radiated away towards our detectors.

### 2.1.1 Observations of the solar atmosphere

The solar atmosphere is defined as the region of the Sun from where photons can escape into space. It is the transition region between the solar interior and the interstellar medium.

#### Below the photosphere: the solar interior

The NUCLEUS or CORE is the central part of the Sun's interior where nuclear fusion converts hydrogen into helium at temperatures of about 15 million Kelvin. This extremely dense region covers about a quarter of the solar radius (García et al., 2007). The nucleus is surrounded by a RADIATIVE ZONE extending to about 70 % of the solar radius. In that region the energy flux is transmitted outwards by electromagnetic radiation. The radiative zone includes the nucleus and is believed to rotate as a rigid body with a constant angular velocity. The CONVECTIVE ENVELOPE above is defined by such a high opacity and such a high temperature gradient that energy transport by radiation becomes inefficient. Instead, almost the entire flux is carried outwards by convection. Starting at the TACCHOCLINE, i.e. the border between radiative zone and convective envelope, the outer layers of the Sun rotate no longer as a rigid body but show differential rotation, i.e. faster at the equator than at the poles with increasing distance to the solar center.

Above these layers, as soon as the accumulated opacity, the optical depth as observed from Earth, drops below unity<sup>1</sup> and solar radiation can escape into space. This is the lower boundary of the solar atmosphere we want to study. The solar atmosphere consists of the three layers photosphere, chromosphere and corona in each of which different structures can be observed.

---

<sup>1</sup> Usually the optical depth at 5000 Å is used to define the solar surface:  $\tau_{5000} = 1$  (see Chapter 2.5.1).

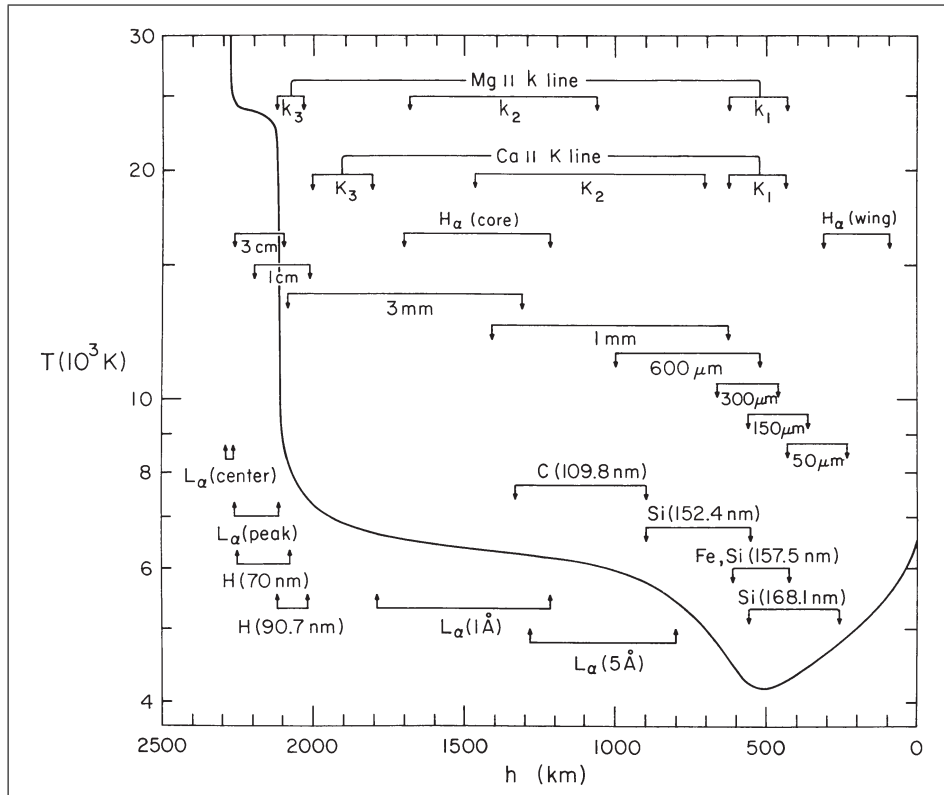


Fig. 2.2 Temperature stratification of the solar atmosphere in the quiet Sun (taken from Vernazza et al. (1981)). Ranging from the transition region between corona and chromosphere down to the temperature minimum that defines the upper limit of the photosphere towards the  $\tau_{5000} = 1$  continuum. The approximate depths where the various continua and lines originate are indicated. This thesis, however, focuses on the photosphere, i.e. the first few hundred km still below the temperature minimum.

### The photosphere

This thesis focuses only on the photosphere which is the layer immediately above the convection zone at which the solar atmosphere becomes transparent at temperatures of about 6000 K. It only spans about 500 km in height but emits the bulk of the electromagnetic radiation observed as the solar spectrum (see Fig. 2.3). It is optically thin in the visible (VIS), ultraviolet (UV) and near infrared (NIR) continua but optically

thick in spectral lines (Stix, 2002). Since the temperature decreases with height for the first few hundred km the visible spectrum of the Sun is an ABSORPTION LINE SPECTRUM (see Fig. 2.2). When a spectral line is observed the higher optical depth at the line core, i.e. at the rest wavelength, causes to observe higher layers than in the line wings. Thus at the rest wavelength we see cooler layers with respect to the continuum. This leads to dark absorption features superimposed at the otherwise continuous spectrum of the brighter continuum. The same line of argument explains LIMB DARKENING an wavelength dependent effect visible in all images of the Sun. Due to geometrical reasons we observe cooler atmospheric layers when we look at the limb of the Sun than when we point at its center. Interestingly, the temperature in Fig. 2.2 does not decrease monotonically when going further away from the solar center as it would be the case for a radiating body in radiative equilibrium, i.e. if the energy were dissipated by electromagnetic radiation alone. Instead, a photospheric temperature minimum is reached at a height of about 500 km. Above, in the chromosphere and corona, much higher temperatures of up to a million K have been reported (see e.g. Golub & Pasachoff, 1997, for details).

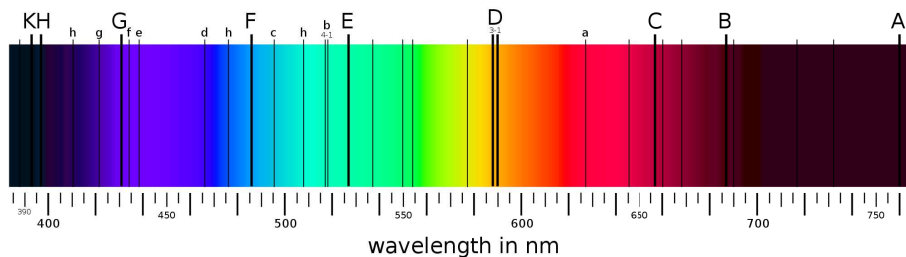


Fig. 2.3 The continuous solar spectrum with the main absorption features, the Fraunhofer lines, in the visible.

The photosphere is dominated by the cellular pattern of *granulation* forming the so-called QUIET SUN. Here, the hot fluid rises in the form of convection cells to the outer border of the turbulent convection zone and cools down by radiating away energy into the transparent photosphere. The material spreads out across the surface, cools and descends again in the narrow INTERGRANULAR LANES at a few  $\text{km s}^{-1}$ . This chaotic process has a timescale of several minutes; the typical size of granules

Tab. 2.1 Properties of magnetic structures observed on the solar surface. As there are sunspots, pores, magnetic knots (MK), and bright points (BP) (Stix, 2002).

parameter	sunspots	pores	MK	BP
$I_c$	0.05 – 0.3	0.2 – 0.7	1.0	$\geq 1.1$
dimension [Mm]	4 – 60	0.1 – 7	$\approx 0.6$	$\leq 0.2$
magnetic flux [ $10^{18}$ Mx]	500 – 3000	50 – 250	$\approx 10$	$\approx 0.1$
magnetic field [ kG ]	$\leq 4$	1 – 2	1 – 2	
typical lifetime	days to weeks	several days	$\approx 1$ h	

is 1–2", about 700–1'400 km on the solar surface. On a bigger scale of about 20'000 km SUPERGRANULES show a similar velocity pattern flowing horizontally from the center towards the edges at a speed of about 0.5 km s<sup>-1</sup>. These larges convection cells have a mean lifetime of about 20 h. Their boundaries form the *photospheric network*.

Apart from the convective nature of the granulation, there are other structures visible in the photosphere that have a clearly magnetic origin. The largest structures, *sunspots* and *pores*, basically sunspots without penumbra, usually appear in the activity belt around the solar equator between  $\pm 35$  deg latitude. They are embedded in magnetically *active regions* and may be accompanied by magnetic knots and plages, i.e. cluster of faculae. Outside active regions extended magnetic networks can be observed almost everywhere on the solar surface.

The elementary magnetic structure seems to be a small bundle of magnetic field lines concentrated by converging motions and convective collapse, a *magnetic flux tube* (Stix, 2002, chap. 8.2). These magnetic structures are scale invariant and a possible lower cutoff of their distribution (Stenflo, 2010) is expected at scales of a few km where the Ohmic diffusion and other dissipative processes eventually operate effectively. In the quiet Sun, the magnetic flux seems to be concentrated in flux tubes within the network as found by Stenflo (1973).

Sunspots are generally thought to represent scaled up versions of the smaller scale thin flux tubes. See the bottom panel of Fig.2.4 that shows a vertical cut through a snapshot of a recent sunspot simulation by Rempel et al. (2009).

Most information about the photosphere has been obtained in the

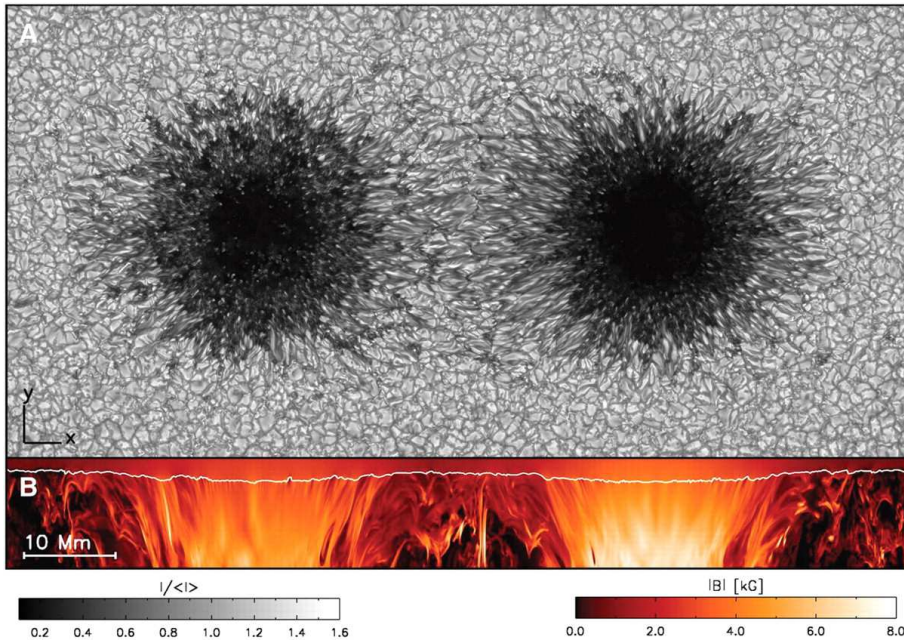


Fig. 2.4 Snapshot from the simulation. (A) Surface brightness map of the sunspot pair and the surrounding convective pattern (granulation). (B) Color representation of the field strength (saturated at 8 kG) in a vertical cut through the midplane of the simulation box at  $y = 25$  Mm. The vertical direction is stretched by a factor of 2. The white line indicates the height level of the visible surface (optical depth unity). Figure taken from Rempel et al. (2009) with kind permission.

optical (VIS) and near infrared (NIR) part of the spectrum. With a few exceptions the lines of the visible part of the Fraunhofer spectrum are formed between the layer of continuum formation and the temperature minimum thus scanning a height range of about 500 km.

The magnetic field and its structure can be observed most precisely in the photosphere. Only at the moderate photospheric temperatures the number densities of species absorbing in the optical and infrared are high enough such that the Zeeman-Effect can be used to probe the magnetic field at the solar surface. This field creates phenomena extending over several orders of magnitude in spatial size, from the well known sunspots visible by the naked eye (several 10 000 km), over pores (1000 km) down

to small-scale magnetic flux elements ( $<100$  km). The size distribution of magnetic structures is still under debate (Stenflo, 2010). See Table 2.1) for a comparison of the bigger magnetic features.

### **Above: chromosphere, transition region, corona, solar wind**

The *chromosphere* is the layer above the photosphere and extends for some 1000 km. Here, the temperature rises again from the temperature minimum of about 4000 K to about 25 000 K in its upper layers. The chromosphere is optically thin in UV, VIS and NIR continua, but optically thick in strong spectral lines (Judge, 1998). It is usually observed with monochromatic filters centered at strong lines the most prominent of which are the yellow Calcium Ca II H and K lines at 3933 Å and 3968 Å and the red Hydrogen Balmer- $\alpha$  line ( $H_\alpha$ ) at 6563 Å. These lines are the standard to be observed when probing the activity of the Sun (Holzreuter, 2009). Above the chromosphere, the *transition region* connects to the *corona*, the mystical outer layer extending to several solar radii. This region can be best observed at radio wavelengths, with X-rays or off-limb during solar eclipses. Its temperatures are enormous:  $\approx 2$  million K! Radiatively, the corona cannot be heated by the radiation field from the layers below. In order to save the second law of thermodynamics there must exist one or more non-thermal processes, either mechanical or magnetic, that fuel this layer (Golub & Pasachoff, 1997).

The *solar wind* is a continuous stream of ionized particles evaporating from the upper layers of the corona. Due to the high thermal conductivity of the corona, high temperatures can be found out to some  $10 R_\odot$ . Here, the thermal energy exceeds the gravitational potential that otherwise binds the coronal plasma. Matter from below streams up to replace the continual loss of material ( $\approx 10^9$  kg s $^{-1}$ ) (Parker, 1958).

### **2.1.2 The Sun as a big dynamo**

Although the Sun's magnetic field can be approximated as a dipole its configuration is much more complex. Its origin seems to be a (combination of) stellar dynamo(s) depending on the Sun's inner structure and differential rotation.

Seen as a huge plasma sphere the Sun itself is a very good electrical conductor and can thus be described by the laws of magnetohydrodynamics (MHD). Following Ampère's law, the solar magnetic dipole field is produced by a circular electric current flowing deep within the star. The source of this solar dynamo is thought to be located at the tachocline, the region at about 2/3 of the solar radius that divides the core from the differentially rotating convection zone (see Fig.2.1). When ropes of magnetic field lines rise they form giant loops that finally penetrate the solar surface. Within these bundles of dense magnetic fields magnetic pressure causes a decline in plasma density. Along the magnetic field convection is prevented causing these areas to be significantly cooler than the rest of the Sun. These are sunspots.

The overall rotation causes the plasma fluid to move through the pre-existing magnetic field inducing electrical currents that retroact on the magnetic field. Due to the differential rotation the flow has a strong shear component that stretches the individual field lines thus amplifying the existing magnetic field. Such systems are called self-exciting MHD dynamos and include a winding up of magnetic field lines due to differential rotation (omega effect) and twisting of single magnetic field lines (alpha effect). The Sun's meridional flow -the flow of plasma along meridian lines from the equator toward the poles at the surface and from the poles to the equator deep inside the convection zone- must also play an important role in the Sun's magnetic dynamo (Dikpati et al., 2010). However, the detailed mechanism of the solar dynamo is not yet known and far from being understood in detail.

A helpful text on solar dynamo theory is Charbonneau (2005) backed up by the monographs of Moffatt (1978) and Krause & Raedler (1980). The text books of Baumjohann & Treumann (1996), Baumjohann & Treumann (1997), and Benz (2002) may serve as both, introduction to and reference for plasma physics and MHD theory.

### 2.1.3 Solar activity

The Solar activity cycle has a period of about 11 years causing the solar energy received at the Earth's upper atmosphere, the total solar irradiance (TSI), to vary between  $1365.5 \frac{W}{m^2}$  at solar minimum, and  $1366.6$

$\frac{W}{m^2}$  at the maximum (e.g. Wenzler, 2005; Fröhlich, 2009, and references therein).

Studying the sunspot record available since 1610 the irregular 11-year cycles of activity have been discovered. Interestingly, it is modulated on longer timescales, e.g. periods of 220 years, as well and was interrupted by a grand minimum, the Maunder minimum in the 17th century. Since the orientation of the magnetic field changes about every 11 years the double period of about 22 years is often noted to describe the period of the solar magnetic cycle.

To predict the future behavior of the activity cycle, short- and long-term, is among the primary goals of solar physics researchers (Cranmer et al., 2010), but predictions failed dramatically for the start of the current cycle 24. One reasonable explanation is that the last 8 cycles have shown an abnormally high activity - the *grand modern maximum*.

Based on the proxy record of cosmogenic  $^{10}\text{Be}$  abundances in the GRIP icecore from Greenland reaching back almost 10 000 years, a statistical analysis by Abreu et al. (2008) predicts a termination of the present grand modern maximum at around 2020.

It might be considered bad luck that the present fleet of spacecrafts dedicated to observing the Sun (SOHO, GOES, RHESSI, Hinode, SDO, STEREO, etc.) that was started during times of high minima now is starved for observational possibilities, e.g. big sunspots or flares.

This thesis on sunspot atmospheres was written in between the end of solar cycle 23 and the begin of solar cycle 24 when only a few sunspots were observed at the Sun.

#### 2.1.4 Models of the solar atmosphere

A solar model atmosphere is a numerical description of the actual solar atmosphere. It consists of the most important physical quantities such as temperature, gas pressure, electron pressure, density, opacity, and the magnetic field vector - all as a function of depth.

There are two ways of computing a model atmosphere: the semi-empirical and the purely theoretical method. In theoretical models the system of appropriately simplified equations describing the physics is solved in a self-consistent way whereas in semi-empirical models the atmosphere is constructed to results in a best possible fit to observational

data. In order to overcome both mathematical and physical difficulties several simplifications have to be made to render the problem computable by current numerical methods and computer power. In model atmospheres for the photosphere, usually the following assumptions apply (Mihalas, 1978, chap. 7).

**Steady state:** In steady state all time-dependent effects are neglected. No dynamics are considered.

**Geometry:** The atmosphere is assumed to be composed of homogeneous, plane-parallel layers whose thickness is much less than the solar radius. In first approximation small-scale inhomogeneities like granulation are neglected. The dimensionality is reduced to one. Since the layers in the Sun are clearly not homogeneous containing magnetic structures as well as quiet sun areas different atmospheres have to be used side by side combined by the parameter filling factor. The filling factor gives the percentage of the magnetic area in one spatial resolution element.

**Momentum balance:** A common assumption is *hydrostatic equilibrium* which means that gravitational and pressure forces of all kinds are balanced. In a plane-parallel atmosphere the hydrostatic equilibrium equation (Grey, 1976) reads:

$$\frac{\partial p_{tot}}{\partial z} = -g\rho, \quad (2.1)$$

where  $p_{tot}$  is the total pressure including magnetic, turbulence, radiation, electronic, and gas pressure,  $g$  is the gravitational acceleration at the solar surface assumed to be constant with depth,  $\rho$  the mass density and  $z$  the geometric height in the atmosphere.

**Local thermodynamic equilibrium (LTE):** The assumption of LTE considerably reduces the calculation effort. LTE means that all processes are in equilibrium and that the radiation field that could give inputs from other locations is coupled only to the local properties of the gas. In the local isothermal equilibrium of radiation and excited states the Boltzmann-statistic describes the distribution of states. LTE implies a collision dominated environment and thus dense and opaque

layers as can be found in the photosphere. However, the most important implication is that the source function equals the Planck function in LTE.

## 2.2 Sunspots

Sunspots appear as black features on the solar surface. They are the most prominent and clearly visible manifestation of solar magnetic field concentrations interacting with plasma. The presence of these intense magnetic field strengths, that suppress the convective flows from below, is the fundamental condition required for the formation of the dark inner core, the *umbra* (Cowling, 1953). The existence of a less dark filamentary halo, the *penumbra* distinguishes sunspots from the smaller pores, but we do not consider the penumbra in this thesis. Sunspots have a diameter of typically 10 000-40 000 km (10–60 arcsec), which translates to a covered area of 0.02 – 0.1% of the visible solar disk. For an extensive overview see the encyclopaedical review on sunspots by Solanki (2003b) and the review on umbra substructure, especially umbral dots (UD) by Thomas & Weiss (2004).

There are two competing hypotheses to explain the sunspots' structure below the photosphere:

**The monolithic model** describes the whole sunspot as a single compact flux tube with a radius comparable to its vertical extend. Driven by convection plumes of plasma, triggered by oscillations, may rise through the sunspot causing short-lived and field free bright dots throughout the umbra (Thomas & Weiss, 2004).

**The cluster model or spaghetti model** describes a single flux-tube at the photospheric level that splits up into a bundle of thin but elongated fluxtubes below that are surrounded by field free matter. In between, columns of hot material rise to the surface being observed as umbral dots (Parker, 1979).

The young field of local helioseismology is addressing this question analyzing measurements of wave travel times and local mode frequencies by inversion techniques very similar to our spectral inversions (Gizon

et al., 2009).

### 2.2.1 The life of a sunspot

The large-scale mechanisms that lead to sunspot formation and their long-term stability remains vague, although the overall picture seems clear: Driven by the differential rotation a magnetic flux rope detaches from its formation region close to the tachocline. As it rises through the convective layer the magnetic rope gets twisted by the Coriolis force forming an  $\Omega$ -shaped loop that finally penetrates the solar surface. The footprints of such a loop extending outwards into the upper solar atmospheric layers are forming a *bipolar magnetic region (BMR)*, observed as an *active region (AR)* due to the emergent magnetic flux. Usually, these BMRs are composed of two regions of opposite magnetic polarity (Hale's law) and are tilted by about 15 deg with respect to east-west direction such that the leading, western polarity is closer to the equator (Hale et al., 1919, Joy's law).

With more and more magnetic flux emerging through the leading polarity's photosphere, pores begin to form. Most of them disappear within hours but occasionally one starts to grow. At a critical size (about 3500 km) it forms a penumbra, the definitional attribute of a sunspot. Recently, Schlichenmaier et al. (2010) observed the formation of a penumbra around a pore within hours. Starting at the side opposing the other polarity the filaments of the penumbra grew around the pore in both directions until the sunspot was surrounded. At this point the spot has reached its maximum size. Between two and four days lie between the first appearance of magnetic structures and the moment of maximum development Harvey (1991). Although most small sunspots are short lived and decay quickly by fragmentation, bigger ones survive for days if not weeks as they gradually decay. Observations indicate that their lifetime linearly depends on their area.

### 2.2.2 The sunspot umbra

The presence of a strong magnetic field causes a magnetic pressure ( $p_{mag} = B/8\pi$ ) in addition to the gas pressure within the umbra to counteract

the gas pressure of the environment in hydrostatic equilibrium. It effectively creates a hole in the photospheric layer leading to the Wilson depression, i.e. a dent of the  $\tau_{5000} = 1$  surface with a depth of a few 100 km. Furthermore, the magnetic field hinders the convective motions and thus the heat flow from below the photosphere. As a consequence the temperature drops to about 3500 K.

In these coolest regions of a sunspot the typical magnetic field strength ranges from 1–4 kG depending on the sunspot's size. Here, the magnetic field is nearly vertical with respect to the solar surface. Tracing the magnetic field radially outwards towards the sunspot's limb the magnetic field gets inclined down to about 80 deg while the magnetic field strength decreases rapidly (Westendorp Plaza et al., 2001).

### **2.2.3 Semi-empirical models of the sunspot umbra atmosphere**

Sunspot models can be divided into two classes: pure numerical models that are based on purely theoretical considerations and semi-empirical models which are constrained by observations. Numerical models include the radiative MHD simulations (e.g. Rempel et al., 2009) of whole sunspots and their finestructure as well as MHS models focusing on single sunspot properties: there are self-similar models (e.g. Shelyag et al., 2009), pressure distributed models for waves in sunspots (Khomenko & Collados, 2009), current sheet models (Gokhale & Zwaan, 1972), and potential field models (Spruit, 1976)).

Semi-empirical models on the other hand provide the stratification of thermodynamic variables and the magnetic field vector based on empirical data and theoretical considerations of mechanical equilibrium and radiative transfer. They provide a connection to reality by considering observations of steadily increasing quality, i.e. higher spatial and spectral resolution or wider wavelength coverage, as well as complexity, i.e. observation of full Stokes vectors of multiple lines tracing different layers of the solar atmosphere simultaneously.

There are two groups of semi-empirical models. The older comprises spatially unresolved 1D models based on multi-wavelength observations of the continuum and weak and strong absorption lines. Most are single-component, representing a horizontal average over the umbra, while oth-

ers consist of two components, bright and dark, to account for spatially unresolved structures.

The more recent group of semi-empirical models is based on inversions of the radiative transfer equation of polarized light. In contrast to the former group, typically high resolution spectro-polarimetric observations are used as input. A best fit of the spectral line profiles is found by strict mathematical methods as described in Section 2.6 to constrain a depth dependent 1D atmosphere including the magnetic field vector. Sequentially applied to all points of a map the configuration of the sunspot can thus be retrieved.

The contribution functions of the analyzed spectral lines determine a depth range of usually up to 400 km above the continuum layer, i.e. to the temperature minimum between photosphere and chromosphere where LTE can be assumed (see Socas-Navarro, 2007, for NLTE inversions of Ca II extending to the chromosphere). These semi-empirical models found by spectral pRTE inversions can include one or more components to account for straylight or model unresolved magnetic components. Typically, these unresolved magnetic components include different magnetic field strengths and are found to have different temperatures at the same time.

All these models are useful in constraining the structure of a real sunspot atmosphere providing hints on the physical processes behind. They provide background models for studying, e.g., element abundances and wave propagation in sunspots (Felipe et al., 2010).

Below, the most often used umbral models are briefly described.

- The *sunspot sunspot model* by (Avrett, 1981). A composite temperature-density model of sunspot umbrae from the photosphere up to the chromosphere-corona transition region (up to 2280 km above continuum). It combines the low photospheric model of Albregtsen & Maltby (1981), the model for the upper photosphere and lower chromosphere by Lites & Skumanich (1982), and the model of the transition region between chromosphere and corona by Nicolas et al. (1981).
- The model of (Staude et al., 1983) covers the full height range above the umbra from photosphere to corona based on a set of different observations (optical, radio, EUV, X-ray).

- Maltby et al. (1986) improved the model of Avrett (1981) in deeper layers. Based on observations of 15 sunspots he composed a set of three umbra models, each for a different phase of the solar cycle (E: early/hot, M: middle, L:late/cool).

These models belong to the first group, providing only variations of thermodynamic properties. On the other hand side, the models below do rely on inversions including the stratification of the magnetic field strength.

- Collados et al. (1994) reported on models based on inversions (Stokes  $I$  and  $V$  only) of the dark core umbra of both, large and small spots obtaining the temperature, magnetic field vector, and velocity along the line-of-sight.
- Westendorp Plaza et al. (2001) derived the atmospheric parameters (temperature, magnetic field, velocity) for a full sunspot including penumbra based on full Stokes inversions of the Fe I lines at 6302 Å. He employed only one magnetic component (plus one straylight component) to invert each 1 arcsec pixel of his map independently.
- Mathew et al. (2003) provided a similar model from inversions of infrared Fe I lines at 1.56  $\mu\text{m}$ . In Mathew et al. (2004) the authors even provided calculations of the plasma beta and maps of the Wilson depression.
- Socas-Navarro (2005) produced a 3D model of a sunspot (umbra and penumbra) from simultaneous inversions of two photospheric (Fe I at 8497 Å and 8538 Å) and two chromospheric lines (Ca II triplet at 8498 Å and 8542 Å) that can only be computed under non-LTE conditions (see Socas-Navarro et al., 2004, for temperature profiles).

Notable, although not a model of a sunspot umbra but a penumbra, is a single-component model presented by Puschmann et al. (2008) who assumed that the finestructure of the penumbra filaments is resolved in Hinode/SOT data. They checked their model to be divergence-free and in equilibrium in both horizontal and vertical directions.

From the history of umbra models and their increasing complexity, taking into account high resolution spectro-polarimetric measurements

of many lines simultaneously, it seems unavoidable to include molecular absorption features and molecular blends as an additional source for information in cool umbrae as we did in our investigations presented in Chap. 3 and Chap. 4.

Combined, these models reveal an umbra that is cooler than the surrounding field free regions in the photospheric layers, but slightly hotter in the chromosphere. Also, coronal temperatures are reached at lower heights above the sunspot umbrae (see Collados et al., 1994, for comparison plots). But it has to be noted that unlike models for the quiet Sun, sunspot models are always retrieved as representative examples being not applicable in all cases. From the variety of models derived by different methods and authors it can be found that the temperature stratification depends sensitively on the sunspot size and therefore on its brightness and magnetic field strength as well as on the phase of the solar cycle.

#### 2.2.4 Sunspot umbrae finestructure - umbral dots

Sunspots do show a variety of fine structures in both the umbra and the penumbra as can be seen in Fig. 2.5. In this thesis we only concentrate on the umbra.

*Ligtbridges (LB)* are lanes of bright matter dividing the sunspot umbra. Measurements of the convective and magnetic characteristics of LBs could be useful to discriminate between the monolithic and the cluster model. LB are observed to appear during the formation of sunspots as well as during their decay. Their brightness can reach and sometimes exceed the brightness of the quiet sun and they show a central dark lane with horizontally moving grains where the magnetic field might modify but not completely suppress convective motions. Usually, the magnetic field strength is several hundred Gauss smaller and the inclination of the magnetic field is higher than in neighboring umbral areas. Analysis of time-series revealed umbral dots moving away from LBs into the umbra (Berger & Berdyugina, 2003a).

*Umbral dots (UDs)* are umbra substructures of subarcsecond size that were revealed by high resolution observations (see Fig. 2.5) (Danielson, 1964). Umbral dots are considered to be critical for the vertical heat transport through the strong magnetic field of the umbra. Since the umbral magnetic field prohibits convection as seen in the granulation pattern

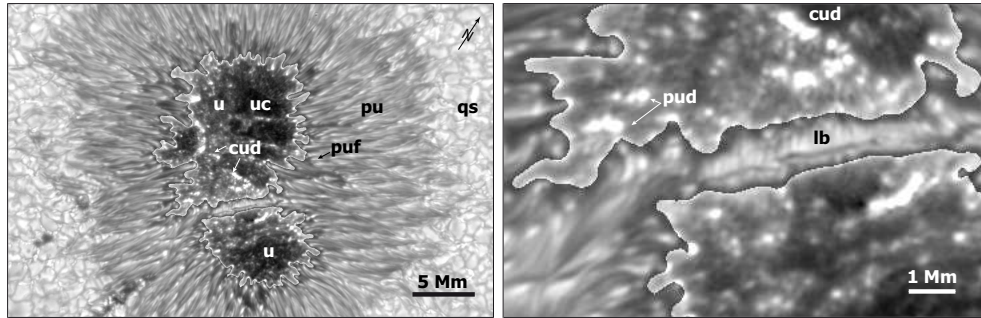


Fig. 2.5 Irregular sunspot NOAA 10 669 observed in the TiO filter around 7054 Å in Sep 2004 at the NSST, La Palma. The superior contrast of the molecular band head image has been further enhanced. Generally, the sunspot made of umbra (u) and the surrounding filamentary penumbra (pu) is floating in the quiet Sun's (qs) granulation pattern. Here, clearly a strong lightbridge (lb) divides the sunspot. Close to the lightbridge and the borders of the umbra many peripheral umbral dots (pud) are visible. Also central umbral dots (cud) can be seen forming network like patterns close to the core umbra (cu), the darkest region. The penumbral filaments and their penumbral bright points are indicated as well.

of the quiet Sun the thermal energy must be transported differently.

As the subsurface structure of sunspots still awaits discovery, two pictures of UD are competing to explain the observations: plumes and columns.

The most recent MHD simulations of sunspots see substructure in the umbra (Rempel et al., 2009). There, rising parcels of hot plasma, nonstationary narrow plumes, can be traced which are field free and thus convective within themselves producing a dark lane at their very center when seen from above. The authors stated that since they begin their simulations with a stable monolithic like arrangement of the magnetic field structure, rising plumes may be a natural consequence of the initial conditions (Schüssler & Rempel, 2005; Schüssler & Vögler, 2006). They also stress that the grid resolution is still insufficient to allow for a detailed comparison with high resolution spectropolarimetric observations, and that their lower boundary conditions are arbitrary.

Observations of umbral dots have, however, revealed properties that

are compatible with these simulations (Riethmüller et al., 2008b). There are even several observations of dark lanes dividing the umbral dots (Bharti et al., 2007; Rimmele, 2008).

UD cover up to 10 % of the umbra but contribute up to 20 % of the total brightness of the umbra. There are brighter peripheral umbral dots (PUDs) and less bright central umbral dots (CUDs) (Grossmann-Doerth et al., 1986). In the bright umbral ends of penumbral filaments similar small-scale brightenings called penumbral grains (PGs) are found (Muller, 1973).

Within the photosphere, UD show a weaker and more inclined magnetic field and an upflow of 100–300 m s<sup>-1</sup> compared to their surroundings Socas-Navarro et al. (2004). Weaker and almost horizontal magnetic fields are also found in the low layers of bright penumbral filaments in the inner penumbra (Jurčák & Sobotka, 2007). Based on seeing-free spectropolarimetric data from HINODE/SOT Riethmüller et al. (2008b) found from observations and inversions of 30 PUDs and 21 CUDs that, at the continuum formation level, the magnetic field is 510 G (PUDs) and 480 G (CUDs), respectively, weaker than in the surrounding umbra and is more inclined in PUDs than in CUDs. They observed significant upflows of 800 m s<sup>-1</sup> in PUDs, while CUDs did not show any important LOS velocity signature. In the upper photospheric layers, the physical characteristics of PUDs, CUDs, and bright penumbral filaments do not differ significantly from those in their surroundings, indicating that these features are formed deep in the photosphere and below it (Riethmüller et al., 2008b).

Explaining the nature of umbral dots in the context of the monolithic and the spaghetti model unfortunately does not lead to different observational signatures.

But one thing is worth to note for the spaghetti model: As rising plasma parcels push aside the field lines they penetrate the surface and become visible as umbral dots. After their upflow the magnetic field free zone closes producing a localized region in the continuum-forming layers of no field while 100-200 km above that level the field is practically homogeneous again (Degenhardt & Lites, 1993a,b). To test their model using

polarimetric measurements, lines formed very deep in the photosphere need to be observed as done in Chapters 3 and 4.

In the comparably cool environment of sunspot core umbra diatomic molecules can be found. The analysis of their absorption features, in addition to other's, traces the temperature of the umbra atmosphere far better than signatures from atomic lines alone. Since this thesis investigates sunspot umbra and its substructure in particular we need to understand how atomic and molecular absorption features can be analyzed, i.e. how magnetized atmospheres leave information in the light we detect and how we can retrieve this information.

## 2.3 Description of polarized light

Since light is the dominant observational source to remotely retrieve information about astrophysical objects we are generally interested in its complete exploitation. In addition to intensity spectra, analyzed in spectroscopy, the light's polarization, i.e. the time evolution of the plane of oscillation of the electric field vector, can be studied with the tools of spectropolarimetry. Since we are retrieving information about the solar atmosphere from spectropolarimetric data, we have to think about the origin of the observed polarization features and introduce a common description of polarized light: the Stokes formalism.

### 2.3.1 Origin of polarized light

Light can be polarized when two conditions are met: first, there has to be a geometrical symmetry breaking introduced e.g. by a magnetic field, an anisotropic radiation field causing scattering polarization, or the shape of an astrophysical object. Second, we are in need for a quantum mechanical system, i.e. atom, ion or molecule, that is able to imprint this asymmetry into the light, e.g. through orientation within the magnetic field and the Zeeman effect.

A physicist confronted with the task to explain the nature of light might immediately refer to Jackson (1998). There, the 3D wave equations for both, the electric field  $\mathbf{E}$  and the magnetic field  $\mathbf{B}$  in the empty chargeless space are derived from Maxwell's equations:

$$\nabla^2 \mathbf{E} = \mu_0 \epsilon_0 \frac{\partial^2 \mathbf{E}}{\partial t^2}, \quad \nabla^2 \mathbf{B} = \mu_0 \epsilon_0 \frac{\partial^2 \mathbf{B}}{\partial t^2}. \quad (2.2)$$

The solutions of these wave equations are waves propagating at the speed of light. Since  $\mathbf{E}$  and  $\mathbf{B}$  must be orthogonal to each other and the propagation vector  $\mathbf{k}$ , an electromagnetic wave is already fully characterized by a description of  $\mathbf{k}$  and  $\mathbf{E}$ . If  $\mathbf{k}$  points along the  $\hat{z}$ -axis a general wave can be written as the sum of two orthogonal waves oscillating in the plane defined by the  $\hat{x}$ - and  $\hat{y}$ -directions, respectively:

$$\begin{aligned} E_x(\mathbf{r}, t) &= E_{0,x} \cdot \cos(\mathbf{k} \cdot \mathbf{r} - \omega \cdot t + \delta_x), \\ E_y(\mathbf{r}, t) &= E_{0,y} \cdot \cos(\mathbf{k} \cdot \mathbf{r} - \omega \cdot t + \delta_y), \end{aligned} \quad (2.3)$$

where both waves are described by the real amplitudes  $E_{0,x}$  and  $E_{0,y}$ , their phases  $\delta_x$  and  $\delta_y$ , and their common frequency  $\omega$  and location  $\mathbf{r}$ . Solutions like Eq. 2.3 are called *monochromatic* (of a single color or frequency), *time-harmonic* (sinusoidally with time), *plane waves*. Alternatively, these free parameters can be combined into the complex amplitude  $\mathcal{E}$  given by  $\mathcal{E}_{0,x} = E_{0,x} \cdot e^{-i\delta_x}$ ,  $\mathcal{E}_{0,y} = E_{0,y} \cdot e^{-i\delta_y}$  and

$$\begin{aligned} \mathbf{E}(\mathbf{r}, t) &= \text{Re} \{ \mathcal{E}(\mathbf{r}, t) \} = \text{Re} \{ \mathcal{E}_0 \cdot e^{i\mathbf{k}\mathbf{r} - i\omega t} \} \\ &= \text{Re} \{ \hat{e}_x \cdot E_{0,x} \cdot e^{i\mathbf{k}\mathbf{r} - i\omega t + \delta_x} + \hat{e}_y \cdot E_{0,y} \cdot e^{i\mathbf{k}\mathbf{r} - i\omega t + \delta_y} \} \end{aligned} \quad (2.4)$$

This complex representation can be very convenient for polarization calculus using the polarization tensor as shown in del Toro Iniesta (2003). However, please be aware of the multitude of possible sign conventions in polarimetry (Rees, 1987).

The intensity of an electromagnetic wave, i.e. the time-averaged amount of transported energy per area is given by

$$I = c \epsilon_0 \langle \mathbf{E}^2 \rangle = \frac{c \epsilon_0}{2} (E_{0,x}^2 + E_{0,y}^2) \quad (2.5)$$

The relative strength of  $E_{0,x}^2$  and  $E_{0,y}^2$  and especially their phase difference describe the polarization state of the wave, i.e. the way the vector  $\mathbf{E}(\mathbf{r}, t)$  behaves with regard to its propagation direction.

**Elliptic polarization** is the most general case. Here, the tip of the  $\mathbf{E}(\mathbf{r}, t)$  vector continually traces an ellipse in a plane perpendicular to the propagation direction. Now, two special cases can be distinguished:

**Linear polarization** is obtained if two partial waves are in phase ( $\delta = 0$  or  $\delta = \pi$ ) such that the short axis of the ellipse vanishes. The resulting dynamic of  $\mathbf{E}$  is an oscillation along a line.

**Circular polarization** is observed if the amplitudes are equal and each component is at maximum when the other is passing zero:  $E_{0,x}^2 = E_{0,y}^2$  and  $\delta = \pi/2$  or  $3\pi/2$ . Thus, the tip of the  $\mathbf{E}$  vector traces a full circle. According to the sense of rotation, right- and lefthanded polarized light is distinguished.

A circular polarizations can be written as the sum of two linear polarizations and vice versa. In analogy, the general elliptical state can be described as a sum of linearly and circularly polarized light.

### 2.3.2 Stokes formalism

Since astronomical cameras record intensity  $I$  rather than field strength  $\mathbf{E}$  the Stokes vector formalism<sup>2</sup>, that characterizes polarized light exclusively in terms of intensities, is widely used to express partial polarization of light.

The formalism is based on six polarizing filters, each of which projects the incoming light onto a pair of complementary polarization states, transmitting one of them and rejecting another. The filter set is made of four linear polarizers at  $\alpha = 0^\circ, 90^\circ, 45^\circ$  and  $-45^\circ$ , as well as right- and left-handed circular polarizer (see Fig. 2.6). The light beam is fed through each filter consecutively and the transmitted intensities are registered.

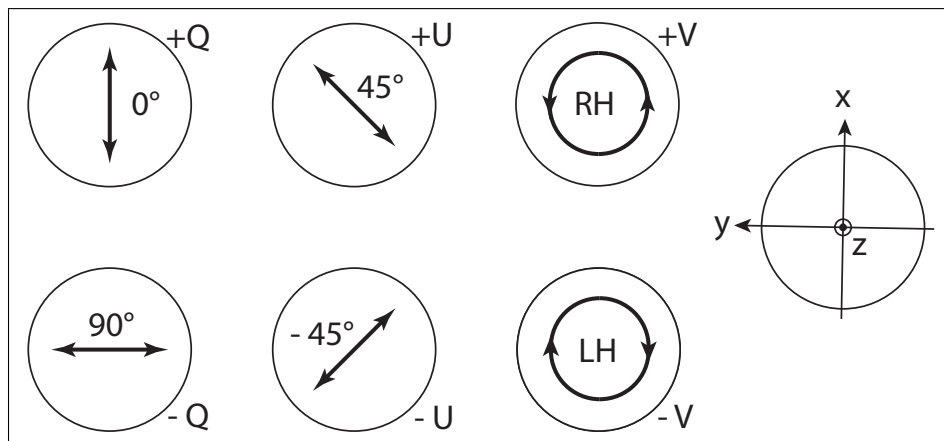


Fig. 2.6 The six Stokes filters. The propagation vector  $\mathbf{k}$  points towards the reader along the  $z$ -axis. The arrows indicate the variation of the  $\mathbf{E}$  vector in a fixed plane perpendicular to the propagation direction of the radiation field.

Thus the Stokes vector can be defined operationally for ensembles of

<sup>2</sup> named after Sir George Gabriel Stokes (1819–1903)

photons (in practice) and by means of complex amplitudes for single light waves (in theory):

$$\begin{aligned}
 I &= I_{0^\circ} + I_{90^\circ} &= |\mathcal{E}_x|^2 + |\mathcal{E}_y|^2 \\
 Q &= I_{0^\circ} - I_{90^\circ} &= |\mathcal{E}_x|^2 - |\mathcal{E}_y|^2 \\
 U &= I_{45^\circ} - I_{-45^\circ} &= 2\text{Re}(\mathcal{E}_x \mathcal{E}_y^*) \\
 V &= I_{\text{RH}} - I_{\text{LH}} &= 2\text{Im}(\mathcal{E}_x \mathcal{E}_y^*)
 \end{aligned} \tag{2.6}$$

The three polarization components  $Q$ ,  $U$ , and  $V$  form an orthonormal base of all possible polarization states. Fully left-handed polarized light, for example, would be described by  $\mathbf{S} = I \cdot (1, 0, 0, -1)^\top$ , fully horizontally ( $90^\circ$ ) polarized light would be written  $\mathbf{S} = I \cdot (1, 0, 1, 0)^\top$ . Since the three filter pairs are complementary, the intensity can also be written as  $I = I_{45^\circ} + I_{-45^\circ} = I_{\text{RH}} + I_{\text{LH}}$ . Thus, in order to determine the total Stokes vector only four intensity measurements are necessary, e.g.  $I$ ,  $I_{0^\circ}$ ,  $I_{45^\circ}$ , and  $I_{\text{RH}}$ .

Linear polarizations at angles  $\varphi$  and  $\varphi + \pi$  are indistinguishable often referred to as the degeneracy of the linear polarization. The Stokes vector for fully linearly polarized light at the angle  $\varphi$  would be  $I \cdot (1, \cos 2\varphi, \sin 2\varphi, 0)^\top$ .

For a detailed description of the Stokes formalism and other means to describe polarized light see the excellent monographs by Stenflo (1994) and del Toro Iniesta (2003).

## 2.4 Detection and interpretation of polarized light from a magnetized atmosphere

This section describes the Zeeman effect (ZE) and the Paschen-Back effect (PBE) in atoms and molecules which are the very foundation of our interpretation of the light observed from the magnetic solar atmosphere. Both effects lead to a modification of the energy of atomic or molecular levels in the presence of a magnetic field and thus to a detectable splitting of absorption lines observed. In atoms experiencing a lower magnetic

field strengths we observe the Zeeman effect. At higher magnetic field strengths the splitting of lines has to be described differently by the Paschen-Back effect. Diatomic molecules require a similar formalism as introduced at the end of this section.

We consider an atom with  $n$  electrons whose electronic quantum states are defined by the quantum numbers  $J$ ,  $L$ , and  $S$ , derived from the total angular momentum  $\mathbf{J} = \mathbf{L} + \mathbf{S} = \sum_i \mathbf{l}_i + \sum_i \mathbf{s}_i$  (Russel-Saunders coupling). Under various assumptions, the Hamiltonian of a  $n$ -electron atom in Hartree-Fock approximation reads:

$$\mathcal{H} = \underbrace{\sum_{j=1}^n \left( \frac{\mathbf{p}_j^2}{2m_e} + V(\mathbf{r}_j) \right)}_{\mathcal{H}_0} + \underbrace{\frac{1}{2} \sum_{i \neq j} \frac{e^2}{|\mathbf{r}_i - \mathbf{r}_j|}}_{\mathcal{H}_{ee}} - \underbrace{\frac{e|\mathbf{B}|}{2m_e c} (L_z + 2S_z)}_{\mathcal{H}_B} + \underbrace{\zeta(\mathbf{L} \cdot \mathbf{S})}_{\mathcal{H}_{LS}} \quad (2.7)$$

where  $V(\mathbf{r})$  is a spherical symmetric potential field of the atom core located at  $\mathbf{r}$ ,  $e$  the charge of the electrons,  $m_e$  their mass,  $\mathbf{p}_j$  their momenta, and  $c$  the speed of light.  $L_z$  and  $S_z$  are the projections of the respective angular momenta along the preferred axis introduced by the magnetic field  $\mathbf{B}$  uniform in  $z$ -direction ( $\mathbf{B} = |\mathbf{B}| \hat{z}$ ).

To arrive at this Hamiltonian the quadratic Zeeman effect ( $|\mathbf{B}| \geq 10$  kG) is omitted and interactions of the magnetic field with the orbital motions of the electrons and with their magnetic moments are considered (combined in  $\mathcal{H}_B$ ). In addition, the magnetic moment of the electrons interacts with the effective magnetic field caused by their orbital motion resulting in a spin-orbit interaction. In the case of Russel-Saunders coupling, i.e.  $\mathcal{H}_{ee} > \mathcal{H}_{LS}$ , this spin-orbit Hamiltonian is labeled LS-term.  $\zeta$  is the spin-orbit coupling constant with dimensions of energy, the factor 2 before  $S_z$  is an approximation for the electron spin gyromagnetic g-ratio.

With the Lamor frequency,  $\omega_L = (e|\mathbf{B}|)/2m_e c$ , we can define the ratio  $\gamma = \hbar\omega_L/\zeta$  between the energies associated to the  $\mathcal{H}_B$  and the  $\mathcal{H}_{LS}$  terms.

**The Zeeman regime** is defined by  $\gamma \ll 1$ , where  $\mathbf{S}$  precesses much

faster about  $\mathbf{J}$  than about  $\mathbf{B}$  and  $\mathcal{H}_B$  can be considered a small perturbation to  $\mathcal{H}_0 + \mathcal{H}_{ee} + \mathcal{H}_{LS}$ .

In the **complete Paschen-Back regime**, when  $\gamma \gg 1$  the internal energy due to the magnetic field is larger than the LS-coupling ( $\mathcal{H}_B > \mathcal{H}_{LS}$ ). Here, the order of the interactions changes. Now the strong magnetic field introduces a preferred axis to which all single orbit angular momenta and single spin angular momenta couple. In that strong field regime we use the *jj* coupling scheme, i.e. the single total angular momenta,  $\mathbf{J}_i = \mathbf{L}_i + \mathbf{S}_i$ , are computed before they are combined to obtain the total angular momentum,  $\mathbf{J}$ , of each state. The good quantum numbers here are  $\mathbf{J}^2$  and  $J_z$ .

The intermediate case is termed **incomplete Paschen-Back regime** when  $\gamma \approx 1$  and the energies of  $\mathcal{H}_B$  and  $\mathcal{H}_{LS}$  are comparable.

### 2.4.1 Zeeman effect in atoms

The Russel-Saunders (also: LS) coupling scheme allows the same magnetic perturbation as to the Hamiltonian of a one electron system. The observables are  $\mathbf{L}^2$ ,  $\mathbf{S}^2$ ,  $\mathbf{J}^2$ , and  $J_z$ , the component of the total angular momentum operator along the direction of the magnetic field. They form a complete set of commuting operators so that their associated parameters, L, S, J, and M are good quantum numbers and atomic states |LSJM) characterized by them are eigenvectors of all observables. If first-order time-independent perturbation theory is applied, it is found that the  $(2J+1)$ -degeneracy of each energy level disappears due to its splitting into magnetic sublevels whose energy is given by

$$E_{J,m,B} = E_J + \mu_0 g_J m B \quad (2.8)$$

Here,  $E_J$  is the energy of the atomic level without an external magnetic field, i.e.  $E_J$  is eigenvalue of  $\mathcal{H}_0 + \mathcal{H}_{ee}$  (see Fig. 2.7). The eigenvalue of  $J_z$  is  $\hbar M$  with  $M = [-J \cdots + J]$  and  $\mu_0 = e\hbar/(2m_e)$  the Bohr magneton. The absolute amplitude of the magnetic field vector is denoted by  $B$  and  $g_J$  is the Landé factor of the corresponding level. In the LS coupling scheme the Landé factor,  $g_J$ , can be written as

$$g_J = 1 + \frac{J(J+1) + S(S+1) - L(L+1)}{2J(J+1)} \quad (2.9)$$

For any given transition the effective Landé factor can be computed according to Shenstone & Blair (1929) to indicate the magnetic sensitivity of a given absorption line by expressing the center-of-gravity shift for an anomalous splitting pattern (see also Landi Degl'Innocenti, 1982):

$$g_{\text{eff}} = (g_J^l + g_J^u) + \frac{1}{4} (g_J^l - g_J^u) (J^l (J^l + 1) - J^u (J^u + 1)) \quad (2.10)$$

For some levels, e.g.  ${}^4D_{\frac{1}{2}}$  and  ${}^5F_1$  the Landé factor is zero. Within the limits of first order perturbation theory these levels do not split (Harvey & Breckinridge, 1973).

A simple case of the Zeeman effect seen in the Fe I line at 5250.208 Å is illustrated in Fig. 2.7. The lower level splits into three energetically different sublevels whereas the upper level is insensitive to the magnetic field. This is the simplest possible situation: a normal Zeeman triplet.

In general, we encounter the so-called *anomalous Zeeman effect* with multiplets (not only triplets) whose individual components are usually not resolved. If the Landé factors of the upper and lower lines both are distinct from zero all energy levels have to be calculated and the dipole transition rules applied to obtain the allowed transitions. Unfortunately, Zeeman components of different polarizations are generally mixed spectrally. However, there is the possibility to combine lines with the same polarization and define an effective Landé factor,  $g_{\text{eff}}$ , to always obtain a triplet.

The Zeeman strength,  $S_q(M_u, M_l)$ , of the transition between a lower (l) and an upper (u) level is given in Table 2.3, the shifts  $v_k(M_u, M_l)$  are

$$v_k(M_u, M_l) = \frac{e\lambda_0^2 B}{4\pi mc^2 \Delta\lambda_D} (g_l M_l - g_u M_u), \quad (2.11)$$

where  $g_i$  are the Landé factors assuming LS coupling and  $B$  is the magnetic field strength. Finally, the Doppler width is defined as

$$\Delta\lambda_D = \lambda_0 (\xi^2 + 2k_B T/m_a)^{1/2} / c \quad (2.12)$$

Tab. 2.2 Properties of the main atomic spectral lines used in our investigations. In the last row  $h$  denotes the approximate formation height of the line core.

atom	$\lambda$ [ Å ]	Transition ( $^{2S+1}L_J$ )	$g_{\text{eff}}$	$h$ [ km ]
Fe I	5250.208	$^5D_0 - ^7D_1$	3.0	200–400
Fe I	5250.6	$^5P_2 - ^5P_3$	2.2	200–400
Fe I	6301.5	$^5P_2 - ^5D_2$	1.67	300–500
Fe I	6302.5	$^5P_1 - ^5D_0$	2.50	200–460

	$\Delta J = -1$	$\Delta J = 0$	$\Delta J = +1$
S <sub>-</sub>	$(J-M)(J-M-1)$	$(J-M)(J+M+1)$	$(J+M+1)(J+M+2)$
S <sub>0</sub>	$J^2 - M^2$	$M^2$	$(J+1)^2 - M^2$
S <sub>+</sub>	$(J+M)(J+M+1)$	$(J+M)(J-M+1)$	$(J+M+1)(J-M+2)$

Tab. 2.3 Unnormalized strengths of Zeeman components.

including the microvelocity,  $\xi$ , and the mass of the atomic species,  $m_a$ .

### 2.4.2 Zeeman effect in molecules

This theoretical section shall lead towards the Zeeman effect in molecules without being an exhaustive primer on the theory of diatomic molecules. Please see the classic Herzberg (1939) for more details on molecules in general, Tennyson (2005) for an educative introductory overview and Berdyugina & Solanki (2002) and references therein for the latest theoretical developments.

In 1969 H. Wöhl did show that the Zeeman effect can also be observed in diatomic molecules (Wohl, 1969b,a). Similar to the atomic case the magnetic dipole moment of a molecule interacts with an external magnetic field. In the following section we introduce all necessary concepts to understand the magnetic sensitivity of the TiO (0,0) R<sub>3</sub> band head of the  $\gamma$  system ( $A^3\Phi-X^3\Delta$ ) at 7054 Å. We use this system for our inversions since it has been reported to be both, most magnetically sensitive, especially in the P<sub>3</sub> and R<sub>3</sub> branches with effective Landé factors  $|g_{\text{eff}}| \leq 1.1$

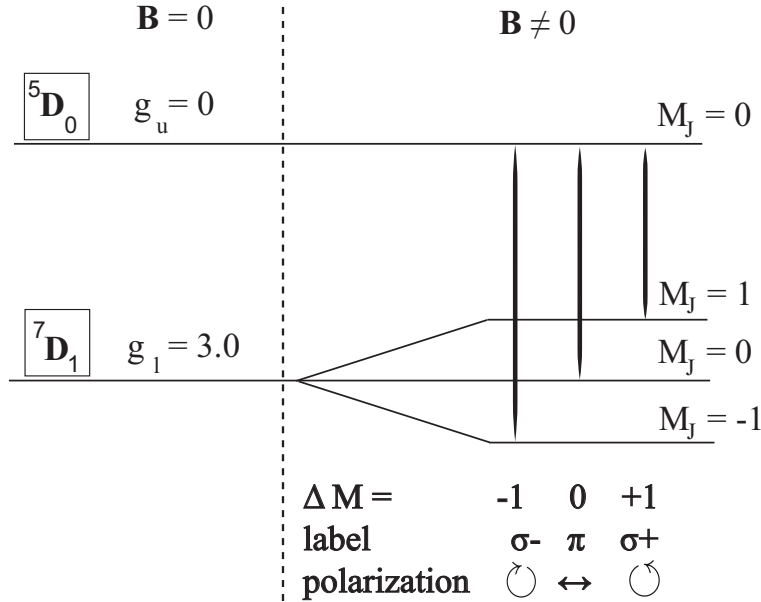


Fig. 2.7 Scheme of the Zeeman effect for the 5250.208 Å Fe I line.

(Berdyugina & Solanki, 2002), and the strongest molecular absorption feature one the Sun in the visible.

The system's triplet state can be described by Hund's case (a), especially for transitions between lower rotational levels. However, the intermediate case (a)-(b) leads to a more precise treatment. The Zeeman regime is still appropriate for this system since perturbations of a few kG, the order of magnetic fields in sunspots, are still weaker than the internal momenta coupling.

In a diatomic molecule the total angular momentum,  $\mathbf{J}$ , is composed of the electron spin,  $\mathbf{S}$ , the projection of electronic orbital angular momentum ( $\mathbf{L}$ ) on the internuclear axis,  $\mathbf{\Lambda}$ , and the angular momentum of the nucleus,  $\mathbf{R}$ .

In case the spin,  $\mathbf{S}$ , and the orbital angular momentum,  $\mathbf{\Lambda}$ , of the electron are not zero, we have to distinguish different coupling cases. These five Hund's coupling cases are termed alphabetically and define extreme examples of how to combine the angular momenta. In the following we concentrate on Hund's case (a), (b), and the intermediate case (a)-(b)

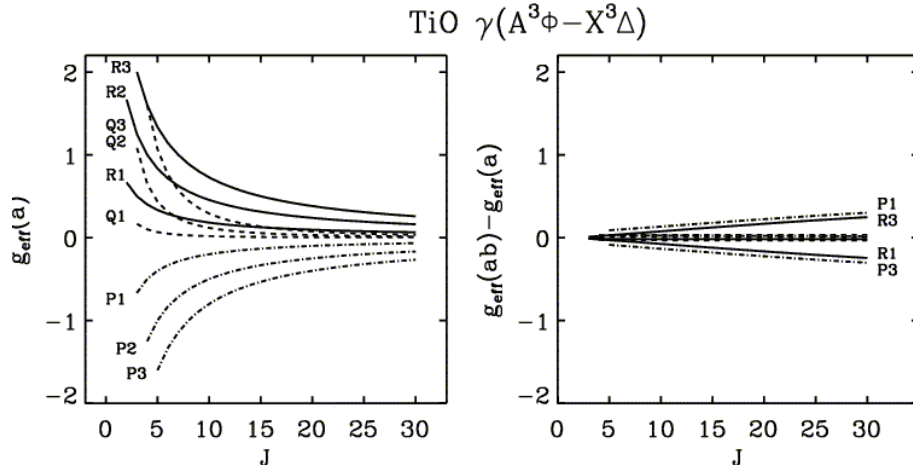


Fig. 2.8 Effective Landé factors for the TiO molecule computed for the Hund's case (a). Figure taken from Berdyugina & Solanki (2002) with kind permission.

which are relevant to this thesis<sup>3</sup> (see Fig. 2.9).

### The Hund's cases

We assume an arbitrary orientation of the TiO molecule with respect to the magnetic field.

**In Hund's case (a)** both, the electronic orbital momentum,  $\mathbf{L}$ , and the electronic spin,  $\mathbf{S}$ , are coupled to the internuclear axis. Both interact only very weakly with the nuclear angular momentum,  $\mathbf{R}$  (see Fig. 2.9).

The projection of  $\mathbf{L}$  and  $\mathbf{S}$  to the internuclear axis are  $\Lambda$  and  $\Sigma$ , respectively. These are the good quantum numbers describing the system. The total angular momentum,  $\Omega = \Lambda + \Sigma$ , has to be calculated as vector sum:

<sup>3</sup> **Hund's case (c)** occurs in diatomic molecules made of heavy atoms. Here, the spin-orbit coupling is so strong that  $\mathbf{L}$  and  $\mathbf{S}$  couple together and the combination precesses around the internuclear axis.  $\Omega$  still equals  $\Lambda + \Sigma$ , but  $\Lambda$  and  $\Sigma$  themselves do not have well-defined values.

**In Hund's case (d)** the coupling between  $\mathbf{L}$  and the internuclear axis is very weak, while that between  $\mathbf{L}$  and the axis of rotation is strong.

**Hund's case (e)** is similar to case (d) with the single addition that  $\mathbf{L}$  and  $\mathbf{S}$  are strongly coupled together.

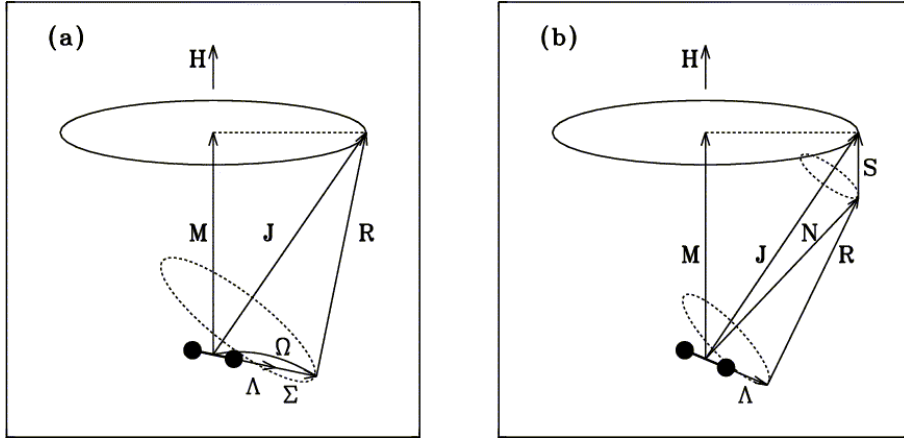


Fig. 2.9 Hund's cases for diatomic molecules like TiO. Figure taken from Berdyugina & Solanki (2002) with kind permission.

$$\Omega = |\Lambda + \Sigma| . \quad (2.13)$$

The combination of  $\Omega$  and the nuclear angular momentum,  $\mathbf{R}$ , yields the total angular momentum  $\mathbf{J}$ :

$$\mathbf{J} = \Omega + \mathbf{R}, \quad (2.14)$$

where  $\Omega$  and thus  $J$  are integer (half-integer) if the number of electrons is even (odd). The quantum number  $J$  cannot be smaller than  $\Omega$  as  $\mathbf{J} = \Omega, \Omega+1, \Omega+2, \dots$ . Since the multiplet splitting is larger than the rotational splitting the rotational energy in Hund's case (a) is that of a symmetric top.

**Hund's case (b)** is likely to occur in light molecules.  $\mathbf{L}$  is coupled to the internuclear axis whereas, due to a very weak spin-orbit coupling,  $\mathbf{S}$  is only weakly coupled to the same axis (see right panel of Fig. 2.9).

If  $\mathbf{S}$  is not coupled to the internuclear axis and  $\Lambda = 0$ ,  $\Sigma$  and  $\Omega$  are undefined. In order to obtain good quantum numbers  $\Lambda$  and  $\mathbf{R}$  are combined to form the total angular momentum without spin,  $\mathbf{N}$ , in the usual way:

$$\mathbf{N} = \Lambda + \mathbf{R}, \quad (2.15)$$

with the quantum number  $N = \Lambda, \Lambda+1, \Lambda+2, \dots$ .

Tab. 2.4 Selection rules for the Hund's cases (a) and (b).

Hund's case (b)	Hund's case (a)
$\Delta J = J_u - J_l = 0, \pm 1 (0 \leftrightarrow 0)$	
$\Delta \Lambda = \Lambda_u - \Lambda_l = 0, \pm 1$	
$\Delta S = S_u - S_l = 0$	$\Delta \Sigma = \Sigma_u - \Sigma_l = 0$
$\Delta N = N_u - N_l = 0, \pm 1$	$\Delta \Omega = \Omega_u - \Omega_l = 0, \pm 1$
with $\Delta N \neq 0$ for $\Lambda \rightarrow 0$	
if $\Delta J = \Delta N$ : main P, Q, R branches	
if $\Delta J \neq \Delta N$ : satellite branches	

The total angular momentum including spin,  $\mathbf{J}$ , is formed by  $\mathbf{N}$  and  $\mathbf{S}$ :

$$\mathbf{J} = \mathbf{N} + \mathbf{S}, \quad (2.16)$$

with the quantum number  $J = N + S, N + S - 1, \dots, |N - S|$ . Since each rotational level splits into  $(2S+1)$  multiplet components the rotational splitting is larger than the multiplet splitting.

**The intermediate case (a)-(b)** is a better approximation of the reality since molecules are best described by a mix of the idealized Hund cases. To first approximation however, one of the schemes is usually more accurate than the others.

Often, with increasing rotational  $J$ , a transition might take place from one coupling case to another since the electrons might not follow the rotation of the nuclei. Angular moments coupled to the internuclear axis for small rotational  $J$  values are uncoupled with increasing rotation.

### The molecular Zeeman effect

This section has been taken from Berdyugina & Solanki (2002). In order to respond to an external magnetic field a molecular must possess a magnetic moment,  $\mu$ . The largest contribution comes from the electron spin and orbital momenta,  $\mathbf{L}$  and  $\mathbf{S}$ , respectively such that

$$\mu = \mu_L + \mu_S = \mu_0 (\mathbf{L} + 2\mathbf{S}). \quad (2.17)$$

Here,  $\mu_0 = e \hbar / (2 m_e c)$  is the Bohr magneton. If the two moments are zero the contributions from the nuclei and the rotation of the molecule

must be taken into account.

The energy shift,  $\Delta E$ , due to the magnetic interaction is given by

$$\Delta E = -\mu \mathbf{H} = -\mu_0 (\mathbf{L} + 2\mathbf{S}) \mathbf{H} = -(\mathbf{L} + 2\mathbf{S}) \mathbf{B} \quad (2.18)$$

The energies of the  $(2J+1)$  magnetic components thus depend on how the angular momenta are coupled to the rotation of the molecule.

**The Zeeman effect** in Hund's case (a) is described by a strong coupling of  $\mathbf{L}$  and  $\mathbf{S}$  to the internuclear axis. The magnetic moment along this axis equals  $(\Lambda + 2\Sigma)$ . The precession motions of  $\Omega$  and  $\mathbf{J}$  about the magnetic field can be averaged as  $\Omega/\sqrt{J(J+1)}$  and  $M/\sqrt{J(J+1)}$ . Thus the energy shift of the magnetic splitting of all levels  $J$  in Hund's case (a) is given by

$$\Delta E = \underbrace{\frac{(\Lambda + 2\Sigma)\Omega}{J(J+1)}}_{=g_m} M \mathbf{B} = g_m M \mathbf{B}, \quad (2.19)$$

where  $g_m$  is the molecular analogon of the Landé factor that describes how strong the splitting of the degenerate levels is.

For most molecular transitions observed in solar spectra the weak field approximation is valid in the Zeeman regime, i.e. the magnetic splitting is not dominating the line broadening. In that case, the effective Landé factor is useful to describe the splitting pattern of the anomalous Zeeman effect by the splitting pattern of a normal Zeeman pattern, i.e. a triplet.

Since the splitting is determined only by the quantum numbers of the transition and is independent of molecular constants the expressions for the effective Landé factors for the rotational branches are determined by the selection rules (see Table 2.4):

$$\begin{aligned} g_{\text{eff}}(R - \text{branch}) &= \frac{1}{2} (g_u(J_u + 1) - g_l J_l) \\ g_{\text{eff}}(Q - \text{branch}) &= \frac{1}{2} (g_u + g_l) \\ g_{\text{eff}}(P - \text{branch}) &= \frac{1}{2} (-g_u J_u + g_l(J_l + 1)) \end{aligned} \quad (2.20)$$

Note that since the effective Landé factors of the R- and P-branch are always of opposite sign, the effective Landé factors can assume negative

values. Also, the magnetic splitting of rotational levels is symmetrical, proportional to the field strength, and drops rapidly for increasing values of  $J$ .

For more details and descriptions see Berdyugina & Solanki (2002); Berdyugina et al. (2003, 2005); Afram (2008) and references therein.

### 2.4.3 Paschen-Back effect in molecules

In molecules the magnetic field strength at which the PBE becomes important is different for each system. For the MgH  $A^2\Pi - X^2\Sigma^+$  at 5200 Å used in the THEMIS inversions this threshold has been found to be at 280 G (Berdyugina et al., 2005).

For the intermediate Hund's case (a)-(b) the electric dipole selection rules allow the same transitions as in the case (b). However, since the quantum numbers change when leaving the Zeeman regime ( $\Delta J = \Delta N$ ) for the Paschen-Bach regime ( $\Delta J \neq \Delta N$ ) the rotational branches R, P and Q with  $\Delta J = +1, -1, 0$ , respectively, are called main branches and *satellite branches* appear, e.g.  $^P R$ ,  $^Q P$ , where the left superscript denotes the branch type according to the value of  $\Delta N$ .

### 2.4.4 Observational consequences

The main observational consequence of this level splitting due to an external magnetic field is a splitting of the spectral line formed between two such levels, where each of the lines components is polarized. This splitting can already be observed in the solar intensity spectrum (Stokes  $I$ ) as described by the discoverer Zeeman (1897). G.E. Hale made use of the Zeeman effect in intensity observations to prove the existence of magnetic fields on the Sun (Hale, 1908).

The description in the semi-classical picture (see e.g. Jackson, 1998) is termed *normal Zeeman effect*. Here, the motion of an electron orbiting a nucleus can be seen as an oscillation in three dimensions due to Coulomb attraction. Virtually, the motion of this light electron can be disentangled into the motions of virtual electrons described as linear oscillators: one parallel to the preferred axis of the magnetic field (the  $\hat{z}$ -axis in Fig. 2.11) and two perpendicular being interpreted as circular motions in the  $\hat{x}$ - $\hat{y}$ -plane. An external magnetic field aligned with the  $\hat{z}$ -axis disturbs this

situation introducing a Lorentz force proportional to  $\mathbf{v} \times \mathbf{B}$ , thus shifting the components of the line by a wavelength difference. The wavelength shift  $\Delta\lambda_B$  is given by

$$\Delta\lambda_B = 4.7 \cdot 10^{-13} \lambda_0^2 g_{eff} B. \quad (2.21)$$

This equation states that the spectral splitting of the  $\sigma$  components due to the Zeeman effect is directly proportional to the effective Landé factor, the magnetic field strength and the quadratic rest wavelength. Hence, choosing transitions with high Landé factors at higher wavelengths (e.g. NIR) is favorable to detect the magnetic field strength by Zeeman splitting.

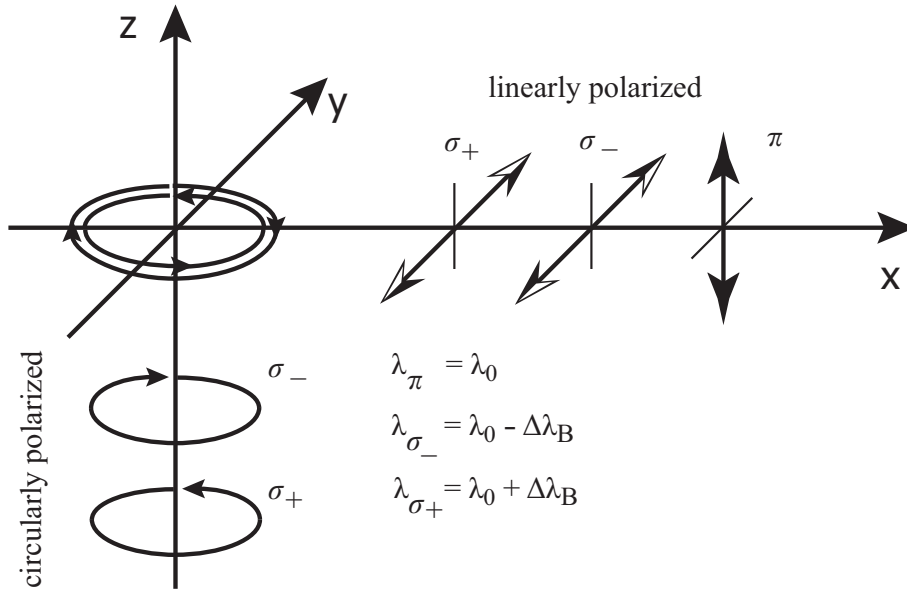


Fig. 2.10 Deconstruction of the light electron oscillating in an external magnetic field. As a result the line splits in a central  $\pi$ -, and two shifted  $\sigma$  components.

Depending on the orientation of the magnetic field vector with respect to the line-of-sight (LOS) we distinguish two line splitting scenarios:

**longitudinal Zeeman effect:** Observing parallel to the magnetic field orientation (LOS  $\parallel \mathbf{B}$ ) only the two circular components,  $\sigma_-$  and

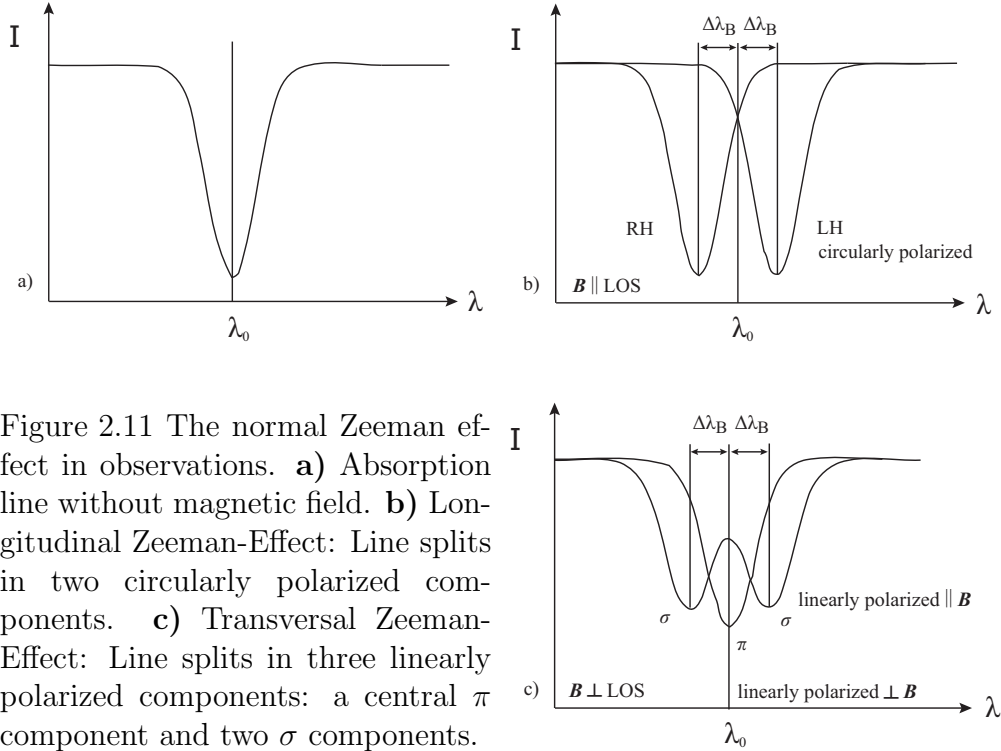


Figure 2.11 The normal Zeeman effect in observations. **a)** Absorption line without magnetic field. **b)** Longitudinal Zeeman-Effect: Line splits in two circularly polarized components. **c)** Transversal Zeeman-Effect: Line splits in three linearly polarized components: a central  $\pi$  component and two  $\sigma$  components.

$\sigma_+$  can be seen since the radiation characteristic of the dipole forbids the radiation of energy in the direction of the oscillation ( $\hat{z}$ -axis). These circular components form the Stokes  $V$  profile (see Fig. 2.11).

**transversal Zeeman effect:** Observing normal to the magnetic field from any point in the  $\hat{x} - \hat{y}$ -plane ( $\text{LOS} \perp \mathbf{B}$ ) the three differently polarized components are recorded. The Stokes  $Q$  and the Stokes  $U$  profiles show traces of this linear polarized radiation.

In the general case, both effects will combine. Thanks to the description of polarized radiative transport by Unno (1956), the analysis of additional polarimetric information (Stokes parameters  $Q$ ,  $U$ , and  $V$ ), i.e. the relative strengths and the profiles of the Stokes parameters, allows to infer the full magnetic field vector. See Fig. 2.11 for a deconstruction of the observable line profiles.

## 2.5 Polarized Radiative transfer in atoms

The propagation of polarized light in a magnetic field is described by the polarized radiative transfer equation (pRTE). After many unsuccessful approaches this theory was developed by Unno (1956). Further contributions were made by Rachkovsky (1962), and Beckers (1969). A generalized approach based on quantum electrodynamics was introduced by Landi Degl’Innocenti & Landi Degl’Innocenti (1972) and Landolfi et al. (1984) and is nicely described in Degl’Innocenti & Landolfi (2004). Please see also Stenflo (1994) for a coherent description and derivation from first principles.

In the following the equations are given in a form that reflects the implementation of the code SPINOR Frutiger (2000).

The intensity of a light beam,  $I_\lambda$ , traveling over an infinitesimal path length,  $ds$ , can be partly absorbed by opacity,  $\kappa_\lambda$ , or increased by emissivity,  $\epsilon_\lambda$ ,

$$\frac{dI_\lambda}{ds} = -\kappa_\lambda I_\lambda + \epsilon_\lambda. \quad (2.22)$$

In the polarized case we drop the explicit wavelength dependence. The set of radiative transfer equations for the full Stokes vector  $\mathbf{S}=(I_\lambda, Q_\lambda, U_\lambda, V_\lambda)^T$  can then be written as

$$\frac{d\mathbf{S}}{ds} = -\mathbf{K}\mathbf{S} + \mathbf{j} \quad (2.23)$$

where  $\mathbf{K}$  is the total absorption matrix,

$$\mathbf{K} = \kappa_c (\mathbb{1} + \boldsymbol{\eta}) = \boldsymbol{\eta} + \eta_c, \quad (2.24)$$

and  $\mathbf{j}$  the total emission vector

$$\mathbf{j} = \mathbf{j}_c + \mathbf{j}_l = \kappa_c \begin{pmatrix} S_c \\ 0 \\ 0 \\ 0 \end{pmatrix} + S_l \begin{pmatrix} \eta_I \\ \eta_Q \\ \eta_U \\ \eta_V \end{pmatrix} \quad (2.25)$$

In the limiting case of LTE the source functions for the continuum,  $S_c$ , and the line,  $S_l$ , are equal to the Planck function:

$$S = B(\lambda, T) = \frac{2hc^2}{\lambda_0^5} \left( e^{\frac{hc}{\lambda_0 T}} - 1 \right)^{-1} \quad (2.26)$$

At the right hand side of Eqs. 2.24 and 2.25 the parts emerging from the continuum (c) and the spectral lines (l) have been separated. The line absorption matrix  $\eta$  could further be divided into a symmetric part responsible for absorption effects and an asymmetric part describing anomalous dispersion. The latter is responsible for *Faraday rotation*, i.e. the transformation of polarization states during propagation, and originates from the real part of the refractive index of the material. The total absorption matrix reads:

$$\mathbf{K} = \begin{pmatrix} \eta_I & \eta_Q & \eta_U & \eta_V \\ \eta_Q & \eta_I & 2\rho_V & -2\rho_U \\ \eta_U & -2\rho_V & \eta_I & 2\rho_Q \\ \eta_V & 2\rho_U & -2\rho_Q & \eta_I \end{pmatrix} + \mathbb{1}, \quad (2.27)$$

and its components are given by (Stenflo, 1994, chap.11):

$$\begin{aligned} \eta_I &= \frac{1}{2} \Phi_0 \sin^2 \gamma - \frac{1}{2} \left( 1 - \frac{1}{2} \sin^2 \gamma \right) (\Phi_+ - \Phi_-) \\ \eta_Q &= \frac{1}{2} \left[ \Phi_0 - \frac{1}{2} (\Phi_+ - \Phi_-) \right] \sin^2 \gamma \cos 2\chi \\ \eta_U &= \frac{1}{2} \left[ \Phi_0 - \frac{1}{2} (\Phi_+ - \Phi_-) \right] \sin^2 \gamma \sin 2\chi \\ \eta_V &= \frac{1}{2} (\Phi_+ - \Phi_-) \cos \gamma \end{aligned}$$

with the general absorption profiles being defined as:

$$\Phi_{0,\pm}(v) = \frac{\kappa_o}{\kappa_c} \sum_M S_q(M_l, M_u) H(a, v - v_k(M_l, M_u) + \omega_{LOS}) \quad (2.28)$$

where  $v = (\lambda - \lambda_0)/\Delta\lambda$  is the distance from the line center in Doppler units and

$$\omega_{LOS} = v_{LOS} \lambda_0 / (c \Delta \lambda_0) \quad (2.29)$$

the components of the line-of-sight velocity in Doppler units,  $a = (\Gamma_{rad} + \Gamma_{Stark} + \Gamma_{v.d.Waals})\lambda_0^2/(4\pi c\Delta\lambda_D)$  is the damping parameter of the Voigt profile  $H(a, v)$  defined as

$$H(a, v) = \frac{a}{\pi} \int_{-\infty}^{\infty} \frac{\exp(-y^2)}{(v-y)^2 + a^2} dy \quad (2.30)$$

and the sum in Eq. 2.28 includes all components where  $M_l$  ( $M_u$ ) is the lower (upper) magnetic quantum number of the Zeeman split states.

The magneto-optical terms  $\rho_{Q,U,V}$  are obtained similarly by replacing the absorption profile  $\Phi_{0,\pm}$  by the dispersion profile  $\Psi_{0,\pm}$  in Eqs. 2.28 and 2.28 and the Voigt profile  $H$  by the Faraday-Voigt profile  $F$  in Eq. 2.28.

The term  $\kappa_o/\kappa_c$  scales the profiles and accounts for quantum mechanical effect, e.g. the oscillator strength. Taking into account the variability of this ratio distincts our inversions from ME inversions (see Sect. 2.6.3).

### 2.5.1 The optical depth scale

Describing atmospheres, the optical depth,  $\tau$ , is used as a relative height scale, since an absolute geometrical height scale is not known a priori. It is defined by integrating the absorption along the line-of-sight,  $ds$ , starting at the observer:

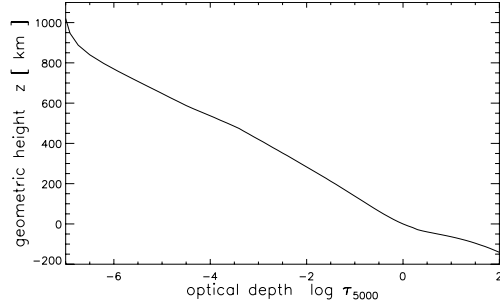
$$\tau_{5000} = \int \kappa(\lambda = 5000\text{\AA}) ds \quad (2.31)$$

Generally, the optical depth depends on the wavelength. For comparison, all  $\tau$  scales and thus all atmospheric parameters depending on  $\tau$  are given for the standard wavelength 5000 Å in this work. It is convenient to use the logarithmic scale of  $\tau$  since, within the photosphere, the geometrical height,  $z$ , and  $\log \tau$  are linear by approximation (see Fig. 2.12). In radiative transfer  $\tau_c$  and  $\tau_l$  stand for the continuum and line core, respectively.

### 2.5.2 Height of line formation

When inferring the stratification of atmospheric parameters like the temperature or the magnetic field, the height of formation of a spectral line

Figure 2.12 Optical depth vs. geometric height for the standard quiet sun atmosphere, HSRA. Note, that to a good approximation the  $\log \tau$  scale is proportional to the geometric height.



within a given atmosphere links our observations to a certain location within the atmosphere.

Most unfortunately, spectral lines are not created at a single height but get contributions from a range of heights where the environment is suitable to sustain that particular transition and from which photons can escape.

Generally, when scanning through an absorption line from the line wings to the line center, the line wings are formed deepest, close to the continuum. The line center, however, is formed in higher layers further away from the continuum. Close to the line core the photons must have been formed higher.

In the isotropic case of a non-magnetized atmosphere the solution of the RTE for the intensity  $I$  is given by

$$I(\tau = 0) = \int_0^\infty \underbrace{S(\tau_c)\kappa(\tau_c)e^{-\tau_c \int_0^{\tau_c} \kappa(t) dt}}_{=C(\tau_c)} dt \quad (2.32)$$

and the integrand is called *contribution function* that tells us how the different atmospheric layers do contribute to the observed spectrum. Since the CF is no Delta function it can only indicate the range of height within the atmosphere probed by this spectral line (see Stenflo, 1994, for the different CF definitions). By scanning the line's profile from its wings towards its core we probe different heights. In this thesis we use the line depression contribution function.

Modeling a stellar atmosphere by inversions we are looking for the dependence of the Stokes profiles on small perturbations of the single physical parameters. These are given by *response functions (RF)* which are the solutions of the pRTE. Following e.g. (see del Toro Iniesta, 2003,

Chap. 10) they can be regarded as decomposition of the CF:

$$\delta I(\tau = 0) = \sum_{i=1}^m \int_0^{\infty} \underbrace{\mathbf{R}_i(\tau_c) \delta_i(\tau_c)}_{=C_i(\tau_c)} d\tau_c \quad (2.33)$$

For a clear and accurate introduction to RF, CF and their application in inversion techniques do not miss to consult Stenflo (1994, Chap. 11.4), (del Toro Iniesta, 2003, Chap. 10) and references therein.

## 2.6 The art of inversions

The term *direct modeling*, often also forward calculation, refers to the computation of the four Stokes profiles of one or more (blended) spectral lines based on their atomic input data and given model atmosphere(s). Thus, the code solves the polarized radiative transfer equations (pRTE), i.e. the Unno-Rachkovky equations, for the given geometry and atmospheric model under certain assumptions like LTE. We do provide a physical setup and get the Stokes profiles.

*Spectral inversions* or *indirect modeling* describe automated iterative procedures that combine the direct modeling with a minimization algorithm. Based on a set of initial starting values the direct modeling code provides the synthetic Stokes profiles that are compared to given observations. A measure of the fit quality, similar to chi square, is determined and iteratively reduced by changing the initial values consistently within given parameter ranges. We do provide observations and a physical model and get the atmospheric parameters of the observed target.

This approach is extremely useful when analyzing spatially unresolved solar spectra. Information,  $X$ , about the solar photosphere can be obtained by analyzing the emerging light,  $Y$ . Most unfortunately, a general explicit relation of the form

$$X = g(Y) \quad (2.34)$$

does not exist for all physical quantities we are interested in. Thus, rendering a direct analysis difficult, i.e. too rich of assumptions or simply impossible. With reasonable effort (and mild assumptions), however, we can compute artificial spectra,  $Y'$ , based on parameterized model

atmospheres  $M(X)$  of the solar atmosphere, where the parameters  $X$  are either physical or observational in nature:

$$Y' = f(M(X)) \quad (2.35)$$

Note, that  $f$  is the solution of the (polarized) radiative transfer equation (pRTE) describing the state of the light as it passes through the atmosphere.

Comparing the artificial spectrum,  $Y'$ , with the observed spectrum,  $Y$ , we may quantify the resemblance by a merit function similar to  $\chi^2$ , the sum over squared differences between the empirically and the synthetically determined observables. Iterating this process with different models and the goal to minimize the merit function will lead us to a model atmosphere  $M(X_{\text{final}})$  and thus the sought for best-fit parameters,  $X_{\text{final}}$ , of the solar atmosphere.

The best-fit parameters obtained from an inversion procedure<sup>4</sup> are only as good as the model atmosphere! It is therefore of paramount importance to choose an atmosphere that is simple and practical on the one hand side and but also takes into account all relevant physics on the other hand side.

In general, inversions are employed in astronomy when observational data are a convolution of some quantity of astrophysical interest and a known or measured effect. The latter can be a known property of the instrument used for the observation, an effect of projection on the sky or, as in helioseismology, a convolution along the ray path of a seismic wave below the solar surface. Since the measured data is sampled discretely and suffers from measurement errors of various kinds, it is rare that an exact analytical inversion can be obtained. Sampling and data errors are especially in astrophysics hard to control (Pijpers, 1995).

### 2.6.1 STOPRO and SPINOR

STOPRO and SPINOR are the implementations of direct and indirect modeling and employed as workhorses throughout the thesis. Both codes have been written in FORTRAN 90.

---

<sup>4</sup> The term inversions historically comes from the inversion of the curvature matrix, a significant part of each non-linear, iterative fitting procedure, and not necessarily from the idealized relation between  $f$  and  $g$ .

STOPRO computes the full STOKes PROfiles of atomic and molecular absorption lines in magnetized atmospheres.

SPINOR uses STOPRO and contains all of its features. It is based on Response functions, uses the Levenberg-Marquardt algorithm as minimization and a Hermitian solver for the Unno-Rachkovsky equations. Implementation details and more complex model geometry opportunities are documented in the thesis of Frutiger Frutiger et al. (2000).

The features and *assumptions* of SPINOR employed for spatially unresolved magnetic elements, e.g. observed on the solar surface, are:

- Inverting the full Stokes vector of many spectral (and not necessarily adjacent) absorption features *simultaneously* and thus
- inferring the stratification of thermodynamic atmospheric quantities as a function of optical depth ( $\tau$ )
- by solving Unno-Rachkovsky equations based on Response functions in Local Thermodynamic Equilibrium (LTE)
- for blends of atomic and molecular (TiO, MgH, CN, CH) absorption features
- in hydrostatic equilibrium assuming mass conservation.

For an overview of the inversion process please read the PhD thesis of the programmer Frutiger et al. (2000, B.1). A short first sight introduction to SPINOR and STOPRO has been written by (Lagg, 2005).

### 2.6.2 Other implementations

In addition to SPINOR there are many other successful implementations of inversion schemes making inversions a widely accepted and largely used tool that is continually refined. The family of inversion codes based on or derived from SIR is used extensively in the community. As well as SPINOR, the SIR implementation and further extensions have been extensively tested and perfected to define their range of stability, applicability, reliability and determine the uniqueness of their results. Please do consult the excellent book of del Toro Iniesta (2003) for more details on SIR and the references therein for applications and further developments.

### 2.6.3 Milne-Eddington inversions

The overwhelming amount of incoming data of present and future observatories requires inversion techniques that are much faster than general numerical inversion implementations like SPINOR or SIR, preferably processing the data in real time. A widely used simplifying assumption is the so-called *Milne-Eddington (ME) approximation*. This procedure was invented by Auer et al. (1977) and further improved by Skumanich & Lites (1987).

For Milne-Eddington inversions the following assumptions are made (Stenflo, 1994, chap.11.6):

- The absorption matrix  $\eta$  is constant with optical depth  $\tau$ , therefore:
- the magnetic field vector,  $\mathbf{B}$ , is homogeneous and constant with optical depth  $\tau$  over the region of line formation, and
- the source function  $S_\nu$  (in LTE equal to the Planck function) is assumed to be linear in  $\tau$ :  $(S_\nu(\tau) = S_0 + \beta\tau)$ .

With these assumptions the pRTE can be solved analytically. To minimize the merit function,  $\chi^2$ , between synthetic and observational profiles the gradient of  $\chi^2$  with respect to each free parameter,  $\alpha$ , of the inversion can be calculated:

$$\nabla_{\alpha_j} (\chi^2(\boldsymbol{\alpha})) = \nabla_{\alpha_j} (\mathbf{S}_{obs}(\lambda) - \mathbf{S}_{syn}(\lambda))^2 = \frac{1}{\Delta\alpha_j} (\chi^2(\boldsymbol{\alpha} + \Delta\alpha_j) - \chi^2(\boldsymbol{\alpha})) \quad (2.36)$$

where the parameter vector  $\boldsymbol{\alpha}$  contains the slope,  $\beta$ , and zero offset,  $S_0$  of the Source function and  $\boldsymbol{\alpha} + \Delta\boldsymbol{\alpha}$  is short for  $(\alpha_1, \alpha_2, \dots, \alpha_j + \Delta\alpha_j, \dots, \alpha_n)$

Thus the gradients of the atmosphere's parameters and thus the Stokes vectors can be computed easily for any given magnetic field. Next to speed, the big advantages are stability, i.e. only few iterations are necessary to converge to a minimum and the perfectly (anti-) symmetric Stokes ( $V$ )  $Q$  and  $U$  profiles due to the inability of the method to account for discontinuities and gradients of physical parameters.

The ME idealization states that throughout the region of line formation the ratio  $\kappa_o/\kappa_c$  is constant (see Sect. 2.5). All effects depending on

different line formation heights are wiped out, leading to a two dimensional image of a three dimensional part of the atmosphere. Therefore, every sophisticated inversion strategy must leave the ME-regime to be able to account for the horizontal stratification, i.e. the dependence on the optical depth  $\tau$ , of all relevant atmospheric parameters.

The reader is encouraged to read the paper by Westendorp Plaza et al. (1998) on the differences between ME and spectral inversions. Note, that all inversions presented in this thesis are spectral inversions, not Milne-Eddington inversions!

#### 2.6.4 Model building with SPINOR

The quality of inversions depends on the ability to model two things well: First the properties of atoms, ions and molecules involved in the transitions under consideration and the related physical processes like excitation, ionization, collisional damping and the like. Second, the structure of the atmosphere itself, i.e. which quantities in which geometrical setup.

Generally, modelling the matter properties is well established by earlier investigations, theory or laboratory experiments, although for particular lines an accurate description is missing. Inversions suffer from the lack of line information but at the same time represent a handy tool to investigate the parameter space of the missing quantities.

Finding a good model for the atmospheric structure depends much on the experience of the investigator who has to construct reasonable atmospheric models as an *a priori* input. Often, limited computational power allows only to consider very simple geometries and set an upper boundary for the number of free parameters to be used.

When the inversion algorithm has found a certain set of atmospheric parameter stratifications –the final atmosphere– one has to keep in mind that this model, how sophisticated it may be, is no direct measurement of field properties but remains always an interpretation of the observations based on the given assumptions.

#### 2.6.5 Quality of the models

For a convenient description of the details leading to the implementation of the SPINOR merit function please see Frutiger et al. (2000).

As a results of the inversion process, i.e. comparing observations and a given model iteratively via a function of merit in order to find its minimum, the reduced chi square value ( $red\chi_{out}^2$ ) can be computed:

$$red\chi_{out}^2 = \frac{1}{\nu} (\chi^2 + \chi_{reg}^2) \quad (2.37)$$

where  $\nu$  is the number of free parameters and  $\chi_{reg}^2$  an additional regularization term, which assures the smoothness of the solutions (Frutiger et al., 2000). The regularization term ( $\chi_{reg}^2$ ) is in the order of  $< 5\%$  of  $\chi^2$ , the number of free parameters depends on the complexity of the model and can be around 100.

Looking closer at the computation of the  $\chi^2$ , where  $Y$  are observations and  $Y^{model}$  are the model curves, we get

$$red\chi_{out}^2 = \frac{1}{\nu} \left( \left[ \sum_{sp=1}^4 \sum_{i=1}^{\#blends} \left( \frac{1}{\sigma_{sp,i}^2} \right) \sum_{n=1}^{\#wlpoints} (Y_{sp,i,n} - Y_{sp,i,n}^{model})^2 \right] + \chi_{reg}^2 \right) \quad (2.38)$$

The  $\sigma_{sp,i}$  entering this equation are weights and special in the sense that they are NOT only the standard deviation errors of the observations (Y)! The original implementation of SPINOR included special weights (in the .wlb files), not only to exclude certain Stokes parameters if needed but also to make use of the increasing spectral resolution power. With that additional weight the inversions code can be forced to find a best fit closer to the observations. Of course, close attention has to be paid to avoid fitting noise patterns and force the code to go for the subtle but often important features of the spectra instead.

This additional term could be written as

$$\sigma_{sp,i} = \frac{\sigma_{sp,i}^{error}}{\sigma_{sp,i}^{force}} \quad (2.39)$$

where  $\sigma_{sp,i}^{force}$  is the additional weight. Thus, the equation for  $red\chi_{out}^2$  now reads:

$$red\chi_{out}^2 = \frac{1}{\nu} \left( \left[ \sum_{sp=1}^4 \sum_{i=1}^{\#blends} \left( \frac{\sigma_{sp,i}^{force}}{\sigma_{sp,i}^{error}} \right)^2 \sum_{n=1}^{\#wlpoints} (Y_{sp,i,n} - Y_{sp,i,n}^{model})^2 \right] + \chi_{reg}^2 \right) \quad (2.40)$$

Due to the use of an additional weighting factor a general model quality parameter like the reduced  $\chi^2$  is always considerably bigger than unity. Introducing a simpler definition of a quality criteria would be helpful to facilitate the assessment of the fit quality.

### 2.6.6 On uncertainties in the model

This section is the shortened version of a description on the determination of uncertainties in SPINOR inversions presented in Frutiger et al. (2000, Chap. 2.3). For a more general discussion of uncertainties in inversions please also see del Toro Iniesta (2003).

When inverting a given model and set of observations by non-linear least-squares fits the Levenberg-Marquardt method is used. Here, for each iterative step the spectra and its derivatives have to be calculated to find the minimum of the merit function. The use of Response functions makes this steps fast and reliable (Westendorp Plaza et al., 1998, and references therein).

In theory, the curvature matrix of the problem can also be used to retrieve standard error estimations. When inverting big curvature matrices to infer the standard deviation numerical inaccuracies become important. These problems can be overcome using singular value decomposition (Ruiz Cobo & del Toro Iniesta, 1992) and by imposing a scaling scheme on the parameter space before calculating the inverse. A parameter scaling becomes necessary because different units are used for each parameter causing the partial derivatives to span over several orders of magnitude. Therefore, the units are adjusted such that the maximum absolute value for any derivative is unity. In the following singular value decomposition the curvature matrix, which contains elements that are too small and thus interpreted as being dominated by numerical effects, gets cleaned by applying an appropriate threshold that sets these elements equal to zero. For the practitioner, these thresholds do effect the

error estimates provided by the inversion code. The effects of different thresholds are discussed in (Frutiger et al., 2000, A.1).

For our studies the uncertainty estimates of SPINOR only were used as indicators of fit quality. The discussions of the model uncertainties were based on statistical error analysis from repetitive inversion runs based on different initial values and varying model details to understand the distribution of resulting atmospheres.

### 2.6.7 Plane-parallel models

A one-dimensional plane-parallel model atmosphere where all parameters depend only on the optical depth is the simplest approach since we look for the spatially averaged stratification of atmospheric parameters (see Chap. 3) or can spatially resolve the structures we are interested in (see Chap. 4).

Table 2.5 lists all parameters that technically can be depth dependent when using SPINOR. They can be combined using any combination of the following inputs (with  $a = T, p, p_e, n, \kappa, \xi, v_{LOS}, B, \gamma, \xi$ ):

- $a$  is constant with depth
- $a_i = a(\log \tau_i)$  is taken from a tabulated input atmosphere with  $i$  depth points
- $T = T(\log \tau)$  is taken from a tabulated input atmosphere but shifted vertically by a given offset
- $B = B_0 + \text{grad } B \cdot \log \tau$ , a linear function including a gradient
- $a_i = a(\log \tau_i)$  is spline interpolated from parameter values given on a preset  $\log \tau$  grid

If not read from a tabulated atmosphere, the gas pressure, the electron pressure, the density, and the continuum opacity are derived from the temperature, gravity surface acceleration and the reference wavelength assuming LTE and hydrostatic equilibrium. These stratifications are calculated using the Uppsala opacity package from the MULTI-code (Carlsson, 1986).

For the radiative transfer it is important to, first, start deep in the atmosphere, where continuum and lines are still optically thick, and,

Tab. 2.5 Parameters of the atmospheric models.

Parameter	Description	Eq. reference
$T$	Gas temperature	2.26
$ B $	magnetic field strength	2.11
$\gamma$	inclination angle	2.28
$\chi$	azimuth angle	2.28
$v_{LOS}$	line-of-sight velocity (upflow: $v_{LOS} \leq 0$ )	2.29
$\xi$	micro-turbulence	2.12

second, cover the full formation height of the line. Therefore, all stratifications are extrapolated downwards until  $\log \tau_{5000} \geq 1.4$ .

### 2.6.8 Multiple components - magnetic filling factor

Assuming that we cannot resolve photospheric features spatially, we have to extend our plane-parallel model. In one resolution element we allow two (or more) atmospheres to co-exist as atmospheric *components*. Each of these components is treated as described above. The surface fraction,  $\alpha_i$ , occupied by each component  $i$  is used as a weight to construct the total normalized Stokes profiles.

$$\mathbf{S} = \sum_{i=0}^{\#comp.} \alpha_i \mathbf{S}_i \quad (2.41)$$

$$1 = \sum_{i=0}^{\#comp.} \alpha_i \quad (2.42)$$

Typically, multiple components are used to account for unresolved magnetic surface features. In the simplest case of a first non-magnetic component and a second magnetic component, the surface fraction filled by the magnetic component is termed *magnetic filling factor* ( $ff$ ).

Note, that when measuring the magnetic field strength of spatially unresolved features via Zeeman-effect one actually measures the product of filling factor and magnetic field strength.

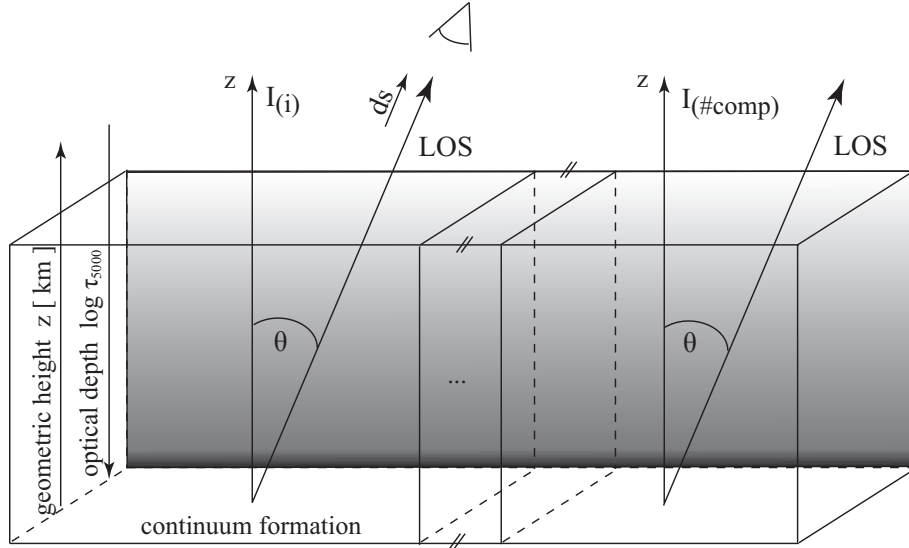


Fig. 2.13 Schematic cut through a multi-component 1D model atmosphere. For each component the radiative transfer equations are solved along the line-of-sight. the total emergent Stokes profiles are computed as the sum over the emergent spectra from each component weighted by its surface fraction  $\alpha$ .

### 2.6.9 A brief test with simulated observations

In the following we test the abilities of the inversion code to recreate atmospheres in a simplified way. We create artificial observations by mixing the spectra of HINODE S1 CU and PUD in different ratios. Since ground based observatories suffer from additional straylight we add 5 % of a spectrum from a quiet Sun pixel and compute a weighted average with filling factors as weights (see Table 2.6). The simulated spectra are shown in Fig. 2.14.

The basic purpose of this test, which is constructed to be really simple, is to see if the fraction of the non-magnetic straylight component is correctly recognized or if its higher temperature is wrongly assigned to the magnetic components.

For the test inversions we used a simplified three component model that has no depth dependencies because we want to keep the shape of the temperature stratifications fixed. These are only allowed to be shifted

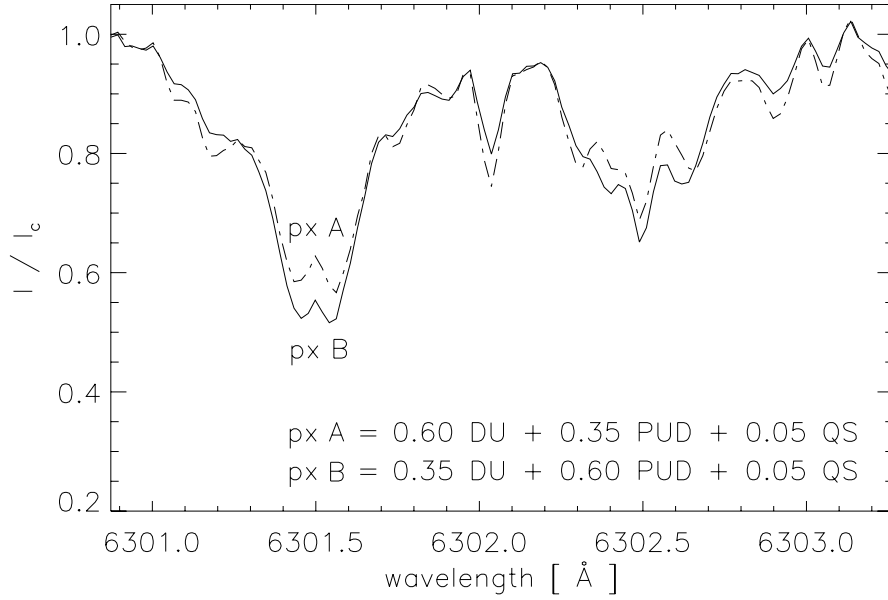


Fig. 2.14 Intensity spectra of artificially created pixels A and B.

Tab. 2.6 Filling factors for simulated observations.

pixel	filling factors DU - PUD - QS (in percent)		
	as constructed	found by inversions	
		HINODE atms.	THEMIS (Kurucz) atms.
px A	60 - 35 - 5	54.8 - 44.2 - 1	53.9 - 42.4 - 3.7
px B	35 - 60 - 5	39.0 - 60.0 - 1	43.3 - 54.4 - 2.3

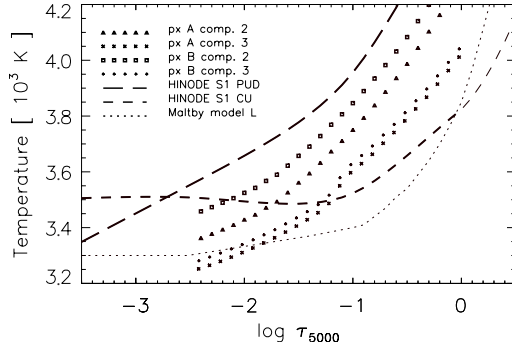


Fig. 2.15 Comparison of temperature stratifications found for sunspot umbrae using the Kurucz atmospheres also employed for the THEMIS inversions.

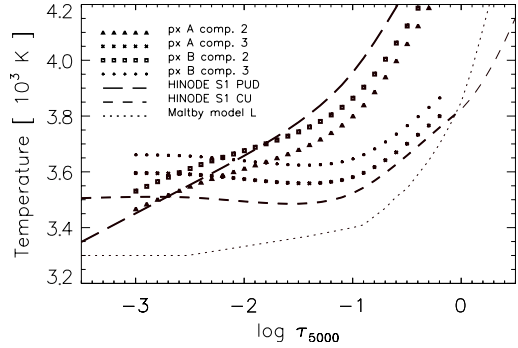


Fig. 2.16 Comparison of temperature stratifications found for sunspot umbrae using the atmospheres from the HINODE analysis also used to create the mock observations.

vertically, i.e. there the effective temperature is a free parameter. We use two different sets of input atmospheres: first, the HINODE atmospheres of PUD and CU already employed to create the mock observations and, second, the standard atmospheres by Kurucz (1992) as in the THEMIS inversions. Note, that the shapes of the temperature curves are quite different. The magnetic field stratification in the two magnetic components is assumed to be linear with a free gradient. The angles of the magnetic field vector,  $\gamma$  and  $\chi$  as well as the line-of-sight velocity, the macro- and microvelocity in each component are modeled constant with depth.

Of course, the outcome depends on the model atmospheres used as input for the inversion. The filling factors of the respective components are found better, yet not perfectly, by the HINODE atmospheres (cf. Table 2.6). Note, that no run could retrieve the 5% fraction of the straylight atmosphere thus adding this additional amount of heat to the two magnetic components.

From the resulting temperature stratifications for the pixels A and B only those of the two magnetic components are plotted in Fig. 2.15 for the atmospheres used in the THEMIS inversions and in Fig. 2.16 for the HINODE atmospheres. The original HINODE PUD and CU stratifications are given for orientation.

All inferred temperature stratifications lie in between the two curves

that correspond to the input HINODE spectra regardless of the atmosphere set used for inversions. With its higher fraction of CU the components of pixel A are in both cases cooler than those of pixel B. But since in all cases the fraction of the straylight component is underestimated all stratifications are found to be generally warmer.

As shown in Fig. 2.14 the spectra of the two artificial pixels are only slightly different. Nevertheless, the code manages to find temperature differences of about a hundred degrees although these spectra are normalized to the local continuum, neglecting the lower brightness of the spectrum relative to the quiet Sun. The code only uses the slight differences in line parameters and therefore exploits the different temperature and magnetic sensitivities of the spectral features blended in the spectrum.

This test shows that straylight can severely influence the results of inversions. In addition, it illustrates that the spectra used to compose the mock observations and their associated temperature and magnetic field stratifications are not orthogonal parts that can be combined in different ratios to compose any sunspot atmosphere.

### 2.6.10 Challenges for inversions

Since the introduction of inversions to the field of solar physics the community argued about the validity of the technique and its results (see del Toro Iniesta, 2003, and references therein). The technique has often been accused of being unstable, non-intuitive and somehow unpredictable. The latest codes and their description in the literature (e.g. del Toro Iniesta, 2003) destroy all but the argument about the missing intuition. On the other side the results are taken from solutions that are mathematically speaking not unique and suffer from cross-talk among the free parameters. These two arguments go hand in hand with the feeling of the beginner to deal with a non-intuitional black box.

A well known example for trade-offs or cross-talk among free parameters is the following: Increasing the temperature produces similar effects as decreasing the magnetic field and increasing the micro-turbulence  $\xi$  slightly. However, this effect is not always visible and varies in amplitude (see del Toro Iniesta, 2003, Chap. 11.1).

For a long time, it was questionable whether inversions of spectropo-

larimetric data of visible lines could distinguish strong magnetic field with low filling factors from weak magnetic fields. Employing HINODE measurements around 6302 Å it has been shown that even ME inversions are able to solve this ambiguity (del Toro Iniesta et al., 2010).

In general one must be cautious with the interpretation of inversion result. The variation of input parameters and values and also slight changes of the atmospheric model are a must to build confidence in the obtained results and test the variability of the fit quality. With SPINOR, in particular when inverting several spectral windows at once, the more technical parameters of the required fit quality ( $\sigma$  values in the .wlb file) and their relative strengths have been very sensible and in some cases most subtle to be set adequately. Here, only trust building series of many inversions led to the results.

The SPINOR inversions done for this thesis have been tested to be highly stable even with most different input parameter values. Any set of inversions was executed to the best knowledge of the modeler and all known precautions were taken to corroborate the results found.

---

# Sunspot umbra model atmospheres

---

R. Wenzel<sup>1</sup>, S. V. Berdyugina<sup>2</sup>, D. M. Fluri<sup>1</sup>, J. Arnaud<sup>3</sup>, A. Sainz Dalda<sup>4</sup>

This chapter is in peer-review for publication in *Astronomy and Astrophysics*.

## Abstract

We construct semi-empirical models of the thermal structure of different sunspot umbra regions.

By inversion of full Stokes spectra observed simultaneously in several spectral regions in the optical at the THEMIS facility we infer the height dependence of physical quantities such as the temperature and the magnetic field strength. These spectra include atomic (Fe I 5250.2 and 5250.6 Å) as well as highly temperature sensitive molecular lines (TiO 7055 Å

---

<sup>1</sup> Institute for Astronomy, ETH Zurich, 8093 Zurich, Switzerland

<sup>2</sup> Kiepenheuer-Institut für Sonnenphysik, 79104 Freiburg, Germany

<sup>3</sup> LUAN, Université de Nice, Nice 06108, France

<sup>4</sup> Stanford-Lockheed Institute for Space Research, Palo Alto, CA, USA

and MgH 5200 Å). The simultaneous inversion of these lines originating from different heights in the solar atmosphere allows us to create a model atmosphere for different regions of this sunspot umbra.

The inferred sunspot model atmospheres found are spatially averaged in order to create standard models for different part of the sunspot umbra (core, dark, intermediate, bright umbra, and light bridge). They cover a depth range of  $\log \tau_{5000} = [-4, 0]$  within the photosphere and consist of two magnetic components accounting for unresolved umbral fine structure. Comparing the temperature stratifications in this sunspot with those reported by other authors we find that our sunspot model is significantly warmer.

### 3.1 Introduction

Sunspot umbrae harbor the strongest magnetic field in the solar atmosphere. The temperature contrast of about 2000 K with respect to the quiet photosphere results from the magnetic field that inhibits convection. This process is not yet fully understood, although efforts to infer semi-empirical models of the umbra and other regions of sunspots started more than 30 years ago. Based on measurements of the intensity center-to-limb variation for a set of wavelengths Avrett (1981) constructed a sunspot umbra model which was later improved by Maltby et al. (1986) who included IR measurements to probe the deepest layers. More recent models were based on high precision, full Stokes spectro-polarimetric measurements of various lines in narrow spectral regions and the improvement of inversion techniques. For whole sunspots this was done in the optical (Fe I lines at 6301.5 and 6302.5 Å) by Westendorp Plaza et al. (2001) and in the infrared (Fe I and OH lines at 15 648.5 and 15 652.8 Å) by Mathew et al. (2003). Other models inferring atmospheric stratifications were concentrating on single spatial resolution elements (Socas-Navarro, 2007) or on special features like umbral dots (e.g. Socas-Navarro et al., 2004; Riethmüller et al., 2008a).

In this paper we aim at deriving model atmospheres of different subregions in the sunspot umbra. We apply inversion to the full Stokes vector simultaneously in three spectral windows which include both atomic and molecular lines. The first window is centered at the prominent Fe I lines

at 5250 Å, the second at the TiO  $\gamma(0,0)$  R<sub>3</sub> band head at 7055 Å, and the third at absorption lines of MgH A-X at 5200 Å. This choice of lines allows us to focus on the sunspot umbra since TiO lines are extremely temperature sensitive and are observed only in environments with a temperature  $\leq 4500$  K. MgH lines are both temperature and pressure sensitive and are strongest at about 4000–4500 K which covers most of the umbra. The use of many lines in one simultaneous inversion increases the height range of the inferred atmosphere. This is especially true for molecular lines which, unlike atoms, can be treated in LTE even in higher layers. In addition, employing several lines of the same molecule allows us to probe the atmosphere conditions at an even finer height grid (Berdyugina et al., 2003). Furthermore, since atomic features are often blended by molecular lines, like the employed Fe I lines which are blended with TiO  $\alpha$ -system transitions, molecular lines should be computed along with atomic ones. Combining spectropolarimetry of atomic and molecular lines thus provides a very sensitive tool for detecting and probing magnetic structures in the sunspot umbra. An earlier example of simultaneous inversions of Fe I, MgH, and TiO lines was presented by Afram et al. (2006). In this paper, we further employ the advantage of this approach.

We present observations in Sect. 3.2, details of the inversion in Sect. 3.3, and results and interpretations in Sect. 3.4. In the Appendix E we provide average model atmospheres for subregions of the sunspot umbra.

## 3.2 Observation and data reduction

The data analyzed in this paper were obtained on September 6, 2004, with the MTR spectrograph at the THEMIS facility of the Observatorio del Teide, Tenerife (Arnaud et al., 1998; López Ariste et al., 2000). The sunspot dominating the active region NOAA 10667 was observed simultaneously in five spectral regions in the visible taking advantage of the multi line spectropolarimetric capabilities of THEMIS. Full Stokes spectra were recorded (quasi-) simultaneously for various molecular and atomic species. These observations were earlier reported as the first full-Stokes polarimetry of the TiO  $\gamma(0,0)$  R<sub>3</sub> band lines in a sunspot (Arnaud et al., 2006).

The large, irregular sunspot of the active region NOAA 10667 had

Tab. 3.1 Spectral features used for inversions. For the analysis the TiO window was split into two parts to avoid atmospheric water absorption features.

Window	Range [Å]	Contributing lines	$g_{\text{eff}}$
Fe I	5249.7–5051.3	Fe I 5250.208 Å	3.0
		Fe I 5250.6 Å	2.2
		Ti I 5250.93 Å	1.4
		TiO $\alpha$ system	$\leq 0.07$
TiO	7054.15–7054.55	TiO $\gamma(0,0)$ R <sub>3</sub> band-head	$\leq 0.8$
	7054.80–7055.30	Co I 7054.4 Å	1.4
MgH	5199.40–5199.70	MgH A-X (0,0) Q <sub>12</sub> , P <sub>1</sub>	$\leq 0.2$
		Fe I 5199.53, 5199.69 Å	

a size of about  $16'' \times 25''$ . It contained a strong light bridge, almost in east-west direction, dividing it into two parts with an area ratio of about 2:1 (cf. arrows in Fig. 3.2 and Fig. 3.2). The spot was observed at a heliocentric angle  $\cos \theta = \mu = 0.9$ . It was the leading sunspot of the active region showing negative polarity followed by a small group of spots of positive polarity. The seeing was about  $2''$ , and no image stabilization was available at THEMIS at that time (Arnaud et al., 2006). We slit-scanned the sunspot and its surrounding area in 18 steps with a step size of about  $1.32''$  with the slit oriented parallel to the limb. The slit was  $1''$  wide and  $58''$  long. The spatial sampling of the detectors was about  $0.465$  arcsec/px leading to resolution elements of  $1.4'' \times 0.47''$ . Out of the six spectral windows observed simultaneously three have been chosen for simultaneous spectral inversion. The three windows each span a range of  $6 \text{ \AA}$  at a spectral dispersion between 18 and  $24 \text{ m\AA/px}$ . In order to avoid telluric blends and reduce computational load only parts of them were used for inversions (see Table 3.1).

The Fe I window around  $5250 \text{ \AA}$  includes two strongly magnetically sensitive Fe I lines which have almost identical thermodynamic properties and form at similar heights. Their different Landé factors allow us to determine both the magnetic field strength and the filling factor (Stenflo, 1973). The TiO window around  $7055 \text{ \AA}$  includes the TiO  $\gamma(0,0)$  R<sub>3</sub> band-head and is the strongest molecular absorption feature in the visible spectrum of cool stellar atmospheres (Berdyugina et al., 2003). In

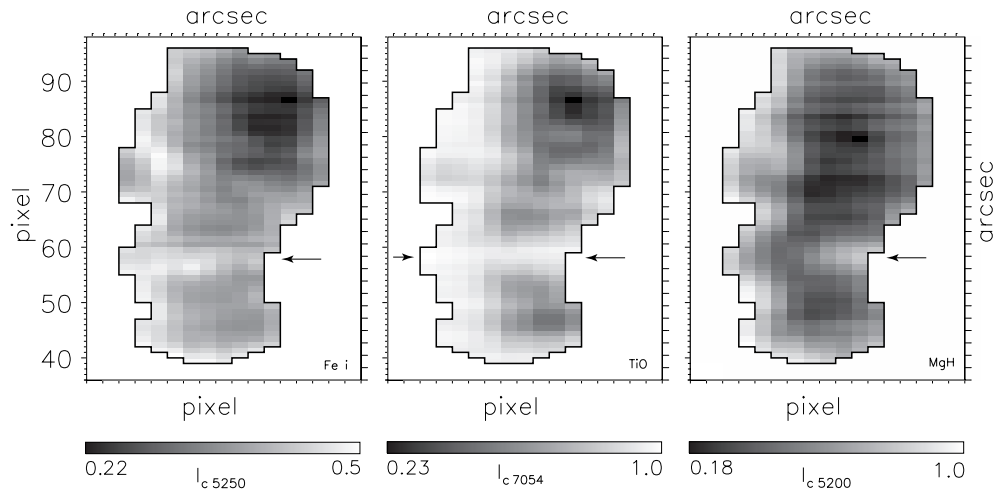


Fig. 3.1 Intensity maps of the observations in the Fe I window (left), i.e. within the line core of the red Fe I line at  $5250.6 \text{ \AA}$ , in the TiO window (middle), i.e. in the band head at  $7054 \text{ \AA}$ , and in the MgH window (right) at  $5199.5 \text{ \AA}$ . All maps are normalized to the average quiet sun continuum intensity of the respective wavelength. For each map three to four spectral resolution elements were binned. All panels only show the sunspot's umbra defined as intensity of less than half of the average quiet sun continuum at  $5250 \text{ \AA}$ . The arrows indicate the location of the strong lightbridge.

addition, the MgH window around 5200 Å includes five magnetically sensitive MgH lines from the A-X (0,0) band. In our observations, however, the observed molecular signals were lower than expected, i.e. only up to 3.5 %  $V/I_c$ .

The normalized brightness maps of the sunspot umbra in the respective spectral windows are presented in Fig. 3.1: The first was obtained in the core of the Fe I 5250.6 Å line, the second in the TiO band-head at 7054.4 Å and the last at 5199.6 Å. Note that each map is normalized to the average quiet sun continuum of the respective wavelength which is different for each map. Only the umbra of the sunspot is shown which is defined by a continuum intensity in the Fe I window of less than one half of the average quiet sun intensity.

One can see the different temperature sensitivity of Fe I, TiO, and MgH. Where the atomic line already saturates, the TiO windows allows us to see the darkest umbral substructures. This behavior is very helpful for constraining the temperature in this regions. The MgH lines are well seen in most of the umbra.

In order to carry out simultaneous inversions with spectra obtained in this three windows, we have co-localized the input maps using a standard 2D-correlation from Press et al. (1992) under the assumption that the sunspot substructures are similar in all observed spectral windows. This cross-correlation is accurate to one spatial resolution element. The co-localization with the highest correlation was employed as input for this investigation. Any deviation from this best co-localization combines signals from different pixels of the maps which leads to bad inversion results.

The THEMIS MTR instrument polarization analysis package consists of two achromatic quarter wave-plates followed by a beam splitter, resulting in a  $(I+S)$  beam and a  $(I-S)$  beam. One polarization sequence consists of a set of six measurements,  $S$  taking successively the values  $Q$ ,  $-Q$ ,  $U$ ,  $-U$ ,  $-V$ , and  $V$ . To reach sufficient sensitivity for weakly polarized molecular lines, this sequence was repeated 10 times for each slit position during a scan. This observational strategy is comparable to a very low polarization modulation of 0.08 Hz frequency. The exposure time depends on the spectral region. For the spectral regions used for the presented analysis, the exposure time was 0.63 seconds. Our strategy also reduced image motion effects on the polarization.

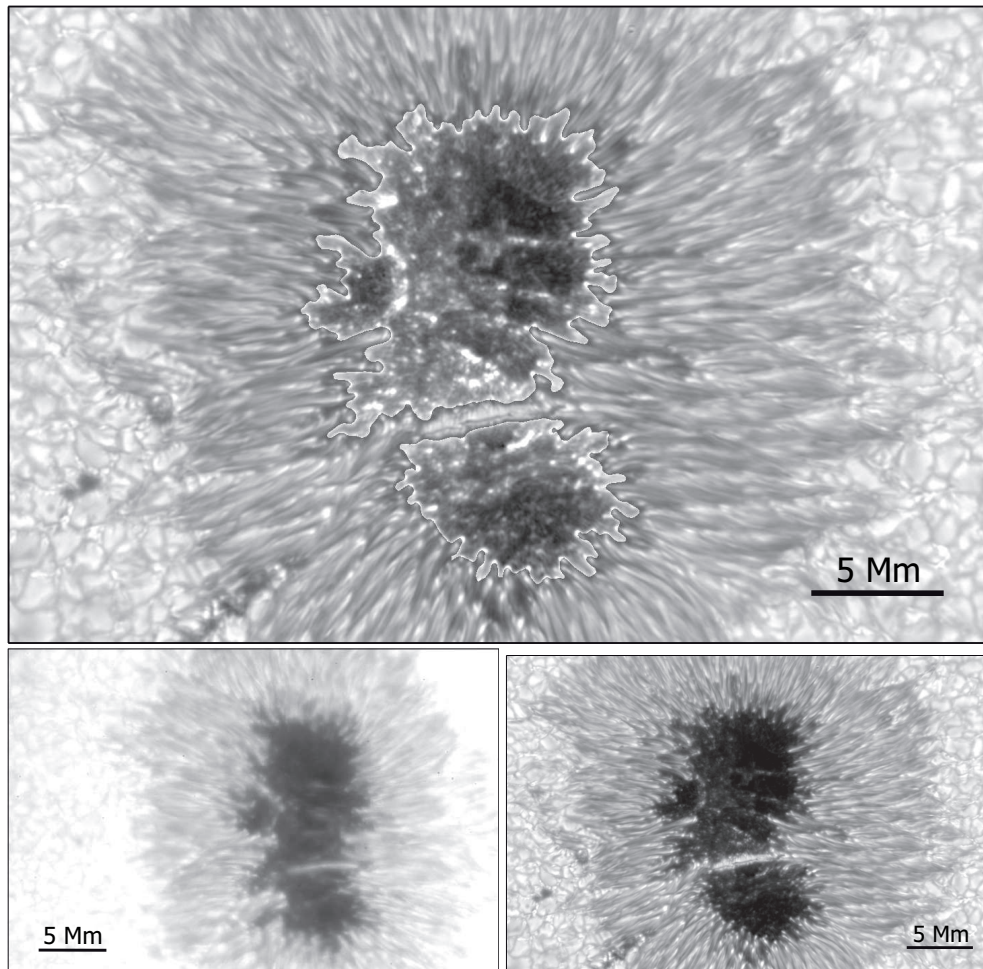


Fig. 3.2 TiO 7055 Å narrow-band filter images of the sunspot NOAA 10667 obtained at the NSST (La Palma) on the same day, Sep 6 (bottom left), and with better seeing conditions on the following day, Sep 7 (top and bottom right), 2004. The image size in the middle is about  $50'' \times 32''$ , corresponding to a spatial size on the sun's surface of about  $35\,700\text{ km} \times 23\,000\text{ km}$ . The middle image is the same as the right one but with an enhanced contrast to pronounce the umbral substructure.

The data set was reduced semi-automatically by the reduction package *Stokes Quick Viewer (SQUV)*, a standard reduction tool for THEMIS MTR data. It implements the demodulation matrix technique, i.e. for our six measured polarization states a demodulation matrix is calculated taking into account the observed wavelength, the THEMIS polarization analyzer characteristics (refraction index and thickness of the waveplates), and the rotation states. Flat-field images were provided to compute the curvature of the spectra. For more information on *SQUV* see Sainz Dalda & López Ariste (2007). To prepare the observations for the inversion code, we integrated over 10 exposures and normalized the spectra to the local continuum. In order to remove small residual vignetting effects the continuum was fitted and corrected with a fourth order polynomial and only the center of the spectral regions were used further. In addition, we corrected the asymmetric profiles for *V-QU* crosstalk on the basis of correlation plots. A sample spectrum used for inversions is given in Fig 3.3.

This sunspot was also imaged during a coordinated program at the NSST (La Palma) with a narrow-band filter (FWHM=7 Å) centered at the same TiO 7055 Å band (no spectropolarimetry). This filter was designed and first used for imaging the solar surface by Berger & Berdyugina (2003b). Because of the exceptional temperature sensitivity this filter has proven to provide very sharp images of structures in the photosphere, penumbra, light bridges, and umbra (see also Riethmüller et al., 2008b). The TiO band images of the sunspot under investigation taken on the day of our observations and on the following day with better seeing conditions are shown in Fig. 3.2. They reveal a complicated structure of the umbra which is densely populated with umbral dots (UD). Only the upper right corner of the umbra appears relatively dark and free of UD. However, if the contrast of the umbra is enhanced (middle image in Fig. 3.2), even that part of the umbra has a complicated web-like structure. The UD population is especially dense near the strong light bridge and the umbra-penumbra border. The UD also align into structures across the umbra, often as a continuation of penumbral filaments. Most prominent structures, such as large concentrations of UD, the light bridge and the darkest core umbra are clearly identified and help us to select regions in our observations for obtaining average models of the umbra substructures.

### 3.3 Inversions

In order to infer an umbra model atmosphere, i.e.  $B = B(\tau)$ ,  $T = T(\tau)$ ,  $p = p(\tau)$ , etc. we use a spectral inversion technique. For these inversions the well-established code SPINOR (Solanki, 1987; Frutiger et al., 2000; Berdyugina et al., 2003) was employed with the molecular Paschen-Back algorithm implemented according to the theory by Berdyugina et al. (2005). This code assumes LTE conditions and solves the Unno-Rachkovsky radiative transfer equations based on response functions. Starting from an initial guess the Stokes profiles were fitted iteratively to the observational data by varying the free parameters of the model atmosphere, e.g. the depth stratification of the temperature. The quality of the fit was measured by a merit function, based on  $\chi^2$ , which is minimized by the Levenberg-Marquardt algorithm (Press et al., 1992). Since SPINOR can account for line blends, several molecular bands and multiple spectral regions (listed in Table 3.1) were inverted simultaneously using the full Stokes vector.

A typical inversion of one pixel of the map, depending on the atmospheric model and line list chosen, took between 2 and 7 hours on a 3 GHz CPU, corresponding to 20–30 iterations, and was considered finished if the differences of the atmospheric parameters obtained for consecutive iterations remained within preset limits ( $\Delta B = 10$  G and  $\Delta T = 10$  K), i.e. when the iteration has converged.

The quality of the fit was measured by the merit function depending on the required fit quality and signal-to-noise. Since weights can only be assigned to whole spectral windows and not to individual line features, a visual inspection was necessary for all pixels of the map to reject bad fits and ensure that the molecular features have been taken into account in the best possible way. Normally, the fit could not reach the noise level of the observations, as often happens due to model limitations. A typical fit is shown in Fig. 3.3.

#### 3.3.1 Initial values

In order to ensure a stable solution of our inversions, we investigated the sensitivity of the solution to initial values of model parameters. We found that the results of the inversions were not very sensitive to them.

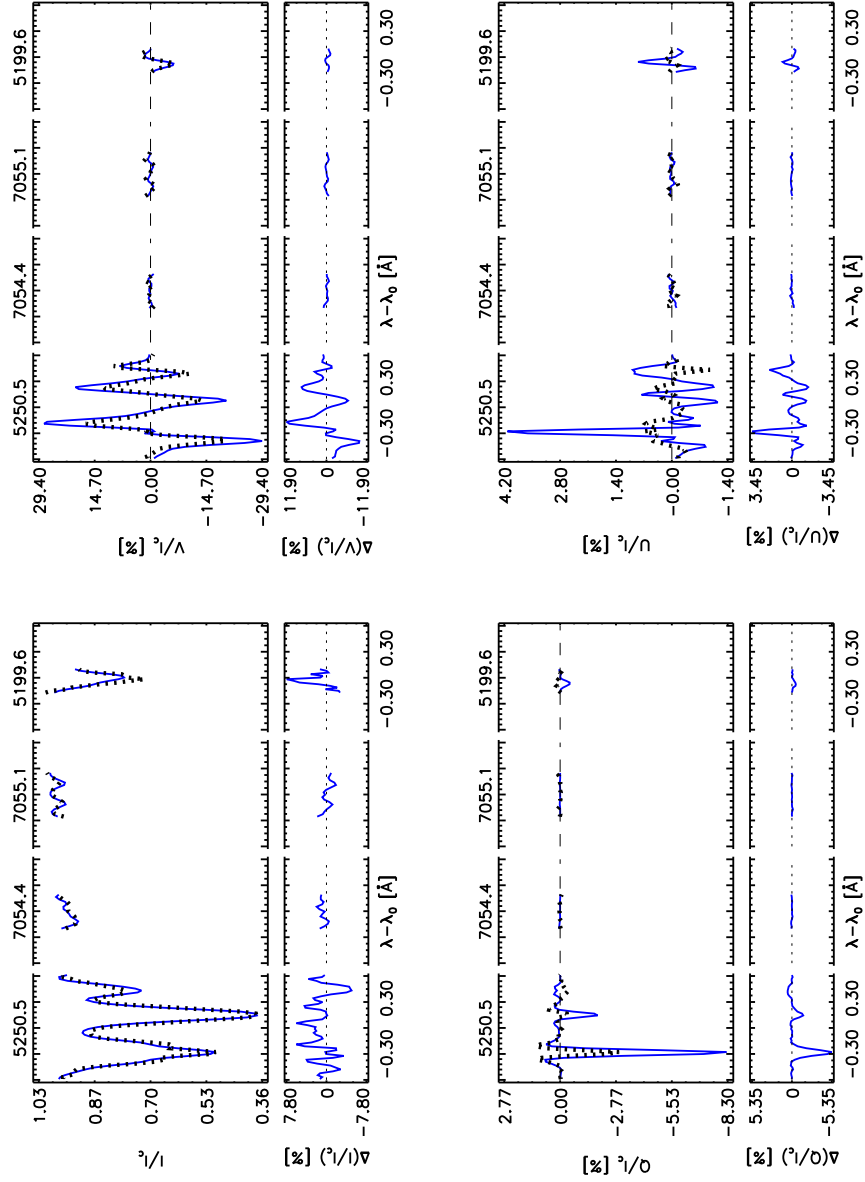


Fig. 3.3 Two component sample fit of the full Stokes vector (core umbra). Observational data (dotted blue line) and its best fit found by inversions (solid black line) are shown in all spectral windows.

Even when initialized with less likely or randomly chosen initial values the inversions led to the same final atmosphere as before although taking more iterations. In order to minimize computational time, sets of standard values were chosen depending on the pixel brightness. These optimized values were obtained as follows. We employed standard model atmospheres by (Kurucz, 1992) with  $\log g = 4.5$ , various  $T_{\text{eff}}$ , a depth independent magnetic field strength  $B$ , and the angles  $\gamma$  and  $\chi$  representing the inclination and azimuth of the magnetic field vector with respect to the line of sight. Using STOPRO, which is the part of SPINOR for direct modeling, we synthesized a set of Stokes profiles in the observed windows for a reasonable range of the parameters. These were further combined with Stokes profiles of a field-free photosphere with  $T_{\text{eff}}=5750$  K using a magnetic filling factor  $f$ . The best fit parameters determined via a  $\chi^2$  minimization procedure were used as initial guess for subsequent inversions with depth-dependent parameters.

### 3.3.2 Models with a single magnetic component

We first inverted only the Fe I window around 5250 Å since, because of their exceptionally high Landé factors, the signals of the dominating Fe I lines are the highest in all Stokes parameters in all selected windows. Here, a two component model, one magnetic component and one non-magnetic component accounting for straylight, was employed. The strengths and profiles of the atomic lines were calibrated against a quiet sun model atmosphere with  $T_{\text{eff}}=5750$  K (Kurucz, 1992). Including molecular blends present in this window improved the fit further but still have not given satisfactory results. Nevertheless, these two-component inversions do provide next approximation to the final atmosphere. Similarly, simultaneous inversions of all three spectral windows, including the TiO and MgH bands, did not provide satisfactory fits (data not shown), as long as a single magnetic component plus a photospheric straylight component were used. Only by introducing a second, cooler magnetic component did the fit quality improve as measured by the merit function which increased by about 30%.

### 3.3.3 Models with two magnetic components

In our final inversions we employed a three-component model atmosphere to calculate the synthetic Stokes profiles (see Fig. 3.3). The first component is a field-free quiet sun atmosphere accounting for straylight ( $T_{\text{eff}}=5750$  K, Kurucz, 1992), whereas the second and third components represent magnetic parts of the sunspot atmosphere. In each pixel we thus allow three atmospheric components to coexist. They are combined using three filling factor parameters,  $f_1$ ,  $f_2$ , and  $f_3$ , whose sum equals 1. The magnetic filling factors represent the fractional area of the resolution element penetrated by the magnetic field whereas every field-free contribution within a pixel is considered to be straylight. Typical values for straylight,  $(1 - f_2 - f_3)$ , in the umbra are a few percent as indicated in Table 3.3. For each pixel of the map the values of these parameters were determined independently (see Fig. 3.5).

For clarity, we address the second and third components as the warm and cool magnetic components, respectively.

The model we implemented allowed us to iterate the temperature stratification of both magnetic components at five reference depth points located at  $\log \tau_{5000} = -3.5, -2.5, -1.5, -0.5, \text{ and } 0$ . In the interest of robust inversions, the magnetic field strength of the cool magnetic component was set to follow a linear function with an arbitrary gradient, whereas the magnetic field strength of the warm magnetic component was allowed to vary freely at the depth points listed above. To further reduce the number of free parameters the line-of-sight velocity, the azimuth angle  $\chi$  and the inclination angle  $\gamma$  of the magnetic field as well as the micro- and the macroturbulent velocity parameters were iterated depth independently. The temperature profile of the field-free straylight component was fixed (quiet sun) but was allowed to be shifted along the temperature axis.

Increasing the complexity of the model by introducing two instead of only one magnetic component was necessary to account for the averaging effect of the comparably large spatial resolution elements ( $1.4'' \times 0.47''$ ) combined with the seeing of  $2''$ . As a result, the substructures of the umbra due to UDs remained unresolved in the THEMIS recordings (Fig. 3.1). The presence of a large number of UDs was only revealed by the intensity images obtained at the NSST facility (Fig. 3.2, also see

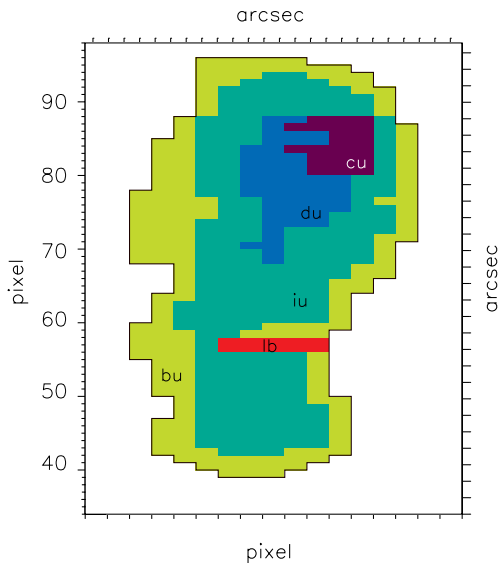


Figure 3.4 Subregions of the observed umbra. From the umbral-penumbral border to the center we distinguish bright umbra (bu), intermediate umbra (iu), dark umbra (du), and core umbra (cu) (for region's definitions see Table 3.2). In addition, a lightbridge region (lb) is defined. The inversions were done for each pixel independently.

Riethmüller et al. (2008b) for a more detailed analysis). Thus, by introducing a second magnetic component we basically model the unresolved substructures of the sunspot umbra (e.g. Sobotka et al., 1993).

### 3.4 Results

In this section we present model atmospheres for different subregions of the umbra as obtained by inversions. We use the brightness of each pixel in the normalized map of the full FeI window to distinguish the core umbra (cu), dark umbra (du), intermediate umbra (iu), and bright umbra (bu) subregions (see Fig. 3.4). These regions have been defined by their continuum intensity in the FeI window normalized to the quiet sun (see Table 3.2). The selection also reflects the strength of the TiO and MgH absorption features both peaking in the dark and core umbra region. The lightbridge (lb) pixels were identified by visual inspection.

The model atmospheres obtained are only reliable in the depth range  $\log \tau_{5000} = [-4, 0]$  as indicated by the contribution functions of the lines employed (see bottom part of Fig. 3.13). The radiative transfer for the

Tab. 3.2 Definitions of the umbra subregions. The umbra was subdivided into five regions according to the continuum intensity in the Fe I window normalized to the average quiet sun.

region	# pixels	Brightness
core umbra (cu)	24	$I \leq 0.22$
dark umbra (du)	55	$0.22 \leq I \leq 0.25$
intermediate umbra (iu)	261	$0.25 \leq I \leq 0.36$
bright umbra (bu)	201	$0.36 \leq I \leq 0.50$
lightbridge (lb)	10	$0.38 \dots 0.50$

inversions, however, has been calculated for a broader range of depths to ensure that the continuum becomes optically thick and that the full depth range where the spectral line is formed is covered.

In the next sections we present THEMIS inversion results as maps of atmospheric parameters at several optical depths, correlate each pixel's temperature with the magnetic field strength and derive average stratifications for the temperature and the magnetic field strength in all umbral subregions.

### 3.4.1 Maps of umbra model atmospheres

As first results of the inversions we present maps of the filling factors (Fig. 3.5), temperature (Fig. 3.6), and magnetic field strength (Fig. 3.7) of the two magnetic components. These horizontal cuts provide a useful overview of the whole umbra area, whereas the depth stratifications of the temperature (Fig. 3.9) and magnetic field strength (Fig. 3.10) allow for a more precise comparison of the different umbra subregions (Fig. 3.11).

Inspecting the maps of the filling factors, two trends can be found (see Fig. 3.5). From the outer edges towards the core umbra region the straylight fraction is declining by a factor of two and the filling factor of the cool magnetic component is increasing slightly. This is consistent with the smaller number of umbral dots apparent in the NSST image (see Fig. 3.2). The difference is only detectable because we included molecular lines that are temperature sensitive in the core umbra.

Temperature maps of the two magnetic components at different optical depths in the atmosphere are presented in Fig. 3.6. Not surprisingly,

Tab. 3.3 Results of the inversions: Average filling factors of the three model components for the umbral subregions defined in Fig. 3.4 and of the total magnetic component  $\langle f \rangle$ .

subregion	$\langle f_1 \rangle$ (straylight)	$\langle f_2 \rangle$ ( $B$ , warm)	$\langle f_3 \rangle$ ( $B$ , cool)	$\langle f \rangle$
core umbra	0.03	0.52	0.45	0.97
dark umbra	0.04	0.51	0.45	0.96
intermediate umbra	0.05	0.51	0.44	0.95
bright umbra	0.07	0.51	0.42	0.93
lightbridge	0.07	0.51	0.42	0.93

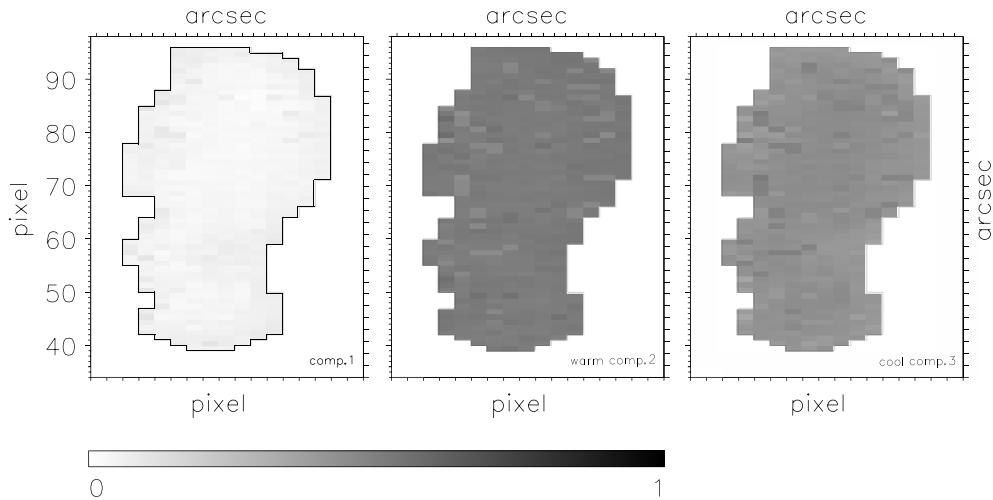


Fig. 3.5 Results of the inversion: Maps of the filling factors of the straylight component (left), and the warm (middle) and cool (right) magnetic components. All filling factors were assumed depth independent.

the substructure within the umbra present in the observational input data (cf. Fig. 3.1) is reflected in the temperature maps resulting from the inversions. Based on these maps the second and third component are termed warm magnetic and cool magnetic, respectively. The lightbridge and morphological details can be identified most prominently in the deeper parts of the atmosphere at  $\log \tau_{5000}$  of 0 and  $-1$ . The contribution functions of the inverted lines reach their maxima at these depths (cf. Fig. 3.13) so that the temperature maps for these layers are best compared to the intensity images taken at the NSST (Fig. 3.2).

In addition, the temperature maps of the cool magnetic component at  $\log \tau_{5000}$  of 0 and  $-0.5$  reflect the properties of the input map of the TiO window (cf. Fig. 3.1). In these panels only the darkest regions, traced by TiO, are pronounced. At higher levels the temperature in the cool magnetic component reveals a more uniform pattern similar to the input MgH window.

Maps of the magnetic field strength of the two magnetic components are shown in Fig. 3.7. In the warm magnetic component the general umbral structure is apparent also in the magnetic field strength (top of Fig. 3.7): the magnetic field strength increases towards the darkest parts of the sunspot, the umbral core region, while the lightbridge is easily discerned thanks to smaller magnetic field strengths. In the cool magnetic component the lightbridge and the general umbral structure are more disguised but a trend to higher magnetic field strengths towards the center of the umbra can be seen. The pixelated nature of these maps may be explained by a varying quality of the fit to the contributing molecular features. Since they have a low signal strength in our observations and comparatively low Landé factors it is a matter of carefully weighting of the spectral features to fit them properly by our simultaneous inversions and infer the magnetic properties at the depth layers dominated by molecules.

### 3.4.2 Correlation between magnetic field strength and temperature

The correlation between the magnetic field and the temperature is presented as a scatter plot in Fig. 3.8. All pixels within the sunspot umbra at the optical depths  $\log \tau_{5000} = -2.5, -1.5,$  and  $-0.5$  are plotted.

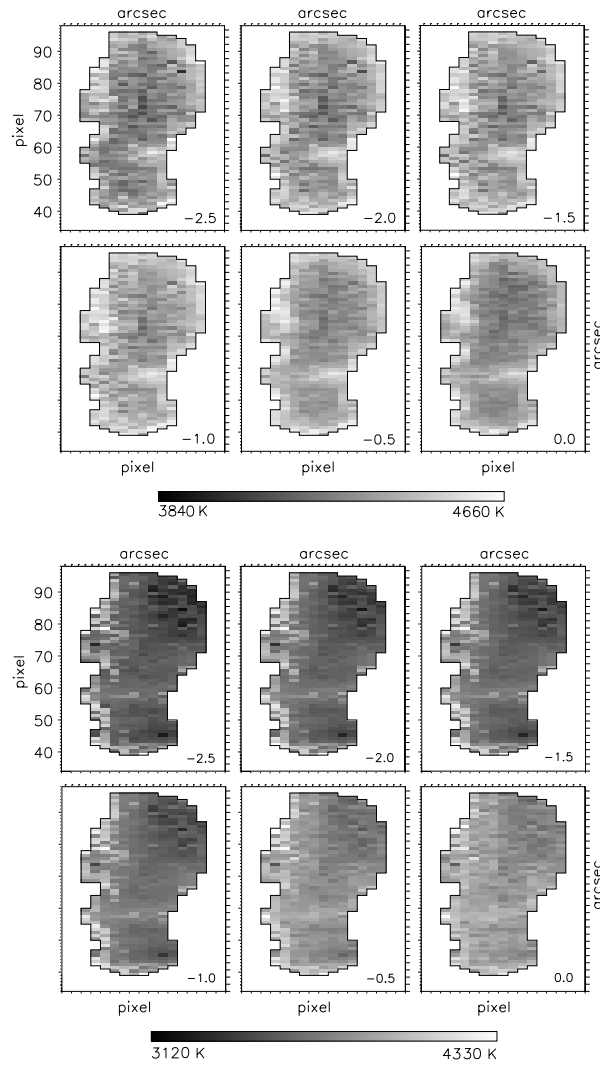


Fig. 3.6 Results of the inversions: Temperature maps of the warm (top row) and cool (bottom row) magnetic component showing different cuts of the sunspot umbra atmosphere at fixed  $\log \tau_{5000}$  levels ranging from  $-2.5$  down to  $0.0$  in half integer steps from left to right. In each row all maps share a common scale.

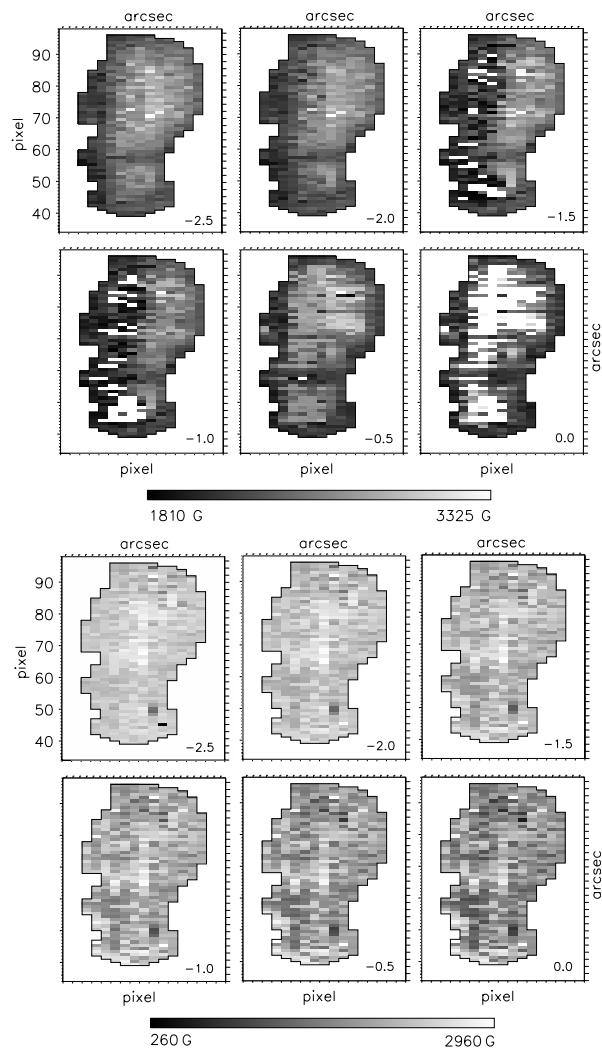


Fig. 3.7 The same as Fig. 3.6 but for the magnetic field strength.

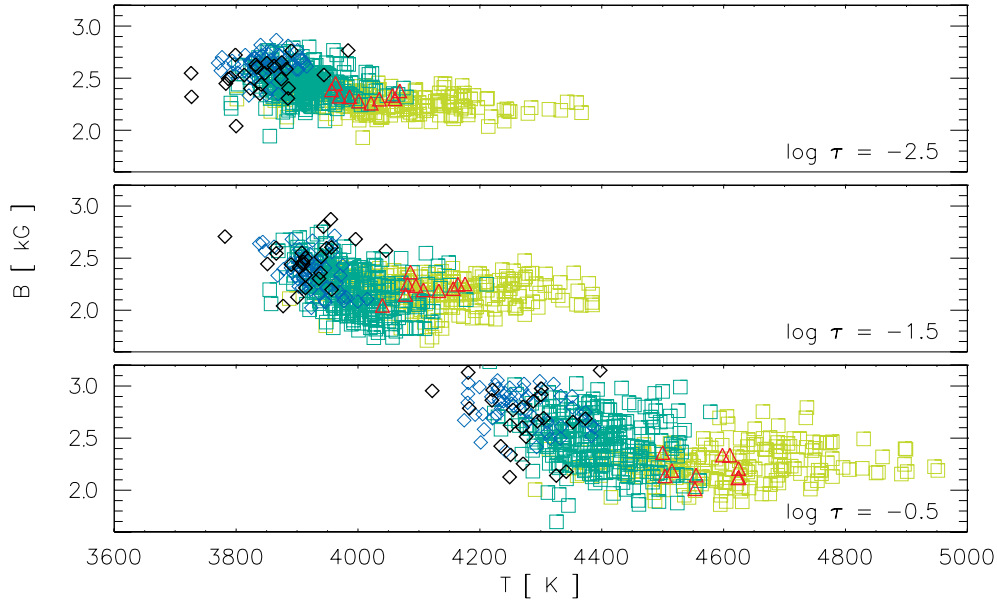


Fig. 3.8 Scatter plot of the magnetic field strength,  $B$ , versus temperature,  $T$ , at the three optical depths  $\log \tau = -2.5$ ,  $-1.5$ , and  $-0.5$ . Umbral pixels are indicated as squares (bu, iu) and diamonds (du, cu) of different colors corresponding to their subregion while lightbridge pixels are represented by red triangles. The color code is the same as in Fig. 3.4.

Quantitatively our results are similar to that of previous investigations (Westendorp Plaza et al., 2001; Martinez Pillet & Vazquez, 1993): the magnetic field strength decreases with rising temperature.

An interesting peculiarity is that within the dark umbra the coolest pixels are not associated with the highest magnetic fields. This can be due to the fact that the Fe I lines are dominating the determination of both the filling factors and the magnetic field strengths because of their high and different Landé factors. In our models the filling factor can only be set constant with depth. So, at the depths probed by the molecular features it might be inaccurate, e.g. too high, leading to an underestimation of the magnetic field strength in these lower layers of the atmosphere (cf. Fig. 3.10). Since this effect is most pronounced for pixels with high molecular signals it might add to the pixelated nature of the cool component's magnetic field maps in Fig. 3.7. The molecules

involved provide excellent additional constraints for the temperature at lower heights, but because of their small Landé factors and their faint signals, they cannot help to find the strength and orientation of the magnetic field vector at the same depth. This effect is also seen when inverting only one of the molecular windows simultaneously with the Fe I window.

### 3.4.3 Vertical stratification of temperature and magnetic field strength

The temperature stratifications of all umbra pixels are plotted in Fig. 3.9 grouped by region and atmospheric component. The same has been done for the magnetic field strength in Fig. 3.10. In both figures each panel also shows the median and the quartiles of the distribution of stratifications as error bars.

The average stratifications of the temperature and the magnetic field strength of the different umbra subregions (as defined in Table 3.2 and Fig. 3.4) are compared for each component in Fig. 3.11. To infer the combined atmospheres, their filling factors were used as weights. The shaded areas indicate the depths where our findings are less constrained by the contribution functions of the analyzed lines (see bottom of Fig. 3.13).

Generally, the darker regions are cooler and bear a higher magnetic field strength. In the warm magnetic component the temperature differences within the umbra subregions at any given depth are only up to 300 K. Within the cool magnetic component, however, all regions can be distinguished with a temperature difference of up to 500 K. The temperature differences between the umbra regions strongly correlate with the strength of molecular features: In the warm magnetic component the magnetic field decreases with increasing optical depth by about 500 G around  $\log \tau_{5000} = -1$ . In the cool magnetic component the linearly modeled magnetic field strength stratification declines with increasing optical depth. As pointed out in Sect. 3.4.2 the constant filling factors predominantly determined by the dominant Fe I lines may be responsible for this result.

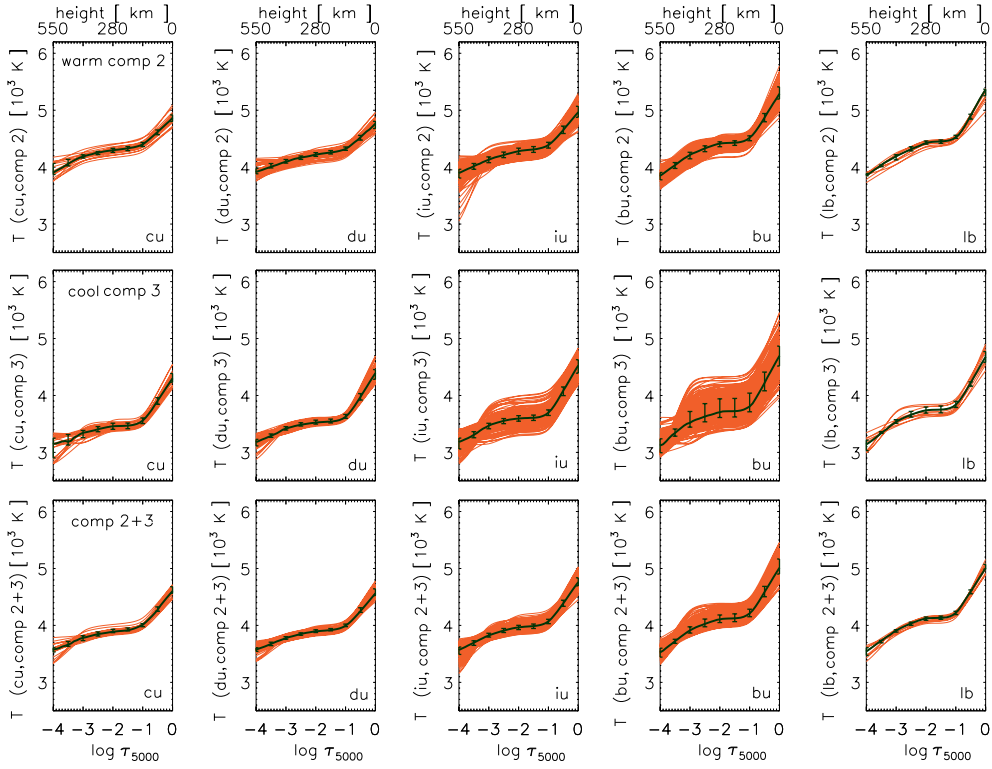


Fig. 3.9 Results of the inversions: Temperature stratification for all pixels of the umbra map. The first two rows show the magnetic components separately. In the third row a total magnetic component was constructed as a combination of the second and third component weighted by filling factors, without straylight. The columns show the umbra subregions: core umbra (cu), dark umbra (du), intermediate umbra (iu), bright umbra (bu), and lightbridge (lb). For each distribution of temperature curves, the median and the quartiles are plotted to provide an estimate of the deviations.

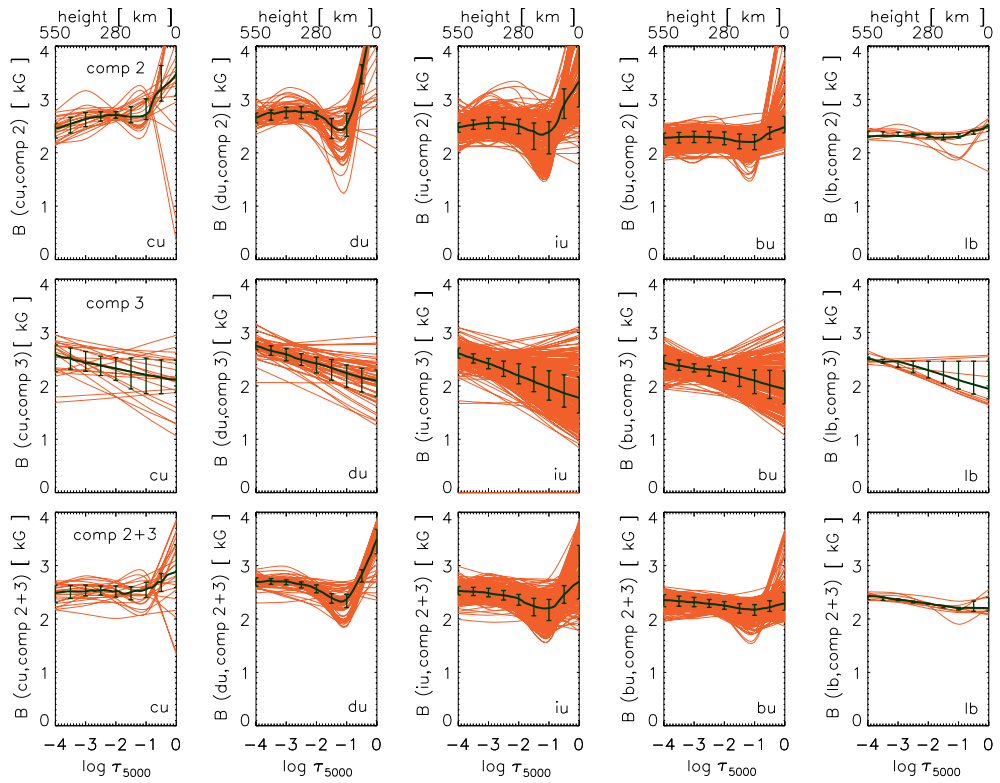


Fig. 3.10 The same as Fig. 3.9 but for the magnetic field strength.

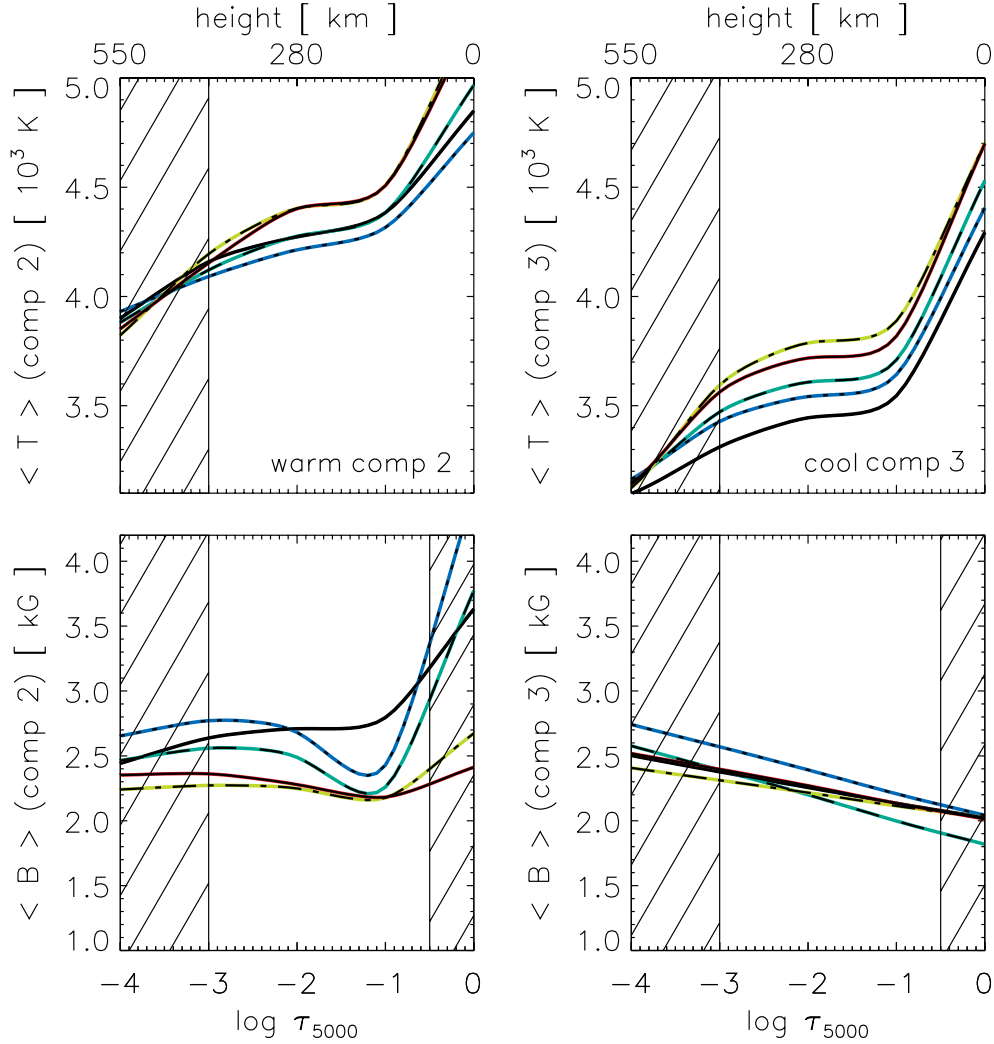


Fig. 3.11 Results of the inversion: Average stratifications of the temperature (upper row) and of the magnetic field strength (lower row). Both quantities are shown for the warm (first column) and the cool (second column) magnetic component. The five curves in each panel show temperature and magnetic field strength averaged over the different umbral subregions defined in Table 3.2 and Fig. 3.4: core umbra (solid line), dark umbra (blue dotted), intermediate umbra (green dashed), bright umbra (light green dashed-dotted) and lightbridge (red solid). The shaded areas indicate depth levels that provide minimal information (compare to the typical line contribution functions plotted at the bottom panel of Fig. 3.13).

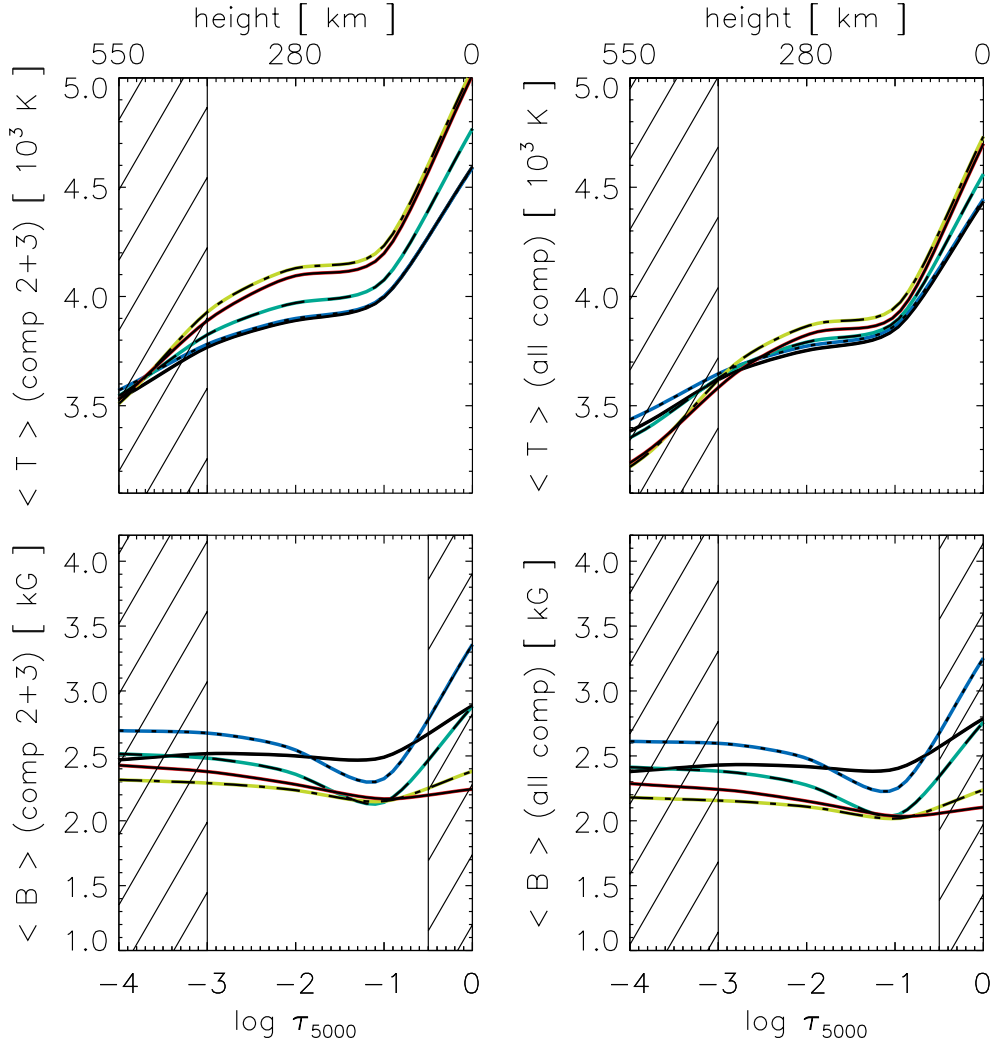


Fig. 3.12 (Continuation of Fig. 3.11) Results of the inversion: Average stratifications of the temperature (upper row) and of the magnetic field strength (lower row). Both quantities are shown for the average of the magnetic components weighted by filling factors (left column) and the weighted average off all components including straylight (right column). The five curves in each panel show temperature and magnetic field strength averaged over the different umbral subregions defined in Table 3.2 and Fig. 3.4: core umbra (solid line), dark umbra (blue dotted), intermediate umbra (green dashed), bright umbra (light green dashed-dotted) and lightbridge (red solid). The shaded areas indicate depth levels that provide minimal information (compare to the typical line contribution functions plotted at the bottom panel of Fig. 3.13).

### 3.4.4 Average umbra model atmospheres

Averaging over all umbra subregions, average temperature stratifications can be computed for both the warm and the cool component separately or even including all components. In Fig. 3.13 our temperature stratifications are compared to Maltby's umbra models (Maltby et al., 1986) which have been something like the standard for many years. They combine models of different layers relying on pinhole photometer intensity observations of 15 large sunspots in the VIS and NIR at the photospheric level (Albregtsen & Maltby, 1981). Depending on the phase of the sunspot cycle, warm (early) and cool (late) temperature stratifications were provided.

Our total average temperature stratification is composed of a cool and a warm component. The cool component is very similar to the warm umbra model of Maltby in the range  $\log \tau_{5000} = [-4, -1]$  but has a steeper temperature gradient towards the deepest layers of the atmosphere. Since the molecular features in our inverted spectra are most sensitive at exactly that depth we conclude that this result is significant. The vertical temperature stratification of the warm component is very similar to that of the cool component, but shifted upward by about 700 K. Its temperature gradient in the lowest layers, however, is slightly less steep to meet the temperature regime of the convection zone below  $\log \tau_{5000} = 0$ .

Our sunspot was observed during the late phase of the solar cycle 23, and its umbra is about 300 K warmer than predicted by the models of Maltby. This result is in agreement with a general trend during, at least, the last decade as reported by Penn & Livingston (2006). They determined from Zeeman measurements of the Fe I line at 15 648 Å and nearby OH features that the maximum sunspot magnetic field has been decreasing from 1998 through 2005 at a rate of about 50 G yr<sup>-1</sup>, together with a decline of molecular line strength observed. This general trend could also explain why the signals of the molecular bands we observed were not as strong as predicted for a sunspot of this size.

### 3.4.5 Umbral dots

Our inversions of umbral spectra require two magnetic components, warm and cold, with almost equal filling factors throughout the sunspot umbra. From the NSST observations (see Fig. 3.2) we know that the in-

vestigated umbra showed a particularly rich substructure composed of peripheral (PUD) and central umbra dots (CUD). Therefore, we inter-

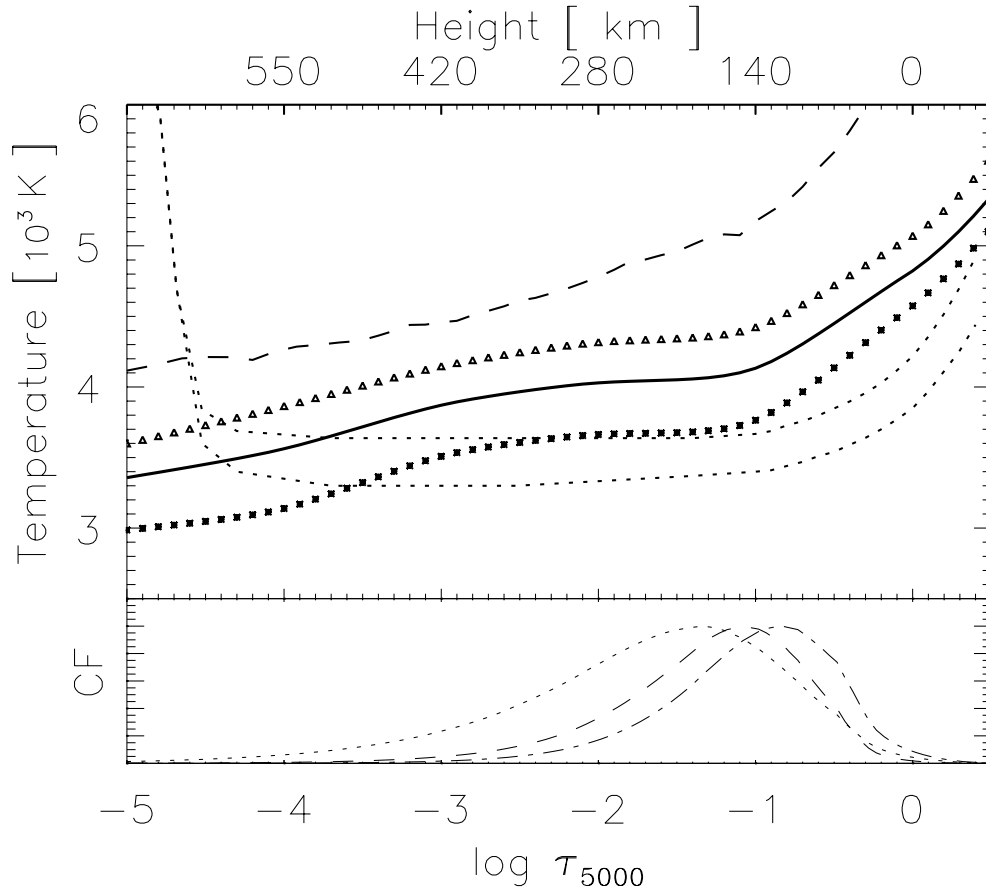


Fig. 3.13 *Top*: A comparison of different umbra models. Our model averaged over the whole umbra is solid line, and its warm and cold components are triangles and squares, respectively. As reference the models of Maltby's cool (late) and warm (early) umbra atmosphere (dotted) and the the FAL-C model of the quiet sun (dashed) by Fontenla et al. (1993) are given. *Bottom*: The normalized line depression contribution functions (CF) are given for FeI (dotted), TiO- $\gamma$  (dashed), and MgH (dash-dotted) lines. The contribution functions of TiO  $\alpha$  and  $\gamma$  system are similar. The geometrical height scale is that found for the average dark umbra.

---

pret our warm magnetic component as the fraction of the atmosphere that mainly consists of warm umbral dots (UD) and our cool magnetic component primarily as their cool diffuse background (DB).

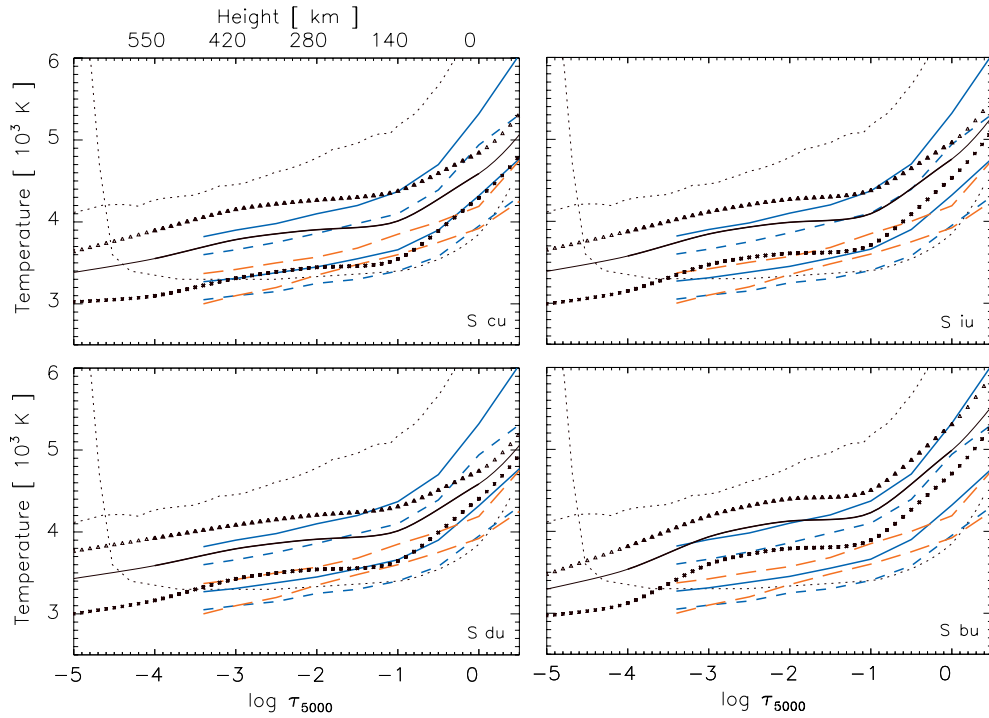


Fig. 3.14 Comparison of found umbra models to models from other authors. Here we show a comparisons to models from Sobotka. Clockwise from the bottom left the panels show dark umbra, core umbra, intermediate umbra, and bright umbra. Each plot contains the FAL-C model of the quiet sun (Fontenla et al., 1993) and the (coolest) Maltby E model as reference (small dashed lines). In black our results are given: the two magnetic components (triangles and squares) as well as the combined atmosphere including straylight (bold line). To indicate the extrapolated tails where our stratifications are not constrained by the contributing lines (cf. Fig. 3.13) they are plotted less thick. Note, that the geometrical height given was derived from our average dark umbra model. See discussion in Sect. 3.4.5.

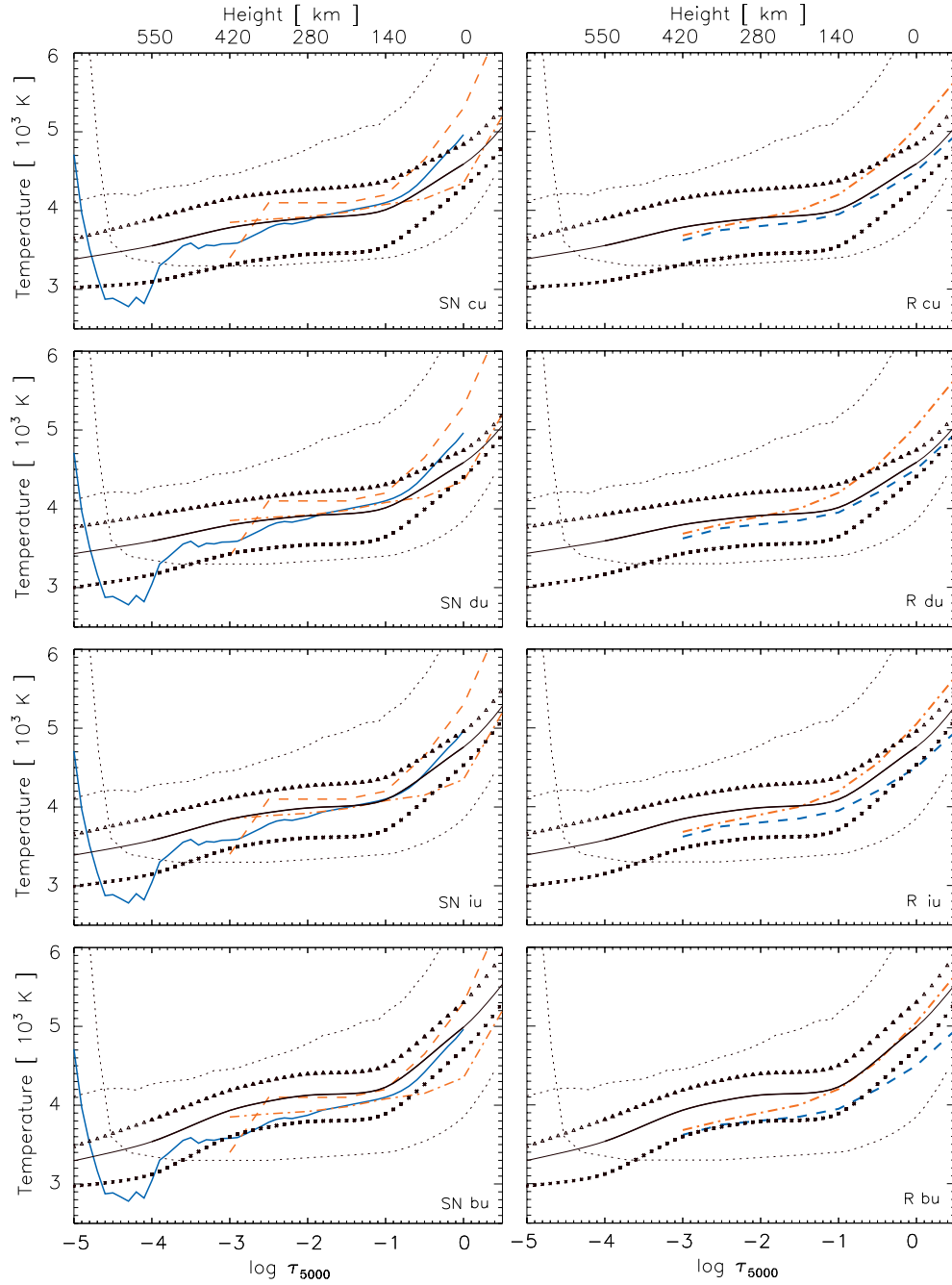


Fig. 3.15 Same as Fig. 3.14 but for the models of Socas-Navarro (left column) and Riethmüller (right column).

We compared the amount of umbral substructure seen in the middle image of Fig. 3.2 with the filling factors obtained by our inversions. For that purpose the NSST intensity image was correlated with the THEMIS image and thus with the region mask defined in Fig. 3.4. As a measure of the umbral substructure the fraction of dark pixels in each umbral region was determined and found to be proportional to the filling factor of the cool magnetic component regardless of the threshold set to obtain that fraction from the histogram of the masked image. A more sophisticated analysis of the UD substructure and dynamics of UD in this sunspot can be found in Riethmüller et al. (2008b).

Several authors investigated umbral dots, whether peripheral or central, and their cooler diffuse backgrounds (Sobotka et al., 1993). Lately, this was done by inverting sunspots' spectra to determine their vertical temperature stratification (e.g. Socas-Navarro et al., 2004; Riethmüller et al., 2008a). In Fig. 3.14 we compare our results to these other models of umbral dots, their diffuse background and core umbra.

The first column of Fig. 3.14 shows a comparison with a dark umbra model (solid line) by Socas-Navarro (2007, pixel A) and an umbral dot model (dashed line) including its diffuse background (dashed-dotted line) by Socas-Navarro et al. (2004). The dark umbra model was created by inverting full Stokes spectra of two photospheric Fe II and two chromospheric Ca II lines around 8500 Å. Therefore, this model extends towards higher layers. The model was inferred for a single dark umbral pixel with a relative intensity of 0.46 compared to the intensity of the quiet sun in a sunspot about half as big as the sunspot we investigated. Subsequently, this model of the dark umbra is warmer than ours. The cool component of our bright umbra matches the temperature of that dark umbra pixel with a similar fraction of straylight. Although, our temperature curve matches rather well at higher layers, it is up to 300 K cooler at the depths it is most sensitive.

The models for the UD and DB by Socas-Navarro (2007) shown in the first column of Fig. 3.14 were derived by full Stokes inversions of the 6302 Å region observed with the La Palma Stokes Polarimeter, NSST. Following our interpretation that the warm and cool magnetic components represent mainly UD and DB, respectively, a comparison of these profiles may imply that our method can distinguish the two components far better, even though they are not spatially resolved, since the UD and

DB models are very similar until they diverge at lower levels whereas the two magnetic components of our dark umbra model are separated by about 700 K.

In the second column we compare our findings to models of UD (dashed-dotted line) and DB (dashed line) derived from full Stokes inversions of HINODE/SOT-SP data at 6302 Å (Riethmüller et al., 2008a). These models are averages over 51 single UD and close DB in a sunspot (NOAA AR 10 933) about the same size as ours. The DB of this model fits best with the cool component of our bright umbra. Interestingly, the separation between UD and DB is only about 300 K compared to the temperature difference of our components of 600 (900) K for the bright umbra (core umbra).

In the third column we plot two models for the darkest part of the umbra, the dark nucleus (DN, long dashed lines), and models for two single umbral dots and their respective background (UD/DB pairs indicated by solid and dashed lines) by (Sobotka et al., 1993). These temperature curves were found by down-scaling the reference temperature distribution of the undisturbed photosphere to model high resolution ground-based spectra of Fe I at 5434.5 Å of single spatial resolution elements. Again, our models show a less steep gradient towards the continuum layer, except for the bright umbra. One of the DN models is only slightly cooler than our core umbra cool component, the other's temperature is comparable to that of our dark umbra or intermediate umbra cool component. When comparing our models with the UD/DB pairs two similarities are found. First, the temperature stratifications of the UD/DB pairs show a temperature difference similar to our separation of the warm and cold component in the dark umbra. Second, the two pairs show temperature curves of similar shape. It is notable that one of the DB models exactly matches the temperature of our core umbra cool component, whereas the other is about 200 K cooler.

## 3.5 Conclusions

For a single sunspot we observed the full Stokes vector simultaneously in several spectral windows including magnetic atomic lines (Fe I) and molecular absorption features of TiO and MgH. We combined the spectral windows

and analyzed all pixels in the sunspot's umbra independently by simultaneous inversion of the full Stokes profiles of all the selected lines. This is the first time TiO  $\gamma$ , TiO  $\alpha$  and MgH A-X absorption features have been inverted simultaneously.

In order to study the umbral substructure five subregions of the sunspot umbra were defined and average atmospheric models were created for these subregions. The resulting average atmospheres are composed of two components, warm and cool. They are shown in the Appendix and are available as ASCII files.

From our inversions we conclude:

- In our resulting atmospheres, the contribution functions of the selected molecular lines peak below the atomic lines.
- We need to introduce an atmospheric model consisting of two magnetic components and one straylight component in order to achieve an acceptable fit to all Stokes profiles including the dominant Fe I lines and any of the additional molecular features.
- The two magnetic components are warm and cool fractions of the umbral atmosphere that are not spatially resolved in our observations. These warm and cool fractions are interpreted as being composed of umbral dots (UD) and their cool diffuse background (DB), respectively.
- A comparison of the warm umbra model of Maltby et al. (1986) with the cool component of our average sunspot model shows similarities in higher and slight differences in the lower depths where our method is most sensitive. For the phase of the solar cycle when our sunspot was observed the cooler umbra model of Maltby should apply, but our final model of the average umbra is about 400 K warmer than expected. This is in agreement with a trend reported by Penn & Livingston (2006) that the maximum magnetic field in sunspots decreased at 50 G per year during the last decade. It also explains the surprisingly small signals of molecular features seen in the sunspot.
- According to the brightness in the Fe I window we subdivided the umbra (see Fig. 3.4) and computed average stratifications for its

subregions. These regionalized temperature stratifications are compared to those found by other authors for different structures: Taking into account the different sunspot sizes and straylight levels we see a good agreement of our bright umbra cool component with the umbra model reported by Socas-Navarro (2007) and our core umbra cool component with the dark nucleus models of Sobotka et al. (1993).

- Comparing our regionalized temperature stratifications to semi-empirical models of UD and DB we note that the similar profile and temperature difference between our components is matched by two models for UD and DB by Sobotka et al. (1993). Statistically averaged models of UD and DB based on HINODE/SOT-SP observations and single component inversions without straylight component show a separation of a few hundred degrees (Riethmüller et al., 2008a).
- Simultaneous inversion of molecular and atomic lines gives additional constraints for determining the temperature stratification. By including TiO and MgH absorption features we are able to separate the temperatures of the two magnetic components better than previous authors.
- Unfortunately, the selected molecular lines, being very weak in the observed spot, in combination with atomic lines have not increased the quality of the magnetic field determination. Reasons may also include low Landé factors of the molecular lines and the deficiency in the implementation of the filling factor, which was assumed to be constant with depth and was predominantly set by the Fe I lines. At the height the molecular lines probe, an ill-constrained filling factor would consequently reduce the inferred magnetic field strength.

We do encourage future multi-wavelength inversions including known molecular features that may test the presented atmospheric models and its components with different sunspots to answer the question whether the properties of the magnetic components found are of general nature and only the mixture of the two components varies from spot to spot.

*Acknowledgements* We thank V. Zakharov for providing the NSST image of the sunspot and B. Lites and H.-M. Schmid for their valuable comments. The computations were carried out on Brutus, the central high-performance cluster at ETH Zurich. SVB acknowledges the EURYI Award from the ESF ([www.est.org/euryi](http://www.est.org/euryi)). This work is supported by the SNF grant PE002-104552.

---

# Sunspot umbrae: from small to large

---

R. Wenzel<sup>1</sup>, D. M. Fluri<sup>1</sup>, S. V. Berdyugina<sup>2</sup>

This chapter is in peer-review for publication in *Astronomy and Astrophysics*.

## **Abstract**

Investigating the fine structure of a sunspot umbra helps understanding the energy transport and heating mechanism(s) in sunspots.

We analyzed and compared three sunspot umbrae of different sizes and with different amount of umbral dots by inferring their model atmospheres from spectropolarimetry.

Full Stokes observations at 630.1 nm of the three sunspots NOAA 10 930, 10 933, and 10 944 were obtained in 2006–2007 near the solar disk center by the spectropolarimeter aboard HINODE/SOT. We retrieved model atmospheres including the depth stratifications of the temperature, mag-

---

<sup>1</sup> Institute for Astronomy, ETH Zurich, 8093 Zurich, Switzerland

<sup>2</sup> Kiepenheuer-Institut für Sonnenphysik, 79104 Freiburg, Germany

netic field strength, and line-of-sight velocity for each umbra by employing a state of the art inversion technique implemented in the code SPINOR. Our spectral inversions simultaneously included the full Stokes vector for the dominant atomic Fe I lines as well as the molecular features of TiO and CaH present in the observations.

The depth-dependent model atmospheres were obtained for various substructures of the sunspot umbra such as umbral dots (peripheral and central), diffuse umbra background, and dark umbral cores. Their properties were found to be strongly dependent on the size of the sunspot. We discuss and compare our findings with previous results.

The obtained model atmospheres of the umbra fine structure provide a reliable reference for a comparison with sunspot simulations and for identifying mechanisms of their heating.

## 4.1 Introduction

Sunspots are the manifestation of the interaction between magnetic flux bundles and the convection layer below the solar surface, i.e. the photosphere. In the central part of a matured sunspot, sunspot umbra, a vertically aligned magnetic fields inhibits convective motions which is the main energy transport mechanism in the photosphere (e.g., Biermann, 1942). In addition, the magnetic pressure contributing to the umbra horizontal force balance implicates a lower gas pressure. Both effects lead to a lower temperature of the umbra and, hence, to its dark appearance with respect to the surrounding quiet sun photosphere. The effective temperature of the umbra is known to depend on the its size (e.g., Collados et al., 1994). Next to this easily observable measure, it may as well be dependent on the richness of its fine structure, i.e. relative areas of hot umbral dots (UDs) and cool core umbra. This subject is addressed in this paper.

Our study makes use of the archive of the HINODE satellite which enables us to explore the fine structure on the sun down to the spatial resolution of  $0.3''$ . We chose three sunspot umbrae of different sizes observed near the disk center and carried out spectral inversions to infer their atmospheres within a few hundred kilometers above the  $\log \tau = 0$

level. In contrast to many previous studies, our inversions include numerous blends of molecular features of TiO and CaH within the observed wavelength range of  $2\text{\AA}$ . These lines are strongly temperature sensitive and form in cooler parts of the sunspot umbra, which is essential for a detailed comparative study of differently sized umbrae.

It was earlier pointed out by Kopp & Rabin (1992b) that studying the relation between magnetic field strength and temperature in sunspots has been hindered in the past (and still now) by three major issues: (i) the straylight contamination of any ground-based observations at an unknown level, (ii) the variety of sunspot sizes, their different structure and (umbral) substructure, and (iii) the accuracy of the determination of the magnetic field strength.

With the *Solar Optical Telescope* (SOT) aboard the HINODE satellite observing from space without an atmospheric seeing the straylight contamination is drastically reduced compared to ground based instruments. In addition, the ongoing observations have filled an archive with plenty different sunspots and other solar magnetic features recorded in the full Stokes vector by the spectropolarimeter (SP) attached to SOT. An analysis of the polarized light thus allows for simultaneous determination of thermodynamic and magnetic properties of sunspots.

Such studies were previously carried out by several groups. Collados et al. (1994) were perhaps the first to simultaneously determine the magnetic field strength and inclination and thermodynamic quantities of the core umbra in three sunspots (at limb angles  $\cos \theta = \mu = 0.8 - 0.9$ ) with different sizes (radius  $r = 6'' - 11''$ ). Their analysis is based on observations obtained at the Gregory-Coudé Telescope (GCT) of the Observatorio del Teide in 1989 by Martinez Pillet & Vazquez (1993). Five Stokes  $I$  and Stokes  $V$  spectra of three Fe I lines with different magnetic and temperature sensitivities (at  $6297.8\text{\AA}$ ,  $6301.5\text{\AA}$ , and  $6302.5\text{\AA}$ ) are inverted simultaneously using the spectral inversion code of Ruiz Cobo & del Toro Iniesta (1992). As a result they presented a cool (large) and a hot (small) almost straylight-free umbral model. Also Mathew et al. (2007) found a strong dependence of the umbral brightness on its radius by evaluating 164 sunspots with an umbral radius between  $5''$  and  $15''$  and at  $\mu > 0.94$  selected from continuum full disk images observed by SOHO-MDI.

The existence of a strong vertical magnetic field forming the sunspot implies that its strength and the temperature should be inversely propor-

tional within an umbra. Observationally, there is clear evidence for such a relation (Kopp & Rabin, 1992a; Martinez Pillet & Vazquez, 1993) that was further exploited to determine the peak magnetic field strength ( $B$ ) from continuum intensity ( $I$ ) images (Norton & Gilman, 2004). However, the  $B$ - $I$  correlation within a particular umbra was found to vary between sunspots. Physically, these variations could be explained by different sizes of the investigated umbrae and by differences in their substructure, i.e. by the contents of bright UDs.

Umbral dots are small bright phenomena, about 200 km (0.2'') in diameter, with a lifetime of  $\approx 15$  minutes that are seen in all but the darkest subregions of the umbra. Since their discovery by Chevalier (1916) and characterization (e.g., Sobotka et al., 1992a,b; Riethmüller et al., 2008b) they have been regarded as important ingredients for the energy balance and heat transport within the umbra, which in turn define its brightness (e.g., Deinzer, 1965). Therefore, understanding the nature of the umbral substructures and their relation to supposedly suppressed convection requires determining a realistic model of sunspots.

Various UDs are suspected to have different origins and are therefore differentiated into central and peripheral umbral dots (CUDs and PUDs, respectively). PUDs seem to stem from penumbral grains moving into the umbra and their intensity decreases continuously with time as they move radially inwards. CUDs, on the other hand, are fairly immobile hot features whose intensity first increases linearly before darkening linearly with time. Although having a similar physical size it was suggested that these are two distinct types of UDs (e.g., Kitai et al., 2007; Riethmüller et al., 2008b).

Recently, Riethmüller et al. (2008a) and Watanabe et al. (2009) analyzed various properties of UDs within the sunspots NOAA 10 933 and 10 944, respectively, using HINODE observations. The authors correlated the UDs dynamic properties (lifetime, occurrence rate, proper motion) with their atmospheric parameters, i.e. magnetic field strength and orientation, line of sight velocity etc.. However, the UDs properties were obtained from spectral inversions of the Fe I lines only or by employing inversions for a single layer Milne-Eddington atmosphere (Watanabe et al., 2009). For our analysis we have chosen partly the same targets to obtain complementary and comparable results.

In the following sections we describe the observations and data prepa-

ration (Section 4.2), the analysis by spectral inversion (Section 4.3) and the results of the inversion (Section 4.4). We discuss the results in Section 4.5 where we compare the atmospheres of the different umbrae and their substructures.

## 4.2 Observations and data reduction

Our targets were umbrae of stable sunspots with different sizes at the end of the solar cycle 23. We analyzed spectropolarimetric full Stokes data observed with the spectropolarimeter (SP) aboard HINODE/SOT (Kosugi et al., 2007; Tsuneta et al., 2008; Ichimoto et al., 2008).

The SP was designed to observe the full Stokes vector with a precision down to  $10^{-3}$  or better relative to the continuum in the range of the FeI 6301.5 and 6302.5 Å absorption lines. Its slit ( $0.16'' \times 164''$ , oriented North–South) scans an active region with a spectral resolution of about 21.5 mÅ and a spatial resolution of about  $0.32''$  (2 pixels). The image stabilization system guarantees a  $0.01''$  accuracy.

We processed the level-0 data product obtained at the Hinode Data Center with the standard *SP\_PREP* routine developed by B. Lites which is available as part of the Solar-Soft package. This routine applies dark current and flat-field corrections and takes care of other instrumental effects like the thermal shifts in the spectral and slit dimensions as well as drift corrections. We verified the standard wavelength calibration of the level-1 data by our own calibration routines and found no significant differences. The resulting Stokes vector was normalized to the local continuum intensity (single pixels).

The observed range is dominated by the two magnetically sensitive FeI lines at 6301.5 Å and 6302.5 Å having effective Landé factors of 1.67 and 2.5, respectively. In addition, molecular absorption features of multiple CaH and TiO bands are present in this spectral range (Wallace et al., 2005). In cooler parts of the sunspot umbra the molecular lines dominate the spectrum (see Fig. 4.5 for a typical spectrum of the core umbra). The molecular line parameters were calculated according to Berdyugina et al. (2003, 2005).

The SP datasets selected for this study were all obtained in the same observation mode (scn\_sum=1, camssum=1, exptime=4.8 s). We chose

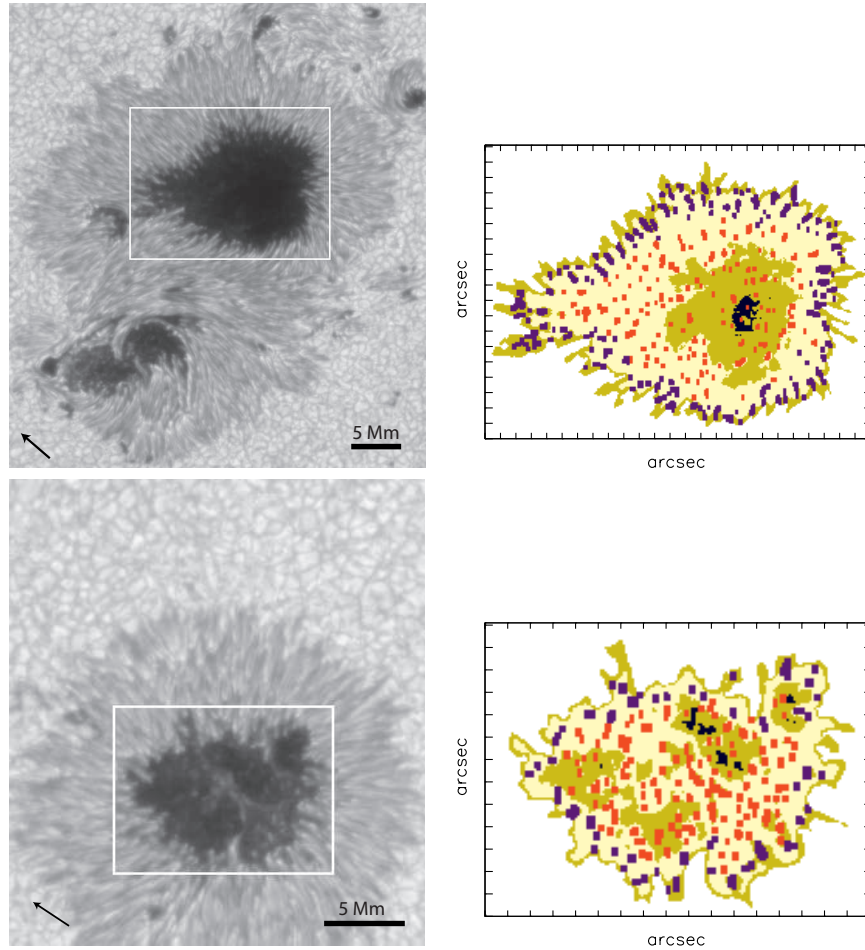


Fig. 4.1 **Left column:** Intensity images of the sunspots NOAA 10930 (S1, top) and 10933 (S2, bottom) in the spectral window of the HINODE-SOT/SP (6301–6303 Å). The umbra regions analyzed in this paper are outlined by squares. See Table 4.1 for details. **Right column:** Subregions of the umbrae. All panels show only the regions with the intensity of less than half of the average quiet sun continuum. The locations of central umbral dots (CUDs) and peripheral umbral dots (PUDs) were identified by eye and are marked by orange and violet colors, respectively. The core umbra (CU) was defined as the region composed of the darkest 1% of all pixels (black). The diffuse background (DB) is made of all pixels with the intensity between 10% and 40% of the average quiet sun intensity (light yellow). The dark umbra (DU) is composed of pixels with the intensity of less than 10% excluding the CU pixels (dark yellow).

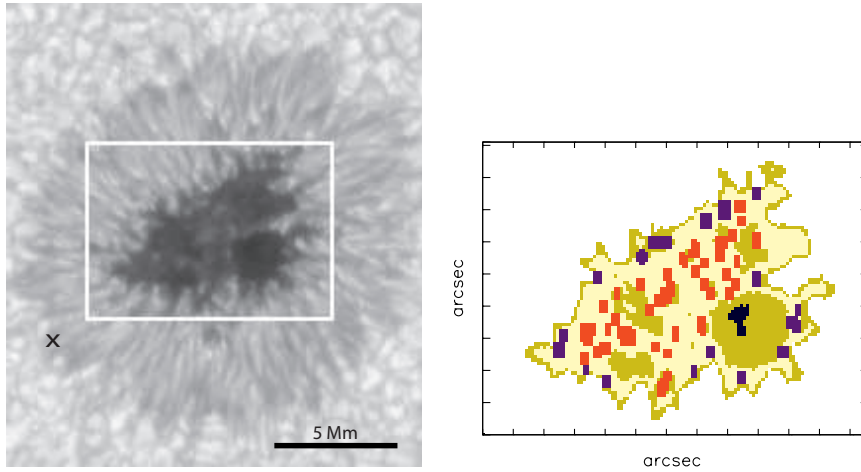


Fig. 4.2 Same as Fig. 4.1 but for sunspots NOAA 10944 (S3).

only sunspots that were observed at the solar center ( $\mu \geq 0.99$ ) showing a fully developed penumbra and a compact and simple umbra without lightbridges. Several sunspots in the Hinode catalogue matched these criteria, but only three were taken covering the widest range of umbral area. From the available scans only the umbra region, defined by half of the average quiet sun's continuum intensity, is used as input for our analysis.

The biggest umbra (s1) was extracted from the dominating sunspot in the complex active region NOAA 10930 observed on Dec 12, 2006, 10:10 UT. It is fairly round with a single dark core umbra. The mid size umbra (s2) taken from the NOAA 10933 on Jan 6, 2007, 04:30 UT, features a chain of umbral dots that divides the core umbra in two major parts. The smallest umbra (s3) was taken from the single sunspot NOAA 10944 observed on Feb 28, 2007, 17:57 UT. Its coolest subregion is close to its South-East edge. It is the smallest umbra found in the Hinode archive that is fully surrounded by a penumbra. The intensity images of the sunspots are shown in Fig. 4.1. More information on the observed sunspots and the datasets is given in Table 4.1.

Each umbra was subdivided into a core umbra (CU) made of the darkest 1% of all pixels, the peripheral and central umbral dots (PUDs and CUDs), the diffuse background (DB) which contains all pixels with an intensity between 10% and 40% of the average quiet sun intensity,

Tab. 4.1 Properties of the observed sunspots.

label	s1	s2	s3
NOAA number	10 930	10 933	10 944
obs time (UT)	Dec 12 2006 (10:10 )	Jan 01 2007 (04:30)	Feb 28 2007 (17:57)
heliocentric angle $\mu$	0.9995	0.9999	0.9999
size (s.u.)	440 $\beta, \gamma, \delta$	220 $\beta$	100 $\beta$
#umbra px	24 200	10 500	4060
#sunspot px	105 000	76 000	30 000
ratio sunspot/umbra	4.33	7.23	7.39
minimum intensity	$0.054 \cdot I_{c,qs}$	$0.14 \cdot I_{c,qs}$	$0.12 \cdot I_{c,qs}$
umbra polarity	negative	positive	positive

and the dark umbra (DU) with the intensity less than 10% but excluding the CU (see Fig. 4.1). The umbral dots in the dataset were identified by eye in a consistent way to ensure that the created masks are only containing pixels that are clearly dominated by these features. The DB and CU mask were created based on brightness thresholds. In addition, pixels associated with UDs as well as their nearest neighbourhood were excluded from the DB and CU mask.

### 4.3 Inversions

We use a spectral inversion technique to infer the model atmospheres of the umbrae, i.e.  $T = T(\tau)$ ,  $B = B(\tau)$ , etc.. The inversion code SPINOR developed by Solanki (1987), Frutiger et al. (2000) and Berdyugina et al. (2003) was employed including the molecular Paschen-Back algorithm implemented according to the theory by Berdyugina et al. (2005). This code assumes LTE conditions and solves the Unno-Rachkovsky radiative transfer equations using response functions (RF). Starting from an initial guess the Stokes profiles are fitted iteratively to the observational data by varying the free parameters of the model atmosphere. The quality of the fit is measured by a merit function, based on  $\chi^2$ , which is minimized by the Levenberg-Marquardt algorithm used within the inversion code as well as by visual inspection. Since SPINOR can treat line blends, several molecular bands, and multiple spectral regions at once, we could run

simultaneous inversions for the full Stokes vector of atomic and molecular lines. The spectral range inverted at once was covering almost the full spectral range observed by the SP, 6301.1–6303.1 Å. Due to memory limitations we divided it into two spectral windows, each centered around one of the strongest Fe I lines.

We model the SP observations using only one atmospheric component which facilitates the interpretation and reduces the computational time. Tests with models including additional atmospheric components did not improve the fit. This is in agreement with the findings of, e.g., Riethmüller et al. (2008a). Please note, that using a single component model does not imply that we fully resolve the magnetic structures. The influence of the straylight may just be small enough to be neglected by the spectral inversion.

To find the best fit models we carried out extensive tests varying all relevant atmospheric parameters, their initial values and their depth dependence and position of depth nodes. We found that the following set of free parameters in the model leads to best fits: (i) temperature, magnetic field strength, and line-of-sight velocity are varied with depth at three nodes  $\log \tau_{5000} = -2.5, -1.0,$  and  $0.0$ , and (ii) the inclination  $\gamma$  and azimuth  $\chi$  angles of the magnetic field vector, the microturbulence and the macroturbulence parameter are constant in depth. These make in total 13 free parameters for each pixel. The atmosphere was evaluated between  $\log \tau_{5000} = +1$  and  $-6$  to ensure that the whole depth range of the spectral line formation is covered.

We present examples of observed Stokes parameters and their best fits for three pixels with different brightnesses taken from umbra s1 to illustrate typical profiles for a peripheral umbral dot (Fig. 4.3), diffuse background (Fig. 4.4), and core umbra (Fig. 4.5). As the brightness declines and the magnetic field strength rises, the strong Fe I lines become Zeeman-split. In addition, molecular features are becoming as strong as the Zeeman  $\sigma$ - and  $\pi$ - components of the Fe I lines blending significantly all Stokes profiles. The fit to the umbral pixels becomes more and more difficult as the pixels' brightness decreases and the magnetic field strength increases. The reason may be not only the simplicity of the applied model but also the line list used. Unfortunately, not all lines appearing at a lower temperature can be identified and not all line parameters are known to the necessary precision or were derived theoret-

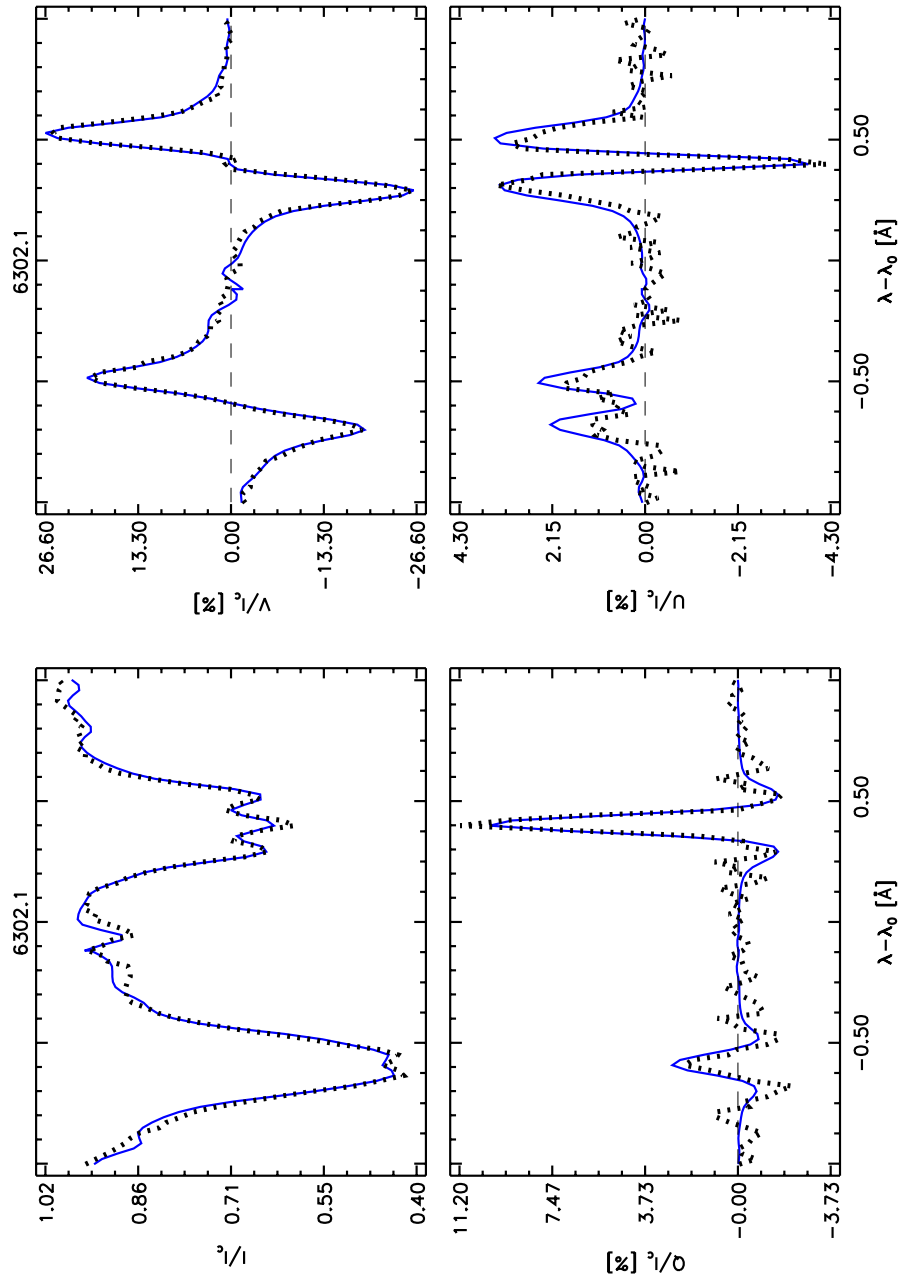


Fig. 4.3 An example of observed Stokes profiles (dotted) and corresponding best fits found by spectral inversion (solid) for a hot peripheral umbral dot in the sunspot umbra s1. This pixel's continuum intensity  $I_c = 25.3\%$  of the average quiet sun continuum intensity  $\langle I_{c,qs} \rangle$ .

ically under certain approximations (Berdyugina et al., 2005). However, these synthetic spectra represent the best fits possible so far for sunspot umbrae.

## 4.4 Results

The results of the spectral inversions for the three sunspot umbra s1, s2 and s3 are shown in Figs. 4.6, 4.8, and 4.10, respectively. Average depth stratifications of the temperature, magnetic field strength, line-of-sight velocity and the inclination angle of the magnetic field vector for the substructures within each umbra are presented in Fig. 4.12. A comparison of the substructure properties at the average line formation depth for different umbrae is shown in Fig. 4.14. The latter also includes results previously obtained by Collados et al. (1994), Wenzel, R. et al., in review (2011) and Berdyugina (2011), also using inversion techniques applied to spectropolarimetric observations.

### 4.4.1 Sunspot umbrae model atmospheres

The inversion results presented in Fig. 4.6 corroborate that the umbra s1 is coolest at its center and in general becomes hotter as we approach the penumbra. Considering the  $\log \tau_{5000} = -1$  level, where most lines form, we also find the highest magnetic field strengths at the center of the umbra. Most interestingly, the overall magnetic field strength seems to decrease towards the penumbra.

Surprisingly, the distribution of the inclination angle of the magnetic field vector,  $\gamma$ , does not correlate with the magnetic field strength: the most vertical field is found in the diffuse background towards to the disk center while at the opposite side (far side) the magnetic field is rather inclined. We investigated the original Stokes profiles and found that this is not an artifact of our inversion but is already present in the observations. At the location where we find the most vertical  $\gamma$  we observed the maximum Stokes  $V$  signal and almost no linear Stokes  $Q$  and  $U$  signals. However, the ratio between the Stokes  $V$  and the linear Stokes  $Q$  and  $U$  signals which is responsible for the determination of  $\gamma$  drops towards the far side of the spot. The reason for this unexpected behavior of the magnetic field vector could be the complexity of the

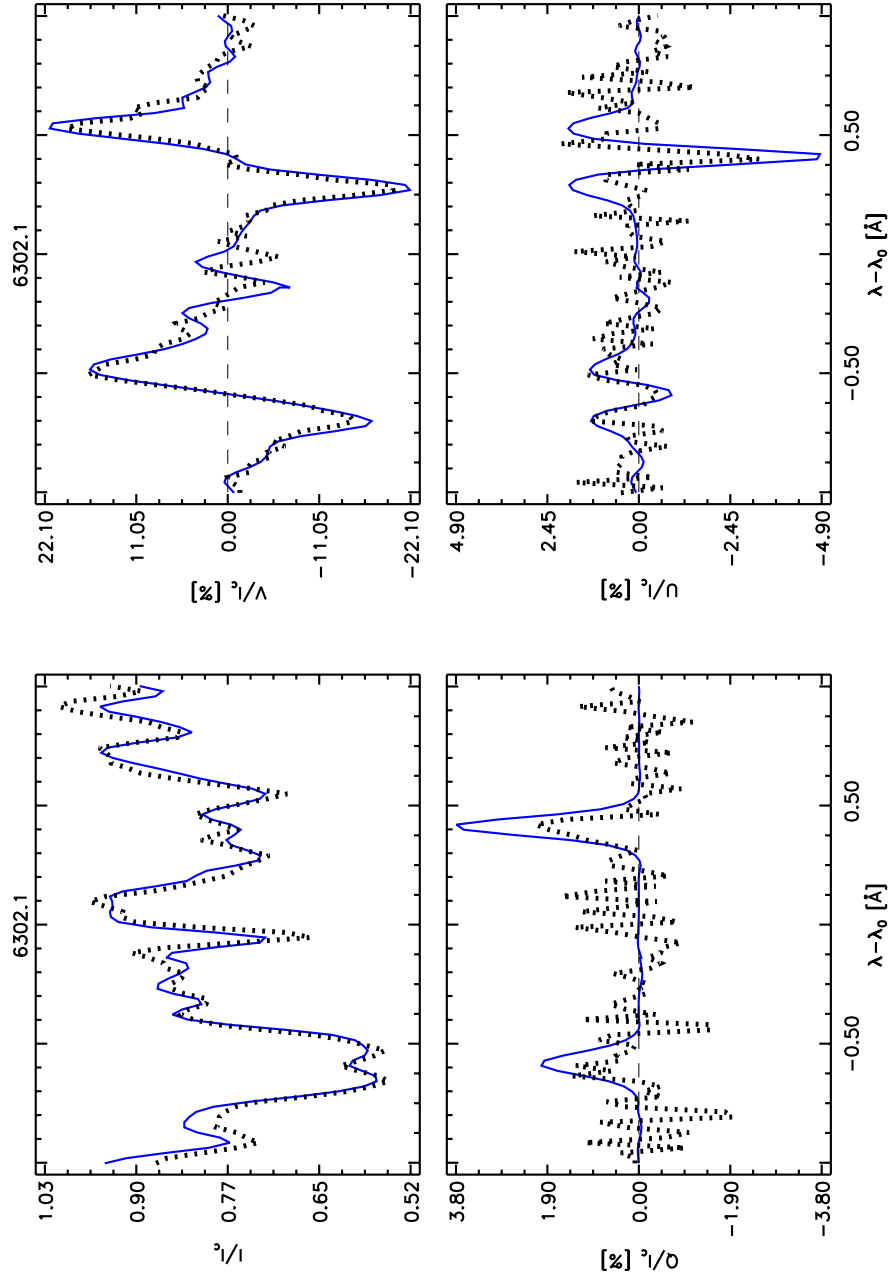


Fig. 4.4 The same as Fig. 4.3 but for the diffuse background pixel in the sunspot umbra s1 with  $I_c = 0.125 \cdot \langle I_{c,qs} \rangle$ .

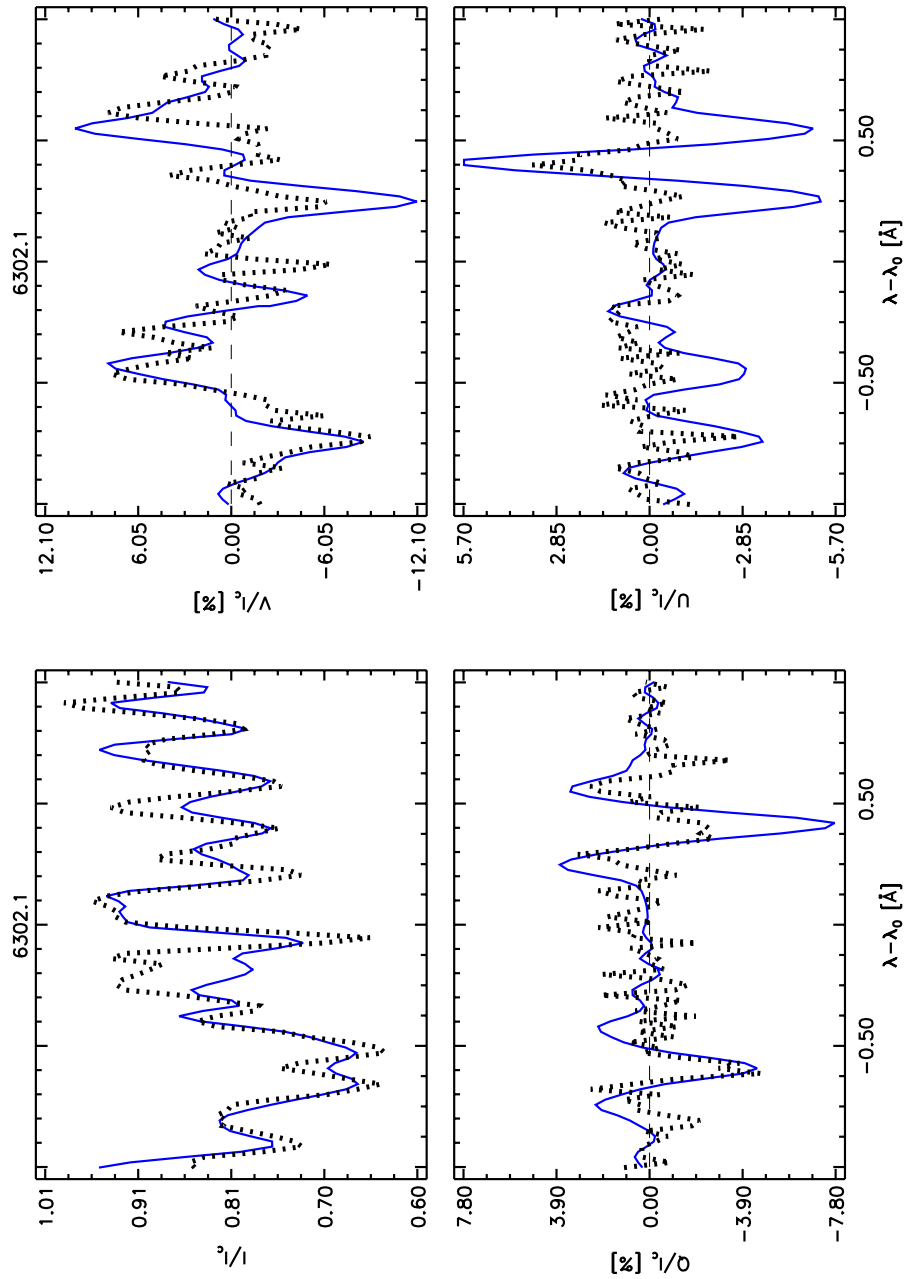


Fig. 4.5 The same as Fig. 4.3 but for the core umbra pixel in the sunspot umbra s1 with  $I_c = 0.062 \cdot \langle I_{c,qs} \rangle$ .

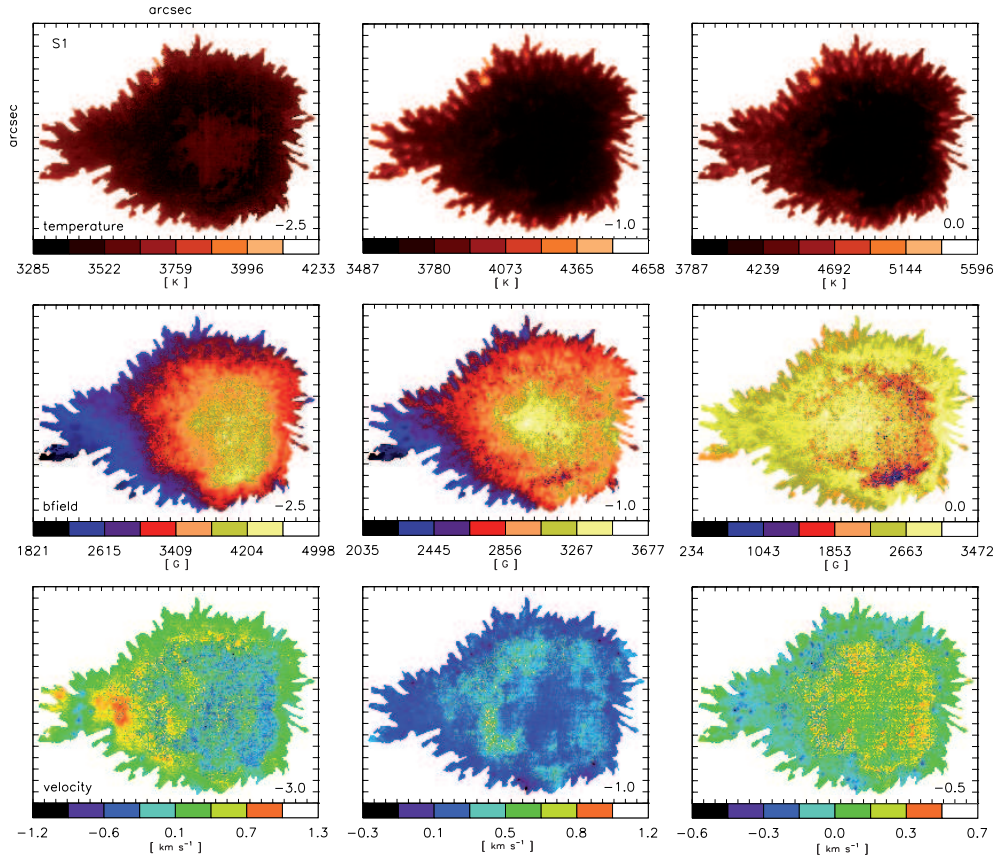


Fig. 4.6 Results of the inversions for the sunspot umbra s1. **First row:** temperature at the  $\log \tau_{5000}$  levels  $-2.5$ ,  $-1.0$ , and  $0.0$ . *Second row:* magnetic field strength at the same  $\log \tau_{5000}$  levels. *Third row:* line-of-sight velocity at the same  $\log \tau_{5000}$  levels. See Fig. 4.7 for more.

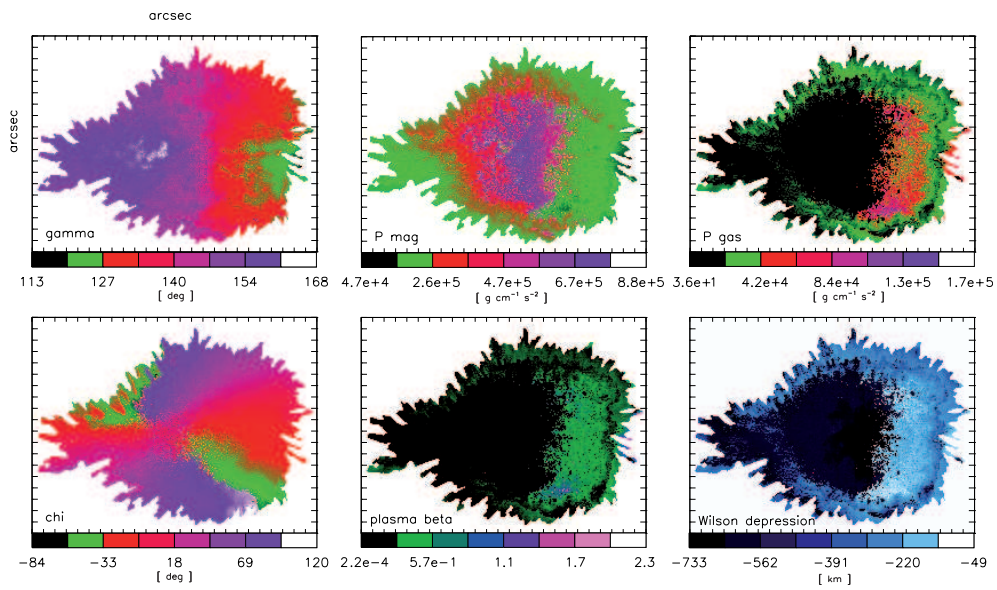


Fig. 4.7 Continuation of Fig. 4.6. **Top row:** inclination angle of the magnetic field vector,  $\gamma$ , magnetic pressure evaluated at  $\log \tau_{5000} = 0$  and corresponding gas pressure. **Bottom row:** azimuth angle of the magnetic field vector,  $\chi$ , plasma-beta and the Wilson depression at  $\log \tau_{5000} = 0$ .

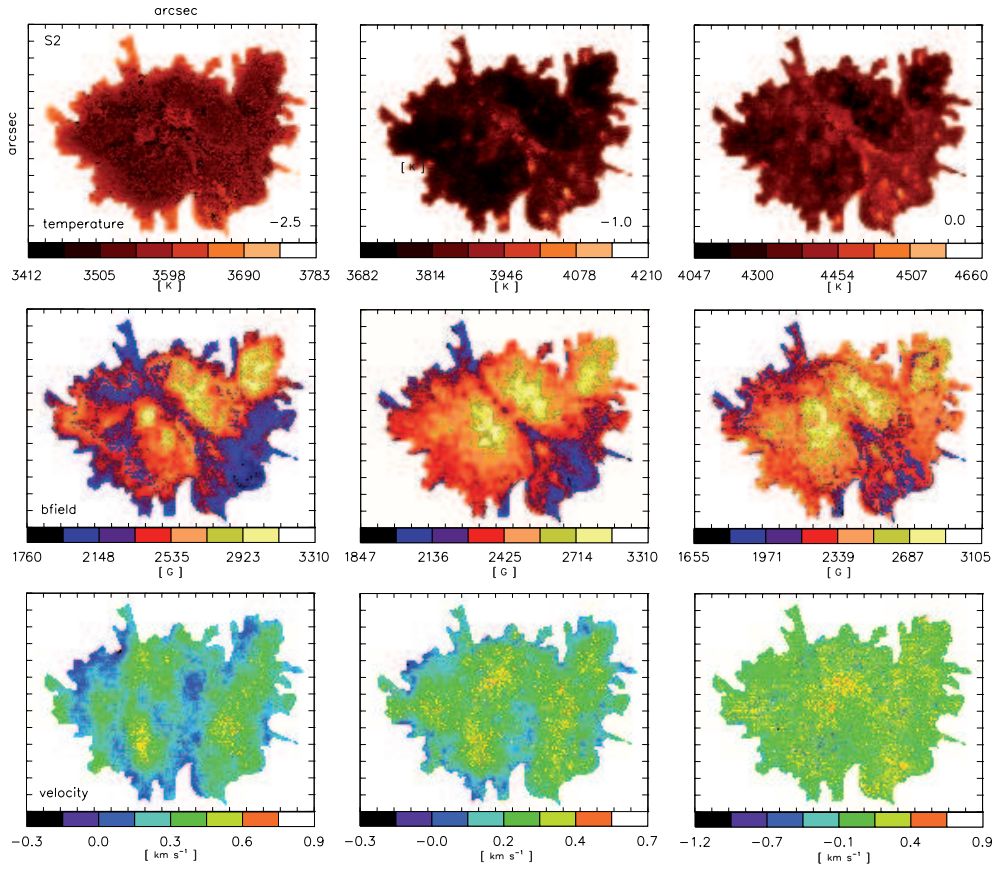


Fig. 4.8 The same as Fig. 4.6 but for the sunspot umbra s2.

sunspot group from which we extracted this umbra (see Fig. 4.1, left panel), which indicates a magnetic field connection to the following spot in the group.

The most prominent umbral substructures are seen in the umbra s2 (see Fig. 4.8). The chain of umbral dots dividing the umbra is clearly visible at all depth layers in the temperature and magnetic field strength maps. Similar to the smallest umbra s3 (Fig. 4.10) the coolest subregions are generally the ones with the highest magnetic field strengths. These two solitary sunspots show umbral magnetic fields that are most inclined at the umbra center. The symmetric pattern shown in the map of the azimuth angle,  $\chi$ , confirms the  $\mu$  values of the observations to be very

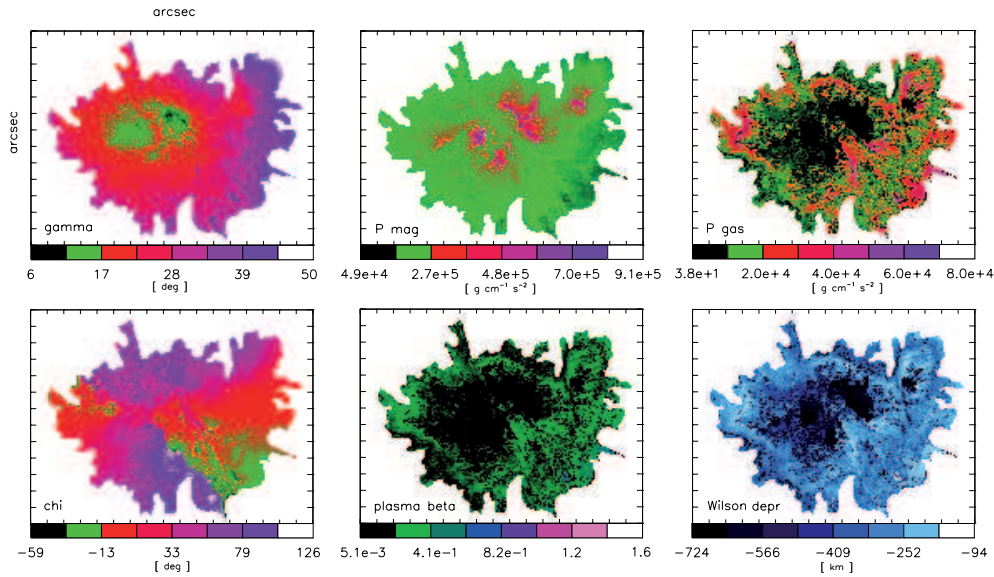


Fig. 4.9 The same as Fig. 4.7 but for the sunspot umbra s2.

close to unity. As indicated in the right panel of Fig. 4.1 sunspot umbra S3 was observed right at the solar center.

#### 4.4.2 Wilson depression and plasma beta

From the inferred umbra atmospheres we derived maps of the Wilson depression  $Z_w$  and the plasma beta  $= p_{\text{gas}}/p_{\text{mag}}$  for each sunspot umbra (see panels in the lower right corner of Figs. 4.6, 4.8, and 4.10). In order to obtain the Wilson depression with respect to the quiet sun we assume static pressure equilibrium at all geometrical heights  $z$ . Thus the gas pressure taken from a standard atmosphere (Kurucz, 1992, ,  $T_{\text{eff}} = 5750$  K) has to be balanced by the total pressure within the umbra at the same height. The pressure in each umbral pixel is a combination of the gas pressure and the magnetic pressure, neglecting the horizontal tension forces due to bending of field lines. Following Mathew et al. (2004) the Wilson depression is defined as

$$Z_w = z_{\text{qs}}(\tau_{5000} = 1) - z_{\text{px}}(\tau_{5000} = 1) = -z(\tau_{5000} = 1), \quad (4.1)$$

where we use the continuum optical depths at  $5000 \text{ \AA}$ . We adapt the usual convention for setting the origin of the height scale  $z$  at  $\log \tau_{5000} = 0$

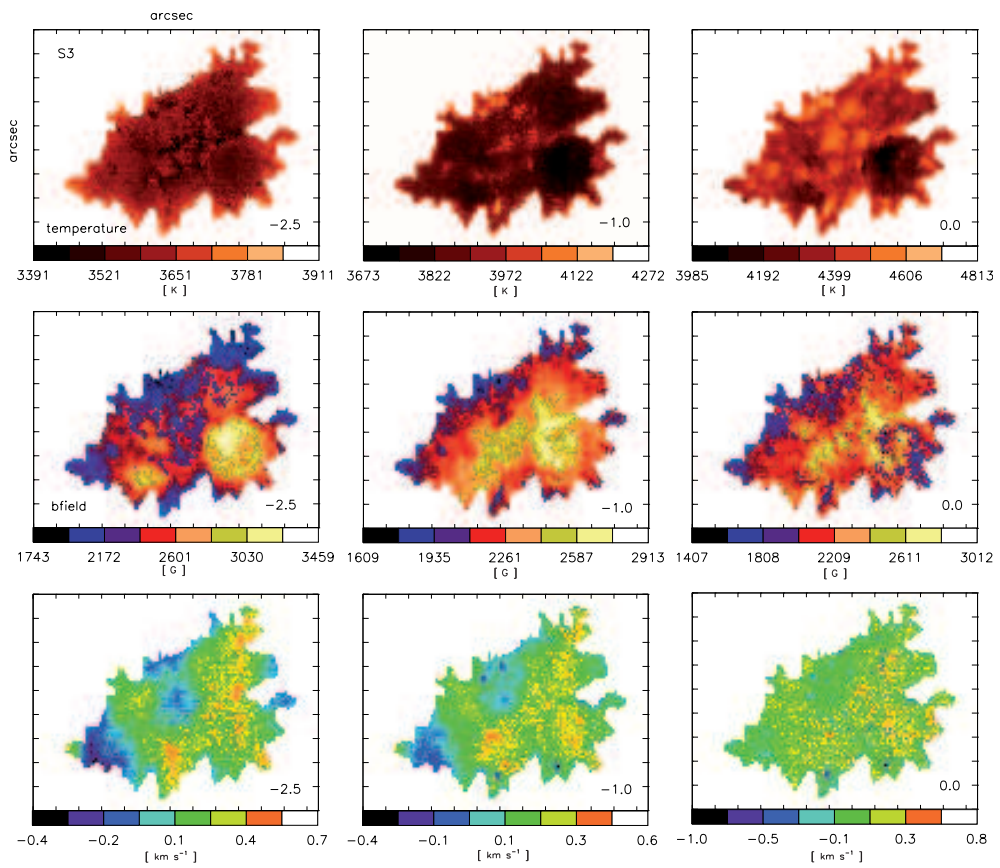


Fig. 4.10 The same as Fig. 4.6 but for the sunspot umbra S3.

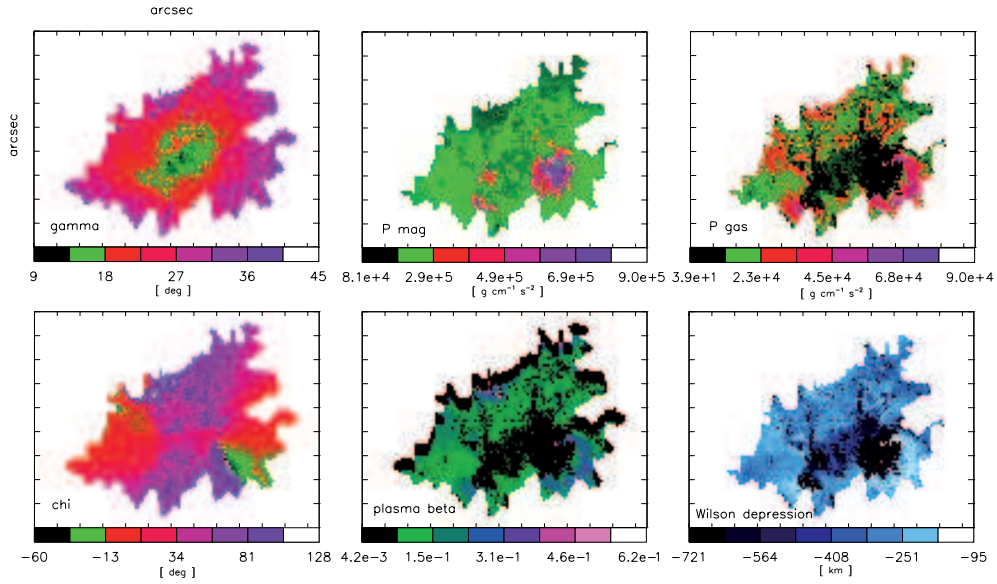


Fig. 4.11 The same as Fig. 4.7 but for the sunspot umbra S3.

from where it increases in the direction of decreasing  $\tau$ . Basically, we are shifting the pixels in our sunspot umbra maps, which are 1D column atmospheres, with respect to each other to achieve the pressure balance. We thus convert each spatial pixel's local height scale,  $z_{\text{px}}$ , into a general height scale  $z$  with respect to the height scale of the quiet sun atmosphere,  $z_{\text{qs}}$ . Since our inferred atmospheres are stretching only a few hundred kilometers we are limited in height. This is why we can only provide lower limits to the Wilson depression of the darkest regions in each sunspot umbra.

Since the sunspots were observed at the solar disk center, the magnetic pressure ( $p_{\text{mag}} = B_z/8\pi$ ) is calculated by projecting the magnetic field vector on the line-of-sight using the inferred inclination angles  $\gamma$ . Within the umbra the magnetic pressure is larger than the gas pressure. Therefore, we find a plasma  $\beta$  below unity for the major part of the sunspots umbrae, which is in agreement with Mathew et al. (2004) and indicates a domination of the magnetic field over kinetic motions in the umbra.

As illustrated in the last four panels of Figs. 4.6, the less inclined  $\gamma$  leads to a weaker vertical component of the magnetic field vector, hence to a lower magnetic pressure, and finally to a shallower Wilson depression at the far side of the umbra s1. For both smaller sunspot umbrae s2 and s3 the maps of the Wilson depression show deeper and shallower subregions of the umbra which are cospatial with the apparent dark umbra and UDs seen in the temperature maps. According to our knowledge this is the first time the height profile within a sunspot umbra has been determined from observations showing detailed substructures as the chain of umbral dots in sunspot umbra s2.

### 4.4.3 Vertical stratification of the model atmospheres

Within each sunspot umbra we find distinct subregions that are characterized by different average vertical stratifications (see Fig. 4.12). Within the darkest umbra s1 the core umbra, the diffuse background and the peripheral umbral dots are best distinguishable. Here, the average CUDs curve is even cooler than the average DB. This can be attributed to the fact that the umbra is so big that a lot of CUDs were identified in the cooler central region of the umbra. In the smaller umbrae the temperature curve of the average CUDs and the average DB cross at about  $\log \tau_{5000} = -1.5$ , i.e. towards the solar surface the CUDs become warmer and therefore brighter approaching the average temperature of PUDs. Here, a trend might be visible: in the smaller umbrae the distinction between PUDs and CUDs vanishes in the lower layers (around  $\log \tau_{5000} = -0.5$ ) pointing towards a common origin. This is clearly not the case in the bigger umbra s1.

Interestingly, the magnetic field strength declines towards lower layers. This is a common feature of inversions which origin is not yet fully understood. (Wenzel, R. et al., in review, 2011) discuss this issue and provide possible explanation. For the brighter structures, even for the DB, the magnetic field stratifications are similar within errors and consistent with a constant depth dependence of the magnetic field.

The line-of-sight velocity measurements are inconclusive due to their large errors although there is a tendency towards slightly positive, i.e. downwards directed mass flows.

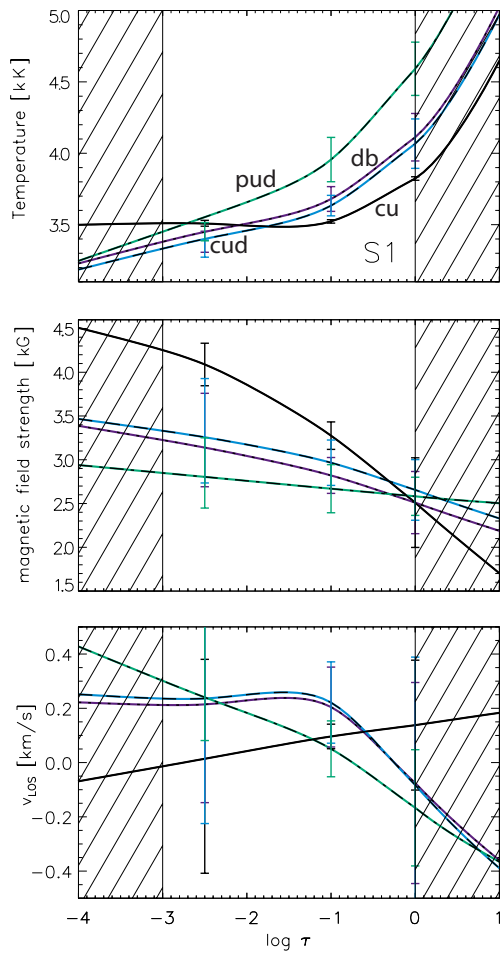


Figure 4.12 Results of the inversions. The vertical stratifications for the temperature, magnetic field strength, and line-of-sight velocity (rows) for the sunspot umbrae s1. In each panel the average stratifications are given for the core umbra (CU), the diffuse background (DB), central umbral dots (CUDs), and peripheral umbral dots (PUDs). The error bars indicate the 1- $\sigma$  limit of the distribution of stratifications in that subregion.

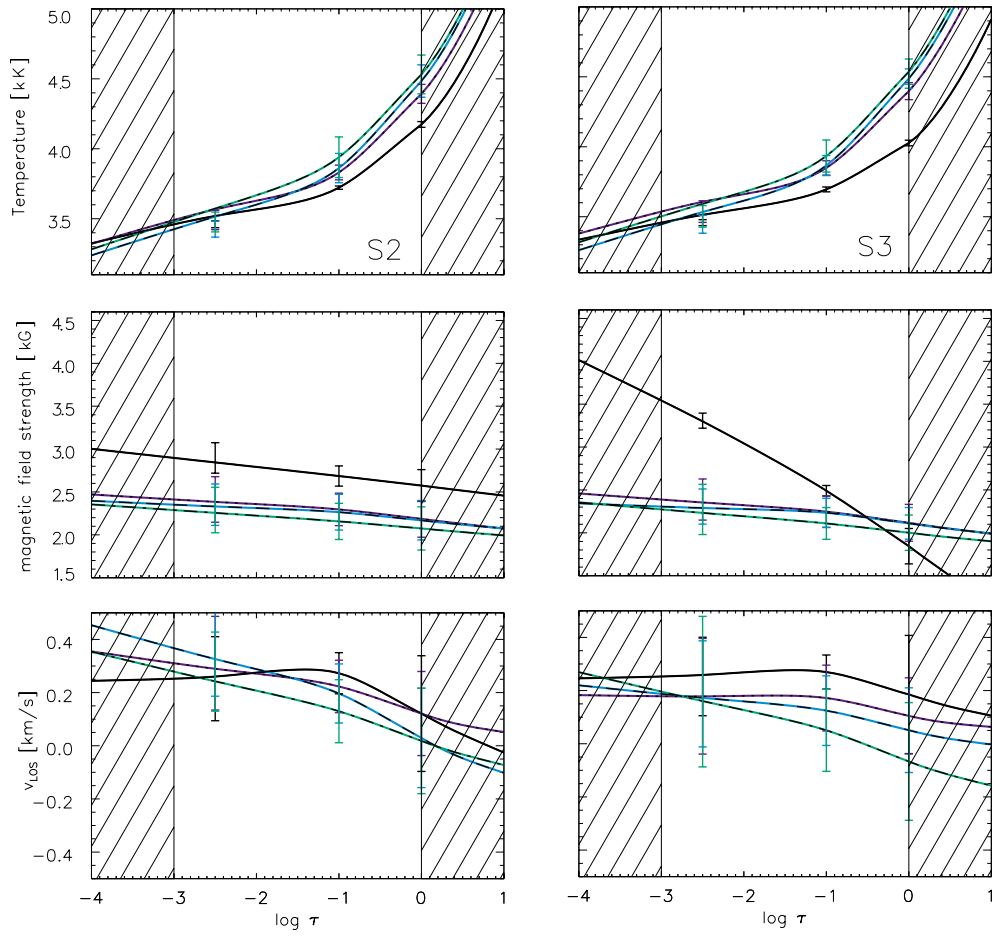


Fig. 4.13 Same as Fig. 4.12 but for sunspot umbrae s2, and s3 (columns).

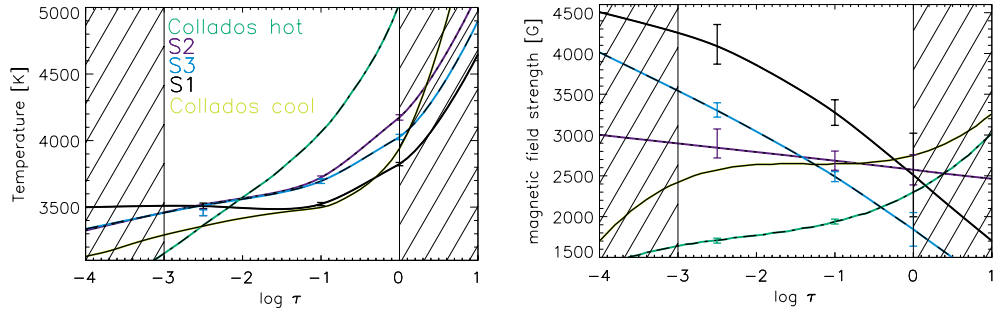


Fig. 4.14 A comparison of the inversion results. The average stratifications of the temperature and magnetic field strength within the core umbra of all analyzed sunspots. The hot and cold umbra model of Collados et al. (1994) are given as references.

## 4.5 Discussion and conclusions

We have inferred model atmospheres for three complete sunspot umbrae observed from space by the Hinode/SOT-Spectropolarimeter. To deduce the atmospheric parameters within the first few hundreds kilometers above the height of the continuum formation and their dependence on the optical depth, i.e. a model atmosphere, we employed the spectral inversions code SPINOR. The simultaneous inversion of each pixel's full Stokes vector over the full spectral range of  $2 \text{ \AA}$  has taken into account blends of atomic and molecular absorption lines. Including temperature and magnetically sensitive molecular absorption features of TiO and CaH we were able to trace the darkest regions in the sunspot umbra and infer the thermodynamic and magnetic parameters of a model atmosphere of the umbral subregions simultaneously.

We compare the derived models of the sunspot core umbrae in Fig. 4.14. The average temperature in the core umbra of the biggest sunspot umbra s1 is about 300 K cooler (at  $\log \tau_{5000} = -1$ ) than the core umbra of the two smaller sunspots. The overall agreement of the temperature curves of the two smaller sunspots is astonishing. Thus, similar to Collados et al. (1994), we have derived two different sunspot models dependent on the size which may point to intrinsic different properties of large and small sunspots. The cool umbra model of Collados et al. agrees quite well with our model of the bigger, cooler sunspot umbra s1. The hot

umbra model of Collados et al., however, has a far too steep temperature gradient as compared to our stratifications, i.e. that model is really for hot sunspots.

Not surprisingly, the magnetic field strength was found to be strongest in the biggest sunspot umbra s1. The overall trend of the magnetic field stratification is to decrease towards lower layers. This might be an artifact of the inversion method when dealing with a large number of single inversions of noisy Stokes profiles.

To compare the atmospheric parameters of the core umbra for different spots we chose the depth  $\log \tau_{5000} = -1$ , where our inversions are best constrained by the contribution functions of the spectral lines. The parameters of several sunspot umbrae analyzed in this and other studies are presented in Fig. 4.15. The large sunspot S0 is NOAA 10923 analyzed by Berdyugina (2011). It matches our selection criteria of the S1, S2 and S3 spots and was analyzed with the same inversion code. Additional data points are the cool and the hot component of a core umbra model of sunspot NOAA 10667 observed simultaneously in many spectral windows at the ground based telescope THEMIS and inverted with the same spectral inversion code Wenzel, R. et al., in review (2011). Furthermore, we compare to the hot and the cool umbra models of Collados et al. (1994) obtained for the same wavelength region from a ground based telescope and analyzed with a different spectral inversion method.

One has to keep in mind that we compare the darkest regions of differently sized sunspots, which may have intrinsically different physical properties. In this context, it is important to emphasize that the CU region of the smallest sunspot umbra s3, for instance, is comparable in brightness with the DB of the biggest sunspot s1. Due to its location close to the umbral-penumbral border it might harbor more hot umbral dots than we were able to detect. Thus, the CU s3 model atmosphere may not necessarily reflect a core umbra atmosphere. The coolest temperatures were inferred in the core umbra of s1. In this region the magnetic field must be locally strong enough to inhibit convective motions and therefore reduced the number of UDs observed.

In our analysis we find differences in the average curves of temperature, magnetic field strength and line-of-sight velocity of PUDs and CUDs only in the biggest sunspot s1 (see Fig. 4.12). For the smaller sunspot umbrae the temperature profiles are close to each other fusing into one

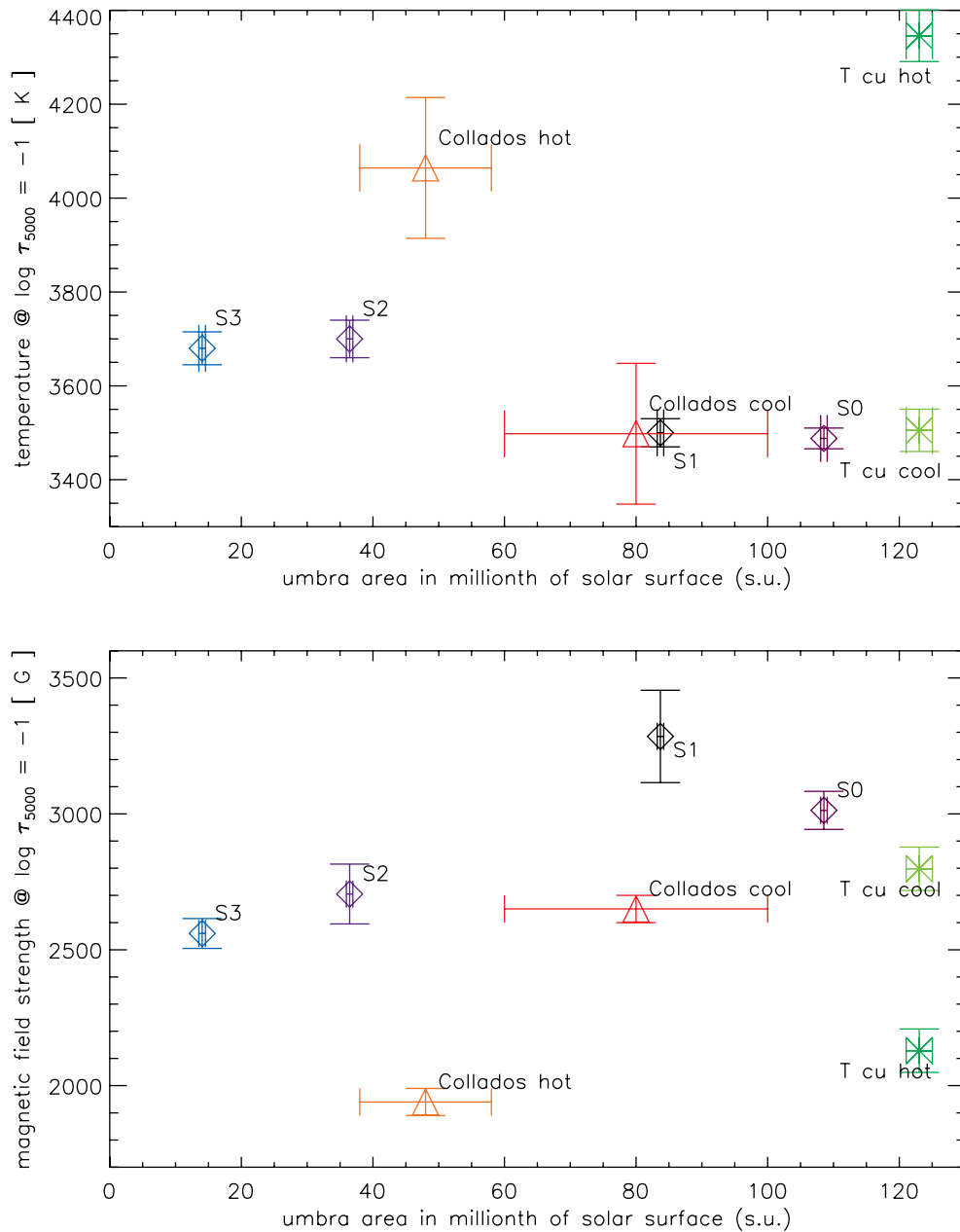


Fig. 4.15 A comparison of sunspot properties at  $\log \tau_{5000} = -1$  with respect to the size of the umbra area in millionth of the full visible solar disk (s.u.). In addition to the sunspot umbrae S1, S2, and S3 we include further recent results from full Stokes spectral inversions. The larger sunspot NOAA 10923, termed S0, was analyzed in detail in Berdyugina (2011). Furthermore, the hot and cool sunspot umbra model of Collados et al. (1994) and the cool and warm magnetic component of the core umbra of sunspot NOAA 10667, T cu, analyzed in Wenzel, R. et al., in review (2011) are included.

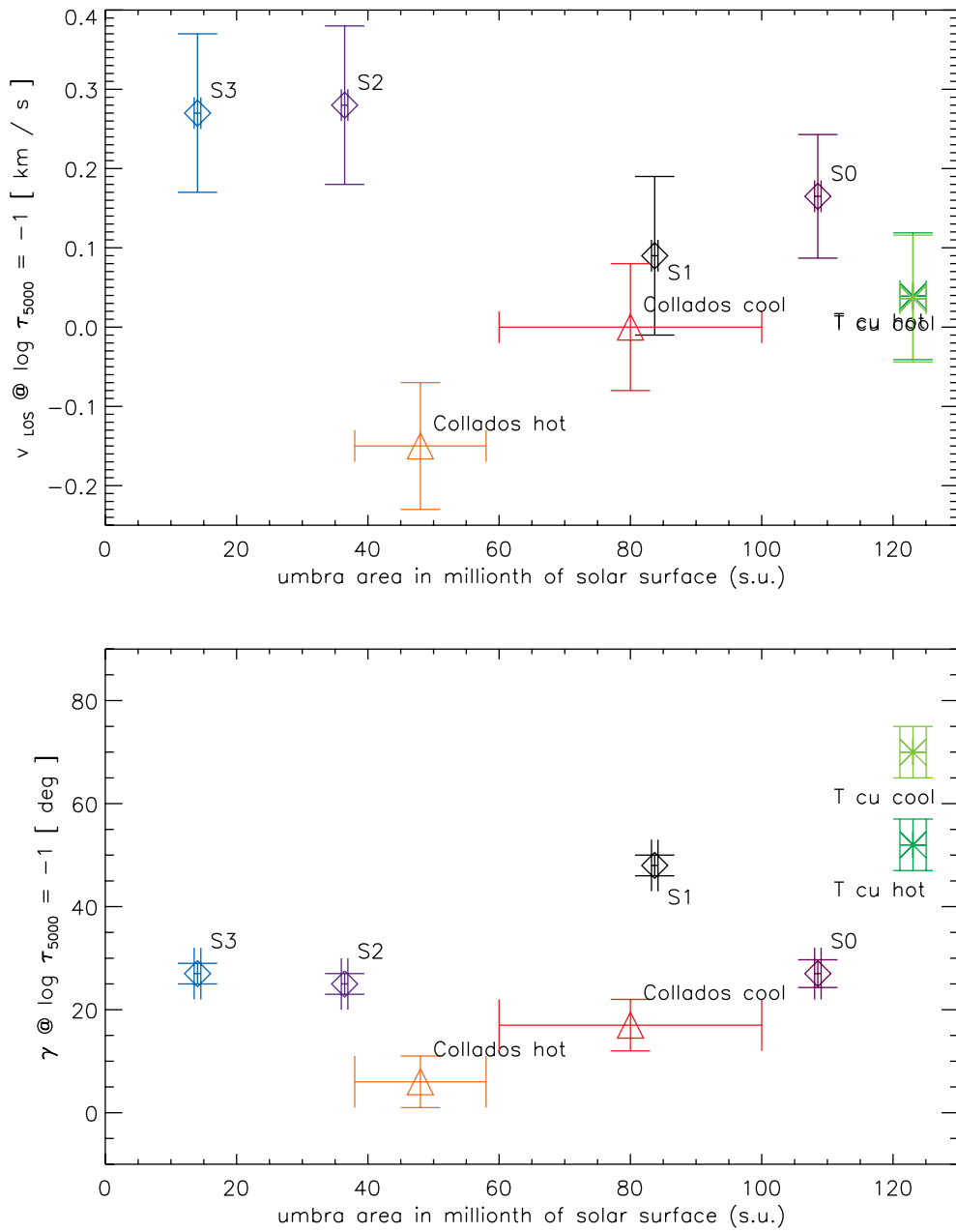


Fig. 4.16 Same as Fig. 4.15 but for  $v_{\text{LOS}}$  and  $\gamma$ .

curve at the solar surface. This implies that the suspected different origin and evolution scenario of PUDs and CUDs may only be valid for larger and cooler spots. We also corroborate the findings of Socas-Navarro et al. (2004) that UDs in general have a reduced magnetic field strength compared to their environment. Our results of their line-of-sight velocities are in agreement with a null or very low downflows.

The Wilson depression maps found for the sunspot umbrae are showing a rich landscape associated with the observed brightness and magnetic field strength that can be probed by our analysis. The regions of the UDs are on average higher than those of the DB by about 400 km. The coolest umbra is even deeper by at least the same amount. Due to the limited height of our inferred atmospheres we can only provide a lower limit on the Wilson depressions for all sunspot umbrae which is about 730 km.

As Fig. 4.15 shows, there are significant differences between sunspots of different sizes, although some data points in this figure were deduced for sunspots from different activity cycles, from different observations and by different inversion techniques. Also, as pointed out above, a comparison of the darkest regions of sunspot umbrae does not necessarily imply comparing regions of similar physical properties. These circumstances call for further systematic and homogeneous investigations of sunspot umbrae. An analysis of a significantly higher number of sunspots from the HINODE archive with the same technique as presented here would improve our understanding of UDs and allow for a reliable determination of the trend in physical properties of various substructures in the umbra.

*Acknowledgements* This work is supported by the SNF grant PE002-104552. The computations were carried out on Brutus, the central high-performance cluster at ETH Zurich. SVB acknowledges the EURYI Award from the ESF ([www.est.org/euryi](http://www.est.org/euryi)). RW acknowledges the support of ETHZ. Hinode is a Japanese mission developed and launched by ISAS/JAXA, collaborating with NAOJ as a domestic partner, NASA and STFC (UK) as international partners. Scientific operation of the Hinode mission is conducted by the Hinode science team organized at ISAS/JAXA. This team mainly consists of scientists from institutes in the partner countries. Support for the post-launch operation is provided by JAXA and NAOJ (Japan), STFC (U.K.), NASA, ESA, and NSC (Norway).



---

# Summary and Outlook

---

This chapter summarizes the findings of this thesis. By putting them in the context provided by the latest literature its implications and connections to the open questions in the field of solar physics are revisited. An outlook suggesting further work closes the thesis.

## 5.1 Summary: Contribution of this thesis

In this thesis we have built model atmospheres for sunspot umbrae. We applied a state-of-the-art technique, multi line spectral inversions, to new observations, both ground based (see Chapter 3) and space borne (see Chapter 4). As a result we were able to probe atmospheric conditions of the magnetized solar atmosphere at the photospheric level.

A great advantage of our analysis is the inclusion of molecular features, namely TiO, CaH, and MgH, which are very temperature sensitive in the temperature range present in sunspot umbrae and trace its darkest and coolest regions. Since many atomic absorption lines that form in the photosphere are blended with molecular features, simultaneous inversions are necessary to fit the complex spectra. The inversions in this thesis are

the first that include so many molecular lines for a wide spectral range of up to 2 Å (cf. Chapter 4).

Since our observations include the full Stokes vector we can use the spectropolarimetric information to determine the magnetic and thermodynamic properties of the sunspot umbra atmosphere at once. Thus, we were able to infer semi-empirical models of sunspot umbrae and their substructures that are both physically rigid and well constrained by observations.

The empirical knowledge of the brightness and thermal structure of sunspots is important for a variety of reasons: First, sunspot (spectral) brightness is an important parameter entering into studies of solar total and spectral irradiance. Second, it is needed for accurate line profile calculations to enable studies of sunspot dynamics. Third, the models produced can be used in theoretical simulations of energy transport mechanisms. By comparing (semi-)empirical with theoretically predicted thermal and magnetic stratifications the inhibition of convective energy transport in umbrae and penumbrae can be studied as a function of height. Thus, the question at which layers within the solar atmosphere mechanical energy transport and deposition become important can be addressed. As sunspots are the strongest magnetic features on the Sun at an atmospheric level that we can observe, learning more about their atmosphere adds to the major undertaking of understanding the solar atmosphere and its peculiarities, i.e. coronal heating, as a whole.

Unfortunately, we are not able to distinguish between the two competing explanations for the structure of sunspots below the surface, the spaghetti model and the monolithic model.

### **5.1.1 THEMIS investigation: multi line inversion of ground based sunspot observations**

In Chapter 3 we constructed semi-empirical models of different regions within a certain sunspot's umbra. This is the first detailed study that includes FeI, MgH, and TiO absorption features and was made possible by unique simultaneous spectropolarimetric observations in multiple spectral windows at the THEMIS facility at the end of solar cycle 23.

We showed that multi line spectral inversions including a variety of molecular absorption features from different parts of the optical spectrum

can be used in a simultaneous analysis. As different spectral absorption features probe different heights of the solar atmosphere this is one way to increase the height range and sensitivity of our models.

The model that fits the observations best includes three atmospheric components, i.e. one straylight component and two magnetic components, warm and cold. We link these magnetic components to the substructure of the umbra, i.e. umbral dots and their diffuse background, and compare the findings of our method with models by other authors.

The ability to disentangle different components from spatially unresolved observations provides us with a realistic picture of the complexity of the solar plasma.

### 5.1.2 HINODE study: a comparison of several sunspot umbrae of different sizes

In a subsequent study we analyzed observations from the HINODE satellite to look into sunspot umbrae of different sizes. The spatial resolution of 0.3 " allowed us to selectively analyze umbral substructure, i.e. peripheral and central umbral dots and the core umbra.

In contrast to the former study, which required a complex three component atmosphere, we were able to model these observations with a one-component atmosphere due to the improved spatial resolution, pointing and reduced straylight of this dataset.

We found that our sample of three sunspot umbrae is actually well matched by two sunspot models. In addition, a real dark core can only be found in big sunspots. Calculating the Wilson depression of all sunspot umbrae, we recovered the rich umbra substructure height profiles for the first time (see Fig. 5.1). A vertical cut of the sunspot umbra is presented in Fig. 5.2 showing the physical link between the directly observed brightness and the inferred Wilson depression.

Since our results are based on observations from a huge archive, we hope that we initiate a systematic investigation of many more sunspots and their dynamics with this method.

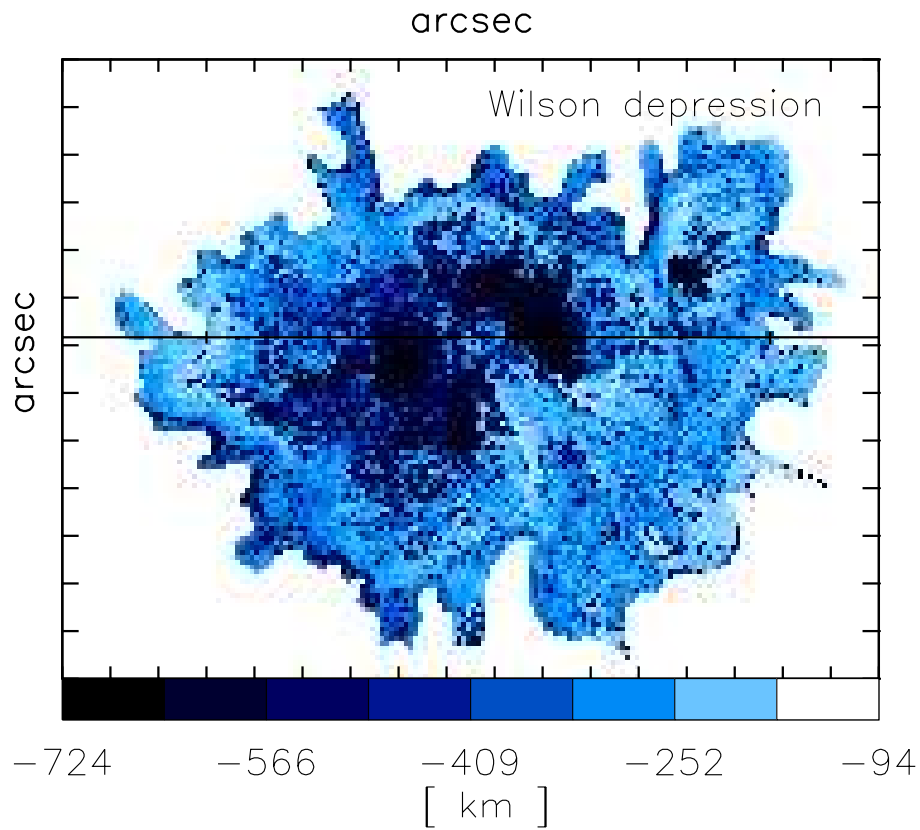


Fig. 5.1 Wilson depression of sunspot umbra S2 from Chapter 4. The black horizontal line marks the position of the vertical cut presented in Fig. 5.2.

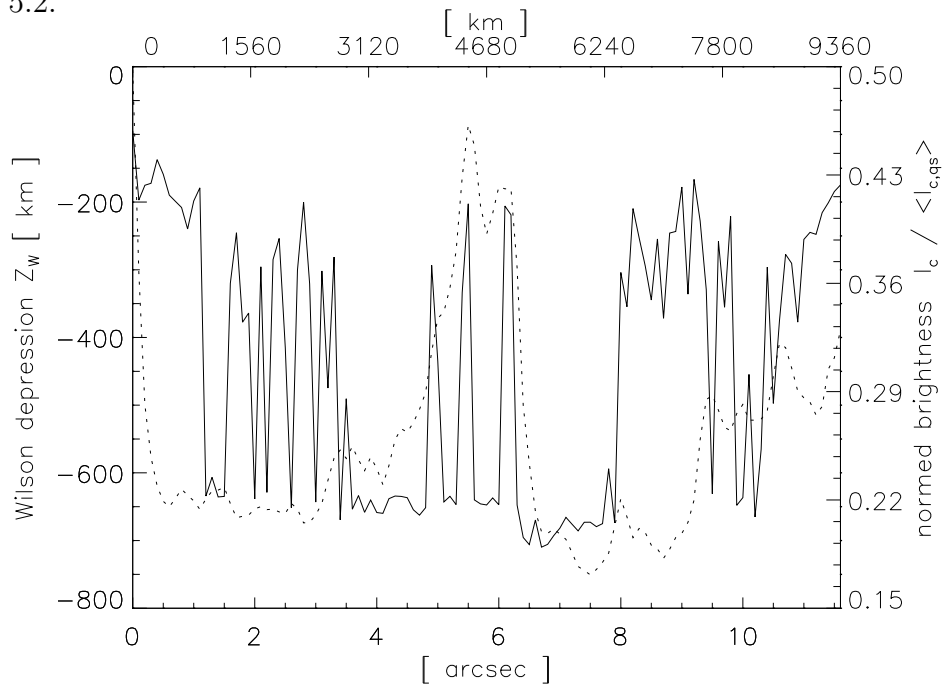


Fig. 5.2 Vertical cut through the sunspot umbra S2. The Wilson depression  $Z_W$  (solid line) and the continuum brightness relative to the average quiet sun continuum (dotted) are given.

### 5.1.3 Comparing the derived models

As a comparison of the results Fig. 5.3 shows temperature stratifications of peripheral umbral dots (PUD) and the dark core umbra (CU) in the biggest HINODE sunspot from the investigation in Chapter 4 and the magnetic components of the THEMIS model of the dark umbra (du) from Chapter 3. A quiet sun model and the umbra models of Maltby are added for comparison (Maltby et al., 1986).

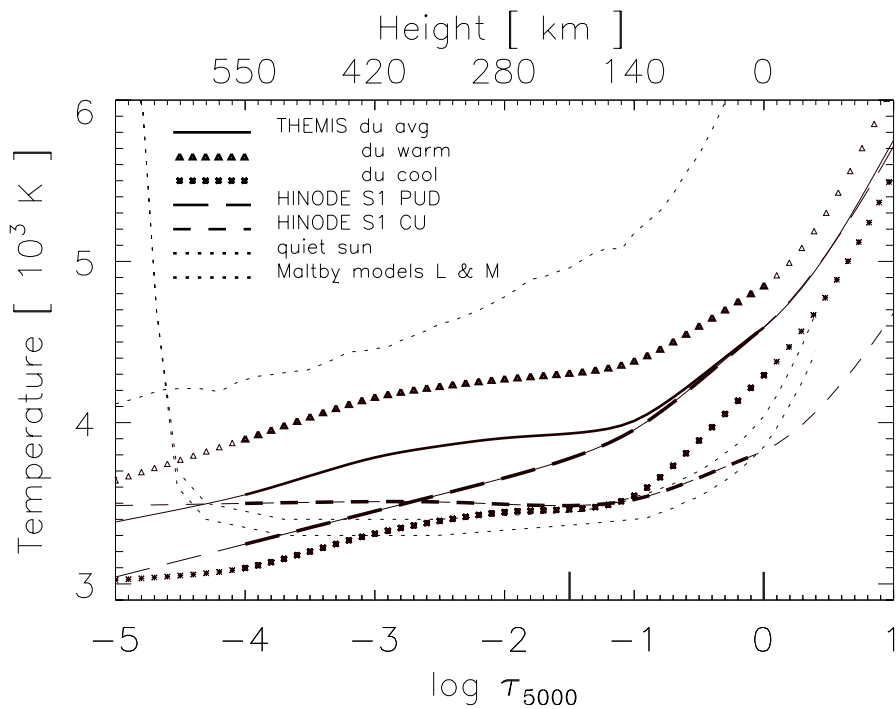


Fig. 5.3 A comparison of temperature stratifications found for different sunspot umbrae. The depth regions where our models are best constrained are indicated by the bold symbols.

Interestingly, the cool component of the THEMIS model has a similar temperature to that of the core umbra of the biggest HINODE sunspot. As both sunspots are rather big this fact points towards an intrinsic minimum temperature in sunspots in general associated with a possible global size limit.

The warm component of the THEMIS model is about 500 K hotter than the PUD stratification from HINODE. Of course this difference could be attributed to the differences of the two sunspots. But since we associated the warm component with the bright structures in the THEMIS analysis it might be worth testing if our method has underestimated the straylight component, and instead has increased the temperature in the warm magnetic component artificially.

#### 5.1.4 The nature of umbral dots

Umbral dots, as seen in observations of the sunspot umbra, are considered to be generally magnetoconvective in nature (see Degenhardt & Lites, 1993a, and references therein). Simulations by Schüssler & Vögler (2006) showed that UDs under certain assumptions even would have finestructure caused by internal convection: a dark lane across their apparent surface. Similar dark lanes within UDs have already been observed (Bharti et al., 2007).

In this section, we look for possible traces of convection in our results, discuss the possible heating function of UDs in the umbra and speculate about their physical origin.

##### Are umbral dots convective?

In a stellar plasma the temperature gradient determines the form of energy transport from the hot interior to the outer layers. If the temperature gradient is small we observe heat transport by radiation of photons; if the temperature gradient becomes sufficiently large we observe heat transport through convection, i.e. via gas motions.

With our models we inferred the gas temperature stratification for distinct subregions of the sunspot umbra. Since we are in LTE the temperature of the gas is equivalent to the radiation temperature.

Convective motions start when the (radiative) temperature gradient becomes larger than the convective temperature gradient, i.e. if

$$\nabla T > \nabla T_{ad}. \quad (5.1)$$

This convective temperature gradient can be conveniently defined for

Tab. 5.1 Temperature gradients for PUD and CUD region evaluated according to Eq. 5.2 at  $\log \tau_{5000} = 0.0$ .

$\gamma$	1.1	1.2	1.3	1.5	1.67
$\nabla T_{ad.}  _{PUD}$	450	826	1144	1652	1990
$\nabla T  _{PUD}$	990				
$\nabla T_{ad.}  _{CU}$	860	1577	2183	3154	3796
$\nabla T  _{CU}$	660				

a rising bubble of gas expanding adiabatically:

$$\nabla T_{ad.} = (1 - \gamma^{-1}) \frac{T}{p_{gas}} \nabla p_{gas} \quad (5.2)$$

where  $\gamma$  is the adiabatic constant, the ratio of specific heats.

We take the temperature gradients for PUDs and CU from Fig. 5.3 at the optical depth level  $\log \tau_{5000} = 0.0$ . As at all depths, here the temperature gradient of the CU is lower than that of the PUDs which can be explained by the higher  $H^-$  opacity in the hot PUDs.

We deduce the numerical values for the temperature gradients of the PUD and CU region depending on the adiabatic exponent  $\gamma$  according to Eq. 5.2. The value of  $\gamma = (f + 2)/f$  depends on the degrees of freedom of the gas and will decrease if they increase. A decrease of  $\gamma$  from the monoatomic value of  $5/3$  is possible due to the presence of radiation, ionization of gas fractions, or, at the lower temperatures of the CUD, due to a higher fraction of polyatomic gases (Grey, 1976, p.126).

We see that for certain values of  $\gamma$  the criterium for convection is fulfilled in PUD whereas it is never true for the CUD region. The latter is consistent with the observation that convection is clearly inhibited in the CU, compared to e.g. the granulation pattern of the quiet sun, due to the strong magnetic field. Based on our model atmospheres it is plausible that UDs are convective.

## Heating the umbra

The brightness of a sunspot and its umbra is primarily determined by the underlying heat transport processes. In higher layers radiative equilibrium is established whereas the energy processes close to the solar

surface, i.e. in sunspot umbrae at the height of the lower photosphere, are thought to be dominated by umbral dots (Maltby, 1992).

The total heating of the umbra sums up to 20 % of the heat flux density of the quiet sun leading to the question what makes a sunspot so bright (Solanki, 2003b). Sunspot umbral dots are the best answer so far due to their generic heat they transport as they rise through the plasma.

Within umbral dots the heat energy might not only originate from hot gas below the sunspot structure but, due to the existence of strong magnetic fields, from Joule heating (Joshi et al., 2007).

In addition, the hot walls of the umbral-penumbral transition are radiating heat into the umbral interior. But since sunspots extend over several thousand kilometers in horizontal range and have a typical depth, the Wilson depression, between 400 and 1000 km (Mathew et al., 2004) the contribution of the hot walls is minim.

There is a lack of literature on the umbral heating on the photospheric level. The fate of the blocked heat below a sunspot is discussed by (Spruit, 1992). He shows that the majority is distributed in the convection zone and only about 10 % of the blocked energy rises around the sunspot structure to be seen as bright ring (Rast et al., 1999, and references therein).

The question of umbral heating via UDs is directly related to the fractional area of UDs in a given umbra, i.e. how *noisy* the umbrae appear. Early studies based on intensity images revealed that sunspots with a radius of more than about 4'' have a stable UD fraction of 5 %. The brightness of smaller sunspots, however, was found to be strongly influenced by varying UD fractions of 50 % down to 5 % Sobotka (1988); Maltby (1992).

For the last solar cycle 23 Penn & Livingston (2006) reported on a general trend of declining peak magnetic field strengths in sunspots. From 1998 to 2005 they found a decrease of 50 G yr<sup>-1</sup>. In this context it would be worth to re-evaluate this *salt-and-pepper* relation for currently observed sunspots by using algorithms that identify UDs and thus improving the objectivity of the method (Watanabe et al., 2009; Riethmüller et al., 2008b).

An interesting feature in all temperature stratifications of sunspot umbrae in this thesis and in literature is the fact that there seems to be lower limit for the temperature stratification in the photosphere (see

Fig. 5.3). The coolest temperatures within a sunspot are determined by its size (Spruit & Simon, 1987). In addition, only sunspots over a certain size seem to have a core umbra at all which is believed to be free of umbral dots (Maltby, 1992; Watanabe et al., 2009).

### Speculating about the nature of umbral dots

There are at least two models that explain the physical origin of the umbral dots observed in sunspot umbrae.

In the monolithic sunspot model bright umbral dots are hot upflows that are penetrated by weaker magnetic fields. In simulations that were initiated with a monolithic sunspot umbra they emerge naturally (Rempel et al., 2009; Hurlburt et al., 1996).

In the spaghetti model umbral dots are thought to be field-free material in between all the thin flux tubes from below the sunspot umbra (Choudhuri, 1986; Parker, 1979).

Most unfortunately, the observational signatures of umbral dots in a monolithic umbra and a spaghetti model umbra are not expected to be very different from each other.

But as the first is the one best studied in theory and simulations due to its relative simplicity and the second seems to fit more appropriately to the otherwise chaotic convective layer below the solar surface both models may have to be combined and a distinction might not be possible or sensible. In fact, elements of both models could be taken to explain the observed differences between PUDs and CUDs. As PUDs seem to evolve from penumbral grains whose light curves are steadily decaying as they enter the umbra floating towards its center, CUDs are barely moving while first increasing and later decreasing in intensity (Riethmüller et al., 2008b; Watanabe et al., 2010).

It is pure speculation to assign a certain model to each subtype of umbral dots without observational proof. But penumbral grains are interpreted as the footprints of the upflow channels in the moving tube model of Schlichenmaier (2002). Within the simulation model these penumbral grains migrate towards the penumbral/umbral border as seen in observations. It seems therefore straight forward to assume a connection between PUDs and the moving tubes of the penumbra in which hot material rises. This might be the structure underlying PUDs.

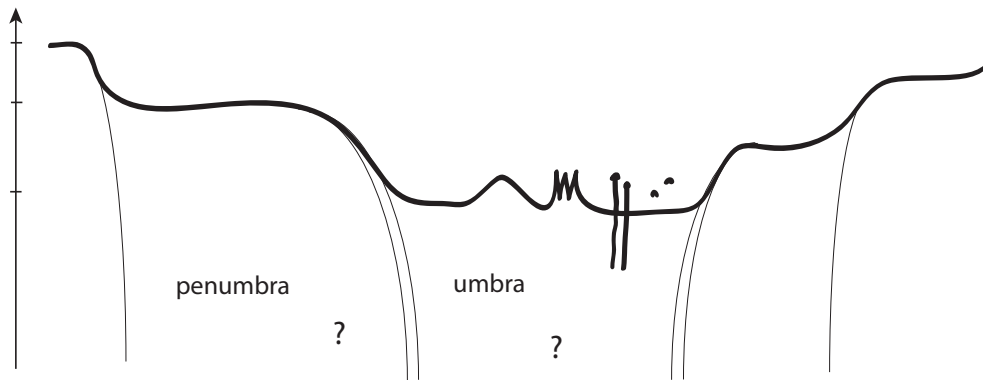


Fig. 5.4 Cartoon of the vertical structure of a sunspot (not to scale).

CUDs on the contrary could be the trace of a monolithic umbra configuration as seen in simulations. On the other hand, however, the model developed by Choudhuri (1986), refined and numerically tested as umbral flux tube model by Degenhardt & Lites (1993a,b), favors another interpretation: the spaghetti. Within such a fluxtube, not only single rising parcels of material can be imagined but chains thereof. Or certain parcels might cool down enough to sink, heat and rise again like an elevator in its shaft.

In Fig. 5.4 we show a cartoon of a vertical cut of a sunspot that has a penumbra and an umbra. As can be seen in results from our analysis (cf. Fig. 5.2) the Wilson depression traces substructures of the umbra, i.e. umbral dots. But due to limited spatial resolution of  $0.3''$  these traces may appear as bumps or combs within the umbra.

As datasets with increased spatial resolution become available UD's may be recognized to be the observational traces of columns of hot plasma from below (spaghetti model) or plumes of rising plasma parcels (monolithic model).

The results of our spectropolarimetric analysis do not allow us to distinguish between columns of hot plasma and rising plumes. All umbral dots we found had a line-of-sight velocity indicating a slight downward movement (about  $200 \text{ km sec}^{-1}$ ) and were not magnetic field free, but were penetrated by a magnetic field that was reduced by about 500 G (at  $\log \tau_{5000} = -1$ ) with respect to the core umbra. This is in very good agreement with previously reported results (Socas-Navarro et al., 2004;

Riethmüller et al., 2008a).

For future studies it has to be noted that nowadays typical observations recorded at the very solar center, where the line-of-sight and the local normal are identical, are easier to analyze by spectral inversions. But a time series of observations that might include following a sunspot as it is dragged along the solar surface might allow for an inclined view. Here, the 1D model approach might be challenged. As dynamic analyses of umbral dots were already carried out (Bharti et al., 2007; Prasad Choudhary et al., 2010; Watanabe et al., 2010) and some sunspots were already observed by HINODE at several positions on the solar disk these studies seem to be feasible.

## 5.2 The future is bright

With the spacecrafts SDO, the two STEREOs, Hinode and the planned Hinode successor solar C there is a fleet of satellites observing the Sun simultaneously and continuously producing petabytes of data. In addition, new ground-based telescopes such as the 4m ATST (Keil et al., 2003; Keller, 2003) or the EST (Collados, 2008) are being built and designed to acquire the necessary spectropolarimetric multi line data to study basic phenomena taking place in the Sun at all atmospheric layers (del Toro Iniesta & Orozco Suárez, 2010).

As the next generation of observatories driving solar physics become available to the community we have to ask if the data analysis tools can meet the demands. One of the most used but also most complex techniques that can determine the physics of the solar atmosphere are spectral inversions of spectropolarimetric multi line observations. Improvements of this tool might include multi line blends and wavelength dependent weighting to select and put emphasis on special spectral regions, e.g. line cores of strongly temperature sensitive lines, full 3D polarized radiative transfer and non-LTE capability to access higher atmospheric layers in addition to an automatic use to allow dynamic studies.

Complementary to the determination of semi-empirical models, full MHD simulations of the solar atmosphere, sunspots (Rempel et al., 2009) or even the sunspot umbrae (Schüssler & Vögler, 2006) try to investigate the full solar atmosphere starting from first principles (and approxima-

tions). But due to a lack of computational power ab-initio simulation spanning the range from the tachocline up to the solar corona are not feasible within my lifespan (Schüssler, 2008). The outcome of these simulations has to be carefully checked against the observations, some of which can be found in Chapters 3 and 4.

As input to any analysis of stellar spectra line lists and their accuracy are key. The available sources (Heiter et al., 2008; Kurucz, 2009) are continuously complemented and improved by laboratory experiments, astrophysical investigations, and theoretical calculations. But since, especially in highly magnetized objects like sunspots, the analysis depends on the subtleties of the observed spectra and the correct theoretical treatment of the underlying atomic or molecular species, any increase in complexity in theoretical calculations of e.g. molecular vibrational spectra has the potential to improve the analytic power of these tools tremendously (Berdyugina et al., 2003, 2005).

The work-horse of these investigations is the inversion code SPINOR. From the experiences made with more than 100'000 inversions it can be confirmed that SPINOR and its forward modeling part STOPRO are extremely flexible, stable and reliable tools for the study of solar (and stellar) atmospheres. Its main purpose is to simultaneously invert all four Stokes profiles of several blends, i.e. composition of many lines, weighting each profile differently. Finding the optimum balance of these weights was critical for the study presented in Chapter 3. In addition to the challenges presented by a variety of different possible geometries and multi ray approaches this is one example of valuable improvements for future versions of this program.

As a results of our 1D inversions including many atmospheric components we found that our atmospheric model might have been improved by a depth dependent filling factor of each atmospheric component. This model approach would need a carefully selected input to break the degeneracy of the magnetic field strength and filling factor over a range of depths. At the implementation stage, this possibility was not considered, rendering an amendment of the code a major redesign being both desirable and complex. However, for a next generation of inversion codes it should be included.

Stepping back and taking a look at the development of inversion techniques in general, a wish list including several features may be com-

posed to tackle the scientific questions under consideration and find self-consistent vertical and horizontal models for the major part of the atmospheres of sunspots and other interesting solar magnetic features (Ruiz Cobo, 2007; del Toro Iniesta et al., 2010).

On the basis of spectropolarimetric observations with high-resolution (0.1'' and below) and high polarimetric sensitivity ( $10^{-4}$ ) of several spectral features at once, future inversion codes should enable researchers to take into account blends of many spectral lines, atomic and molecular in origin. SPINOR and several other codes already fulfill that requirement but can be further improved, e.g. by weighting different parts of all available spectra differently as not all spectral features are carrying significant atmospheric information or cannot be calculated with the necessary accuracy.

The ability to compute in non-LTE regimes is a must when extending the range of the models to the chromosphere or even higher (Socas-Navarro, 2011). With increasing spatial resolution also small-scale geometries become observable, forcing the modeler to take into account e.g. flux tubes, current sheets, or magnetopauses, while keeping the number of free parameters of the model as small as possible. To increase realism, inversions are required to leave the 1.5D stage and include lateral radiative transfer effects in between the 1D line-of-sight columns. First steps are being made towards 3D models of magnetic structures to tackle the present concepts by more rigorous testing for consistency (horizontal and vertical stability, smooth transition between atmospheric layers according to geometry, divergence-free structures). Models for the quiet sun photosphere are already in the 3D stage helping to determine the real solar abundance of elements (Socas-Navarro, 2011; Serenelli et al., 2009).

With increasing complexity not only Zeeman and Paschen-Back effect but also the complementary Hanle effect must be taken into account if we wish to measure the small scale magnetic fields and their orientation in the Sun precisely (Trujillo Bueno, 2009).

Last but not least, the dynamic nature of solar magnetism requires us to create analysis procedures that are not only stable and reliable but also fast and easy enough to use for a sequence of observations. At the moment Milne-Eddington inversions are used for this mass-analysis (Watanabe et al., 2009, 2010) but there is a desire for more complexity.

An eruption of the entire northern solar hemisphere has been observed by the SDO and the twin STEREO spacecrafts on August 1, 2010. The massive event could be decomposed to a dozen significant shock waves, flares, filament eruptions, and CMEs spanning 180 degrees of solar longitude and 28 hours of time and was the first detailed observation of truly global solar activity (Schrijver & Title, 2011).

This event shows the complexity of solar magnetic activity and that it is still not well enough understood. With the research presented in this thesis I hope to have contributed towards an increased understanding of magnetism on the Sun – and the soon-to-come near-earth space weather report.

---

## References

---

- Abreu, J. A., Beer, J., Steinhilber, F., Tobias, S. M., & Weiss, N. O. 2008, *Geophys. Res. Lett.*, 35, 20109
- Afram, N. 2008, PhD thesis, PhD Thesis, ETH Zurich (No.17960)
- Afram, N., Berdyugina, S. V., Fluri, D. M., Solanki, S. K., Lagg, A., Petit, P., & Arnaud, J. 2006, in *Astronomical Society of the Pacific Conference Series*, Vol. 358, *Astronomical Society of the Pacific Conference Series*, ed. R. Casini & B. W. Lites, 375–+
- Albregtsen, F. & Maltby, P. 1981, *Sol. Phys.*, 71, 269
- Arnaud, J., Berdyugina, S. V., Fluri, D. M., Afram, N., Solanki, S. K., & Raouafi, N. 2006, in *Astronomical Society of the Pacific Conference Series*, Vol. 358, *Astronomical Society of the Pacific Conference Series*, ed. R. Casini & B. W. Lites, 319–+
- Arnaud, J., Mein, P., & Rayrole, J. 1998, in *ESA Special Publication*, Vol. 417, *Crossroads for European Solar and Heliospheric Physics. Recent Achievements and Future Mission Possibilities*, 213–+
- Asensio Ramos, A., Socas-Navarro, H., López Ariste, A., & Martínez González, M. J. 2007, *ApJ*, 660, 1690

- Auer, L. H., House, L. L., & Heasley, J. N. 1977, *Sol. Phys.*, 55, 47
- Avrett, E. H. 1981, in *The Physics of Sunspots*, ed. L. E. Cram & J. H. Thomas, 235–255
- Baumjohann, W. & Treumann, R. 1996, *Basic space plasma physics* (London: Imperial College Press)
- . 1997, *Advanced space plasma physics* (London: Imperial College Press)
- Beckers, J. M. 1969, *Sol. Phys.*, 9, 372
- Benz, A. 2002, *Astrophysics and space science library*, Vol. 279, *Plasma Astrophysics - Kinetic processes in solar and stellar coronae* (Dordrecht Boston London: Kluwer Academic Publisher)
- Berdyugina, S. V. 2005, *Living Reviews in Solar Physics*, 2, 8
- . 2010, ArXiv e-prints
- Berdyugina, S. V. 2011, in *Astronomical Society of the Pacific Conference Series*, Vol. 118, *Solar Polarization 6*, ed. J. Kuhn et al., 178–+
- Berdyugina, S. V., Braun, P. A., Fluri, D. M., & Solanki, S. K. 2005, *A&A*, 444, 947
- Berdyugina, S. V. & Solanki, S. K. 2002, *A&A*, 385, 701
- Berdyugina, S. V., Solanki, S. K., & Frutiger, C. 2003, *A&A*, 412, 513
- Berger, T. E. & Berdyugina, S. V. 2003a, *ApJ*, 589, L117
- . 2003b, *ApJ*, 589, L117
- Bharti, L., Joshi, C., & Jaaffrey, S. N. A. 2007, *ApJ*, 669, L57
- Biermann, L. 1942, *ZAp*, 21, 320
- Brutus cluster ETH Zurich. 2010, <http://www.clusterwiki.ethz.ch>

- Carlsson, M. 1986, A computer program for solving multi-level NON-LTE radiative transfer problems in moving or static atmospheres, Uppsala Astronom. Observatory
- Charbonneau, P. 2005, *Living Reviews in Solar Physics*, 2, 2
- Chevalier, S. 1916, "Ann. Obs. Astron. Zo-S", 9, B1
- Choudhuri, A. R. 1986, *ApJ*, 302, 809
- Collados, M. 2008, 12th European Solar Physics Meeting, Freiburg, Germany, held September, 8-12, 2008, p.6.3, 12, 6
- Collados, M., Martinez Pillet, V., Ruiz Cobo, B., del Toro Iniesta, J. C., & Vazquez, M. 1994, *A&A*, 291, 622
- Cowling, T. G. 1953, *Solar Electrodynamics*, ed. Kuiper, G. P., 532–+
- Cox, A. N. 2000, *Allen's astrophysical quantities*, ed. Cox, A. N.
- Cranmer, S. R., Hoeksema, J. T., & Kohl, J. L., eds. 2010, *Astronomical Society of the Pacific Conference Series*, Vol. 428, SOHO-23: Understanding a Peculiar Solar Minimum
- Danielson, R. E. 1964, *ApJ*, 139, 45
- Degenhardt, D. & Lites, B. W. 1993a, *ApJ*, 404, 383
- . 1993b, *ApJ*, 416, 875
- Degl'Innocenti, E. L. & Landolfi, M. 2004, *Astrophysics and space science library*, Vol. 307, Polarization in spectral lines (Dordrecht Boston London: Kluwer Academic Publisher)
- Deinzer, W. 1965, *ApJ*, 141, 548
- del Toro Iniesta, J. 2003, *Introduction to Spectropolarimetry* (Cambridge: Cambridge University Press)
- del Toro Iniesta, J. C. 2003, *Astronomische Nachrichten*, 324, 383
- del Toro Iniesta, J. C. & Orozco Suárez, D. 2010, *Astronomische Nachrichten*, 331, 558

- del Toro Iniesta, J. C., Orozco Suárez, D., & Bellot Rubio, L. R. 2010, *ApJ*, 711, 312
- Dikpati, M., Gilman, P. A., de Toma, G., & Ulrich, R. K. 2010, *Geophys. Res. Lett.*, 37, 14107
- Felipe, T., Khomenko, E., Collados, M., & Beck, C. 2010, *ApJ*, 722, 131
- Fontenla, J. M., Avrett, E. H., & Loeser, R. 1993, *ApJ*, 406, 319
- Fröhlich, C. 2009, *A&A*, 501, L27
- Frutiger, C. 2000, PhD thesis, ETH Zurich
- Frutiger, C., Solanki, S. K., Fligge, M., & Bruls, J. H. M. J. 2000, *A&A*, 358, 1109
- García, R. A., Turck-Chièze, S., Jiménez-Reyes, S. J., Ballot, J., Pallé, P. L., Eff-Darwich, A., Mathur, S., & Provost, J. 2007, *Science*, 316, 1591
- Gizon, L., Schunker, H., Baldner, C. S., Basu, S., Birch, A. C., Bogart, R. S., Braun, D. C., Cameron, R., Duvall, T. L., Hanasoge, S. M., Jackiewicz, J., Roth, M., Stahn, T., Thompson, M. J., & Zharkov, S. 2009, *Space Sci. Rev.*, 144, 249
- Gokhale, M. H. & Zwaan, C. 1972, *Sol. Phys.*, 26, 52
- Golub, L. & Pasachoff, J. M. 1997, *The Solar Corona*, ed. Golub, L. & Pasachoff, J. M.
- Grey, D. 1976, *Cambridge Astrophysical Series, Vol. 20, The observation and analysis of stellar photospheres* (Cambridge: Cambridge University Press)
- Grossmann-Doerth, U., Schmidt, W., & Schroeter, E. H. 1986, *A&A*, 156, 347
- Hale, G. E. 1908, *ApJ*, 28, 315
- Hale, G. E., Ellerman, F., Nicholson, S. B., & Joy, A. H. 1919, *ApJ*, 49, 153

- Harvey, J. W. & Breckinridge, J. B. 1973, *ApJ*, 182, L137+
- Harvey, K. L. 1991, in *Lecture Notes in Physics*, Berlin Springer Verlag, Vol. 387, *Flare Physics in Solar Activity Maximum 22*, ed. Y. Uchida, R. C. Canfield, T. Watanabe, & E. Hiei, 62–+
- Heiter, U., Barklem, P., Fossati, L., Kildiyarova, R., Kochukhov, O., Kupka, F., Obbrugger, M., Piskunov, N., Plez, B., Ryabchikova, T., Stempels, H. C., Stütz, C., & Weiss, W. W. 2008, *Journal of Physics Conference Series*, 130, 012011
- Herzberg, G. 1939, *Wissenschaftliche Forschungsberichte*, Vol. 50, *Molekulspektren und Molekuelstruktur* (Dresden und Leipzig: Verlag von Theodor Seinkopf)
- Holzreuter, R. 2009, in *Astronomical Society of the Pacific Conference Series*, Vol. 405, *Astronomical Society of the Pacific Conference Series*, ed. S. V. Berdyugina, K. N. Nagendra, & R. Ramelli, 101–+
- Hurlburt, N. E., Matthews, P. C., & Proctor, M. R. E. 1996, *ApJ*, 457, 933
- Ichimoto, K., Lites, B., Elmore, D., Suematsu, Y., Tsuneta, S., Katsukawa, Y., Shimizu, T., Shine, R., Tarbell, T., Title, A., Kiyohara, J., Shinoda, K., Card, G., Lecinski, A., Ständer, K., Nakagiri, M., Miyashita, M., Noguchi, M., Hoffmann, C., & Cruz, T. 2008, *Sol. Phys.*, 249, 233
- Jackson, J. 1998, *Classical Electrodynamics* 3rd ed. (John Wiley and Sons)
- Joshi, C., Bharti, L., & Jaaffrey, S. N. A. 2007, *Sol. Phys.*, 245, 239
- Judge, P. G. 1998, *ApJ*, 500, 1009
- Jurčák, J. & Sobotka, M. 2007, *Sol. Phys.*, 241, 223
- Keil, S. L., Rimmele, T., Keller, C. U., Hill, F., Radick, R. R., Oschmann, J. M., Warner, M., Dalrymple, N. E., Briggs, J., Hegwer, S. L., & Ren, D. 2003, in *Presented at the Society of Photo-Optical Instrumentation*

- Engineers (SPIE) Conference, Vol. 4853, Society of Photo-Optical Instrumentation Engineers (SPIE) Conference Series, ed. S. L. Keil & S. V. Avakyan, 240–251
- Keller, C. U. 2003, in *Astronomical Society of the Pacific Conference Series*, Vol. 286, *Current Theoretical Models and Future High Resolution Solar Observations: Preparing for ATST*, ed. A. A. Pevtsov & H. Uitenbroek, 31–+
- Khomenko, E. & Collados, M. 2009, *A&A*, 506, L5
- Kitai, R., Watanabe, H., Nakamura, T., Otsuji, K., Matsumoto, T., Ueno, S., Nagata, S., Shibata, K., Muller, R., Ichimoto, K., Tsuneta, S., Suematsu, Y., Katsukawa, Y., Shimizu, T., Tarbell, T. D., Shine, R. A., Title, A. M., & Lites, B. 2007, *PASJ*, 59, 585
- Kopp, G. & Rabin, D. 1992a, *Sol. Phys.*, 141, 253
- Kopp, M. G. & Rabin, D. 1992b, in *Astronomical Society of the Pacific Conference Series*, Vol. 26, *Cool Stars, Stellar Systems, and the Sun*, ed. M. S. Giampapa & J. A. Bookbinder, 246–+
- Kosugi, T., Matsuzaki, K., Sakao, T., Shimizu, T., Sone, Y., Tachikawa, S., Hashimoto, T., Minesugi, K., Ohnishi, A., Yamada, T., Tsuneta, S., Hara, H., Ichimoto, K., Suematsu, Y., Shimojo, M., Watanabe, T., Shimada, S., Davis, J. M., Hill, L. D., Owens, J. K., Title, A. M., Culhane, J. L., Harra, L. K., Doschek, G. A., & Golub, L. 2007, *Sol. Phys.*, 243, 3
- Krause, F. & Raedler, K. H. 1980, *Mean-field magnetohydrodynamics and dynamo theory*, ed. Krause, F. & Raedler, K. H.
- Kurucz, R. L. 1992, in *IAU Symposium*, Vol. 149, *The Stellar Populations of Galaxies*, ed. B. Barbuy & A. Renzini, 225–+
- Kurucz, R. L. 2009, in *American Institute of Physics Conference Series*, Vol. 1171, *American Institute of Physics Conference Series*, ed. I. Hubeny, J. M. Stone, K. MacGregor, & K. Werner, 43–51
- Lagg, A. 2005, *STOPRO and SPINOR Introduction*

- Landi Degl'Innocenti, E. 1982, *Sol. Phys.*, 77, 285
- Landi Degl'Innocenti, E. & Landi Degl'Innocenti, M. 1972, *Sol. Phys.*, 27, 319
- Landolfi, M., Landi Degl'Innocenti, E., & Arena, P. 1984, *Sol. Phys.*, 93, 269
- Lites, B. W. & Skumanich, A. 1982, *ApJS*, 49, 293
- López Ariste, A., Rayrole, J., & Semel, M. 2000, *A&AS*, 142, 137
- Maltby, P. 1992, in *NATO ASIC Proc. 375: Sunspots. Theory and Observations*, ed. J. H. Thomas & N. O. Weiss, 103–120
- Maltby, P., Avrett, E. H., Carlsson, M., Kjeldseth-Moe, O., Kurucz, R. L., & Loeser, R. 1986, *ApJ*, 306, 284
- Martinez Pillet, V. & Vazquez, M. 1993, *A&A*, 270, 494
- Mathew, S. K., Lagg, A., Solanki, S. K., Collados, M., Borrero, J. M., Berdyugina, S., Krupp, N., Woch, J., & Frutiger, C. 2003, *A&A*, 410, 695
- Mathew, S. K., Martínez Pillet, V., Solanki, S. K., & Krivova, N. A. 2007, *A&A*, 465, 291
- Mathew, S. K., Solanki, S. K., Lagg, A., Collados, M., Borrero, J. M., & Berdyugina, S. 2004, *A&A*, 422, 693
- Mihalas, D. 1978, *Stellar atmospheres (2nd)* (San Francisco: W.H. Freeman and Co.)
- Moffatt, H. K. 1978, *Magnetic field generation in electrically conducting fluids*, ed. Moffatt, H. K.
- Muller, R. 1973, *Sol. Phys.*, 32, 409
- Nicolas, K. R., Bartoe, J., Brueckner, G. E., & Kjeldseth-Moe, D. 1981, in *The Physics of Sunspots*, ed. L. E. Cram & J. H. Thomas, 167–190
- Norton, A. A. & Gilman, P. A. 2004, *ApJ*, 603, 348

- Parker, E. N. 1958, *ApJ*, 128, 664
- . 1975, *Sol. Phys.*, 40, 291
- . 1979, *ApJ*, 234, 333
- Penn, M. J. & Livingston, W. 2006, *ApJ*, 649, L45
- Pijpers, F. P. 1995, *INTERnet*, 14
- Prasad Choudhary, D., MacDonald, G. A., Deng, N., & Shimizu, T. 2010, in *American Astronomical Society Meeting Abstracts*, Vol. 216, *American Astronomical Society Meeting Abstracts*, 401.11–+
- Press, W. H., Teukolsky, S. A., Vetterling, W. T., & Flannery, B. P. 1992, *Numerical recipes in FORTRAN. The art of scientific computing*
- Puschmann, K. G., Ruiz Cobo, B., & Martinez Pillet, V. 2008, *ArXiv e-prints*
- Rachkovsky, D. N. 1962, *Izv. Krymsk. Astrofiz. Obs.*, 28, 259
- Rast, M. P., Fox, P. A., Lin, H., Lites, B. W., Meisner, R. W., & White, O. R. 1999, *Nature*, 401, 678
- Rees, D. E. 1987, *A Gentle Introduction to Polarized Radiative Transfer*, ed. Kalkofen, W., 213–+
- Rempel, M., Schüssler, M., & Knölker, M. 2009, *ApJ*, 691, 640
- Riethmüller, T. L., Solanki, S. K., & Lagg, A. 2008a, *ApJ*, 678, L157
- Riethmüller, T. L., Solanki, S. K., Zakharov, V., & Gandorfer, A. 2008b, *A&A*, 492, 233
- Rimmele, T. 2008, *ApJ*, 672, 684
- Ruiz Cobo, B. 2007, in *Modern solar facilities - advanced solar science*, ed. F. Kneer, K. G. Puschmann, & A. D. Wittmann, 287–+
- Ruiz Cobo, B. & del Toro Iniesta, J. C. 1992, *ApJ*, 398, 375
- Sainz Dalda, A. & López Ariste, A. 2007, *A&A*, 469, 721

- Schlichenmaier, R. 2002, *Astronomische Nachrichten*, 323, 303
- Schlichenmaier, R., Rezaei, R., Bello González, N., & Waldmann, T. A. 2010, *A&A*, 512, L1+
- Schrijver, C. & Title, A. 2011, *JGR Space Physics*, in press
- Schüssler, M. 2008, 12th European Solar Physics Meeting, Freiburg, Germany, held September, 8-12, 2008, p.1.1, 12, 1
- Schüssler, M. & Rempel, M. 2005, *A&A*, 441, 337
- Schüssler, M. & Vögler, A. 2006, *ApJ*, 641, L73
- Serenelli, A. M., Basu, S., Ferguson, J. W., & Asplund, M. 2009, *ApJ*, 705, L123
- Shelyag, S., Zharkov, S., Fedun, V., Erdélyi, R., & Thompson, M. J. 2009, *A&A*, 501, 735
- Shenstone, A. & Blair, H. 1929, *Philos. Mag.*, 8, 765
- Skumanich, A. & Lites, B. W. 1987, *ApJ*, 322, 473
- Sobel'man, I. 1972, *International Series of monographs in natural philosophy*, Vol. 40, *Introduction to the theory of atomic spectra* (Oxford: Pergamon Press)
- Sobotka, M. 1988, *Bulletin of the Astronomical Institutes of Czechoslovakia*, 39, 236
- Sobotka, M., Bonet, J. A., & Vazquez, M. 1992a, *A&A*, 257, 757
- . 1992b, *A&A*, 260, 437
- . 1993, *ApJ*, 415, 832
- Socas-Navarro, H. 2005, *ApJ*, 631, L167
- . 2007, *ApJS*, 169, 439
- . 2011, *ArXiv e-prints*

- Socas-Navarro, H., Martínez Pillet, V., Sobotka, M., & Vázquez, M. 2004, *ApJ*, 614, 448
- Solanki, S. K., K. N. A. 2003a, *JOURNAL OF GEOPHYSICAL RESEARCH*, 108, 1200
- Solanki, S. K. 1987, PhD thesis, PhD thesis No. 8309, ETH, Zürich, (1987)
- . 2003b, *A&A Rev.*, 11, 153
- Solanki, S. K., Inhester, B., & Schüssler, M. 2006, *Reports on Progress in Physics*, 69, 563
- Solanki, S. K. & Unruh, Y. C. 2004, *MNRAS*, 348, 307
- Spruit, H. C. 1976, *Sol. Phys.*, 50, 269
- Spruit, H. C. 1992, in *NATO ASIC Proc. 375: Sunspots. Theory and Observations*, ed. J. H. Thomas & N. O. Weiss, 163–171
- Spruit, H. C. & Simon, G. W. 1987, in *Bulletin of the American Astronomical Society*, Vol. 19, *Bulletin of the American Astronomical Society*, 943–+
- Staude, J., Hildebrandt, J., Fuerstenberg, F., Krueger, A., Jakimiec, J., Obridko, V. N., Siarkowski, M., Sylwester, B., & Sylwester, J. 1983, *Acta astronomica*, 33, 441
- Stenflo, J. 1994, *Astrophysics and space science library*, Vol. 189, *Solar magnetic fields - Polarized radiation diagnostics* (Dordrecht Boston London: Kluwer Academic Publishers)
- Stenflo, J. O. 1973, *Sol. Phys.*, 32, 41
- . 2010, *A&A*, 517, A37+
- Stenflo, J. O. & Keller, C. U. 1997, *A&A*, 321, 927
- Stix, M. 2002, *The sun - An introduction*, 2nd ed., *AA library* (Berlin, Heidelberg: Springer)

- Strassmeier, K. G. 1999, *A&A*, 347, 225
- . 2009, *A&A Rev.*, 17, 251
- Tennyson, J. 2005, *Advanced Physics Texts*, Vol. 2, *Astronomical spectroscopy* (London: Imperial College Press)
- Thomas, J. H. & Weiss, N. O. 2004, *ARA&A*, 42, 517
- Trujillo Bueno, J. 2009
- Tsuneta, S., Ichimoto, K., Katsukawa, Y., Nagata, S., Otsubo, M., Shimizu, T., Suematsu, Y., Nakagiri, M., Noguchi, M., Tarbell, T., Title, A., Shine, R., Rosenberg, W., Hoffmann, C., Jurcevich, B., Kushner, G., Levay, M., Lites, B., Elmore, D., Matsushita, T., Kawaguchi, N., Saito, H., Mikami, I., Hill, L. D., & Owens, J. K. 2008, *Sol. Phys.*, 249, 167
- Unno, W. 1956, *PASJ*, 8, 108
- Vernazza, J. E., Avrett, E. H., & Loeser, R. 1981, *ApJS*, 45, 635
- Wallace, L., Hinkle, K., & Livingston, W. C. 2005, *An atlas of sunspot umbral spectra in the visible from 15,000 to 25,500 cm<sup>-1</sup> (3920 to 6664 Å)*, ed. Wallace, L., Hinkle, K., & Livingston, W. C.
- Watanabe, H., Kitai, R., & Ichimoto, K. 2009, *ApJ*, 702, 1048
- Watanabe, H., Tritschler, A., Kitai, R., & Ichimoto, K. 2010, *Sol. Phys.*, 266, 5
- Wenzel, R. et al., in review. 2011, *A&A*
- Wenzler, T. 2005, PhD thesis, Eidgenoessische Technische Hochschule Zuerich (Switzerland), Switzerland
- Westendorp Plaza, C., del Toro Iniesta, J. C., Ruiz Cobo, B., & Martínez Pillet, V. 2001, *ApJ*, 547, 1148
- Westendorp Plaza, C., del Toro Iniesta, J. C., Ruiz Cobo, B., Martínez Pillet, V., Lites, B. W., & Skumanich, A. 1998, *ApJ*, 494, 453

Wohl, H. 1969a, *A&A*, 3, 487

—. 1969b, *A&A*, 3, 378

Wolf, R. 1850, *Astronomische Mitteilungen der Eidenssischen Sternwarte  
Zurich*

Zeeman, P. 1897, *ApJ*, 5, 332

## A Solar facts

Tab. A.1 Facts about the Sun as collected by Cox (2000).

Property	numerical value
diameter	$D_{\odot} = 13.91 \cdot 10^8 \text{ m}$
mass	$M_{\odot} = 1.989 \cdot 10^{30} \text{ kg}$
average density	$\rho_{\odot} = 1409 \text{ kg m}^{-3}$
chemical composition	70% H, 28% He
metallicity	per Definition 0 ( $\lg[\text{Fe}/\text{H}] - \lg[\text{Fe?}/\text{H?}] = 0$ )
gravity at solar surface	$g_{\odot} = 273.96 \text{ m s}^{-2}$
escape velocity at solar surface	$v_{\odot} = 618 \text{ km s}^{-1}$
mass loss due to solar wind	$\approx 1 \cdot 10^9 \text{ kg s}^{-1}$
temperature	
at the center	$T_c = 1.48 \cdot 10^7 \text{ K}$
at the surface (photosphere)	$T_{\odot} = 5800 \text{ K}$
in the chromosphere	$T_{\odot} = 5800 \text{ K}$
in the corona	$T = 1 - 2 \cdot 10^6 \text{ K}$
solar age	$t_{\odot} = 4.57 \cdot 10^9 \text{ yr}$
time until central H burning ends	$\approx 4.5 - 5 \text{ Gyr}$
synodic rotation period at equator	$P = 27.3 \text{ d}$
siderial rotation period at equator	$P = 25.4 \text{ d}$
at altitude $\pm 70$ deg	$P = 35.0 \text{ d}$
rotation velocity at equator	$v \approx 1860 \text{ m s}^{-1}$
rotation period of a sunspot	$P = 29.0 \text{ d}$
apparent diameter	$31', 59.3''$
mean distance Sun-Earth	$1\text{AU} = 149\,597\,870 \text{ km}$
distance at perihelion	$147.1 \cdot 10^6 \text{ km}$
distance at aphelion	$152.1 \cdot 10^6 \text{ km}$
total solar irradiance (TSI)	$1.365 \text{ W m}^{-2}$
solar luminosity	$L_{\odot} = 3.8 \cdot 10^{26} \text{ W}$
color-index	0.6
absolute magnitude	4.5
apparent magnitude	-26.7
specific surface radiation	$6.318 \cdot 10^7 \text{ W m}^{-2}$

## B Find Initial Models for SPINOR (FIMS)

Find Initial Models for SPINOR (FIMS) is a collection of bash scripts and a Fortran code that was written to find the initial values for model parameters used in SPINOR inversions. After the development of the code and severe testing it was found that our inversions are not that sensitive to specific initial values. Therefore, FIMS has not been polished for third party use.

FIMS aims to find the initial values for the four most important model parameters: Temperature ( $T$ ), magnetic field strength ( $B$ ), magnetic inclination angle ( $\gamma$ ), and magnetic azimuth angle ( $\chi$ ). In the present stage the code assumes a two component atmosphere, with one of the components being a quiet sun atmosphere accounting for straylight, e.g. Kurucz. A fifth parameter, the filling factor ( $ff$ ), varies the dilution of the magnetized atmosphere by the straylight.

FIMS follows a two-step strategy: first, build a database of synthetic spectra by varying the five parameters ( $T$ ,  $B$ ,  $ff$ ,  $\gamma$ ,  $\chi$ ) over a reasonable range with a certain grid step. Second, compare each observation, i.e. each single point from a sunspot map, to the synthetic database in order to find the best match.

The following scheme describes the use of FIMS:

Tab. B.1: Working scheme for the FIMS package.

<b>produce synthetic database using SPINOR</b>	
computations performed on multi-core computer	
%> bash FIMSstart.bash	manipulates sto.inp based on preset parameter ranges and grid steps and starts single instances of SPINOR
%> bash FIMScs.bash	controls one instance of SPINOR
%> FIMSdat2hdf5.exe	combines synthetic spectra in hdf5 db
<b>compare observations to synthetic spectra database</b>	
%> fims.exe	build final synthetic spectra by adding straylight via filling factor and find best match to observations
<b>use fims.dat file in pre_riic (see appendix C)</b>	

FIMS produces a file (fims.dat) that matches the three best initial models ( $T$ ,  $B$ ,  $\text{ff}$ ,  $\gamma$ ,  $\chi$ ) to each observation. This dataset can be used as starting point for inversions.

## C Rigid Inversion Control (RIC) package

Rigid Inversion Control (RIC) is a collection of bash scripts and IDL routines that enables the user to run SPINOR inversions simultaneously on a multiple core computer featuring a batch queue system. It's purpose is to limit the computational time, i.e. number of iterations, by applying a simple convergence criterion and to consistently handle the I/O for trivially paralleled computations.

All inversions presented in this thesis have been computed using the SPINOR code. For practical reasons the convergence criteria of the SPINOR code are not sufficient, i.e. the extra sigma introduced (ref chi sqr of SPINOR) causes the algorithm to iterate until the maximum number of iterations is reached even if the fit has converged sufficiently well before. The script ric.bash starts SPINOR for a fix number of iterations (5), checks the first temperature and bfield line in the output (finp file) and compares it to previous values. If the differences fall below the preset values the inversion is considered to have converged.

The whole suite of routines and scripts has been written to perform on a local computer running IDL (preparation and visualization) and a remote multi-core cluster without IDL (computation). The single node queue of the ETHZ Brutus cluster (Brutus cluster ETH Zurich, 2010) is ideal for having sunspot maps consisting of more than 30 000 pixels inverted in about three days.

In addition to a distributed strategy a purely local variety of the RIC package allows to invert any number of observations locally and sequentially. It thus facilitates the test of different parameters in a hands-on fashion.

The following scheme describes the general use of RIC:

Tab. C.1: Working scheme for the RIC package.

local system with IDL (e.g. hydrus)	remote multiple core system (e.g. brutus)
<p><b>preparation:</b></p> <p>collect all input files (atmospheres, linelists, observations, .wlb files) and edit <i>pre_ric.pro</i> for details of the inv.inp file IDL&gt; pre_ric produces jobtarfiles bearing an unique timestamp, e.g. Mon20_Sep_2010_20_14_26.tar including all necessary files to invert a given number of observations transfer jobtarfiles</p>	<p>find all scripts in dir /cluster/home/./ric/</p> <p>jobtarfiles are placed in dir /cluster/work/./data/</p>
	<p><b>computation:</b></p> <p>%&gt; bash make_joblist.bash prepares joblist for bash queue %&gt; bash ric_starter.bash queues the jobtarfiles %&gt; bash ric_status.bash information on running jobs %&gt; bash ric_tidyup.bash includes log files (can be skipped)</p>
<p><b>archive and visualization:</b></p> <p>IDL&gt; post_ric, nc=3 archives and plots all spectra and atmospheric parameters IDL&gt; make_atm_5000, 'archive/' collects atmospheric data of whole sunspot in single data block (.sav file)</p>	<p>transfer returned jobtarfiles</p>
<p><b>analysis</b></p>	

## D The coordinate systems on the Sun

The magnetic field vector  $\mathbf{B}$  is usually expressed in the observer's coordinate system, defined by the line-of-sight ( $z'$ ) and the solar limb ( $x'$ ), by use of the inclination angle  $\gamma$  and the azimuthal angle  $\chi$ <sup>1</sup> (see Fig. D.0). The normal and tangential components of the magnetic field vector, however, can be inferred by following the coordinate transformation from the observer's to the local solar reference system.

The transformation is basically a rotation about the common  $x = x'$ -axis. First, convert the spherical coordinates into Cartesian coordinates:

$$\begin{pmatrix} x' \\ y' \\ z' \end{pmatrix} = \begin{pmatrix} +B \sin \gamma \cos \chi \\ -B \sin \gamma \sin \chi \\ +B \cos \gamma \end{pmatrix} \quad (\text{D.1})$$

Second, rotate about the common  $x = x'$ -axis by the angle  $\theta$ :

$$\begin{pmatrix} x \\ y \\ z \end{pmatrix} = \begin{pmatrix} 1 & 0 & 0 \\ 0 & \cos \theta & -\sin \theta \\ 0 & \sin \theta & \cos \theta \end{pmatrix} \begin{pmatrix} x' \\ y' \\ z' \end{pmatrix} \quad (\text{D.2})$$

such that

$$B_z = B \cdot (-\sin \theta \sin \gamma \sin \chi + \cos \theta \cos \gamma) \quad (\text{D.3})$$

---

<sup>1</sup> In the SPINOR definition  $\chi$  is defined to increase counterclockwise starting at the  $x'$ -axis parallel to the solar limb.



## **E Atmospheres of Chapter 3**

Tab. E.1 Model atmosphere of the core umbra region (CU) of sunspot umbra S1 (NOAA 10 930).

log $\tau_{5000}$	height [cm]	T [K]	$P_{gas}$ [g cm <sup>-1</sup> s <sup>-2</sup> ]	$P_{electr.}$ [g <sup>-1</sup> s <sup>-2</sup> ]	$\kappa$ [g <sup>-1</sup> ]	$\rho$ [cm <sup>-3</sup> ]	B [G]	$\zeta_{\mu}$ [cm s <sup>-1</sup> ]	$v_{LOS}$ [cm s <sup>-1</sup> ]	$\gamma_B$ [deg]	$\chi_B$
-4.000	4.06E+07	3082.4	1.492E+03	1.03E-02	2.88E-03	7.77E-09	2479.5	6.3E+04	3.6E+04	109.2	33.1
-3.900	3.96E+07	3112.6	1.718E+03	1.21E-02	3.21E-03	8.83E-09	2464.8	6.3E+04	3.6E+04	109.2	33.1
-3.800	3.86E+07	3147.2	1.973E+03	1.44E-02	3.59E-03	9.99E-09	2450.3	6.3E+04	3.6E+04	109.2	33.1
-3.700	3.76E+07	3184.5	2.259E+03	1.73E-02	4.03E-03	1.13E-08	2435.8	6.3E+04	3.6E+04	109.2	33.1
-3.600	3.67E+07	3223.5	2.579E+03	2.08E-02	4.54E-03	1.27E-08	2421.4	6.3E+04	3.6E+04	109.2	33.1
-3.500	3.57E+07	3263.3	2.936E+03	2.53E-02	5.13E-03	1.42E-08	2407.0	6.3E+04	3.6E+04	109.2	33.1
-3.400	3.48E+07	3303.1	3.335E+03	3.09E-02	5.82E-03	1.59E-08	2392.7	6.3E+04	3.6E+04	109.2	33.1
-3.300	3.38E+07	3342.2	3.779E+03	3.79E-02	6.60E-03	1.78E-08	2378.5	6.3E+04	3.6E+04	109.2	33.1
-3.200	3.29E+07	3379.9	4.275E+03	4.61E-02	7.47E-03	2.00E-08	2364.2	6.3E+04	3.6E+04	109.2	33.1
-3.100	3.19E+07	3415.1	4.830E+03	5.56E-02	8.42E-03	2.23E-08	2350.0	6.3E+04	3.6E+04	109.2	33.1
-3.000	3.10E+07	3446.1	5.455E+03	6.61E-02	9.43E-03	2.50E-08	2335.7	6.3E+04	3.6E+04	109.2	33.1
-2.900	3.00E+07	3471.7	6.161E+03	7.69E-02	1.05E-02	2.81E-08	2321.4	6.3E+04	3.6E+04	109.2	33.1
-2.800	2.91E+07	3493.1	6.963E+03	8.82E-02	1.16E-02	3.16E-08	2307.0	6.3E+04	3.6E+04	109.2	33.1
-2.700	2.81E+07	3511.7	7.876E+03	1.00E-01	1.28E-02	3.55E-08	2292.5	6.3E+04	3.6E+04	109.2	33.1
-2.600	2.71E+07	3528.3	8.920E+03	1.14E-01	1.41E-02	4.01E-08	2277.9	6.3E+04	3.6E+04	109.2	33.1
-2.500	2.61E+07	3543.4	1.011E+04	1.28E-01	1.55E-02	4.53E-08	2263.3	6.3E+04	3.6E+04	109.2	33.1
-2.400	2.51E+07	3557.3	1.147E+04	1.44E-01	1.70E-02	5.13E-08	2248.5	6.3E+04	3.6E+04	109.2	33.1
-2.300	2.40E+07	3570.1	1.304E+04	1.62E-01	1.87E-02	5.82E-08	2233.6	6.3E+04	3.6E+04	109.2	33.1
-2.200	2.30E+07	3581.6	1.482E+04	1.81E-01	2.05E-02	6.61E-08	2218.6	6.3E+04	3.6E+04	109.2	33.1
-2.100	2.19E+07	3591.4	1.687E+04	2.02E-01	2.25E-02	7.52E-08	2203.6	6.3E+04	3.6E+04	109.2	33.1
-2.000	2.09E+07	3598.8	1.923E+04	2.25E-01	2.46E-02	8.57E-08	2188.4	6.3E+04	3.6E+04	109.2	33.1
-1.900	1.98E+07	3603.4	2.195E+04	2.48E-01	2.69E-02	9.80E-08	2173.1	6.3E+04	3.6E+04	109.2	33.1
-1.800	1.87E+07	3605.9	2.508E+04	2.73E-01	2.93E-02	1.12E-07	2157.7	6.3E+04	3.6E+04	109.2	33.1
-1.700	1.76E+07	3607.6	2.871E+04	3.01E-01	3.19E-02	1.29E-07	2142.2	6.3E+04	3.6E+04	109.2	33.1
-1.600	1.65E+07	3609.2	3.290E+04	3.31E-01	3.47E-02	1.49E-07	2126.6	6.3E+04	3.6E+04	109.2	33.1
-1.500	1.54E+07	3611.9	3.774E+04	3.66E-01	3.78E-02	1.71E-07	2110.9	6.3E+04	3.6E+04	109.2	33.1
-1.400	1.43E+07	3616.7	4.332E+04	4.07E-01	4.14E-02	1.97E-07	2095.3	6.3E+04	3.6E+04	109.2	33.1
-1.300	1.32E+07	3625.0	4.973E+04	4.56E-01	4.54E-02	2.27E-07	2079.7	6.3E+04	3.6E+04	109.2	33.1
-1.200	1.21E+07	3639.0	5.706E+04	5.17E-01	5.02E-02	2.60E-07	2064.3	6.3E+04	3.6E+04	109.2	33.1
-1.100	1.10E+07	3661.8	6.537E+04	5.96E-01	5.60E-02	2.97E-07	2048.9	6.3E+04	3.6E+04	109.2	33.1
-1.000	9.97E+06	3698.1	7.468E+04	7.06E-01	6.33E-02	3.36E-07	2033.9	6.3E+04	3.6E+04	109.2	33.1
-0.900	8.91E+06	3752.0	8.493E+04	8.63E-01	7.30E-02	3.75E-07	2019.1	6.3E+04	3.6E+04	109.2	33.1
-0.800	7.88E+06	3819.4	9.604E+04	1.08E+00	8.51E-02	4.13E-07	2004.7	6.3E+04	3.6E+04	109.2	33.1
-0.700	6.87E+06	3895.5	1.080E+05	1.37E+00	9.99E-02	4.52E-07	1990.6	6.3E+04	3.6E+04	109.2	33.1
-0.600	5.88E+06	3977.2	1.208E+05	1.75E+00	1.18E-01	4.92E-07	1976.8	6.3E+04	3.6E+04	109.2	33.1
-0.500	4.91E+06	4062.3	1.344E+05	2.24E+00	1.38E-01	5.35E-07	1963.4	6.3E+04	3.6E+04	109.2	33.1
-0.400	3.94E+06	4149.4	1.491E+05	2.86E+00	1.61E-01	5.77E-07	1950.1	6.3E+04	3.6E+04	109.2	33.1
-0.300	2.98E+06	4237.1	1.650E+05	3.61E+00	1.87E-01	6.23E-07	1936.9	6.3E+04	3.6E+04	109.2	33.1
-0.200	2.00E+06	4324.5	1.822E+05	4.52E+00	2.16E-01	6.71E-07	1923.6	6.3E+04	3.6E+04	109.2	33.1
-0.100	1.01E+06	4410.2	2.011E+05	5.60E+00	2.47E-01	7.24E-07	1910.0	6.3E+04	3.6E+04	109.2	33.1
0.000	0.00E+00	4492.9	2.220E+05	6.86E+00	2.80E-01	7.83E-07	1896.1	6.3E+04	3.6E+04	109.2	33.1
0.098	-1.01E+06	4583.3	2.445E+05	8.40E+00	3.16E-01	8.38E-07	1882.2	6.3E+04	3.6E+04	109.2	33.1
0.196	-2.03E+06	4680.7	2.686E+05	1.03E+01	3.56E-01	8.99E-07	1868.3	6.3E+04	3.6E+04	109.2	33.1
0.292	-3.04E+06	4784.6	2.945E+05	1.27E+01	4.01E-01	9.63E-07	1854.4	6.3E+04	3.6E+04	109.2	33.1
0.387	-4.05E+06	4894.3	3.222E+05	1.56E+01	4.50E-01	1.03E-06	1840.5	6.3E+04	3.6E+04	109.2	33.1
0.481	-5.06E+06	5009.3	3.518E+05	1.91E+01	5.03E-01	1.09E-06	1826.6	6.3E+04	3.6E+04	109.2	33.1
0.573	-6.08E+06	5129.1	3.832E+05	2.35E+01	5.61E-01	1.16E-06	1812.7	6.3E+04	3.6E+04	109.2	33.1
0.665	-7.09E+06	5253.3	4.166E+05	2.89E+01	6.26E-01	1.23E-06	1798.8	6.3E+04	3.6E+04	109.2	33.1
0.757	-8.10E+06	5381.5	4.520E+05	3.60E+01	7.03E-01	1.30E-06	1785.0	6.3E+04	3.6E+04	109.2	33.1
0.850	-9.11E+06	5513.3	4.894E+05	4.52E+01	7.97E-01	1.38E-06	1771.2	6.3E+04	3.6E+04	109.2	33.1
0.945	-1.01E+07	5648.4	5.290E+05	5.75E+01	9.13E-01	1.45E-06	1757.4	6.3E+04	3.6E+04	109.2	33.1
1.045	-1.11E+07	5786.5	5.707E+05	7.43E+01	1.06E+00	1.53E-06	1743.6	6.3E+04	3.6E+04	109.2	33.1

Tab. E.2 Umbra model atmosphere - warm magnetic component average of full umbra. Note that the sunspot was observed at  $\mu = 0.9$ .

$\log \tau_{5000}$	height [cm]	T [K]	$P_{gas}$ [g cm <sup>-1</sup> s <sup>-2</sup> ]	$P_{electr.}$ [g <sup>-1</sup> ]	$\kappa$ [g <sup>-1</sup> ]	$\rho$ [cm <sup>-3</sup> ]	B [G]	$\zeta_{\mu}$ [cm s <sup>-1</sup> ]	$v_{LOS}$ [cm s <sup>-1</sup> ]	$\gamma_B$ [deg]	$\chi_B$
-4.000	5.06E+07	3795.6	9.959E+02	4.59E-02	4.65E-03	4.09E-09	2354.1	1.3E+05	3.9E+04	127.9	107.7
-3.900	4.95E+07	3823.7	1.136E+03	5.32E-02	5.17E-03	4.63E-09	2362.3	1.3E+05	3.9E+04	127.9	107.7
-3.800	4.83E+07	3852.2	1.294E+03	6.16E-02	5.75E-03	5.23E-09	2370.8	1.3E+05	3.9E+04	127.9	107.7
-3.700	4.71E+07	3881.1	1.473E+03	7.12E-02	6.39E-03	5.90E-09	2379.3	1.3E+05	3.9E+04	127.9	107.7
-3.600	4.60E+07	3910.0	1.676E+03	8.24E-02	7.09E-03	6.66E-09	2387.7	1.3E+05	3.9E+04	127.9	107.7
-3.500	4.48E+07	3938.9	1.906E+03	9.51E-02	7.88E-03	7.51E-09	2396.1	1.3E+05	3.9E+04	127.9	107.7
-3.400	4.36E+07	3967.6	2.167E+03	1.10E-01	8.75E-03	8.47E-09	2404.1	1.3E+05	3.9E+04	127.9	107.7
-3.300	4.24E+07	3995.8	2.462E+03	1.26E-01	9.70E-03	9.55E-09	2411.8	1.3E+05	3.9E+04	127.9	107.7
-3.200	4.12E+07	4023.3	2.798E+03	1.45E-01	1.07E-02	1.08E-08	2418.8	1.3E+05	3.9E+04	127.9	107.7
-3.100	4.00E+07	4049.7	3.179E+03	1.67E-01	1.19E-02	1.22E-08	2424.8	1.3E+05	3.9E+04	127.9	107.7
-3.000	3.88E+07	4074.2	3.613E+03	1.90E-01	1.32E-02	1.37E-08	2429.3	1.3E+05	3.9E+04	127.9	107.7
-2.900	3.76E+07	4096.4	4.107E+03	2.17E-01	1.46E-02	1.55E-08	2431.7	1.3E+05	3.9E+04	127.9	107.7
-2.800	3.64E+07	4116.8	4.669E+03	2.46E-01	1.61E-02	1.76E-08	2432.5	1.3E+05	3.9E+04	127.9	107.7
-2.700	3.52E+07	4135.9	5.308E+03	2.79E-01	1.78E-02	1.99E-08	2432.0	1.3E+05	3.9E+04	127.9	107.7
-2.600	3.39E+07	4154.0	6.036E+03	3.15E-01	1.97E-02	2.25E-08	2430.5	1.3E+05	3.9E+04	127.9	107.7
-2.500	3.27E+07	4171.3	6.865E+03	3.56E-01	2.18E-02	2.55E-08	2427.8	1.3E+05	3.9E+04	127.9	107.7
-2.400	3.14E+07	4187.8	7.809E+03	4.01E-01	2.41E-02	2.89E-08	2424.0	1.3E+05	3.9E+04	127.9	107.7
-2.300	3.02E+07	4203.5	8.884E+03	4.52E-01	2.66E-02	3.28E-08	2418.4	1.3E+05	3.9E+04	127.9	107.7
-2.200	2.89E+07	4218.0	1.011E+04	5.08E-01	2.94E-02	3.72E-08	2410.5	1.3E+05	3.9E+04	127.9	107.7
-2.100	2.77E+07	4230.9	1.151E+04	5.70E-01	3.25E-02	4.22E-08	2399.1	1.3E+05	3.9E+04	127.9	107.7
-2.000	2.64E+07	4241.5	1.310E+04	6.37E-01	3.58E-02	4.79E-08	2382.4	1.3E+05	3.9E+04	127.9	107.7
-1.900	2.51E+07	4249.0	1.492E+04	7.09E-01	3.94E-02	5.45E-08	2359.0	1.3E+05	3.9E+04	127.9	107.7
-1.800	2.38E+07	4254.4	1.700E+04	7.86E-01	4.34E-02	6.20E-08	2330.9	1.3E+05	3.9E+04	127.9	107.7
-1.700	2.25E+07	4258.7	1.938E+04	8.71E-01	4.78E-02	7.06E-08	2300.4	1.3E+05	3.9E+04	127.9	107.7
-1.600	2.12E+07	4262.7	2.211E+04	9.63E-01	5.25E-02	8.05E-08	2269.6	1.3E+05	3.9E+04	127.9	107.7
-1.500	1.99E+07	4267.4	2.523E+04	1.07E+00	5.78E-02	9.18E-08	2240.3	1.3E+05	3.9E+04	127.9	107.7
-1.400	1.86E+07	4273.6	2.880E+04	1.18E+00	6.36E-02	1.05E-07	2214.7	1.3E+05	3.9E+04	127.9	107.7
-1.300	1.73E+07	4282.4	3.288E+04	1.32E+00	7.00E-02	1.19E-07	2195.6	1.3E+05	3.9E+04	127.9	107.7
-1.200	1.60E+07	4295.6	3.755E+04	1.48E+00	7.73E-02	1.36E-07	2187.1	1.3E+05	3.9E+04	127.9	107.7
-1.100	1.47E+07	4315.5	4.285E+04	1.67E+00	8.57E-02	1.54E-07	2194.8	1.3E+05	3.9E+04	127.9	107.7
-1.000	1.34E+07	4345.8	4.886E+04	1.93E+00	9.55E-02	1.75E-07	2227.6	1.3E+05	3.9E+04	127.9	107.7
-0.900	1.20E+07	4389.7	5.562E+04	2.26E+00	1.07E-01	1.97E-07	2293.3	1.3E+05	3.9E+04	127.9	107.7
-0.800	1.07E+07	4444.0	6.320E+04	2.69E+00	1.20E-01	2.22E-07	2383.9	1.3E+05	3.9E+04	127.9	107.7
-0.700	9.44E+06	4505.0	7.169E+04	3.21E+00	1.35E-01	2.48E-07	2490.9	1.3E+05	3.9E+04	127.9	107.7
-0.600	8.13E+06	4570.3	8.121E+04	3.84E+00	1.52E-01	2.77E-07	2608.2	1.3E+05	3.9E+04	127.9	107.7
-0.500	6.82E+06	4638.3	9.190E+04	4.58E+00	1.70E-01	3.08E-07	2732.0	1.3E+05	3.9E+04	127.9	107.7
-0.400	5.49E+06	4707.7	1.039E+05	5.47E+00	1.90E-01	3.44E-07	2859.3	1.3E+05	3.9E+04	127.9	107.7
-0.300	4.14E+06	4777.7	1.175E+05	6.50E+00	2.12E-01	3.83E-07	2987.9	1.3E+05	3.9E+04	127.9	107.7
-0.200	2.78E+06	4847.3	1.328E+05	7.72E+00	2.37E-01	4.26E-07	3115.6	1.3E+05	3.9E+04	127.9	107.7
-0.100	1.40E+06	4915.7	1.500E+05	9.15E+00	2.64E-01	4.75E-07	3240.5	1.3E+05	3.9E+04	127.9	107.7
0.000	0.00E+00	4981.8	1.695E+05	1.08E+01	2.95E-01	5.30E-07	3359.6	1.3E+05	3.9E+04	127.9	107.7
0.098	-1.40E+06	5062.3	1.911E+05	1.29E+01	3.29E-01	5.84E-07	3479.4	1.3E+05	3.9E+04	127.9	107.7
0.196	-2.80E+06	5156.1	2.150E+05	1.57E+01	3.71E-01	6.45E-07	3597.0	1.3E+05	3.9E+04	127.9	107.7
0.292	-4.20E+06	5261.9	2.413E+05	1.95E+01	4.21E-01	7.09E-07	3713.3	1.3E+05	3.9E+04	127.9	107.7
0.387	-5.59E+06	5378.8	2.701E+05	2.45E+01	4.83E-01	7.76E-07	3828.4	1.3E+05	3.9E+04	127.9	107.7
0.481	-6.99E+06	5505.8	3.016E+05	3.15E+01	5.61E-01	8.47E-07	3942.7	1.3E+05	3.9E+04	127.9	107.7
0.573	-8.39E+06	5641.9	3.359E+05	4.13E+01	6.64E-01	9.21E-07	4056.6	1.3E+05	3.9E+04	127.9	107.7
0.665	-9.79E+06	5786.3	3.732E+05	5.54E+01	8.01E-01	9.97E-07	4170.9	1.3E+05	3.9E+04	127.9	107.7
0.757	-1.12E+07	5938.3	4.135E+05	7.58E+01	9.86E-01	1.08E-06	4286.8	1.3E+05	3.9E+04	127.9	107.7
0.850	-1.26E+07	6097.0	4.569E+05	1.05E+02	1.24E+00	1.16E-06	4405.4	1.3E+05	3.9E+04	127.9	107.7
0.945	-1.40E+07	6261.9	5.036E+05	1.48E+02	1.57E+00	1.24E-06	4528.2	1.3E+05	3.9E+04	127.9	107.7
1.045	-1.54E+07	6432.1	5.536E+05	2.09E+02	2.02E+00	1.33E-06	4656.1	1.3E+05	3.9E+04	127.9	107.7

Tab. E.3 Umbra model atmosphere - cool magnetic component of core umbra region (cu). Note that the sunspot was observed at  $\mu = 0.9$ .

$\log \tau_{5000}$	height [cm]	T [K]	$P_{gas}$ [g cm <sup>-1</sup> s <sup>-2</sup> ]	$P_{electr.}$ [g cm <sup>-1</sup> s <sup>-2</sup> ]	$\kappa$ [g <sup>-1</sup> ]	$\rho$ [cm <sup>-3</sup> ]	B [G]	$\zeta_{\mu}$ [cm s <sup>-1</sup> ]	$v_{LOS}$ [cm s <sup>-1</sup> ]	$\gamma_B$ [deg]	$\chi_B$
-4.000	3.92E+07	3097.7	1.526E+03	9.70E-03	2.83E-03	8.25E-09	2502.8	4.8E+04	7.5E+04	115.1	52.5
-3.900	3.82E+07	3114.5	1.766E+03	1.11E-02	3.13E-03	9.46E-09	2489.8	4.8E+04	7.5E+04	115.1	52.5
-3.800	3.72E+07	3134.1	2.039E+03	1.28E-02	3.47E-03	1.08E-08	2477.0	4.8E+04	7.5E+04	115.1	52.5
-3.700	3.62E+07	3155.4	2.348E+03	1.47E-02	3.84E-03	1.23E-08	2464.3	4.8E+04	7.5E+04	115.1	52.5
-3.600	3.52E+07	3177.8	2.698E+03	1.70E-02	4.26E-03	1.40E-08	2451.6	4.8E+04	7.5E+04	115.1	52.5
-3.500	3.42E+07	3200.7	3.095E+03	1.96E-02	4.73E-03	1.58E-08	2439.1	4.8E+04	7.5E+04	115.1	52.5
-3.400	3.32E+07	3223.9	3.546E+03	2.27E-02	5.25E-03	1.80E-08	2426.6	4.8E+04	7.5E+04	115.1	52.5
-3.300	3.22E+07	3247.0	4.056E+03	2.64E-02	5.83E-03	2.04E-08	2414.1	4.8E+04	7.5E+04	115.1	52.5
-3.200	3.12E+07	3269.6	4.635E+03	3.07E-02	6.49E-03	2.31E-08	2401.8	4.8E+04	7.5E+04	115.1	52.5
-3.100	3.02E+07	3291.3	5.291E+03	3.56E-02	7.21E-03	2.62E-08	2389.5	4.8E+04	7.5E+04	115.1	52.5
-3.000	2.93E+07	3311.5	6.035E+03	4.12E-02	8.00E-03	2.97E-08	2377.2	4.8E+04	7.5E+04	115.1	52.5
-2.900	2.83E+07	3329.6	6.880E+03	4.73E-02	8.86E-03	3.38E-08	2365.1	4.8E+04	7.5E+04	115.1	52.5
-2.800	2.73E+07	3346.2	7.843E+03	5.40E-02	9.79E-03	3.83E-08	2352.9	4.8E+04	7.5E+04	115.1	52.5
-2.700	2.63E+07	3361.6	8.941E+03	6.15E-02	1.08E-02	4.36E-08	2340.8	4.8E+04	7.5E+04	115.1	52.5
-2.600	2.53E+07	3376.2	1.019E+04	6.98E-02	1.19E-02	4.96E-08	2328.7	4.8E+04	7.5E+04	115.1	52.5
-2.500	2.43E+07	3390.1	1.162E+04	7.91E-02	1.31E-02	5.64E-08	2316.6	4.8E+04	7.5E+04	115.1	52.5
-2.400	2.34E+07	3403.3	1.326E+04	8.95E-02	1.44E-02	6.42E-08	2304.5	4.8E+04	7.5E+04	115.1	52.5
-2.300	2.24E+07	3415.7	1.512E+04	1.01E-01	1.59E-02	7.31E-08	2292.4	4.8E+04	7.5E+04	115.1	52.5
-2.200	2.14E+07	3427.1	1.726E+04	1.14E-01	1.75E-02	8.34E-08	2280.3	4.8E+04	7.5E+04	115.1	52.5
-2.100	2.03E+07	3437.1	1.970E+04	1.28E-01	1.92E-02	9.53E-08	2268.2	4.8E+04	7.5E+04	115.1	52.5
-2.000	1.93E+07	3444.9	2.251E+04	1.44E-01	2.10E-02	1.09E-07	2256.1	4.8E+04	7.5E+04	115.1	52.5
-1.900	1.83E+07	3450.0	2.575E+04	1.61E-01	2.30E-02	1.25E-07	2243.9	4.8E+04	7.5E+04	115.1	52.5
-1.800	1.73E+07	3453.2	2.948E+04	1.79E-01	2.51E-02	1.44E-07	2231.7	4.8E+04	7.5E+04	115.1	52.5
-1.700	1.63E+07	3455.6	3.378E+04	1.99E-01	2.73E-02	1.66E-07	2219.4	4.8E+04	7.5E+04	115.1	52.5
-1.600	1.53E+07	3458.1	3.877E+04	2.22E-01	2.97E-02	1.92E-07	2207.2	4.8E+04	7.5E+04	115.1	52.5
-1.500	1.42E+07	3461.4	4.452E+04	2.48E-01	3.24E-02	2.22E-07	2195.0	4.8E+04	7.5E+04	115.1	52.5
-1.400	1.32E+07	3466.7	5.116E+04	2.79E-01	3.54E-02	2.57E-07	2182.7	4.8E+04	7.5E+04	115.1	52.5
-1.300	1.22E+07	3475.4	5.881E+04	3.16E-01	3.88E-02	2.97E-07	2170.6	4.8E+04	7.5E+04	115.1	52.5
-1.200	1.12E+07	3489.3	6.757E+04	3.60E-01	4.27E-02	3.42E-07	2158.5	4.8E+04	7.5E+04	115.1	52.5
-1.100	1.02E+07	3511.4	7.753E+04	4.17E-01	4.75E-02	3.91E-07	2146.6	4.8E+04	7.5E+04	115.1	52.5
-1.000	9.22E+06	3545.9	8.872E+04	4.92E-01	5.36E-02	4.43E-07	2134.8	4.8E+04	7.5E+04	115.1	52.5
-0.900	8.25E+06	3596.9	1.011E+05	5.97E-01	6.16E-02	4.94E-07	2123.2	4.8E+04	7.5E+04	115.1	52.5
-0.800	7.29E+06	3660.4	1.145E+05	7.37E-01	7.17E-02	5.44E-07	2111.8	4.8E+04	7.5E+04	115.1	52.5
-0.700	6.35E+06	3732.1	1.290E+05	9.24E-01	8.40E-02	5.94E-07	2100.5	4.8E+04	7.5E+04	115.1	52.5
-0.600	5.43E+06	3808.9	1.446E+05	1.17E+00	9.89E-02	6.44E-07	2089.4	4.8E+04	7.5E+04	115.1	52.5
-0.500	4.52E+06	3888.9	1.612E+05	1.49E+00	1.17E-01	6.98E-07	2078.5	4.8E+04	7.5E+04	115.1	52.5
-0.400	3.62E+06	3970.7	1.790E+05	1.90E+00	1.37E-01	7.52E-07	2067.7	4.8E+04	7.5E+04	115.1	52.5
-0.300	2.72E+06	4053.1	1.980E+05	2.41E+00	1.61E-01	8.09E-07	2057.0	4.8E+04	7.5E+04	115.1	52.5
-0.200	1.82E+06	4135.1	2.186E+05	3.04E+00	1.88E-01	8.69E-07	2046.2	4.8E+04	7.5E+04	115.1	52.5
-0.100	9.18E+05	4215.7	2.408E+05	3.81E+00	2.18E-01	9.34E-07	2035.4	4.8E+04	7.5E+04	115.1	52.5
0.000	0.00E+00	4293.4	2.651E+05	4.73E+00	2.50E-01	1.01E-06	2024.4	4.8E+04	7.5E+04	115.1	52.5
0.098	-9.18E+05	4378.1	2.912E+05	5.87E+00	2.87E-01	1.07E-06	2013.4	4.8E+04	7.5E+04	115.1	52.5
0.194	-1.84E+06	4469.1	3.190E+05	7.34E+00	3.31E-01	1.15E-06	2002.4	4.8E+04	7.5E+04	115.1	52.5
0.289	-2.75E+06	4565.9	3.487E+05	9.18E+00	3.79E-01	1.22E-06	1991.5	4.8E+04	7.5E+04	115.1	52.5
0.382	-3.67E+06	4667.9	3.804E+05	1.15E+01	4.33E-01	1.30E-06	1980.5	4.8E+04	7.5E+04	115.1	52.5
0.473	-4.59E+06	4774.6	4.140E+05	1.42E+01	4.91E-01	1.38E-06	1969.5	4.8E+04	7.5E+04	115.1	52.5
0.562	-5.51E+06	4885.6	4.496E+05	1.75E+01	5.53E-01	1.46E-06	1958.5	4.8E+04	7.5E+04	115.1	52.5
0.648	-6.43E+06	5000.6	4.874E+05	2.14E+01	6.19E-01	1.54E-06	1947.6	4.8E+04	7.5E+04	115.1	52.5
0.732	-7.34E+06	5119.0	5.271E+05	2.60E+01	6.87E-01	1.62E-06	1936.6	4.8E+04	7.5E+04	115.1	52.5
0.812	-8.26E+06	5240.6	5.689E+05	3.14E+01	7.60E-01	1.71E-06	1925.6	4.8E+04	7.5E+04	115.1	52.5
0.890	-9.18E+06	5365.0	6.129E+05	3.79E+01	8.33E-01	1.79E-06	1914.6	4.8E+04	7.5E+04	115.1	52.5
0.965	-1.01E+07	5492.2	6.591E+05	4.56E+01	9.13E-01	1.89E-06	1903.6	4.8E+04	7.5E+04	115.1	52.5

Tab. E.4 Umbra model atmosphere - warm magnetic component of core umbra region (cu). Note that the sunspot was observed at  $\mu = 0.9$ .

$\log \tau_{5000}$	height [cm]	T [K]	$P_{gas}$ [g cm <sup>-1</sup> s <sup>-2</sup> ]	$P_{electr.}$ [g <sup>-1</sup> ]	$\kappa$ [g <sup>-1</sup> ]	$\rho$ [cm <sup>-3</sup> ]	B [G]	$\zeta_{\mu}$ [cm s <sup>-1</sup> ]	$v_{LOS}$ [cm s <sup>-1</sup> ]	$\gamma_B$ [deg]	$\chi_B$
-4.000	5.14E+07	3900.6	1.001E+03	4.90E-02	4.76E-03	4.07E-09	2442.1	1.1E+05	5.4E+04	148.1	120.4
-3.900	5.02E+07	3927.7	1.143E+03	5.67E-02	5.29E-03	4.61E-09	2462.7	1.1E+05	5.4E+04	148.1	120.4
-3.800	4.90E+07	3955.1	1.303E+03	6.55E-02	5.87E-03	5.22E-09	2483.5	1.1E+05	5.4E+04	148.1	120.4
-3.700	4.78E+07	3982.5	1.485E+03	7.56E-02	6.52E-03	5.90E-09	2504.4	1.1E+05	5.4E+04	148.1	120.4
-3.600	4.66E+07	4010.0	1.691E+03	8.71E-02	7.24E-03	6.67E-09	2525.2	1.1E+05	5.4E+04	148.1	120.4
-3.500	4.54E+07	4037.2	1.925E+03	1.00E-01	8.03E-03	7.54E-09	2545.9	1.1E+05	5.4E+04	148.1	120.4
-3.400	4.42E+07	4064.0	2.190E+03	1.15E-01	8.91E-03	8.52E-09	2566.2	1.1E+05	5.4E+04	148.1	120.4
-3.300	4.30E+07	4090.1	2.491E+03	1.32E-01	9.87E-03	9.62E-09	2586.0	1.1E+05	5.4E+04	148.1	120.4
-3.200	4.17E+07	4115.1	2.833E+03	1.51E-01	1.09E-02	1.09E-08	2604.8	1.1E+05	5.4E+04	148.1	120.4
-3.100	4.05E+07	4138.4	3.221E+03	1.73E-01	1.21E-02	1.23E-08	2622.3	1.1E+05	5.4E+04	148.1	120.4
-3.000	3.93E+07	4159.0	3.663E+03	1.96E-01	1.34E-02	1.39E-08	2637.6	1.1E+05	5.4E+04	148.1	120.4
-2.900	3.80E+07	4176.3	4.166E+03	2.22E-01	1.48E-02	1.58E-08	2650.2	1.1E+05	5.4E+04	148.1	120.4
-2.800	3.68E+07	4191.0	4.740E+03	2.49E-01	1.64E-02	1.79E-08	2660.7	1.1E+05	5.4E+04	148.1	120.4
-2.700	3.55E+07	4203.9	5.393E+03	2.80E-01	1.81E-02	2.03E-08	2669.6	1.1E+05	5.4E+04	148.1	120.4
-2.600	3.43E+07	4215.6	6.138E+03	3.14E-01	1.99E-02	2.30E-08	2677.6	1.1E+05	5.4E+04	148.1	120.4
-2.500	3.30E+07	4226.5	6.988E+03	3.52E-01	2.20E-02	2.61E-08	2684.7	1.1E+05	5.4E+04	148.1	120.4
-2.400	3.17E+07	4236.8	7.957E+03	3.93E-01	2.43E-02	2.97E-08	2691.3	1.1E+05	5.4E+04	148.1	120.4
-2.300	3.04E+07	4246.6	9.063E+03	4.39E-01	2.68E-02	3.37E-08	2697.1	1.1E+05	5.4E+04	148.1	120.4
-2.200	2.91E+07	4256.0	1.033E+04	4.90E-01	2.96E-02	3.83E-08	2702.2	1.1E+05	5.4E+04	148.1	120.4
-2.100	2.79E+07	4264.8	1.177E+04	5.47E-01	3.26E-02	4.36E-08	2706.3	1.1E+05	5.4E+04	148.1	120.4
-2.000	2.66E+07	4272.9	1.341E+04	6.09E-01	3.59E-02	4.96E-08	2708.9	1.1E+05	5.4E+04	148.1	120.4
-1.900	2.53E+07	4280.2	1.530E+04	6.77E-01	3.96E-02	5.65E-08	2709.7	1.1E+05	5.4E+04	148.1	120.4
-1.800	2.40E+07	4287.0	1.745E+04	7.52E-01	4.36E-02	6.43E-08	2709.4	1.1E+05	5.4E+04	148.1	120.4
-1.700	2.26E+07	4293.7	1.991E+04	8.35E-01	4.79E-02	7.33E-08	2708.8	1.1E+05	5.4E+04	148.1	120.4
-1.600	2.13E+07	4300.6	2.272E+04	9.27E-01	5.28E-02	8.35E-08	2708.6	1.1E+05	5.4E+04	148.1	120.4
-1.500	2.00E+07	4308.1	2.594E+04	1.03E+00	5.81E-02	9.52E-08	2709.8	1.1E+05	5.4E+04	148.1	120.4
-1.400	1.87E+07	4316.9	2.962E+04	1.15E+00	6.40E-02	1.09E-07	2713.5	1.1E+05	5.4E+04	148.1	120.4
-1.300	1.74E+07	4327.4	3.382E+04	1.28E+00	7.05E-02	1.24E-07	2721.0	1.1E+05	5.4E+04	148.1	120.4
-1.200	1.60E+07	4340.9	3.862E+04	1.44E+00	7.79E-02	1.41E-07	2734.7	1.1E+05	5.4E+04	148.1	120.4
-1.100	1.47E+07	4358.9	4.408E+04	1.62E+00	8.62E-02	1.60E-07	2757.9	1.1E+05	5.4E+04	148.1	120.4
-1.000	1.34E+07	4383.6	5.028E+04	1.85E+00	9.58E-02	1.82E-07	2795.5	1.1E+05	5.4E+04	148.1	120.4
-0.900	1.20E+07	4417.3	5.729E+04	2.14E+00	1.07E-01	2.06E-07	2851.9	1.1E+05	5.4E+04	148.1	120.4
-0.800	1.07E+07	4457.8	6.517E+04	2.49E+00	1.20E-01	2.32E-07	2922.8	1.1E+05	5.4E+04	148.1	120.4
-0.700	9.40E+06	4502.7	7.404E+04	2.92E+00	1.34E-01	2.61E-07	3002.9	1.1E+05	5.4E+04	148.1	120.4
-0.600	8.08E+06	4550.5	8.400E+04	3.43E+00	1.50E-01	2.93E-07	3089.1	1.1E+05	5.4E+04	148.1	120.4
-0.500	6.76E+06	4599.9	9.521E+04	4.02E+00	1.68E-01	3.28E-07	3179.0	1.1E+05	5.4E+04	148.1	120.4
-0.400	5.43E+06	4650.4	1.078E+05	4.72E+00	1.88E-01	3.67E-07	3270.8	1.1E+05	5.4E+04	148.1	120.4
-0.300	4.09E+06	4701.2	1.220E+05	5.52E+00	2.10E-01	4.11E-07	3363.4	1.1E+05	5.4E+04	148.1	120.4
-0.200	2.74E+06	4751.7	1.381E+05	6.44E+00	2.33E-01	4.60E-07	3455.6	1.1E+05	5.4E+04	148.1	120.4
-0.100	1.38E+06	4801.5	1.563E+05	7.50E+00	2.60E-01	5.15E-07	3546.1	1.1E+05	5.4E+04	148.1	120.4
0.000	0.00E+00	4849.7	1.768E+05	8.71E+00	2.89E-01	5.77E-07	3633.3	1.1E+05	5.4E+04	148.1	120.4
0.098	-1.38E+06	4913.7	1.997E+05	1.02E+01	3.21E-01	6.39E-07	3721.1	1.1E+05	5.4E+04	148.1	120.4
0.196	-2.76E+06	4992.1	2.251E+05	1.22E+01	3.59E-01	7.08E-07	3807.6	1.1E+05	5.4E+04	148.1	120.4
0.292	-4.13E+06	5083.6	2.532E+05	1.47E+01	4.02E-01	7.81E-07	3893.3	1.1E+05	5.4E+04	148.1	120.4
0.387	-5.51E+06	5187.2	2.840E+05	1.78E+01	4.50E-01	8.58E-07	3977.9	1.1E+05	5.4E+04	148.1	120.4
0.481	-6.89E+06	5301.8	3.179E+05	2.17E+01	5.03E-01	9.40E-07	4061.2	1.1E+05	5.4E+04	148.1	120.4
0.573	-8.27E+06	5426.5	3.549E+05	2.67E+01	5.63E-01	1.03E-06	4143.0	1.1E+05	5.4E+04	148.1	120.4
0.665	-9.64E+06	5560.3	3.952E+05	3.33E+01	6.37E-01	1.11E-06	4223.4	1.1E+05	5.4E+04	148.1	120.4
0.757	-1.10E+07	5702.5	4.390E+05	4.22E+01	7.32E-01	1.21E-06	4302.8	1.1E+05	5.4E+04	148.1	120.4
0.850	-1.24E+07	5852.3	4.862E+05	5.47E+01	8.59E-01	1.30E-06	4382.0	1.1E+05	5.4E+04	148.1	120.4
0.945	-1.38E+07	6009.1	5.372E+05	7.27E+01	1.03E+00	1.40E-06	4462.4	1.1E+05	5.4E+04	148.1	120.4
1.045	-1.52E+07	6172.0	5.919E+05	9.89E+01	1.28E+00	1.50E-06	4545.2	1.1E+05	5.4E+04	148.1	120.4

Tab. E.5 Umbra model atmosphere - cool magnetic component of dark umbra region (du). Note that the sunspot was observed at  $\mu = 0.9$ .

$\log \tau_{5000}$	height [cm]	T [K]	$P_{gas}$ [g cm <sup>-1</sup> s <sup>-2</sup> ]	$P_{electr.}$ [g cm <sup>-1</sup> s <sup>-2</sup> ]	$\kappa$ [g <sup>-1</sup> ]	$\rho$ [cm <sup>-3</sup> ]	B [G]	$\zeta_{\mu}$ [cm s <sup>-1</sup> ]	$v_{LOS}$ [cm s <sup>-1</sup> ]	$\gamma_B$ [deg]	$\chi_B$
-4.000	4.06E+07	3163.9	1.507E+03	1.06E-02	2.96E-03	7.71E-09	2742.1	7.8E+04	5.2E+04	123.0	39.2
-3.900	3.96E+07	3187.8	1.735E+03	1.24E-02	3.28E-03	8.80E-09	2724.6	7.8E+04	5.2E+04	123.0	39.2
-3.800	3.86E+07	3213.9	1.994E+03	1.46E-02	3.65E-03	1.00E-08	2707.2	7.8E+04	5.2E+04	123.0	39.2
-3.700	3.76E+07	3241.3	2.286E+03	1.71E-02	4.07E-03	1.14E-08	2689.9	7.8E+04	5.2E+04	123.0	39.2
-3.600	3.66E+07	3269.4	2.615E+03	2.01E-02	4.53E-03	1.29E-08	2672.6	7.8E+04	5.2E+04	123.0	39.2
-3.500	3.56E+07	3297.9	2.988E+03	2.37E-02	5.06E-03	1.46E-08	2655.5	7.8E+04	5.2E+04	123.0	39.2
-3.400	3.46E+07	3326.3	3.407E+03	2.78E-02	5.65E-03	1.64E-08	2638.3	7.8E+04	5.2E+04	123.0	39.2
-3.300	3.36E+07	3354.1	3.880E+03	3.27E-02	6.31E-03	1.86E-08	2621.2	7.8E+04	5.2E+04	123.0	39.2
-3.200	3.26E+07	3380.8	4.414E+03	3.82E-02	7.04E-03	2.09E-08	2604.1	7.8E+04	5.2E+04	123.0	39.2
-3.100	3.16E+07	3405.8	5.016E+03	4.46E-02	7.85E-03	2.36E-08	2587.0	7.8E+04	5.2E+04	123.0	39.2
-3.000	3.06E+07	3428.0	5.698E+03	5.16E-02	8.72E-03	2.67E-08	2569.9	7.8E+04	5.2E+04	123.0	39.2
-2.900	2.96E+07	3446.4	6.473E+03	5.91E-02	9.65E-03	3.01E-08	2552.6	7.8E+04	5.2E+04	123.0	39.2
-2.800	2.86E+07	3462.0	7.355E+03	6.71E-02	1.06E-02	3.41E-08	2535.3	7.8E+04	5.2E+04	123.0	39.2
-2.700	2.76E+07	3475.7	8.363E+03	7.58E-02	1.17E-02	3.87E-08	2517.8	7.8E+04	5.2E+04	123.0	39.2
-2.600	2.66E+07	3488.0	9.517E+03	8.54E-02	1.29E-02	4.39E-08	2500.2	7.8E+04	5.2E+04	123.0	39.2
-2.500	2.56E+07	3499.4	1.084E+04	9.60E-02	1.42E-02	4.99E-08	2482.4	7.8E+04	5.2E+04	123.0	39.2
-2.400	2.45E+07	3509.9	1.235E+04	1.08E-01	1.56E-02	5.68E-08	2464.5	7.8E+04	5.2E+04	123.0	39.2
-2.300	2.35E+07	3519.5	1.408E+04	1.21E-01	1.71E-02	6.48E-08	2446.5	7.8E+04	5.2E+04	123.0	39.2
-2.200	2.24E+07	3528.3	1.607E+04	1.35E-01	1.87E-02	7.39E-08	2428.4	7.8E+04	5.2E+04	123.0	39.2
-2.100	2.14E+07	3535.9	1.836E+04	1.51E-01	2.05E-02	8.44E-08	2410.2	7.8E+04	5.2E+04	123.0	39.2
-2.000	2.03E+07	3541.9	2.098E+04	1.68E-01	2.25E-02	9.66E-08	2391.9	7.8E+04	5.2E+04	123.0	39.2
-1.900	1.92E+07	3545.8	2.400E+04	1.86E-01	2.45E-02	1.11E-07	2373.4	7.8E+04	5.2E+04	123.0	39.2
-1.800	1.82E+07	3548.3	2.749E+04	2.06E-01	2.67E-02	1.27E-07	2355.0	7.8E+04	5.2E+04	123.0	39.2
-1.700	1.71E+07	3550.3	3.151E+04	2.29E-01	2.92E-02	1.47E-07	2336.4	7.8E+04	5.2E+04	123.0	39.2
-1.600	1.60E+07	3552.6	3.616E+04	2.54E-01	3.18E-02	1.69E-07	2317.8	7.8E+04	5.2E+04	123.0	39.2
-1.500	1.49E+07	3556.0	4.152E+04	2.83E-01	3.47E-02	1.95E-07	2299.2	7.8E+04	5.2E+04	123.0	39.2
-1.400	1.39E+07	3561.5	4.769E+04	3.16E-01	3.80E-02	2.25E-07	2280.7	7.8E+04	5.2E+04	123.0	39.2
-1.300	1.28E+07	3570.4	5.478E+04	3.57E-01	4.18E-02	2.60E-07	2262.2	7.8E+04	5.2E+04	123.0	39.2
-1.200	1.17E+07	3584.7	6.288E+04	4.07E-01	4.61E-02	2.98E-07	2243.9	7.8E+04	5.2E+04	123.0	39.2
-1.100	1.07E+07	3607.3	7.207E+04	4.70E-01	5.14E-02	3.41E-07	2225.7	7.8E+04	5.2E+04	123.0	39.2
-1.000	9.63E+06	3642.7	8.238E+04	5.57E-01	5.81E-02	3.85E-07	2207.7	7.8E+04	5.2E+04	123.0	39.2
-0.900	8.60E+06	3694.8	9.376E+04	6.79E-01	6.68E-02	4.31E-07	2190.1	7.8E+04	5.2E+04	123.0	39.2
-0.800	7.60E+06	3759.6	1.061E+05	8.46E-01	7.78E-02	4.75E-07	2172.9	7.8E+04	5.2E+04	123.0	39.2
-0.700	6.62E+06	3832.7	1.195E+05	1.07E+00	9.14E-02	5.20E-07	2155.9	7.8E+04	5.2E+04	123.0	39.2
-0.600	5.65E+06	3911.1	1.337E+05	1.37E+00	1.08E-01	5.66E-07	2139.4	7.8E+04	5.2E+04	123.0	39.2
-0.500	4.71E+06	3992.7	1.490E+05	1.75E+00	1.27E-01	6.15E-07	2123.1	7.8E+04	5.2E+04	123.0	39.2
-0.400	3.77E+06	4076.1	1.653E+05	2.24E+00	1.49E-01	6.64E-07	2107.0	7.8E+04	5.2E+04	123.0	39.2
-0.300	2.84E+06	4160.2	1.829E+05	2.85E+00	1.74E-01	7.16E-07	2091.0	7.8E+04	5.2E+04	123.0	39.2
-0.200	1.90E+06	4243.9	2.019E+05	3.60E+00	2.03E-01	7.72E-07	2075.0	7.8E+04	5.2E+04	123.0	39.2
-0.100	9.60E+05	4326.1	2.225E+05	4.50E+00	2.34E-01	8.32E-07	2058.8	7.8E+04	5.2E+04	123.0	39.2
0.000	0.00E+00	4405.4	2.452E+05	5.55E+00	2.67E-01	8.97E-07	2042.2	7.8E+04	5.2E+04	123.0	39.2
0.098	-9.60E+05	4492.0	2.696E+05	6.86E+00	3.04E-01	9.59E-07	2025.7	7.8E+04	5.2E+04	123.0	39.2
0.193	-1.92E+06	4585.4	2.957E+05	8.52E+00	3.47E-01	1.03E-06	2009.2	7.8E+04	5.2E+04	123.0	39.2
0.287	-2.88E+06	4684.8	3.237E+05	1.06E+01	3.95E-01	1.10E-06	1992.7	7.8E+04	5.2E+04	123.0	39.2
0.378	-3.84E+06	4789.8	3.535E+05	1.30E+01	4.46E-01	1.17E-06	1976.2	7.8E+04	5.2E+04	123.0	39.2
0.468	-4.80E+06	4899.8	3.853E+05	1.60E+01	5.01E-01	1.25E-06	1959.7	7.8E+04	5.2E+04	123.0	39.2
0.554	-5.76E+06	5014.3	4.190E+05	1.96E+01	5.60E-01	1.32E-06	1943.2	7.8E+04	5.2E+04	123.0	39.2
0.638	-6.72E+06	5133.0	4.547E+05	2.38E+01	6.21E-01	1.40E-06	1926.7	7.8E+04	5.2E+04	123.0	39.2
0.720	-7.68E+06	5255.5	4.924E+05	2.87E+01	6.85E-01	1.47E-06	1910.6	7.8E+04	5.2E+04	123.0	39.2
0.798	-8.64E+06	5381.3	5.323E+05	3.47E+01	7.54E-01	1.55E-06	1895.1	7.8E+04	5.2E+04	123.0	39.2
0.874	-9.60E+06	5510.3	5.742E+05	4.20E+01	8.31E-01	1.64E-06	1879.6	7.8E+04	5.2E+04	123.0	39.2
0.949	-1.06E+07	5642.1	6.184E+05	5.12E+01	9.22E-01	1.72E-06	1864.1	7.8E+04	5.2E+04	123.0	39.2

Tab. E.6 Umbra model atmosphere - warm magnetic component of dark umbra region (du). Note that the sunspot was observed at  $\mu = 0.9$ .

$\log \tau_{5000}$	height [cm]	T [K]	$P_{gas}$ [g cm <sup>-1</sup> s <sup>-2</sup> ]	$P_{electr.}$ [g <sup>-1</sup> s <sup>-2</sup> ]	$\kappa$ [g <sup>-1</sup> ]	$\rho$ [cm <sup>-3</sup> ]	B [G]	$\zeta_{\mu}$ [cm s <sup>-1</sup> ]	$v_{LOS}$ [cm s <sup>-1</sup> ]	$\gamma_B$ [deg]	$\chi_B$
-4.000	5.13E+07	3931.0	9.656E+02	5.06E-02	4.79E-03	3.88E-09	2653.5	1.3E+05	3.5E+04	135.5	122.0
-3.900	5.00E+07	3947.3	1.106E+03	5.76E-02	5.30E-03	4.42E-09	2666.5	1.3E+05	3.5E+04	135.5	122.0
-3.800	4.88E+07	3963.6	1.266E+03	6.55E-02	5.86E-03	5.04E-09	2679.9	1.3E+05	3.5E+04	135.5	122.0
-3.700	4.75E+07	3980.0	1.448E+03	7.44E-02	6.49E-03	5.74E-09	2693.3	1.3E+05	3.5E+04	135.5	122.0
-3.600	4.63E+07	3996.4	1.656E+03	8.44E-02	7.18E-03	6.54E-09	2706.7	1.3E+05	3.5E+04	135.5	122.0
-3.500	4.51E+07	4012.7	1.891E+03	9.58E-02	7.94E-03	7.44E-09	2719.8	1.3E+05	3.5E+04	135.5	122.0
-3.400	4.38E+07	4029.0	2.160E+03	1.09E-01	8.78E-03	8.46E-09	2732.6	1.3E+05	3.5E+04	135.5	122.0
-3.300	4.26E+07	4045.1	2.465E+03	1.23E-01	9.71E-03	9.61E-09	2744.6	1.3E+05	3.5E+04	135.5	122.0
-3.200	4.14E+07	4060.9	2.813E+03	1.39E-01	1.07E-02	1.09E-08	2755.5	1.3E+05	3.5E+04	135.5	122.0
-3.100	4.01E+07	4076.4	3.209E+03	1.57E-01	1.19E-02	1.24E-08	2764.7	1.3E+05	3.5E+04	135.5	122.0
-3.000	3.89E+07	4091.4	3.660E+03	1.77E-01	1.31E-02	1.41E-08	2771.2	1.3E+05	3.5E+04	135.5	122.0
-2.900	3.76E+07	4105.6	4.173E+03	2.00E-01	1.45E-02	1.60E-08	2774.3	1.3E+05	3.5E+04	135.5	122.0
-2.800	3.64E+07	4119.3	4.758E+03	2.25E-01	1.60E-02	1.82E-08	2774.5	1.3E+05	3.5E+04	135.5	122.0
-2.700	3.51E+07	4132.5	5.425E+03	2.53E-01	1.77E-02	2.07E-08	2772.6	1.3E+05	3.5E+04	135.5	122.0
-2.600	3.39E+07	4145.4	6.186E+03	2.84E-01	1.95E-02	2.35E-08	2768.9	1.3E+05	3.5E+04	135.5	122.0
-2.500	3.26E+07	4158.0	7.053E+03	3.19E-01	2.16E-02	2.68E-08	2763.4	1.3E+05	3.5E+04	135.5	122.0
-2.400	3.13E+07	4170.3	8.042E+03	3.58E-01	2.38E-02	3.04E-08	2755.8	1.3E+05	3.5E+04	135.5	122.0
-2.300	3.01E+07	4182.2	9.170E+03	4.01E-01	2.63E-02	3.46E-08	2745.3	1.3E+05	3.5E+04	135.5	122.0
-2.200	2.88E+07	4193.5	1.046E+04	4.49E-01	2.90E-02	3.94E-08	2730.7	1.3E+05	3.5E+04	135.5	122.0
-2.100	2.75E+07	4204.1	1.193E+04	5.02E-01	3.20E-02	4.48E-08	2710.2	1.3E+05	3.5E+04	135.5	122.0
-2.000	2.62E+07	4213.5	1.361E+04	5.60E-01	3.52E-02	5.10E-08	2680.8	1.3E+05	3.5E+04	135.5	122.0
-1.900	2.49E+07	4221.3	1.553E+04	6.22E-01	3.87E-02	5.81E-08	2640.0	1.3E+05	3.5E+04	135.5	122.0
-1.800	2.36E+07	4228.1	1.772E+04	6.91E-01	4.26E-02	6.62E-08	2591.2	1.3E+05	3.5E+04	135.5	122.0
-1.700	2.23E+07	4234.5	2.024E+04	7.66E-01	4.68E-02	7.55E-08	2538.6	1.3E+05	3.5E+04	135.5	122.0
-1.600	2.10E+07	4240.8	2.312E+04	8.49E-01	5.15E-02	8.62E-08	2485.6	1.3E+05	3.5E+04	135.5	122.0
-1.500	1.97E+07	4247.5	2.642E+04	9.42E-01	5.66E-02	9.84E-08	2435.5	1.3E+05	3.5E+04	135.5	122.0
-1.400	1.84E+07	4255.3	3.020E+04	1.05E+00	6.22E-02	1.12E-07	2392.3	1.3E+05	3.5E+04	135.5	122.0
-1.300	1.71E+07	4264.7	3.452E+04	1.17E+00	6.85E-02	1.28E-07	2361.0	1.3E+05	3.5E+04	135.5	122.0
-1.200	1.58E+07	4276.8	3.946E+04	1.30E+00	7.56E-02	1.46E-07	2348.9	1.3E+05	3.5E+04	135.5	122.0
-1.100	1.44E+07	4293.2	4.510E+04	1.47E+00	8.36E-02	1.66E-07	2366.5	1.3E+05	3.5E+04	135.5	122.0
-1.000	1.31E+07	4315.9	5.149E+04	1.67E+00	9.28E-02	1.89E-07	2429.5	1.3E+05	3.5E+04	135.5	122.0
-0.900	1.18E+07	4347.1	5.872E+04	1.93E+00	1.04E-01	2.14E-07	2552.2	1.3E+05	3.5E+04	135.5	122.0
-0.800	1.05E+07	4384.7	6.685E+04	2.25E+00	1.16E-01	2.42E-07	2720.4	1.3E+05	3.5E+04	135.5	122.0
-0.700	9.21E+06	4426.5	7.599E+04	2.64E+00	1.30E-01	2.72E-07	2918.1	1.3E+05	3.5E+04	135.5	122.0
-0.600	7.91E+06	4471.0	8.624E+04	3.09E+00	1.46E-01	3.06E-07	3134.8	1.3E+05	3.5E+04	135.5	122.0
-0.500	6.61E+06	4517.2	9.776E+04	3.62E+00	1.64E-01	3.43E-07	3363.1	1.3E+05	3.5E+04	135.5	122.0
-0.400	5.31E+06	4564.2	1.107E+05	4.25E+00	1.83E-01	3.85E-07	3597.9	1.3E+05	3.5E+04	135.5	122.0
-0.300	3.99E+06	4611.6	1.253E+05	4.97E+00	2.04E-01	4.31E-07	3835.0	1.3E+05	3.5E+04	135.5	122.0
-0.200	2.68E+06	4658.7	1.418E+05	5.79E+00	2.28E-01	4.83E-07	4070.6	1.3E+05	3.5E+04	135.5	122.0
-0.100	1.34E+06	4705.1	1.604E+05	6.74E+00	2.54E-01	5.41E-07	4300.8	1.3E+05	3.5E+04	135.5	122.0
0.000	0.00E+00	4750.1	1.814E+05	7.82E+00	2.82E-01	6.06E-07	4520.8	1.3E+05	3.5E+04	135.5	122.0
0.099	-1.34E+06	4810.6	2.048E+05	9.18E+00	3.14E-01	6.71E-07	4742.4	1.3E+05	3.5E+04	135.5	122.0
0.196	-2.69E+06	4885.4	2.309E+05	1.10E+01	3.53E-01	7.44E-07	4960.6	1.3E+05	3.5E+04	135.5	122.0
0.293	-4.03E+06	4973.2	2.596E+05	1.33E+01	3.96E-01	8.21E-07	5176.8	1.3E+05	3.5E+04	135.5	122.0
0.389	-5.38E+06	5072.9	2.913E+05	1.61E+01	4.45E-01	9.01E-07	5390.5	1.3E+05	3.5E+04	135.5	122.0
0.483	-6.72E+06	5183.5	3.260E+05	1.97E+01	4.98E-01	9.86E-07	5601.1	1.3E+05	3.5E+04	135.5	122.0
0.576	-8.06E+06	5304.0	3.639E+05	2.41E+01	5.56E-01	1.08E-06	5808.2	1.3E+05	3.5E+04	135.5	122.0
0.668	-9.41E+06	5433.5	4.052E+05	2.97E+01	6.23E-01	1.17E-06	6011.9	1.3E+05	3.5E+04	135.5	122.0
0.759	-1.08E+07	5571.4	4.499E+05	3.70E+01	7.03E-01	1.27E-06	6212.8	1.3E+05	3.5E+04	135.5	122.0
0.849	-1.21E+07	5716.8	4.983E+05	4.68E+01	8.06E-01	1.37E-06	6412.9	1.3E+05	3.5E+04	135.5	122.0
0.941	-1.34E+07	5869.2	5.505E+05	6.06E+01	9.44E-01	1.47E-06	6614.9	1.3E+05	3.5E+04	135.5	122.0
1.035	-1.48E+07	6027.7	6.066E+05	8.03E+01	1.13E+00	1.58E-06	6822.0	1.3E+05	3.5E+04	135.5	122.0

Tab. E.7 Umbra model atmosphere - cool magnetic component of intermediate umbra region (iu). Note that the sunspot was observed at  $\mu = 0.9$ .

log $\tau_{5000}$	height [cm]	T [K]	$P_{gas}$ [g cm <sup>-1</sup> s <sup>-2</sup> ]	$P_{electr.}$ [g cm <sup>-1</sup> s <sup>-2</sup> ]	$\kappa$ [g <sup>-1</sup> ]	$\rho$ [cm <sup>-3</sup> ]	B [G]	$\zeta_{\mu}$ [cm s <sup>-1</sup> ]	$v_{LOS}$ [cm s <sup>-1</sup> ]	$\gamma_B$ [deg]	$\chi_B$
-4.000	4.10E+07	3149.2	1.514E+03	1.06E-02	2.95E-03	7.83E-09	2577.5	7.1E+04	3.8E+04	110.2	26.6
-3.900	4.00E+07	3176.9	1.743E+03	1.24E-02	3.28E-03	8.92E-09	2558.5	7.1E+04	3.8E+04	110.2	26.6
-3.800	3.90E+07	3207.9	2.001E+03	1.47E-02	3.66E-03	1.01E-08	2539.7	7.1E+04	3.8E+04	110.2	26.6
-3.700	3.80E+07	3241.2	2.293E+03	1.74E-02	4.09E-03	1.14E-08	2521.0	7.1E+04	3.8E+04	110.2	26.6
-3.600	3.70E+07	3275.6	2.620E+03	2.07E-02	4.58E-03	1.29E-08	2502.4	7.1E+04	3.8E+04	110.2	26.6
-3.500	3.60E+07	3310.7	2.988E+03	2.47E-02	5.14E-03	1.45E-08	2483.9	7.1E+04	3.8E+04	110.2	26.6
-3.400	3.50E+07	3345.7	3.400E+03	2.95E-02	5.78E-03	1.63E-08	2465.4	7.1E+04	3.8E+04	110.2	26.6
-3.300	3.40E+07	3380.1	3.861E+03	3.53E-02	6.51E-03	1.83E-08	2447.0	7.1E+04	3.8E+04	110.2	26.6
-3.200	3.31E+07	3413.3	4.378E+03	4.21E-02	7.32E-03	2.06E-08	2428.6	7.1E+04	3.8E+04	110.2	26.6
-3.100	3.21E+07	3444.2	4.959E+03	4.99E-02	8.21E-03	2.31E-08	2410.1	7.1E+04	3.8E+04	110.2	26.6
-3.000	3.11E+07	3471.6	5.614E+03	5.85E-02	9.17E-03	2.59E-08	2391.7	7.1E+04	3.8E+04	110.2	26.6
-2.900	3.01E+07	3494.2	6.355E+03	6.76E-02	1.02E-02	2.92E-08	2373.1	7.1E+04	3.8E+04	110.2	26.6
-2.800	2.91E+07	3513.2	7.198E+03	7.72E-02	1.12E-02	3.29E-08	2354.5	7.1E+04	3.8E+04	110.2	26.6
-2.700	2.81E+07	3529.8	8.159E+03	8.76E-02	1.24E-02	3.72E-08	2335.6	7.1E+04	3.8E+04	110.2	26.6
-2.600	2.71E+07	3544.7	9.256E+03	9.89E-02	1.36E-02	4.20E-08	2316.7	7.1E+04	3.8E+04	110.2	26.6
-2.500	2.61E+07	3558.2	1.051E+04	1.11E-01	1.50E-02	4.76E-08	2297.6	7.1E+04	3.8E+04	110.2	26.6
-2.400	2.50E+07	3570.8	1.195E+04	1.25E-01	1.65E-02	5.40E-08	2278.3	7.1E+04	3.8E+04	110.2	26.6
-2.300	2.40E+07	3582.3	1.360E+04	1.40E-01	1.81E-02	6.14E-08	2258.9	7.1E+04	3.8E+04	110.2	26.6
-2.200	2.29E+07	3592.6	1.548E+04	1.57E-01	1.99E-02	6.98E-08	2239.4	7.1E+04	3.8E+04	110.2	26.6
-2.100	2.19E+07	3601.4	1.765E+04	1.76E-01	2.18E-02	7.96E-08	2219.7	7.1E+04	3.8E+04	110.2	26.6
-2.000	2.08E+07	3608.1	2.014E+04	1.95E-01	2.38E-02	9.09E-08	2199.9	7.1E+04	3.8E+04	110.2	26.6
-1.900	1.97E+07	3612.1	2.301E+04	2.16E-01	2.60E-02	1.04E-07	2180.0	7.1E+04	3.8E+04	110.2	26.6
-1.800	1.86E+07	3614.4	2.633E+04	2.38E-01	2.83E-02	1.19E-07	2159.8	7.1E+04	3.8E+04	110.2	26.6
-1.700	1.75E+07	3615.9	3.017E+04	2.62E-01	3.08E-02	1.37E-07	2139.6	7.1E+04	3.8E+04	110.2	26.6
-1.600	1.64E+07	3617.5	3.460E+04	2.90E-01	3.36E-02	1.58E-07	2119.2	7.1E+04	3.8E+04	110.2	26.6
-1.500	1.53E+07	3620.2	3.972E+04	3.21E-01	3.66E-02	1.82E-07	2098.8	7.1E+04	3.8E+04	110.2	26.6
-1.400	1.42E+07	3625.2	4.562E+04	3.58E-01	4.00E-02	2.10E-07	2078.4	7.1E+04	3.8E+04	110.2	26.6
-1.300	1.31E+07	3633.8	5.239E+04	4.02E-01	4.40E-02	2.42E-07	2058.1	7.1E+04	3.8E+04	110.2	26.6
-1.200	1.20E+07	3648.4	6.013E+04	4.57E-01	4.86E-02	2.78E-07	2037.9	7.1E+04	3.8E+04	110.2	26.6
-1.100	1.09E+07	3672.0	6.891E+04	5.29E-01	5.42E-02	3.18E-07	2017.9	7.1E+04	3.8E+04	110.2	26.6
-1.000	9.83E+06	3709.5	7.873E+04	6.29E-01	6.15E-02	3.59E-07	1998.2	7.1E+04	3.8E+04	110.2	26.6
-0.900	8.78E+06	3765.3	8.952E+04	7.72E-01	7.10E-02	4.00E-07	1978.9	7.1E+04	3.8E+04	110.2	26.6
-0.800	7.76E+06	3834.8	1.012E+05	9.71E-01	8.31E-02	4.39E-07	1960.1	7.1E+04	3.8E+04	110.2	26.6
-0.700	6.75E+06	3913.5	1.137E+05	1.24E+00	9.80E-02	4.80E-07	1941.7	7.1E+04	3.8E+04	110.2	26.6
-0.600	5.77E+06	3997.8	1.270E+05	1.60E+00	1.16E-01	5.21E-07	1923.7	7.1E+04	3.8E+04	110.2	26.6
-0.500	4.81E+06	4085.8	1.412E+05	2.07E+00	1.37E-01	5.66E-07	1906.2	7.1E+04	3.8E+04	110.2	26.6
-0.400	3.86E+06	4175.7	1.564E+05	2.66E+00	1.61E-01	6.10E-07	1888.9	7.1E+04	3.8E+04	110.2	26.6
-0.300	2.91E+06	4266.3	1.727E+05	3.40E+00	1.88E-01	6.56E-07	1871.7	7.1E+04	3.8E+04	110.2	26.6
-0.200	1.96E+06	4356.5	1.903E+05	4.30E+00	2.18E-01	7.05E-07	1854.3	7.1E+04	3.8E+04	110.2	26.6
-0.100	9.90E+05	4445.0	2.095E+05	5.37E+00	2.51E-01	7.58E-07	1836.6	7.1E+04	3.8E+04	110.2	26.6
0.000	0.00E+00	4530.4	2.307E+05	6.62E+00	2.85E-01	8.17E-07	1818.5	7.1E+04	3.8E+04	110.2	26.6
0.097	-9.90E+05	4622.9	2.535E+05	8.14E+00	3.22E-01	8.72E-07	1800.5	7.1E+04	3.8E+04	110.2	26.6
0.191	-1.98E+06	4722.1	2.778E+05	1.00E+01	3.65E-01	9.35E-07	1782.4	7.1E+04	3.8E+04	110.2	26.6
0.283	-2.97E+06	4827.1	3.039E+05	1.23E+01	4.10E-01	9.98E-07	1764.3	7.1E+04	3.8E+04	110.2	26.6
0.372	-3.96E+06	4937.6	3.317E+05	1.51E+01	4.59E-01	1.06E-06	1746.3	7.1E+04	3.8E+04	110.2	26.6
0.459	-4.95E+06	5053.0	3.613E+05	1.84E+01	5.10E-01	1.13E-06	1728.2	7.1E+04	3.8E+04	110.2	26.6
0.543	-5.94E+06	5172.8	3.926E+05	2.23E+01	5.64E-01	1.20E-06	1710.1	7.1E+04	3.8E+04	110.2	26.6
0.624	-6.93E+06	5296.8	4.259E+05	2.69E+01	6.21E-01	1.27E-06	1692.1	7.1E+04	3.8E+04	110.2	26.6
0.702	-7.92E+06	5424.4	4.610E+05	3.26E+01	6.86E-01	1.34E-06	1674.0	7.1E+04	3.8E+04	110.2	26.6
0.779	-8.91E+06	5555.4	4.981E+05	3.98E+01	7.60E-01	1.41E-06	1655.9	7.1E+04	3.8E+04	110.2	26.6
0.855	-9.90E+06	5689.5	5.372E+05	4.90E+01	8.53E-01	1.48E-06	1637.9	7.1E+04	3.8E+04	110.2	26.6
0.930	-1.09E+07	5826.3	5.784E+05	6.12E+01	9.71E-01	1.56E-06	1619.8	7.1E+04	3.8E+04	110.2	26.6

Tab. E.8 Umbra model atmosphere - warm magnetic component of intermediate umbra region (iu). Note that the sunspot was observed at  $\mu = 0.9$ .

$\log \tau_{5000}$	height [cm]	T [K]	$P_{gas}$ [g cm <sup>-1</sup> s <sup>-2</sup> ]	$P_{electr.}$ [g <sup>-1</sup> ]	$\kappa$ [g <sup>-1</sup> ]	$\rho$ [cm <sup>-3</sup> ]	B [G]	$\zeta_{\mu}$ [cm s <sup>-1</sup> ]	$v_{LOS}$ [cm s <sup>-1</sup> ]	$\gamma_B$ [deg]	$\chi_B$
-4.000	5.13E+07	3880.9	1.004E+03	4.76E-02	4.74E-03	4.11E-09	2464.6	1.3E+05	4.3E+04	130.8	109.5
-3.900	5.01E+07	3905.1	1.147E+03	5.48E-02	5.26E-03	4.66E-09	2475.0	1.3E+05	4.3E+04	130.8	109.5
-3.800	4.89E+07	3929.6	1.308E+03	6.31E-02	5.84E-03	5.27E-09	2485.6	1.3E+05	4.3E+04	130.8	109.5
-3.700	4.77E+07	3954.4	1.491E+03	7.25E-02	6.48E-03	5.97E-09	2496.3	1.3E+05	4.3E+04	130.8	109.5
-3.600	4.65E+07	3979.3	1.698E+03	8.33E-02	7.20E-03	6.75E-09	2506.9	1.3E+05	4.3E+04	130.8	109.5
-3.500	4.53E+07	4004.1	1.933E+03	9.56E-02	7.99E-03	7.63E-09	2517.4	1.3E+05	4.3E+04	130.8	109.5
-3.400	4.41E+07	4028.8	2.200E+03	1.10E-01	8.86E-03	8.62E-09	2527.6	1.3E+05	4.3E+04	130.8	109.5
-3.300	4.28E+07	4053.1	2.502E+03	1.26E-01	9.82E-03	9.75E-09	2537.2	1.3E+05	4.3E+04	130.8	109.5
-3.200	4.16E+07	4076.9	2.846E+03	1.44E-01	1.09E-02	1.10E-08	2545.9	1.3E+05	4.3E+04	130.8	109.5
-3.100	4.04E+07	4099.8	3.237E+03	1.64E-01	1.20E-02	1.25E-08	2553.3	1.3E+05	4.3E+04	130.8	109.5
-3.000	3.92E+07	4121.3	3.682E+03	1.87E-01	1.33E-02	1.41E-08	2558.7	1.3E+05	4.3E+04	130.8	109.5
-2.900	3.79E+07	4141.1	4.188E+03	2.12E-01	1.47E-02	1.60E-08	2561.4	1.3E+05	4.3E+04	130.8	109.5
-2.800	3.67E+07	4159.4	4.764E+03	2.40E-01	1.63E-02	1.81E-08	2562.0	1.3E+05	4.3E+04	130.8	109.5
-2.700	3.55E+07	4176.8	5.420E+03	2.71E-01	1.80E-02	2.05E-08	2560.8	1.3E+05	4.3E+04	130.8	109.5
-2.600	3.42E+07	4193.4	6.167E+03	3.05E-01	1.99E-02	2.32E-08	2558.2	1.3E+05	4.3E+04	130.8	109.5
-2.500	3.29E+07	4209.4	7.017E+03	3.44E-01	2.20E-02	2.63E-08	2554.2	1.3E+05	4.3E+04	130.8	109.5
-2.400	3.17E+07	4224.7	7.986E+03	3.88E-01	2.43E-02	2.98E-08	2548.4	1.3E+05	4.3E+04	130.8	109.5
-2.300	3.04E+07	4239.4	9.090E+03	4.36E-01	2.69E-02	3.38E-08	2540.3	1.3E+05	4.3E+04	130.8	109.5
-2.200	2.91E+07	4253.1	1.035E+04	4.90E-01	2.97E-02	3.84E-08	2528.9	1.3E+05	4.3E+04	130.8	109.5
-2.100	2.78E+07	4265.5	1.178E+04	5.48E-01	3.27E-02	4.36E-08	2512.5	1.3E+05	4.3E+04	130.8	109.5
-2.000	2.66E+07	4275.9	1.342E+04	6.13E-01	3.61E-02	4.96E-08	2488.8	1.3E+05	4.3E+04	130.8	109.5
-1.900	2.53E+07	4283.8	1.530E+04	6.81E-01	3.97E-02	5.64E-08	2455.5	1.3E+05	4.3E+04	130.8	109.5
-1.800	2.40E+07	4289.9	1.744E+04	7.56E-01	4.37E-02	6.42E-08	2415.7	1.3E+05	4.3E+04	130.8	109.5
-1.700	2.27E+07	4295.1	1.989E+04	8.37E-01	4.80E-02	7.32E-08	2372.5	1.3E+05	4.3E+04	130.8	109.5
-1.600	2.13E+07	4300.3	2.270E+04	9.27E-01	5.28E-02	8.34E-08	2328.7	1.3E+05	4.3E+04	130.8	109.5
-1.500	2.00E+07	4305.9	2.592E+04	1.03E+00	5.80E-02	9.52E-08	2286.9	1.3E+05	4.3E+04	130.8	109.5
-1.400	1.87E+07	4313.0	2.961E+04	1.14E+00	6.38E-02	1.09E-07	2250.0	1.3E+05	4.3E+04	130.8	109.5
-1.300	1.74E+07	4322.4	3.382E+04	1.27E+00	7.03E-02	1.24E-07	2222.1	1.3E+05	4.3E+04	130.8	109.5
-1.200	1.60E+07	4335.8	3.863E+04	1.42E+00	7.76E-02	1.41E-07	2208.3	1.3E+05	4.3E+04	130.8	109.5
-1.100	1.47E+07	4355.2	4.411E+04	1.61E+00	8.60E-02	1.60E-07	2216.8	1.3E+05	4.3E+04	130.8	109.5
-1.000	1.34E+07	4383.8	5.031E+04	1.85E+00	9.59E-02	1.82E-07	2259.2	1.3E+05	4.3E+04	130.8	109.5
-0.900	1.21E+07	4424.6	5.729E+04	2.16E+00	1.07E-01	2.05E-07	2346.1	1.3E+05	4.3E+04	130.8	109.5
-0.800	1.07E+07	4474.6	6.512E+04	2.56E+00	1.21E-01	2.31E-07	2467.1	1.3E+05	4.3E+04	130.8	109.5
-0.700	9.43E+06	4530.6	7.387E+04	3.04E+00	1.36E-01	2.58E-07	2610.2	1.3E+05	4.3E+04	130.8	109.5
-0.600	8.11E+06	4590.5	8.367E+04	3.62E+00	1.53E-01	2.89E-07	2767.4	1.3E+05	4.3E+04	130.8	109.5
-0.500	6.80E+06	4652.8	9.466E+04	4.31E+00	1.72E-01	3.22E-07	2933.3	1.3E+05	4.3E+04	130.8	109.5
-0.400	5.47E+06	4716.3	1.070E+05	5.12E+00	1.92E-01	3.59E-07	3104.1	1.3E+05	4.3E+04	130.8	109.5
-0.300	4.13E+06	4780.4	1.209E+05	6.06E+00	2.15E-01	4.00E-07	3276.5	1.3E+05	4.3E+04	130.8	109.5
-0.200	2.77E+06	4844.1	1.366E+05	7.15E+00	2.39E-01	4.46E-07	3447.9	1.3E+05	4.3E+04	130.8	109.5
-0.100	1.40E+06	4906.8	1.543E+05	8.41E+00	2.66E-01	4.97E-07	3615.2	1.3E+05	4.3E+04	130.8	109.5
0.000	0.00E+00	4967.3	1.743E+05	9.85E+00	2.96E-01	5.55E-07	3774.9	1.3E+05	4.3E+04	130.8	109.5
0.098	-1.40E+06	5042.8	1.966E+05	1.16E+01	3.29E-01	6.12E-07	3935.1	1.3E+05	4.3E+04	130.8	109.5
0.194	-2.79E+06	5131.9	2.212E+05	1.39E+01	3.67E-01	6.76E-07	4092.0	1.3E+05	4.3E+04	130.8	109.5
0.290	-4.19E+06	5233.6	2.482E+05	1.68E+01	4.10E-01	7.44E-07	4246.6	1.3E+05	4.3E+04	130.8	109.5
0.383	-5.58E+06	5346.6	2.780E+05	2.06E+01	4.59E-01	8.15E-07	4398.9	1.3E+05	4.3E+04	130.8	109.5
0.477	-6.98E+06	5470.0	3.105E+05	2.54E+01	5.18E-01	8.90E-07	4549.0	1.3E+05	4.3E+04	130.8	109.5
0.569	-8.37E+06	5602.9	3.460E+05	3.19E+01	5.91E-01	9.68E-07	4697.9	1.3E+05	4.3E+04	130.8	109.5
0.663	-9.77E+06	5744.5	3.845E+05	4.09E+01	6.88E-01	1.05E-06	4846.7	1.3E+05	4.3E+04	130.8	109.5
0.759	-1.12E+07	5894.0	4.261E+05	5.38E+01	8.19E-01	1.13E-06	4997.3	1.3E+05	4.3E+04	130.8	109.5
0.858	-1.26E+07	6050.6	4.711E+05	7.25E+01	9.99E-01	1.22E-06	5152.0	1.3E+05	4.3E+04	130.8	109.5
0.961	-1.40E+07	6213.7	5.194E+05	9.98E+01	1.25E+00	1.31E-06	5312.9	1.3E+05	4.3E+04	130.8	109.5
1.070	-1.53E+07	6382.6	5.712E+05	1.40E+02	1.58E+00	1.40E-06	5481.8	1.3E+05	4.3E+04	130.8	109.5

Tab. E.9 Umbra model atmosphere - cool magnetic component of bright umbra region (bu). Note that the sunspot was observed at  $\mu = 0.9$ .

log $\tau_{5000}$	height [cm]	T [K]	$P_{gas}$ [g cm <sup>-1</sup> s <sup>-2</sup> ]	$P_{electr.}$ [g cm <sup>-1</sup> s <sup>-2</sup> ]	$\kappa$ [g <sup>-1</sup> ]	$\rho$ [cm <sup>-3</sup> ]	B [G]	$\zeta_{\mu}$ [cm s <sup>-1</sup> ]	$v_{LOS}$ [cm s <sup>-1</sup> ]	$\gamma_B$ [deg]	$\chi_B$
-4.000	4.22E+07	3122.9	1.529E+03	1.03E-02	2.93E-03	8.02E-09	2404.7	5.6E+04	2.6E+04	108.8	39.0
-3.900	4.12E+07	3160.8	1.759E+03	1.23E-02	3.27E-03	9.08E-09	2395.2	5.6E+04	2.6E+04	108.8	39.0
-3.800	4.02E+07	3205.3	2.018E+03	1.49E-02	3.68E-03	1.02E-08	2385.7	5.6E+04	2.6E+04	108.8	39.0
-3.700	3.92E+07	3253.9	2.307E+03	1.82E-02	4.16E-03	1.14E-08	2376.3	5.6E+04	2.6E+04	108.8	39.0
-3.600	3.82E+07	3305.0	2.627E+03	2.26E-02	4.73E-03	1.28E-08	2367.0	5.6E+04	2.6E+04	108.8	39.0
-3.500	3.73E+07	3357.3	2.981E+03	2.84E-02	5.43E-03	1.42E-08	2357.7	5.6E+04	2.6E+04	108.8	39.0
-3.400	3.63E+07	3409.8	3.370E+03	3.59E-02	6.24E-03	1.58E-08	2348.4	5.6E+04	2.6E+04	108.8	39.0
-3.300	3.54E+07	3461.5	3.799E+03	4.54E-02	7.19E-03	1.76E-08	2339.1	5.6E+04	2.6E+04	108.8	39.0
-3.200	3.44E+07	3511.2	4.272E+03	5.71E-02	8.23E-03	1.95E-08	2329.9	5.6E+04	2.6E+04	108.8	39.0
-3.100	3.35E+07	3557.4	4.799E+03	7.05E-02	9.36E-03	2.17E-08	2320.6	5.6E+04	2.6E+04	108.8	39.0
-3.000	3.26E+07	3598.0	5.387E+03	8.51E-02	1.05E-02	2.41E-08	2311.4	5.6E+04	2.6E+04	108.8	39.0
-2.900	3.16E+07	3631.2	6.049E+03	1.00E-01	1.17E-02	2.68E-08	2302.2	5.6E+04	2.6E+04	108.8	39.0
-2.800	3.06E+07	3658.6	6.800E+03	1.15E-01	1.30E-02	2.99E-08	2292.9	5.6E+04	2.6E+04	108.8	39.0
-2.700	2.97E+07	3682.2	7.653E+03	1.32E-01	1.44E-02	3.35E-08	2283.6	5.6E+04	2.6E+04	108.8	39.0
-2.600	2.87E+07	3703.0	8.625E+03	1.49E-01	1.58E-02	3.76E-08	2274.3	5.6E+04	2.6E+04	108.8	39.0
-2.500	2.76E+07	3721.9	9.734E+03	1.68E-01	1.74E-02	4.22E-08	2264.9	5.6E+04	2.6E+04	108.8	39.0
-2.400	2.66E+07	3739.2	1.100E+04	1.90E-01	1.92E-02	4.76E-08	2255.4	5.6E+04	2.6E+04	108.8	39.0
-2.300	2.56E+07	3755.0	1.245E+04	2.13E-01	2.11E-02	5.36E-08	2245.9	5.6E+04	2.6E+04	108.8	39.0
-2.200	2.45E+07	3769.1	1.411E+04	2.39E-01	2.31E-02	6.06E-08	2236.4	5.6E+04	2.6E+04	108.8	39.0
-2.100	2.34E+07	3781.2	1.600E+04	2.66E-01	2.54E-02	6.87E-08	2226.8	5.6E+04	2.6E+04	108.8	39.0
-2.000	2.23E+07	3790.3	1.818E+04	2.96E-01	2.78E-02	7.80E-08	2217.1	5.6E+04	2.6E+04	108.8	39.0
-1.900	2.12E+07	3795.8	2.070E+04	3.26E-01	3.03E-02	8.88E-08	2207.3	5.6E+04	2.6E+04	108.8	39.0
-1.800	2.01E+07	3798.8	2.360E+04	3.58E-01	3.30E-02	1.01E-07	2197.5	5.6E+04	2.6E+04	108.8	39.0
-1.700	1.89E+07	3800.5	2.695E+04	3.93E-01	3.59E-02	1.16E-07	2187.5	5.6E+04	2.6E+04	108.8	39.0
-1.600	1.78E+07	3802.0	3.084E+04	4.31E-01	3.91E-02	1.33E-07	2177.4	5.6E+04	2.6E+04	108.8	39.0
-1.500	1.66E+07	3804.5	3.532E+04	4.74E-01	4.26E-02	1.53E-07	2167.4	5.6E+04	2.6E+04	108.8	39.0
-1.400	1.54E+07	3809.0	4.050E+04	5.25E-01	4.66E-02	1.76E-07	2157.3	5.6E+04	2.6E+04	108.8	39.0
-1.300	1.43E+07	3817.1	4.644E+04	5.85E-01	5.11E-02	2.02E-07	2147.2	5.6E+04	2.6E+04	108.8	39.0
-1.200	1.31E+07	3831.0	5.324E+04	6.61E-01	5.64E-02	2.32E-07	2137.2	5.6E+04	2.6E+04	108.8	39.0
-1.100	1.19E+07	3854.0	6.096E+04	7.60E-01	6.29E-02	2.64E-07	2127.3	5.6E+04	2.6E+04	108.8	39.0
-1.000	1.08E+07	3890.9	6.960E+04	8.97E-01	7.11E-02	2.99E-07	2117.6	5.6E+04	2.6E+04	108.8	39.0
-0.900	9.65E+06	3946.0	7.913E+04	1.09E+00	8.18E-02	3.34E-07	2108.1	5.6E+04	2.6E+04	108.8	39.0
-0.800	8.55E+06	4014.9	8.949E+04	1.37E+00	9.50E-02	3.69E-07	2098.8	5.6E+04	2.6E+04	108.8	39.0
-0.700	7.47E+06	4092.8	1.007E+05	1.73E+00	1.11E-01	4.05E-07	2089.8	5.6E+04	2.6E+04	108.8	39.0
-0.600	6.41E+06	4176.5	1.127E+05	2.19E+00	1.30E-01	4.42E-07	2081.0	5.6E+04	2.6E+04	108.8	39.0
-0.500	5.36E+06	4263.8	1.256E+05	2.78E+00	1.51E-01	4.82E-07	2072.5	5.6E+04	2.6E+04	108.8	39.0
-0.400	4.32E+06	4353.0	1.396E+05	3.50E+00	1.75E-01	5.22E-07	2064.1	5.6E+04	2.6E+04	108.8	39.0
-0.300	3.26E+06	4442.9	1.549E+05	4.37E+00	2.01E-01	5.66E-07	2055.6	5.6E+04	2.6E+04	108.8	39.0
-0.200	2.20E+06	4532.4	1.716E+05	5.42E+00	2.29E-01	6.13E-07	2047.0	5.6E+04	2.6E+04	108.8	39.0
-0.100	1.11E+06	4620.2	1.901E+05	6.65E+00	2.60E-01	6.64E-07	2038.2	5.6E+04	2.6E+04	108.8	39.0
0.000	0.00E+00	4704.9	2.107E+05	8.07E+00	2.93E-01	7.22E-07	2029.2	5.6E+04	2.6E+04	108.8	39.0
0.097	-1.11E+06	4798.6	2.331E+05	9.80E+00	3.28E-01	7.76E-07	2020.1	5.6E+04	2.6E+04	108.8	39.0
0.191	-2.23E+06	4900.4	2.571E+05	1.20E+01	3.68E-01	8.37E-07	2011.1	5.6E+04	2.6E+04	108.8	39.0
0.283	-3.34E+06	5009.6	2.831E+05	1.47E+01	4.13E-01	9.00E-07	2002.0	5.6E+04	2.6E+04	108.8	39.0
0.373	-4.45E+06	5125.6	3.110E+05	1.80E+01	4.63E-01	9.65E-07	1993.0	5.6E+04	2.6E+04	108.8	39.0
0.461	-5.57E+06	5247.8	3.409E+05	2.23E+01	5.19E-01	1.03E-06	1984.0	5.6E+04	2.6E+04	108.8	39.0
0.548	-6.68E+06	5375.7	3.729E+05	2.78E+01	5.85E-01	1.10E-06	1974.9	5.6E+04	2.6E+04	108.8	39.0
0.633	-7.79E+06	5508.6	4.070E+05	3.50E+01	6.65E-01	1.17E-06	1965.9	5.6E+04	2.6E+04	108.8	39.0
0.718	-8.91E+06	5646.2	4.432E+05	4.48E+01	7.65E-01	1.24E-06	1956.8	5.6E+04	2.6E+04	108.8	39.0
0.803	-1.00E+07	5788.0	4.817E+05	5.83E+01	8.94E-01	1.32E-06	1947.8	5.6E+04	2.6E+04	108.8	39.0
0.890	-1.11E+07	5933.5	5.225E+05	7.71E+01	1.06E+00	1.39E-06	1938.7	5.6E+04	2.6E+04	108.8	39.0
0.978	-1.22E+07	6082.5	5.656E+05	1.03E+02	1.28E+00	1.47E-06	1929.7	5.6E+04	2.6E+04	108.8	39.0

Tab. E.10 Umbra model atmosphere - warm magnetic component of bright umbra region (bu). Note that the sunspot was observed at  $\mu = 0.9$ .

$\log \tau_{5000}$	height [cm]	T [K]	$P_{gas}$ [g cm <sup>-1</sup> s <sup>-2</sup> ]	$P_{electr.}$ [g <sup>-1</sup> s <sup>-2</sup> ]	$\kappa$ [g <sup>-1</sup> ]	$\rho$ [cm <sup>-3</sup> ]	B [G]	$\zeta_{\mu}$ [cm s <sup>-1</sup> ]	$v_{LOS}$ [cm s <sup>-1</sup> ]	$\gamma_B$ [deg]	$\chi_B$
-4.000	5.20E+07	3822.8	1.040E+03	4.43E-02	4.72E-03	4.32E-09	2240.8	1.4E+05	3.6E+04	126.0	105.5
-3.900	5.08E+07	3860.1	1.183E+03	5.21E-02	5.26E-03	4.87E-09	2244.2	1.4E+05	3.6E+04	126.0	105.5
-3.800	4.97E+07	3898.3	1.344E+03	6.12E-02	5.86E-03	5.47E-09	2247.7	1.4E+05	3.6E+04	126.0	105.5
-3.700	4.85E+07	3936.9	1.527E+03	7.17E-02	6.53E-03	6.14E-09	2251.2	1.4E+05	3.6E+04	126.0	105.5
-3.600	4.73E+07	3975.8	1.732E+03	8.40E-02	7.27E-03	6.89E-09	2254.6	1.4E+05	3.6E+04	126.0	105.5
-3.500	4.62E+07	4014.6	1.965E+03	9.83E-02	8.09E-03	7.73E-09	2258.1	1.4E+05	3.6E+04	126.0	105.5
-3.400	4.50E+07	4053.0	2.227E+03	1.15E-01	8.99E-03	8.68E-09	2261.4	1.4E+05	3.6E+04	126.0	105.5
-3.300	4.38E+07	4090.8	2.525E+03	1.34E-01	9.99E-03	9.75E-09	2264.5	1.4E+05	3.6E+04	126.0	105.5
-3.200	4.26E+07	4127.6	2.863E+03	1.55E-01	1.11E-02	1.10E-08	2267.3	1.4E+05	3.6E+04	126.0	105.5
-3.100	4.14E+07	4162.6	3.246E+03	1.80E-01	1.23E-02	1.23E-08	2269.7	1.4E+05	3.6E+04	126.0	105.5
-3.000	4.02E+07	4195.0	3.682E+03	2.07E-01	1.36E-02	1.39E-08	2271.5	1.4E+05	3.6E+04	126.0	105.5
-2.900	3.89E+07	4223.9	4.177E+03	2.37E-01	1.51E-02	1.56E-08	2272.4	1.4E+05	3.6E+04	126.0	105.5
-2.800	3.77E+07	4250.1	4.741E+03	2.71E-01	1.67E-02	1.76E-08	2272.5	1.4E+05	3.6E+04	126.0	105.5
-2.700	3.64E+07	4274.4	5.381E+03	3.08E-01	1.84E-02	1.99E-08	2272.1	1.4E+05	3.6E+04	126.0	105.5
-2.600	3.52E+07	4297.3	6.110E+03	3.50E-01	2.04E-02	2.24E-08	2271.2	1.4E+05	3.6E+04	126.0	105.5
-2.500	3.39E+07	4319.0	6.939E+03	3.97E-01	2.26E-02	2.53E-08	2269.9	1.4E+05	3.6E+04	126.0	105.5
-2.400	3.26E+07	4339.7	7.882E+03	4.50E-01	2.50E-02	2.87E-08	2268.0	1.4E+05	3.6E+04	126.0	105.5
-2.300	3.13E+07	4359.0	8.955E+03	5.08E-01	2.77E-02	3.24E-08	2265.4	1.4E+05	3.6E+04	126.0	105.5
-2.200	3.00E+07	4376.6	1.018E+04	5.73E-01	3.06E-02	3.67E-08	2261.7	1.4E+05	3.6E+04	126.0	105.5
-2.100	2.87E+07	4391.9	1.157E+04	6.45E-01	3.38E-02	4.16E-08	2256.5	1.4E+05	3.6E+04	126.0	105.5
-2.000	2.74E+07	4403.6	1.315E+04	7.22E-01	3.73E-02	4.71E-08	2248.9	1.4E+05	3.6E+04	126.0	105.5
-1.900	2.61E+07	4411.0	1.496E+04	8.03E-01	4.12E-02	5.35E-08	2238.2	1.4E+05	3.6E+04	126.0	105.5
-1.800	2.48E+07	4415.2	1.702E+04	8.90E-01	4.54E-02	6.09E-08	2225.5	1.4E+05	3.6E+04	126.0	105.5
-1.700	2.35E+07	4417.7	1.939E+04	9.84E-01	4.99E-02	6.93E-08	2211.8	1.4E+05	3.6E+04	126.0	105.5
-1.600	2.21E+07	4419.8	2.209E+04	1.09E+00	5.49E-02	7.89E-08	2197.8	1.4E+05	3.6E+04	126.0	105.5
-1.500	2.08E+07	4422.5	2.518E+04	1.20E+00	6.05E-02	8.99E-08	2184.5	1.4E+05	3.6E+04	126.0	105.5
-1.400	1.94E+07	4427.2	2.871E+04	1.33E+00	6.65E-02	1.02E-07	2172.9	1.4E+05	3.6E+04	126.0	105.5
-1.300	1.81E+07	4435.4	3.275E+04	1.48E+00	7.34E-02	1.17E-07	2164.1	1.4E+05	3.6E+04	126.0	105.5
-1.200	1.67E+07	4449.2	3.736E+04	1.66E+00	8.11E-02	1.33E-07	2159.9	1.4E+05	3.6E+04	126.0	105.5
-1.100	1.54E+07	4472.0	4.260E+04	1.89E+00	8.99E-02	1.51E-07	2163.0	1.4E+05	3.6E+04	126.0	105.5
-1.000	1.40E+07	4508.4	4.852E+04	2.18E+00	1.00E-01	1.70E-07	2177.0	1.4E+05	3.6E+04	126.0	105.5
-0.900	1.27E+07	4562.7	5.519E+04	2.59E+00	1.13E-01	1.91E-07	2205.5	1.4E+05	3.6E+04	126.0	105.5
-0.800	1.13E+07	4630.6	6.266E+04	3.10E+00	1.27E-01	2.14E-07	2245.0	1.4E+05	3.6E+04	126.0	105.5
-0.700	9.97E+06	4707.5	7.101E+04	3.74E+00	1.42E-01	2.39E-07	2291.7	1.4E+05	3.6E+04	126.0	105.5
-0.600	8.61E+06	4790.0	8.039E+04	4.52E+00	1.60E-01	2.65E-07	2343.0	1.4E+05	3.6E+04	126.0	105.5
-0.500	7.23E+06	4876.1	9.094E+04	5.45E+00	1.78E-01	2.95E-07	2397.1	1.4E+05	3.6E+04	126.0	105.5
-0.400	5.82E+06	4964.1	1.028E+05	6.56E+00	1.99E-01	3.27E-07	2452.7	1.4E+05	3.6E+04	126.0	105.5
-0.300	4.40E+06	5052.7	1.162E+05	7.87E+00	2.22E-01	3.63E-07	2508.9	1.4E+05	3.6E+04	126.0	105.5
-0.200	2.95E+06	5141.0	1.314E+05	9.43E+00	2.48E-01	4.03E-07	2564.8	1.4E+05	3.6E+04	126.0	105.5
-0.100	1.49E+06	5227.6	1.484E+05	1.13E+01	2.77E-01	4.48E-07	2619.3	1.4E+05	3.6E+04	126.0	105.5
0.000	0.00E+00	5311.1	1.676E+05	1.35E+01	3.11E-01	4.98E-07	2671.4	1.4E+05	3.6E+04	126.0	105.5
0.099	-1.49E+06	5408.8	1.889E+05	1.64E+01	3.49E-01	5.48E-07	2723.8	1.4E+05	3.6E+04	126.0	105.5
0.197	-2.97E+06	5519.5	2.122E+05	2.03E+01	3.99E-01	6.03E-07	2775.6	1.4E+05	3.6E+04	126.0	105.5
0.295	-4.46E+06	5641.9	2.379E+05	2.58E+01	4.63E-01	6.62E-07	2827.5	1.4E+05	3.6E+04	126.0	105.5
0.396	-5.94E+06	5775.2	2.660E+05	3.35E+01	5.49E-01	7.23E-07	2880.1	1.4E+05	3.6E+04	126.0	105.5
0.499	-7.43E+06	5918.2	2.967E+05	4.47E+01	6.65E-01	7.87E-07	2933.8	1.4E+05	3.6E+04	126.0	105.5
0.606	-8.91E+06	6070.0	3.300E+05	6.11E+01	8.25E-01	8.53E-07	2989.2	1.4E+05	3.6E+04	126.0	105.5
0.718	-1.04E+07	6229.9	3.661E+05	8.51E+01	1.04E+00	9.22E-07	3046.9	1.4E+05	3.6E+04	126.0	105.5
0.836	-1.19E+07	6396.9	4.050E+05	1.20E+02	1.34E+00	9.94E-07	3107.2	1.4E+05	3.6E+04	126.0	105.5
0.959	-1.34E+07	6570.3	4.469E+05	1.72E+02	1.74E+00	1.07E-06	3170.1	1.4E+05	3.6E+04	126.0	105.5
1.087	-1.49E+07	6749.3	4.919E+05	2.46E+02	2.27E+00	1.14E-06	3235.7	1.4E+05	3.6E+04	126.0	105.5
1.220	-1.63E+07	6933.2	5.399E+05	3.52E+02	2.97E+00	1.22E-06	3303.4	1.4E+05	3.6E+04	126.0	105.5



## **F Atmospheres of Chapter 4**

Tab. F.1 Average model atmosphere of the core umbra region (CU) of sunspot umbra S1 (NOAA 10 930).

$\log \tau_{5000}$	height [cm]	T [K]	$P_{gas}$ [g cm <sup>-1</sup> ]	$P_{electr.}$ [s <sup>-2</sup> ]	$\kappa$ [g <sup>-1</sup> ]	$\rho$ [cm <sup>-3</sup> ]	B [G]	$\zeta_{\mu}$ [cm s <sup>-1</sup> ]	$v_{LOS}$ [cm s <sup>-1</sup> ]	$\gamma_B$ [deg]	$\chi_B$
-4.000	4.38E+07	3499.3	1.146E+03	2.15E-02	3.68E-03	5.18E-09	4507.3	8.7E+04	-6.9E+03	132.5	-36.3
-3.900	4.26E+07	3500.6	1.331E+03	2.38E-02	4.01E-03	6.01E-09	4483.1	8.7E+04	-6.4E+03	132.5	-36.3
-3.800	4.14E+07	3501.9	1.544E+03	2.63E-02	4.37E-03	6.97E-09	4458.8	8.7E+04	-5.8E+03	132.5	-36.3
-3.700	4.02E+07	3503.2	1.790E+03	2.91E-02	4.77E-03	8.08E-09	4434.3	8.7E+04	-5.2E+03	132.5	-36.3
-3.600	3.90E+07	3504.4	2.074E+03	3.21E-02	5.21E-03	9.37E-09	4409.6	8.7E+04	-4.7E+03	132.5	-36.3
-3.500	3.78E+07	3505.6	2.401E+03	3.54E-02	5.68E-03	1.08E-08	4384.7	8.7E+04	-4.1E+03	132.5	-36.3
-3.400	3.67E+07	3506.7	2.778E+03	3.91E-02	6.21E-03	1.26E-08	4359.5	8.7E+04	-3.6E+03	132.5	-36.3
-3.300	3.55E+07	3507.7	3.214E+03	4.31E-02	6.78E-03	1.45E-08	4333.8	8.7E+04	-3.0E+03	132.5	-36.3
-3.200	3.43E+07	3508.7	3.715E+03	4.75E-02	7.40E-03	1.68E-08	4307.6	8.7E+04	-2.5E+03	132.5	-36.3
-3.100	3.32E+07	3509.5	4.293E+03	5.24E-02	8.09E-03	1.94E-08	4280.7	8.7E+04	-1.9E+03	132.5	-36.3
-3.000	3.20E+07	3510.1	4.960E+03	5.77E-02	8.83E-03	2.25E-08	4253.0	8.7E+04	-1.4E+03	132.5	-36.3
-2.900	3.08E+07	3510.4	5.727E+03	6.36E-02	9.65E-03	2.60E-08	4224.1	8.7E+04	-8.3E+02	132.5	-36.3
-2.800	2.97E+07	3510.5	6.612E+03	7.00E-02	1.05E-02	3.01E-08	4193.7	8.7E+04	-2.7E+02	132.5	-36.3
-2.700	2.85E+07	3510.2	7.632E+03	7.71E-02	1.15E-02	3.48E-08	4161.5	8.7E+04	2.8E+02	132.5	-36.3
-2.600	2.74E+07	3509.4	8.808E+03	8.48E-02	1.26E-02	4.02E-08	4126.9	8.7E+04	8.4E+02	132.5	-36.3
-2.500	2.62E+07	3508.0	1.016E+04	9.32E-02	1.37E-02	4.66E-08	4089.2	8.7E+04	1.4E+03	132.5	-36.3
-2.400	2.51E+07	3505.9	1.173E+04	1.02E-01	1.50E-02	5.39E-08	4047.9	8.7E+04	2.0E+03	132.5	-36.3
-2.300	2.40E+07	3503.2	1.353E+04	1.12E-01	1.63E-02	6.25E-08	4003.5	8.7E+04	2.5E+03	132.5	-36.3
-2.200	2.28E+07	3500.2	1.562E+04	1.23E-01	1.78E-02	7.25E-08	3956.6	8.7E+04	3.1E+03	132.5	-36.3
-2.100	2.17E+07	3497.0	1.803E+04	1.36E-01	1.94E-02	8.41E-08	3907.7	8.7E+04	3.7E+03	132.5	-36.3
-2.000	2.06E+07	3493.8	2.081E+04	1.49E-01	2.11E-02	9.77E-08	3857.1	8.7E+04	4.2E+03	132.5	-36.3
-1.900	1.95E+07	3490.9	2.403E+04	1.65E-01	2.30E-02	1.14E-07	3805.2	8.7E+04	4.8E+03	132.5	-36.3
-1.800	1.84E+07	3488.3	2.774E+04	1.82E-01	2.51E-02	1.32E-07	3752.0	8.7E+04	5.4E+03	132.5	-36.3
-1.700	1.73E+07	3486.5	3.202E+04	2.02E-01	2.74E-02	1.54E-07	3697.6	8.7E+04	5.9E+03	132.5	-36.3
-1.600	1.62E+07	3485.5	3.697E+04	2.24E-01	2.98E-02	1.79E-07	3642.1	8.7E+04	6.5E+03	132.5	-36.3
-1.500	1.51E+07	3485.7	4.269E+04	2.50E-01	3.26E-02	2.08E-07	3585.4	8.7E+04	7.0E+03	132.5	-36.3
-1.400	1.40E+07	3487.5	4.928E+04	2.80E-01	3.55E-02	2.42E-07	3527.3	8.7E+04	7.6E+03	132.5	-36.3
-1.300	1.30E+07	3491.4	5.687E+04	3.15E-01	3.89E-02	2.82E-07	3467.6	8.7E+04	8.1E+03	132.5	-36.3
-1.200	1.19E+07	3498.1	6.560E+04	3.56E-01	4.26E-02	3.27E-07	3406.1	8.7E+04	8.6E+03	132.5	-36.3
-1.100	1.09E+07	3508.3	7.563E+04	4.04E-01	4.68E-02	3.79E-07	3342.2	8.7E+04	9.1E+03	132.5	-36.3
-1.000	9.85E+06	3523.1	8.709E+04	4.63E-01	5.16E-02	4.37E-07	3275.4	8.7E+04	9.6E+03	132.5	-36.3
-0.900	8.84E+06	3543.2	1.001E+05	5.34E-01	5.72E-02	5.02E-07	3205.2	8.7E+04	1.0E+04	132.5	-36.3
-0.800	7.84E+06	3567.8	1.149E+05	6.21E-01	6.38E-02	5.74E-07	3132.1	8.7E+04	1.1E+04	132.5	-36.3
-0.700	6.84E+06	3595.7	1.315E+05	7.23E-01	7.13E-02	6.52E-07	3057.0	8.7E+04	1.1E+04	132.5	-36.3
-0.600	5.86E+06	3626.1	1.503E+05	8.45E-01	7.98E-02	7.39E-07	2980.3	8.7E+04	1.1E+04	132.5	-36.3
-0.500	4.88E+06	3658.2	1.713E+05	9.88E-01	8.94E-02	8.35E-07	2902.5	8.7E+04	1.2E+04	132.5	-36.3
-0.400	3.90E+06	3691.4	1.950E+05	1.15E+00	1.00E-01	9.41E-07	2824.1	8.7E+04	1.2E+04	132.5	-36.3
-0.300	2.93E+06	3725.1	2.216E+05	1.35E+00	1.12E-01	1.06E-06	2745.3	8.7E+04	1.3E+04	132.5	-36.3
-0.200	1.95E+06	3758.6	2.515E+05	1.57E+00	1.26E-01	1.19E-06	2666.5	8.7E+04	1.3E+04	132.5	-36.3
-0.100	9.79E+05	3791.6	2.852E+05	1.83E+00	1.40E-01	1.34E-06	2588.1	8.7E+04	1.3E+04	132.5	-36.3
0.000	0.00E+00	3823.4	3.232E+05	2.13E+00	1.56E-01	1.50E-06	2510.4	8.7E+04	1.4E+04	132.5	-36.3
0.099	-9.79E+05	3867.9	3.657E+05	2.51E+00	1.76E-01	1.66E-06	2426.1	8.7E+04	1.4E+04	132.5	-36.3
0.199	-1.96E+06	3924.0	4.126E+05	3.04E+00	2.03E-01	1.84E-06	2343.2	8.7E+04	1.5E+04	132.5	-36.3
0.299	-2.94E+06	3990.6	4.643E+05	3.73E+00	2.36E-01	2.01E-06	2260.6	8.7E+04	1.5E+04	132.5	-36.3
0.401	-3.92E+06	4066.9	5.207E+05	4.67E+00	2.77E-01	2.19E-06	2178.1	8.7E+04	1.6E+04	132.5	-36.3
0.504	-4.90E+06	4151.8	5.819E+05	5.92E+00	3.28E-01	2.37E-06	2095.3	8.7E+04	1.6E+04	132.5	-36.3
0.608	-5.88E+06	4244.5	6.481E+05	7.58E+00	3.90E-01	2.56E-06	2012.4	8.7E+04	1.7E+04	132.5	-36.3
0.713	-6.85E+06	4344.3	7.192E+05	9.80E+00	4.65E-01	2.74E-06	1929.3	8.7E+04	1.7E+04	132.5	-36.3
0.818	-7.83E+06	4450.3	7.954E+05	1.27E+01	5.55E-01	2.93E-06	1846.3	8.7E+04	1.8E+04	132.5	-36.3
0.922	-8.81E+06	4562.1	8.768E+05	1.66E+01	6.58E-01	3.13E-06	1763.8	8.7E+04	1.8E+04	132.5	-36.3
1.026	-9.79E+06	4679.0	9.635E+05	2.15E+01	7.77E-01	3.33E-06	1682.2	8.7E+04	1.8E+04	132.5	-36.3
1.129	-1.08E+07	4800.5	1.056E+06	2.77E+01	9.08E-01	3.53E-06	1602.1	8.7E+04	1.9E+04	132.5	-36.3

Tab. F.2 Average model atmosphere of the diffuse background region (DB) of sunspot umbra S1 (NOAA 10930).

log $\tau_{5000}$	height [cm]	T [K]	$P_{gas}$ [g cm <sup>-1</sup> s <sup>-2</sup> ]	$P_{electr.}$ [g cm <sup>-1</sup> s <sup>-2</sup> ]	$\kappa$ [g <sup>-1</sup> ]	$\rho$ [cm <sup>-3</sup> ]	B [G]	$\zeta_{\mu}$ [cm s <sup>-1</sup> ]	$v_{LOS}$ [cm s <sup>-1</sup> ]	$\gamma_B$ [deg]	$\chi_B$
-4.000	4.28E+07	3228.6	1.455E+03	1.20E-02	3.06E-03	7.21E-09	3388.1	8.0E+04	2.2E+04	145.3	25.8
-3.900	4.18E+07	3244.0	1.675E+03	1.38E-02	3.38E-03	8.27E-09	3372.0	8.0E+04	2.2E+04	145.3	25.8
-3.800	4.07E+07	3259.4	1.927E+03	1.58E-02	3.73E-03	9.47E-09	3355.9	8.0E+04	2.2E+04	145.3	25.8
-3.700	3.97E+07	3274.7	2.214E+03	1.82E-02	4.12E-03	1.08E-08	3339.7	8.0E+04	2.2E+04	145.3	25.8
-3.600	3.86E+07	3290.1	2.542E+03	2.09E-02	4.55E-03	1.24E-08	3323.6	8.0E+04	2.2E+04	145.3	25.8
-3.500	3.76E+07	3305.4	2.915E+03	2.39E-02	5.03E-03	1.42E-08	3307.3	8.0E+04	2.2E+04	145.3	25.8
-3.400	3.66E+07	3320.6	3.339E+03	2.73E-02	5.56E-03	1.62E-08	3291.1	8.0E+04	2.2E+04	145.3	25.8
-3.300	3.55E+07	3335.7	3.823E+03	3.12E-02	6.15E-03	1.84E-08	3274.8	8.0E+04	2.1E+04	145.3	25.8
-3.200	3.45E+07	3350.8	4.374E+03	3.56E-02	6.79E-03	2.10E-08	3258.4	8.0E+04	2.1E+04	145.3	25.8
-3.100	3.35E+07	3365.7	5.002E+03	4.07E-02	7.51E-03	2.40E-08	3241.9	8.0E+04	2.1E+04	145.3	25.8
-3.000	3.24E+07	3380.5	5.717E+03	4.63E-02	8.30E-03	2.73E-08	3225.3	8.0E+04	2.1E+04	145.3	25.8
-2.900	3.14E+07	3395.0	6.531E+03	5.27E-02	9.17E-03	3.11E-08	3208.6	8.0E+04	2.1E+04	145.3	25.8
-2.800	3.04E+07	3409.3	7.460E+03	6.00E-02	1.01E-02	3.54E-08	3191.7	8.0E+04	2.1E+04	145.3	25.8
-2.700	2.93E+07	3423.2	8.518E+03	6.81E-02	1.12E-02	4.03E-08	3174.5	8.0E+04	2.1E+04	145.3	25.8
-2.600	2.83E+07	3436.7	9.725E+03	7.72E-02	1.23E-02	4.59E-08	3157.0	8.0E+04	2.1E+04	145.3	25.8
-2.500	2.72E+07	3449.6	1.110E+04	8.74E-02	1.36E-02	5.23E-08	3139.2	8.0E+04	2.1E+04	145.3	25.8
-2.400	2.61E+07	3461.9	1.268E+04	9.88E-02	1.50E-02	5.97E-08	3120.8	8.0E+04	2.2E+04	145.3	25.8
-2.300	2.51E+07	3473.6	1.448E+04	1.12E-01	1.65E-02	6.81E-08	3102.1	8.0E+04	2.2E+04	145.3	25.8
-2.200	2.40E+07	3485.1	1.653E+04	1.26E-01	1.82E-02	7.77E-08	3082.9	8.0E+04	2.2E+04	145.3	25.8
-2.100	2.29E+07	3496.4	1.888E+04	1.42E-01	2.00E-02	8.87E-08	3063.5	8.0E+04	2.3E+04	145.3	25.8
-2.000	2.18E+07	3507.7	2.157E+04	1.60E-01	2.20E-02	1.01E-07	3043.7	8.0E+04	2.3E+04	145.3	25.8
-1.900	2.08E+07	3519.3	2.465E+04	1.81E-01	2.42E-02	1.16E-07	3023.7	8.0E+04	2.3E+04	145.3	25.8
-1.800	1.97E+07	3531.3	2.817E+04	2.04E-01	2.67E-02	1.32E-07	3003.4	8.0E+04	2.3E+04	145.3	25.8
-1.700	1.86E+07	3543.9	3.219E+04	2.31E-01	2.94E-02	1.51E-07	2982.7	8.0E+04	2.4E+04	145.3	25.8
-1.600	1.75E+07	3557.3	3.679E+04	2.62E-01	3.24E-02	1.72E-07	2961.7	8.0E+04	2.4E+04	145.3	25.8
-1.500	1.64E+07	3571.9	4.204E+04	2.97E-01	3.57E-02	1.97E-07	2940.2	8.0E+04	2.4E+04	145.3	25.8
-1.400	1.53E+07	3588.1	4.802E+04	3.39E-01	3.95E-02	2.25E-07	2918.1	8.0E+04	2.4E+04	145.3	25.8
-1.300	1.42E+07	3606.3	5.484E+04	3.88E-01	4.37E-02	2.56E-07	2895.4	8.0E+04	2.3E+04	145.3	25.8
-1.200	1.31E+07	3627.1	6.258E+04	4.45E-01	4.85E-02	2.91E-07	2871.7	8.0E+04	2.3E+04	145.3	25.8
-1.100	1.20E+07	3651.3	7.136E+04	5.15E-01	5.40E-02	3.31E-07	2847.0	8.0E+04	2.2E+04	145.3	25.8
-1.000	1.09E+07	3679.9	8.126E+04	6.00E-01	6.04E-02	3.74E-07	2820.8	8.0E+04	2.0E+04	145.3	25.8
-0.900	9.79E+06	3713.7	9.239E+04	7.06E-01	6.79E-02	4.22E-07	2792.9	8.0E+04	1.9E+04	145.3	25.8
-0.800	8.70E+06	3751.7	1.048E+05	8.37E-01	7.67E-02	4.73E-07	2763.6	8.0E+04	1.6E+04	145.3	25.8
-0.700	7.62E+06	3793.0	1.187E+05	9.97E-01	8.68E-02	5.30E-07	2733.2	8.0E+04	1.4E+04	145.3	25.8
-0.600	6.54E+06	3836.6	1.342E+05	1.19E+00	9.84E-02	5.91E-07	2702.1	8.0E+04	1.1E+04	145.3	25.8
-0.500	5.47E+06	3881.8	1.513E+05	1.42E+00	1.12E-01	6.58E-07	2670.4	8.0E+04	7.9E+03	145.3	25.8
-0.400	4.39E+06	3928.1	1.704E+05	1.70E+00	1.27E-01	7.31E-07	2638.4	8.0E+04	4.8E+03	145.3	25.8
-0.300	3.30E+06	3974.8	1.917E+05	2.04E+00	1.43E-01	8.11E-07	2606.3	8.0E+04	1.6E+03	145.3	25.8
-0.200	2.21E+06	4021.5	2.153E+05	2.43E+00	1.62E-01	8.99E-07	2574.2	8.0E+04	-1.5E+03	145.3	25.8
-0.100	1.11E+06	4067.6	2.417E+05	2.89E+00	1.83E-01	9.98E-07	2542.2	8.0E+04	-4.6E+03	145.3	25.8
0.000	0.00E+00	4112.5	2.713E+05	3.42E+00	2.06E-01	1.11E-06	2510.6	8.0E+04	-7.5E+03	145.3	25.8
0.099	-1.11E+06	4169.0	3.039E+05	4.10E+00	2.34E-01	1.21E-06	2476.4	8.0E+04	-1.1E+04	145.3	25.8
0.196	-2.23E+06	4236.3	3.396E+05	5.03E+00	2.69E-01	1.33E-06	2442.9	8.0E+04	-1.4E+04	145.3	25.8
0.294	-3.34E+06	4313.2	3.786E+05	6.25E+00	3.10E-01	1.45E-06	2409.6	8.0E+04	-1.7E+04	145.3	25.8
0.391	-4.45E+06	4399.0	4.211E+05	7.83E+00	3.60E-01	1.57E-06	2376.3	8.0E+04	-2.0E+04	145.3	25.8
0.487	-5.57E+06	4492.8	4.671E+05	9.87E+00	4.18E-01	1.70E-06	2343.1	8.0E+04	-2.3E+04	145.3	25.8
0.582	-6.68E+06	4593.9	5.167E+05	1.25E+01	4.85E-01	1.83E-06	2310.0	8.0E+04	-2.6E+04	145.3	25.8
0.675	-7.79E+06	4701.6	5.700E+05	1.57E+01	5.61E-01	1.96E-06	2277.0	8.0E+04	-2.9E+04	145.3	25.8
0.766	-8.90E+06	4815.2	6.271E+05	1.98E+01	6.46E-01	2.10E-06	2244.3	8.0E+04	-3.1E+04	145.3	25.8
0.855	-1.00E+07	4934.3	6.880E+05	2.48E+01	7.39E-01	2.23E-06	2212.0	8.0E+04	-3.4E+04	145.3	25.8
0.940	-1.11E+07	5058.2	7.528E+05	3.09E+01	8.40E-01	2.37E-06	2180.3	8.0E+04	-3.7E+04	145.3	25.8
1.023	-1.22E+07	5186.6	8.216E+05	3.82E+01	9.48E-01	2.52E-06	2149.3	8.0E+04	-3.9E+04	145.3	25.8

Tab. F.3 Average model atmosphere of the core umbral dots (CUD) of sunspot umbra S1 (NOAA 10 930).

$\log \tau_{5000}$	height [cm]	T [K]	$P_{gas}$ [g cm <sup>-1</sup> s <sup>-2</sup> ]	$P_{electr.}$ [g <sup>-1</sup> s <sup>-2</sup> ]	$\kappa$ [g <sup>-1</sup> ]	$\rho$ [cm <sup>-3</sup> ]	B [G]	$\zeta_{\mu}$ [cm s <sup>-1</sup> ]	$v_{LOS}$ [cm s <sup>-1</sup> ]	$\gamma_B$ [deg]	$\chi_B$
-4.000	4.16E+07	3185.7	1.486E+03	1.09E-02	2.98E-03	7.49E-09	3466.7	9.7E+04	2.5E+04	147.6	19.1
-3.900	4.06E+07	3200.6	1.713E+03	1.25E-02	3.28E-03	8.60E-09	3453.4	9.7E+04	2.5E+04	147.6	19.1
-3.800	3.96E+07	3215.4	1.972E+03	1.44E-02	3.62E-03	9.86E-09	3440.0	9.7E+04	2.5E+04	147.6	19.1
-3.700	3.86E+07	3230.2	2.268E+03	1.65E-02	4.00E-03	1.13E-08	3426.6	9.7E+04	2.5E+04	147.6	19.1
-3.600	3.75E+07	3245.0	2.605E+03	1.89E-02	4.42E-03	1.29E-08	3413.1	9.7E+04	2.4E+04	147.6	19.1
-3.500	3.65E+07	3259.8	2.989E+03	2.17E-02	4.88E-03	1.48E-08	3399.7	9.7E+04	2.4E+04	147.6	19.1
-3.400	3.55E+07	3274.5	3.427E+03	2.48E-02	5.38E-03	1.69E-08	3386.2	9.7E+04	2.4E+04	147.6	19.1
-3.300	3.45E+07	3289.1	3.926E+03	2.83E-02	5.95E-03	1.93E-08	3372.6	9.7E+04	2.4E+04	147.6	19.1
-3.200	3.35E+07	3303.7	4.495E+03	3.23E-02	6.57E-03	2.20E-08	3358.9	9.7E+04	2.4E+04	147.6	19.1
-3.100	3.25E+07	3318.1	5.143E+03	3.68E-02	7.26E-03	2.51E-08	3345.1	9.7E+04	2.4E+04	147.6	19.1
-3.000	3.15E+07	3332.5	5.882E+03	4.19E-02	8.02E-03	2.86E-08	3331.2	9.7E+04	2.4E+04	147.6	19.1
-2.900	3.05E+07	3346.6	6.725E+03	4.77E-02	8.85E-03	3.26E-08	3317.1	9.7E+04	2.4E+04	147.6	19.1
-2.800	2.95E+07	3360.5	7.685E+03	5.43E-02	9.77E-03	3.72E-08	3302.8	9.7E+04	2.3E+04	147.6	19.1
-2.700	2.84E+07	3374.1	8.780E+03	6.17E-02	1.08E-02	4.24E-08	3288.2	9.7E+04	2.3E+04	147.6	19.1
-2.600	2.74E+07	3387.4	1.003E+04	7.00E-02	1.19E-02	4.84E-08	3273.3	9.7E+04	2.4E+04	147.6	19.1
-2.500	2.64E+07	3400.1	1.146E+04	7.93E-02	1.31E-02	5.51E-08	3257.8	9.7E+04	2.4E+04	147.6	19.1
-2.400	2.54E+07	3412.3	1.309E+04	8.97E-02	1.45E-02	6.29E-08	3241.8	9.7E+04	2.4E+04	147.6	19.1
-2.300	2.44E+07	3424.1	1.495E+04	1.01E-01	1.59E-02	7.18E-08	3225.3	9.7E+04	2.4E+04	147.6	19.1
-2.200	2.33E+07	3435.7	1.708E+04	1.15E-01	1.75E-02	8.20E-08	3208.3	9.7E+04	2.4E+04	147.6	19.1
-2.100	2.23E+07	3447.2	1.951E+04	1.30E-01	1.93E-02	9.36E-08	3191.0	9.7E+04	2.5E+04	147.6	19.1
-2.000	2.13E+07	3458.7	2.230E+04	1.46E-01	2.12E-02	1.07E-07	3173.3	9.7E+04	2.5E+04	147.6	19.1
-1.900	2.02E+07	3470.5	2.548E+04	1.66E-01	2.34E-02	1.22E-07	3155.3	9.7E+04	2.5E+04	147.6	19.1
-1.800	1.92E+07	3482.8	2.912E+04	1.88E-01	2.57E-02	1.40E-07	3137.0	9.7E+04	2.6E+04	147.6	19.1
-1.700	1.81E+07	3495.6	3.329E+04	2.13E-01	2.83E-02	1.60E-07	3118.2	9.7E+04	2.6E+04	147.6	19.1
-1.600	1.71E+07	3509.4	3.805E+04	2.42E-01	3.12E-02	1.83E-07	3099.0	9.7E+04	2.6E+04	147.6	19.1
-1.500	1.60E+07	3524.3	4.348E+04	2.75E-01	3.45E-02	2.09E-07	3079.3	9.7E+04	2.6E+04	147.6	19.1
-1.400	1.50E+07	3540.8	4.968E+04	3.14E-01	3.81E-02	2.38E-07	3058.8	9.7E+04	2.6E+04	147.6	19.1
-1.300	1.39E+07	3559.2	5.674E+04	3.60E-01	4.21E-02	2.71E-07	3037.6	9.7E+04	2.5E+04	147.6	19.1
-1.200	1.29E+07	3580.3	6.476E+04	4.14E-01	4.67E-02	3.09E-07	3015.3	9.7E+04	2.5E+04	147.6	19.1
-1.100	1.18E+07	3604.8	7.386E+04	4.79E-01	5.20E-02	3.51E-07	2991.6	9.7E+04	2.4E+04	147.6	19.1
-1.000	1.07E+07	3633.6	8.413E+04	5.59E-01	5.82E-02	3.97E-07	2966.3	9.7E+04	2.2E+04	147.6	19.1
-0.900	9.68E+06	3667.6	9.567E+04	6.58E-01	6.54E-02	4.47E-07	2938.9	9.7E+04	2.0E+04	147.6	19.1
-0.800	8.62E+06	3705.8	1.086E+05	7.80E-01	7.38E-02	5.02E-07	2909.9	9.7E+04	1.8E+04	147.6	19.1
-0.700	7.56E+06	3747.2	1.230E+05	9.30E-01	8.36E-02	5.61E-07	2879.6	9.7E+04	1.5E+04	147.6	19.1
-0.600	6.51E+06	3790.9	1.390E+05	1.11E+00	9.48E-02	6.26E-07	2848.4	9.7E+04	1.2E+04	147.6	19.1
-0.500	5.45E+06	3836.3	1.568E+05	1.33E+00	1.08E-01	6.96E-07	2816.6	9.7E+04	8.4E+03	147.6	19.1
-0.400	4.38E+06	3882.7	1.766E+05	1.59E+00	1.22E-01	7.74E-07	2784.3	9.7E+04	5.1E+03	147.6	19.1
-0.300	3.31E+06	3929.5	1.987E+05	1.91E+00	1.38E-01	8.59E-07	2751.9	9.7E+04	1.7E+03	147.6	19.1
-0.200	2.22E+06	3976.3	2.232E+05	2.28E+00	1.57E-01	9.52E-07	2719.5	9.7E+04	-1.7E+03	147.6	19.1
-0.100	1.12E+06	4022.5	2.506E+05	2.71E+00	1.77E-01	1.06E-06	2687.4	9.7E+04	-5.1E+03	147.6	19.1
0.000	0.00E+00	4067.5	2.813E+05	3.22E+00	1.99E-01	1.17E-06	2655.6	9.7E+04	-8.3E+03	147.6	19.1
0.098	-1.12E+06	4124.0	3.151E+05	3.87E+00	2.26E-01	1.28E-06	2621.2	9.7E+04	-1.2E+04	147.6	19.1
0.194	-2.24E+06	4190.8	3.521E+05	4.75E+00	2.60E-01	1.41E-06	2587.5	9.7E+04	-1.5E+04	147.6	19.1
0.289	-3.36E+06	4267.2	3.926E+05	5.90E+00	3.01E-01	1.53E-06	2553.9	9.7E+04	-1.8E+04	147.6	19.1
0.383	-4.48E+06	4352.3	4.366E+05	7.39E+00	3.50E-01	1.66E-06	2520.4	9.7E+04	-2.2E+04	147.6	19.1
0.475	-5.61E+06	4445.1	4.842E+05	9.32E+00	4.07E-01	1.79E-06	2486.9	9.7E+04	-2.5E+04	147.6	19.1
0.566	-6.73E+06	4545.1	5.354E+05	1.18E+01	4.73E-01	1.93E-06	2453.3	9.7E+04	-2.8E+04	147.6	19.1
0.653	-7.85E+06	4651.5	5.905E+05	1.49E+01	5.49E-01	2.06E-06	2419.8	9.7E+04	-3.1E+04	147.6	19.1
0.739	-8.97E+06	4763.7	6.494E+05	1.88E+01	6.34E-01	2.21E-06	2386.5	9.7E+04	-3.4E+04	147.6	19.1
0.821	-1.01E+07	4881.2	7.121E+05	2.36E+01	7.28E-01	2.35E-06	2353.5	9.7E+04	-3.7E+04	147.6	19.1
0.902	-1.12E+07	5003.4	7.789E+05	2.94E+01	8.31E-01	2.49E-06	2321.0	9.7E+04	-4.0E+04	147.6	19.1
0.982	-1.23E+07	5129.9	8.497E+05	3.66E+01	9.42E-01	2.64E-06	2289.3	9.7E+04	-4.2E+04	147.6	19.1

Tab. F.4 Average model atmosphere of the peripheral umbral dots (PUD) of sunspot umbra S1 (NOAA 10930).

log $\tau_{5000}$	height [cm]	T [K]	$P_{gas}$ [g cm <sup>-1</sup> s <sup>-2</sup> ]	$P_{electr.}$ [g <sup>-1</sup> s <sup>-2</sup> ]	$\kappa$ [g <sup>-1</sup> ]	$\rho$ [cm <sup>-3</sup> ]	B [G]	$\zeta_{\mu}$ [cm s <sup>-1</sup> ]	$v_{LOS}$ [cm s <sup>-1</sup> ]	$\gamma_B$ [deg]	$\chi_B$
-4.000	4.30E+07	3246.6	1.458E+03	1.25E-02	3.11E-03	7.17E-09	2939.6	7.1E+04	4.3E+04	143.4	23.7
-3.900	4.20E+07	3267.0	1.675E+03	1.45E-02	3.45E-03	8.18E-09	2930.6	7.1E+04	4.2E+04	143.4	23.7
-3.800	4.09E+07	3287.5	1.921E+03	1.69E-02	3.82E-03	9.33E-09	2921.6	7.1E+04	4.0E+04	143.4	23.7
-3.700	3.99E+07	3307.9	2.200E+03	1.96E-02	4.24E-03	1.06E-08	2912.6	7.1E+04	3.9E+04	143.4	23.7
-3.600	3.89E+07	3328.3	2.517E+03	2.27E-02	4.71E-03	1.21E-08	2903.5	7.1E+04	3.8E+04	143.4	23.7
-3.500	3.79E+07	3348.7	2.877E+03	2.63E-02	5.22E-03	1.37E-08	2894.5	7.1E+04	3.6E+04	143.4	23.7
-3.400	3.68E+07	3369.1	3.285E+03	3.04E-02	5.80E-03	1.56E-08	2885.5	7.1E+04	3.5E+04	143.4	23.7
-3.300	3.58E+07	3389.5	3.748E+03	3.51E-02	6.44E-03	1.77E-08	2876.5	7.1E+04	3.4E+04	143.4	23.7
-3.200	3.48E+07	3409.9	4.272E+03	4.05E-02	7.15E-03	2.01E-08	2867.5	7.1E+04	3.3E+04	143.4	23.7
-3.100	3.38E+07	3430.4	4.867E+03	4.67E-02	7.94E-03	2.27E-08	2858.5	7.1E+04	3.1E+04	143.4	23.7
-3.000	3.28E+07	3450.8	5.542E+03	5.39E-02	8.81E-03	2.57E-08	2849.5	7.1E+04	3.0E+04	143.4	23.7
-2.900	3.18E+07	3471.2	6.307E+03	6.20E-02	9.79E-03	2.91E-08	2840.5	7.1E+04	2.9E+04	143.4	23.7
-2.800	3.07E+07	3491.7	7.174E+03	7.13E-02	1.09E-02	3.30E-08	2831.4	7.1E+04	2.8E+04	143.4	23.7
-2.700	2.97E+07	3512.1	8.157E+03	8.20E-02	1.21E-02	3.73E-08	2822.4	7.1E+04	2.6E+04	143.4	23.7
-2.600	2.87E+07	3532.6	9.273E+03	9.42E-02	1.34E-02	4.22E-08	2813.4	7.1E+04	2.5E+04	143.4	23.7
-2.500	2.76E+07	3553.1	1.054E+04	1.08E-01	1.49E-02	4.77E-08	2804.3	7.1E+04	2.4E+04	143.4	23.7
-2.400	2.66E+07	3573.6	1.197E+04	1.24E-01	1.65E-02	5.39E-08	2795.3	7.1E+04	2.3E+04	143.4	23.7
-2.300	2.55E+07	3594.2	1.360E+04	1.43E-01	1.83E-02	6.09E-08	2786.2	7.1E+04	2.2E+04	143.4	23.7
-2.200	2.45E+07	3615.0	1.545E+04	1.64E-01	2.04E-02	6.89E-08	2777.2	7.1E+04	2.1E+04	143.4	23.7
-2.100	2.34E+07	3636.0	1.754E+04	1.88E-01	2.26E-02	7.78E-08	2768.1	7.1E+04	1.9E+04	143.4	23.7
-2.000	2.23E+07	3657.5	1.992E+04	2.16E-01	2.51E-02	8.79E-08	2759.1	7.1E+04	1.8E+04	143.4	23.7
-1.900	2.13E+07	3679.6	2.261E+04	2.49E-01	2.79E-02	9.93E-08	2750.0	7.1E+04	1.7E+04	143.4	23.7
-1.800	2.02E+07	3702.4	2.566E+04	2.86E-01	3.10E-02	1.12E-07	2741.0	7.1E+04	1.6E+04	143.4	23.7
-1.700	1.91E+07	3726.1	2.912E+04	3.30E-01	3.46E-02	1.27E-07	2731.9	7.1E+04	1.5E+04	143.4	23.7
-1.600	1.80E+07	3751.0	3.303E+04	3.82E-01	3.85E-02	1.43E-07	2722.9	7.1E+04	1.4E+04	143.4	23.7
-1.500	1.69E+07	3777.6	3.746E+04	4.43E-01	4.30E-02	1.61E-07	2713.9	7.1E+04	1.2E+04	143.4	23.7
-1.400	1.58E+07	3806.2	4.246E+04	5.16E-01	4.80E-02	1.82E-07	2704.9	7.1E+04	1.1E+04	143.4	23.7
-1.300	1.47E+07	3837.5	4.808E+04	6.03E-01	5.38E-02	2.04E-07	2695.9	7.1E+04	9.8E+03	143.4	23.7
-1.200	1.36E+07	3872.2	5.440E+04	7.08E-01	6.04E-02	2.29E-07	2686.9	7.1E+04	8.3E+03	143.4	23.7
-1.100	1.25E+07	3911.3	6.148E+04	8.39E-01	6.81E-02	2.56E-07	2678.0	7.1E+04	6.8E+03	143.4	23.7
-1.000	1.14E+07	3956.0	6.936E+04	1.00E+00	7.72E-02	2.86E-07	2669.2	7.1E+04	5.1E+03	143.4	23.7
-0.900	1.03E+07	4007.4	7.809E+04	1.21E+00	8.79E-02	3.18E-07	2660.4	7.1E+04	3.2E+03	143.4	23.7
-0.800	9.15E+06	4064.3	8.772E+04	1.47E+00	1.00E-01	3.51E-07	2651.6	7.1E+04	1.2E+03	143.4	23.7
-0.700	8.04E+06	4125.3	9.830E+04	1.79E+00	1.15E-01	3.87E-07	2642.9	7.1E+04	-9.2E+02	143.4	23.7
-0.600	6.92E+06	4189.3	1.099E+05	2.19E+00	1.32E-01	4.25E-07	2634.2	7.1E+04	-3.1E+03	143.4	23.7
-0.500	5.79E+06	4255.5	1.227E+05	2.68E+00	1.50E-01	4.66E-07	2625.6	7.1E+04	-5.3E+03	143.4	23.7
-0.400	4.66E+06	4322.9	1.368E+05	3.26E+00	1.71E-01	5.11E-07	2616.9	7.1E+04	-7.6E+03	143.4	23.7
-0.300	3.52E+06	4391.0	1.524E+05	3.96E+00	1.94E-01	5.59E-07	2608.2	7.1E+04	-9.9E+03	143.4	23.7
-0.200	2.36E+06	4458.9	1.697E+05	4.78E+00	2.20E-01	6.12E-07	2599.6	7.1E+04	-1.2E+04	143.4	23.7
-0.100	1.19E+06	4526.2	1.890E+05	5.74E+00	2.48E-01	6.70E-07	2590.9	7.1E+04	-1.4E+04	143.4	23.7
0.000	0.00E+00	4591.9	2.105E+05	6.86E+00	2.79E-01	7.35E-07	2582.3	7.1E+04	-1.7E+04	143.4	23.7
0.098	-1.19E+06	4668.5	2.340E+05	8.24E+00	3.13E-01	7.98E-07	2573.0	7.1E+04	-1.9E+04	143.4	23.7
0.195	-2.38E+06	4755.0	2.595E+05	1.00E+01	3.53E-01	8.68E-07	2564.2	7.1E+04	-2.1E+04	143.4	23.7
0.291	-3.57E+06	4850.6	2.873E+05	1.22E+01	3.97E-01	9.40E-07	2555.7	7.1E+04	-2.3E+04	143.4	23.7
0.386	-4.76E+06	4954.4	3.173E+05	1.49E+01	4.46E-01	1.01E-06	2547.4	7.1E+04	-2.6E+04	143.4	23.7
0.479	-5.94E+06	5065.8	3.497E+05	1.83E+01	5.00E-01	1.09E-06	2539.4	7.1E+04	-2.8E+04	143.4	23.7
0.571	-7.13E+06	5184.0	3.844E+05	2.23E+01	5.57E-01	1.17E-06	2531.6	7.1E+04	-3.0E+04	143.4	23.7
0.660	-8.32E+06	5308.4	4.216E+05	2.74E+01	6.21E-01	1.25E-06	2524.0	7.1E+04	-3.2E+04	143.4	23.7
0.747	-9.51E+06	5438.5	4.614E+05	3.37E+01	6.94E-01	1.34E-06	2516.6	7.1E+04	-3.3E+04	143.4	23.7
0.832	-1.07E+07	5573.8	5.039E+05	4.19E+01	7.81E-01	1.42E-06	2509.3	7.1E+04	-3.5E+04	143.4	23.7
0.916	-1.19E+07	5713.9	5.490E+05	5.28E+01	8.90E-01	1.51E-06	2502.0	7.1E+04	-3.7E+04	143.4	23.7
0.998	-1.31E+07	5858.2	5.970E+05	6.77E+01	1.03E+00	1.60E-06	2494.7	7.1E+04	-3.9E+04	143.4	23.7

Tab. F.5 Average model atmosphere of the core umbra region (CU) of sunspot umbra S2 (NOAA 10 933).

log $\tau_{5000}$	height [cm]	T [K]	$P_{gas}$ [g cm <sup>-1</sup> s <sup>-2</sup> ]	$P_{electr.}$ [g <sup>-1</sup> s <sup>-2</sup> ]	$\kappa$ [g <sup>-1</sup> ]	$\rho$ [cm <sup>-3</sup> ]	B [G]	$\zeta_{\mu}$ [cm s <sup>-1</sup> ]	$v_{LOS}$ [cm s <sup>-1</sup> ]	$\gamma_B$ [deg]	$\chi_B$
-4.000	4.23E+07	3324.4	1.364E+03	1.46E-02	3.25E-03	6.52E-09	3002.7	5.5E+04	2.4E+04	24.9	41.4
-3.900	4.12E+07	3338.3	1.572E+03	1.67E-02	3.59E-03	7.48E-09	2992.1	5.5E+04	2.4E+04	24.9	41.4
-3.800	4.02E+07	3352.1	1.808E+03	1.91E-02	3.96E-03	8.58E-09	2981.6	5.5E+04	2.5E+04	24.9	41.4
-3.700	3.91E+07	3365.9	2.078E+03	2.18E-02	4.37E-03	9.82E-09	2971.0	5.5E+04	2.5E+04	24.9	41.4
-3.600	3.80E+07	3379.6	2.386E+03	2.49E-02	4.82E-03	1.12E-08	2960.4	5.5E+04	2.5E+04	24.9	41.4
-3.500	3.70E+07	3393.3	2.738E+03	2.84E-02	5.33E-03	1.28E-08	2949.8	5.5E+04	2.5E+04	24.9	41.4
-3.400	3.59E+07	3407.0	3.138E+03	3.23E-02	5.88E-03	1.47E-08	2939.3	5.5E+04	2.5E+04	24.9	41.4
-3.300	3.48E+07	3420.5	3.595E+03	3.67E-02	6.49E-03	1.68E-08	2928.7	5.5E+04	2.5E+04	24.9	41.4
-3.200	3.38E+07	3433.9	4.116E+03	4.16E-02	7.17E-03	1.91E-08	2918.1	5.5E+04	2.5E+04	24.9	41.4
-3.100	3.27E+07	3447.2	4.710E+03	4.72E-02	7.91E-03	2.18E-08	2907.6	5.5E+04	2.5E+04	24.9	41.4
-3.000	3.17E+07	3460.2	5.387E+03	5.35E-02	8.73E-03	2.49E-08	2897.0	5.5E+04	2.5E+04	24.9	41.4
-2.900	3.06E+07	3473.0	6.160E+03	6.06E-02	9.63E-03	2.84E-08	2886.4	5.5E+04	2.5E+04	24.9	41.4
-2.800	2.96E+07	3485.5	7.041E+03	6.85E-02	1.06E-02	3.23E-08	2875.9	5.5E+04	2.5E+04	24.9	41.4
-2.700	2.85E+07	3497.6	8.048E+03	7.74E-02	1.17E-02	3.69E-08	2865.4	5.5E+04	2.6E+04	24.9	41.4
-2.600	2.74E+07	3509.2	9.197E+03	8.73E-02	1.29E-02	4.21E-08	2854.8	5.5E+04	2.6E+04	24.9	41.4
-2.500	2.64E+07	3520.0	1.051E+04	9.82E-02	1.42E-02	4.80E-08	2844.3	5.5E+04	2.6E+04	24.9	41.4
-2.400	2.53E+07	3530.1	1.201E+04	1.10E-01	1.56E-02	5.48E-08	2833.8	5.5E+04	2.6E+04	24.9	41.4
-2.300	2.42E+07	3539.6	1.374E+04	1.24E-01	1.72E-02	6.26E-08	2823.3	5.5E+04	2.7E+04	24.9	41.4
-2.200	2.32E+07	3548.7	1.571E+04	1.39E-01	1.89E-02	7.15E-08	2812.8	5.5E+04	2.7E+04	24.9	41.4
-2.100	2.21E+07	3557.6	1.796E+04	1.56E-01	2.08E-02	8.18E-08	2802.3	5.5E+04	2.7E+04	24.9	41.4
-2.000	2.10E+07	3566.6	2.055E+04	1.74E-01	2.28E-02	9.35E-08	2791.8	5.5E+04	2.8E+04	24.9	41.4
-1.900	1.99E+07	3575.8	2.351E+04	1.96E-01	2.51E-02	1.07E-07	2781.3	5.5E+04	2.8E+04	24.9	41.4
-1.800	1.89E+07	3585.4	2.691E+04	2.20E-01	2.76E-02	1.23E-07	2770.8	5.5E+04	2.8E+04	24.9	41.4
-1.700	1.78E+07	3595.8	3.079E+04	2.47E-01	3.03E-02	1.40E-07	2760.3	5.5E+04	2.8E+04	24.9	41.4
-1.600	1.67E+07	3607.1	3.524E+04	2.79E-01	3.34E-02	1.60E-07	2749.8	5.5E+04	2.9E+04	24.9	41.4
-1.500	1.56E+07	3619.7	4.031E+04	3.16E-01	3.68E-02	1.83E-07	2739.2	5.5E+04	2.9E+04	24.9	41.4
-1.400	1.46E+07	3634.1	4.611E+04	3.58E-01	4.06E-02	2.10E-07	2728.7	5.5E+04	2.9E+04	24.9	41.4
-1.300	1.35E+07	3650.8	5.271E+04	4.08E-01	4.49E-02	2.39E-07	2718.0	5.5E+04	2.9E+04	24.9	41.4
-1.200	1.24E+07	3670.5	6.021E+04	4.68E-01	4.99E-02	2.72E-07	2707.4	5.5E+04	2.8E+04	24.9	41.4
-1.100	1.14E+07	3694.0	6.871E+04	5.40E-01	5.55E-02	3.09E-07	2696.6	5.5E+04	2.8E+04	24.9	41.4
-1.000	1.03E+07	3722.5	7.828E+04	6.29E-01	6.21E-02	3.50E-07	2685.8	5.5E+04	2.7E+04	24.9	41.4
-0.900	9.25E+06	3756.9	8.902E+04	7.40E-01	7.00E-02	3.95E-07	2674.9	5.5E+04	2.6E+04	24.9	41.4
-0.800	8.21E+06	3796.1	1.010E+05	8.78E-01	7.91E-02	4.43E-07	2663.8	5.5E+04	2.5E+04	24.9	41.4
-0.700	7.18E+06	3839.0	1.143E+05	1.05E+00	8.98E-02	4.95E-07	2652.8	5.5E+04	2.4E+04	24.9	41.4
-0.600	6.15E+06	3884.6	1.291E+05	1.25E+00	1.02E-01	5.50E-07	2641.6	5.5E+04	2.2E+04	24.9	41.4
-0.500	5.13E+06	3932.0	1.454E+05	1.50E+00	1.16E-01	6.11E-07	2630.5	5.5E+04	2.1E+04	24.9	41.4
-0.400	4.11E+06	3980.6	1.635E+05	1.80E+00	1.32E-01	6.77E-07	2619.3	5.5E+04	1.9E+04	24.9	41.4
-0.300	3.09E+06	4029.7	1.836E+05	2.15E+00	1.50E-01	7.49E-07	2608.1	5.5E+04	1.7E+04	24.9	41.4
-0.200	2.07E+06	4078.7	2.059E+05	2.57E+00	1.70E-01	8.28E-07	2596.9	5.5E+04	1.5E+04	24.9	41.4
-0.100	1.04E+06	4127.1	2.306E+05	3.06E+00	1.92E-01	9.16E-07	2585.7	5.5E+04	1.4E+04	24.9	41.4
0.000	0.00E+00	4174.1	2.582E+05	3.62E+00	2.17E-01	1.01E-06	2574.5	5.5E+04	1.2E+04	24.9	41.4
0.099	-1.04E+06	4232.7	2.886E+05	4.36E+00	2.46E-01	1.10E-06	2562.5	5.5E+04	1.0E+04	24.9	41.4
0.197	-2.08E+06	4301.9	3.218E+05	5.37E+00	2.83E-01	1.21E-06	2550.7	5.5E+04	8.8E+03	24.9	41.4
0.295	-3.12E+06	4380.8	3.580E+05	6.68E+00	3.28E-01	1.32E-06	2539.0	5.5E+04	7.2E+03	24.9	41.4
0.394	-4.16E+06	4468.4	3.974E+05	8.41E+00	3.80E-01	1.43E-06	2527.5	5.5E+04	5.7E+03	24.9	41.4
0.492	-5.20E+06	4564.0	4.400E+05	1.06E+01	4.41E-01	1.54E-06	2516.1	5.5E+04	4.3E+03	24.9	41.4
0.589	-6.23E+06	4666.8	4.859E+05	1.35E+01	5.10E-01	1.66E-06	2504.7	5.5E+04	3.0E+03	24.9	41.4
0.685	-7.27E+06	4776.3	5.353E+05	1.70E+01	5.87E-01	1.78E-06	2493.6	5.5E+04	1.7E+03	24.9	41.4
0.779	-8.31E+06	4891.8	5.883E+05	2.14E+01	6.71E-01	1.91E-06	2482.7	5.5E+04	3.8E+02	24.9	41.4
0.871	-9.35E+06	5012.6	6.447E+05	2.66E+01	7.67E-01	2.02E-06	2472.1	5.5E+04	-8.6E+02	24.9	41.4
0.960	-1.04E+07	5138.3	7.046E+05	3.30E+01	8.64E-01	2.15E-06	2461.8	5.5E+04	-2.0E+03	24.9	41.4
1.046	-1.14E+07	5268.5	7.682E+05	4.06E+01	9.60E-01	2.28E-06	2451.8	5.5E+04	-3.2E+03	24.9	41.4

Tab. F.6 Average model atmosphere of the diffuse background region (DB) of sunspot umbra S2 (NOAA 10933).

log $\tau_{5000}$	height [cm]	T [K]	$P_{gas}$ [g cm $^{-1}$ s $^{-2}$ ]	$P_{electr.}$ [g cm $^{-1}$ s $^{-2}$ ]	$\kappa$ [g $^{-1}$ ]	$\rho$ [cm $^{-3}$ ]	B [G]	$\zeta_{\mu}$ [cm s $^{-1}$ ]	$v_{LOS}$ [cm s $^{-1}$ ]	$\gamma_B$ [deg]	$\chi_B$
-4.000	4.61E+07	3320.9	1.377E+03	1.49E-02	3.28E-03	6.61E-09	2471.0	7.1E+04	3.5E+04	26.3	27.1
-3.900	4.49E+07	3338.2	1.583E+03	1.72E-02	3.63E-03	7.56E-09	2465.1	7.1E+04	3.5E+04	26.3	27.1
-3.800	4.38E+07	3355.5	1.818E+03	1.98E-02	4.01E-03	8.64E-09	2459.1	7.1E+04	3.5E+04	26.3	27.1
-3.700	4.26E+07	3372.7	2.085E+03	2.27E-02	4.44E-03	9.86E-09	2453.2	7.1E+04	3.4E+04	26.3	27.1
-3.600	4.15E+07	3389.9	2.389E+03	2.61E-02	4.91E-03	1.12E-08	2447.3	7.1E+04	3.4E+04	26.3	27.1
-3.500	4.04E+07	3407.0	2.735E+03	2.99E-02	5.43E-03	1.28E-08	2441.4	7.1E+04	3.3E+04	26.3	27.1
-3.400	3.92E+07	3424.1	3.128E+03	3.42E-02	6.02E-03	1.46E-08	2435.6	7.1E+04	3.3E+04	26.3	27.1
-3.300	3.81E+07	3441.0	3.575E+03	3.91E-02	6.66E-03	1.66E-08	2429.7	7.1E+04	3.2E+04	26.3	27.1
-3.200	3.69E+07	3457.8	4.083E+03	4.47E-02	7.37E-03	1.89E-08	2423.8	7.1E+04	3.2E+04	26.3	27.1
-3.100	3.58E+07	3474.5	4.662E+03	5.10E-02	8.15E-03	2.14E-08	2418.0	7.1E+04	3.1E+04	26.3	27.1
-3.000	3.47E+07	3490.9	5.320E+03	5.81E-02	9.02E-03	2.44E-08	2412.2	7.1E+04	3.1E+04	26.3	27.1
-2.900	3.35E+07	3507.1	6.068E+03	6.62E-02	9.98E-03	2.77E-08	2406.5	7.1E+04	3.1E+04	26.3	27.1
-2.800	3.24E+07	3522.9	6.920E+03	7.52E-02	1.10E-02	3.14E-08	2400.8	7.1E+04	3.0E+04	26.3	27.1
-2.700	3.12E+07	3538.2	7.890E+03	8.54E-02	1.22E-02	3.57E-08	2395.1	7.1E+04	3.0E+04	26.3	27.1
-2.600	3.01E+07	3553.0	8.996E+03	9.67E-02	1.35E-02	4.06E-08	2389.6	7.1E+04	2.9E+04	26.3	27.1
-2.500	2.90E+07	3567.0	1.026E+04	1.09E-01	1.49E-02	4.61E-08	2384.2	7.1E+04	2.9E+04	26.3	27.1
-2.400	2.78E+07	3580.2	1.170E+04	1.23E-01	1.64E-02	5.24E-08	2378.8	7.1E+04	2.9E+04	26.3	27.1
-2.300	2.66E+07	3592.7	1.334E+04	1.39E-01	1.80E-02	5.97E-08	2373.6	7.1E+04	2.8E+04	26.3	27.1
-2.200	2.55E+07	3604.8	1.522E+04	1.56E-01	1.99E-02	6.79E-08	2368.5	7.1E+04	2.8E+04	26.3	27.1
-2.100	2.43E+07	3616.8	1.737E+04	1.76E-01	2.19E-02	7.74E-08	2363.4	7.1E+04	2.7E+04	26.3	27.1
-2.000	2.32E+07	3628.8	1.982E+04	1.98E-01	2.41E-02	8.82E-08	2358.2	7.1E+04	2.7E+04	26.3	27.1
-1.900	2.20E+07	3641.2	2.263E+04	2.23E-01	2.65E-02	1.00E-07	2353.1	7.1E+04	2.7E+04	26.3	27.1
-1.800	2.08E+07	3654.1	2.583E+04	2.52E-01	2.92E-02	1.15E-07	2347.8	7.1E+04	2.6E+04	26.3	27.1
-1.700	1.96E+07	3667.9	2.949E+04	2.85E-01	3.23E-02	1.30E-07	2342.5	7.1E+04	2.6E+04	26.3	27.1
-1.600	1.85E+07	3682.9	3.367E+04	3.22E-01	3.56E-02	1.49E-07	2336.9	7.1E+04	2.6E+04	26.3	27.1
-1.500	1.73E+07	3699.5	3.842E+04	3.67E-01	3.94E-02	1.69E-07	2331.2	7.1E+04	2.5E+04	26.3	27.1
-1.400	1.61E+07	3718.2	4.383E+04	4.19E-01	4.37E-02	1.92E-07	2325.2	7.1E+04	2.5E+04	26.3	27.1
-1.300	1.49E+07	3739.8	4.996E+04	4.81E-01	4.86E-02	2.18E-07	2318.8	7.1E+04	2.4E+04	26.3	27.1
-1.200	1.38E+07	3765.0	5.689E+04	5.56E-01	5.42E-02	2.47E-07	2311.9	7.1E+04	2.4E+04	26.3	27.1
-1.100	1.26E+07	3794.8	6.469E+04	6.48E-01	6.08E-02	2.79E-07	2304.4	7.1E+04	2.3E+04	26.3	27.1
-1.000	1.14E+07	3830.8	7.342E+04	7.65E-01	6.85E-02	3.14E-07	2296.1	7.1E+04	2.2E+04	26.3	27.1
-0.900	1.03E+07	3873.8	8.313E+04	9.14E-01	7.78E-02	3.51E-07	2286.9	7.1E+04	2.1E+04	26.3	27.1
-0.800	9.12E+06	3922.8	9.387E+04	1.10E+00	8.89E-02	3.91E-07	2276.8	7.1E+04	2.1E+04	26.3	27.1
-0.700	7.98E+06	3976.2	1.057E+05	1.34E+00	1.02E-01	4.33E-07	2266.2	7.1E+04	2.0E+04	26.3	27.1
-0.600	6.84E+06	4032.9	1.187E+05	1.63E+00	1.17E-01	4.78E-07	2255.1	7.1E+04	1.9E+04	26.3	27.1
-0.500	5.71E+06	4091.9	1.329E+05	1.99E+00	1.34E-01	5.27E-07	2243.8	7.1E+04	1.8E+04	26.3	27.1
-0.400	4.58E+06	4152.2	1.486E+05	2.43E+00	1.53E-01	5.79E-07	2232.2	7.1E+04	1.6E+04	26.3	27.1
-0.300	3.44E+06	4213.2	1.659E+05	2.96E+00	1.75E-01	6.36E-07	2220.6	7.1E+04	1.5E+04	26.3	27.1
-0.200	2.30E+06	4274.1	1.849E+05	3.58E+00	1.99E-01	6.97E-07	2208.9	7.1E+04	1.4E+04	26.3	27.1
-0.100	1.16E+06	4334.2	2.061E+05	4.31E+00	2.26E-01	7.65E-07	2197.4	7.1E+04	1.3E+04	26.3	27.1
0.000	0.00E+00	4392.7	2.295E+05	5.16E+00	2.55E-01	8.40E-07	2186.1	7.1E+04	1.2E+04	26.3	27.1
0.099	-1.16E+06	4461.9	2.553E+05	6.24E+00	2.89E-01	9.12E-07	2173.9	7.1E+04	1.1E+04	26.3	27.1
0.198	-2.31E+06	4541.0	2.832E+05	7.67E+00	3.29E-01	9.92E-07	2162.1	7.1E+04	1.0E+04	26.3	27.1
0.297	-3.47E+06	4629.0	3.136E+05	9.48E+00	3.76E-01	1.08E-06	2150.6	7.1E+04	9.3E+03	26.3	27.1
0.396	-4.62E+06	4725.1	3.464E+05	1.17E+01	4.28E-01	1.16E-06	2139.3	7.1E+04	8.5E+03	26.3	27.1
0.495	-5.78E+06	4828.8	3.819E+05	1.46E+01	4.85E-01	1.25E-06	2128.2	7.1E+04	7.8E+03	26.3	27.1
0.593	-6.94E+06	4939.1	4.199E+05	1.80E+01	5.48E-01	1.34E-06	2117.5	7.1E+04	7.3E+03	26.3	27.1
0.690	-8.09E+06	5055.6	4.607E+05	2.21E+01	6.16E-01	1.43E-06	2107.0	7.1E+04	6.7E+03	26.3	27.1
0.785	-9.25E+06	5177.7	5.041E+05	2.70E+01	6.87E-01	1.53E-06	2096.8	7.1E+04	6.2E+03	26.3	27.1
0.878	-1.04E+07	5304.8	5.504E+05	3.29E+01	7.59E-01	1.63E-06	2087.0	7.1E+04	5.8E+03	26.3	27.1
0.969	-1.16E+07	5436.6	5.997E+05	4.00E+01	8.37E-01	1.73E-06	2077.5	7.1E+04	5.4E+03	26.3	27.1
1.056	-1.27E+07	5572.6	6.521E+05	4.88E+01	9.26E-01	1.83E-06	2068.3	7.1E+04	5.0E+03	26.3	27.1

Tab. F.7 Average model atmosphere of the core umbral dots (CUD) of sunspot umbra S2 (NOAA 10 933).

$\log \tau_{5000}$	height [cm]	T [K]	$P_{gas}$ [g cm <sup>-1</sup> s <sup>-2</sup> ]	$P_{electr.}$ [g <sup>-1</sup> s <sup>-2</sup> ]	$\kappa$ [g <sup>-1</sup> ]	$\rho$ [cm <sup>-3</sup> ]	B [G]	$\zeta_{\mu}$ [cm s <sup>-1</sup> ]	$v_{LOS}$ [cm s <sup>-1</sup> ]	$\gamma_B$ [deg]	$\chi_B$
-4.000	4.18E+07	3238.4	1.458E+03	1.23E-02	3.09E-03	7.19E-09	2396.3	9.2E+04	4.5E+04	24.9	22.2
-3.900	4.07E+07	3257.2	1.676E+03	1.42E-02	3.42E-03	8.23E-09	2391.8	9.2E+04	4.4E+04	24.9	22.2
-3.800	3.97E+07	3276.0	1.925E+03	1.65E-02	3.78E-03	9.40E-09	2387.3	9.2E+04	4.4E+04	24.9	22.2
-3.700	3.86E+07	3294.8	2.207E+03	1.90E-02	4.19E-03	1.07E-08	2382.8	9.2E+04	4.3E+04	24.9	22.2
-3.600	3.76E+07	3313.5	2.528E+03	2.19E-02	4.64E-03	1.22E-08	2378.3	9.2E+04	4.2E+04	24.9	22.2
-3.500	3.66E+07	3332.2	2.893E+03	2.53E-02	5.15E-03	1.39E-08	2373.9	9.2E+04	4.1E+04	24.9	22.2
-3.400	3.55E+07	3350.9	3.307E+03	2.91E-02	5.70E-03	1.58E-08	2369.4	9.2E+04	4.0E+04	24.9	22.2
-3.300	3.45E+07	3369.6	3.778E+03	3.35E-02	6.32E-03	1.80E-08	2364.9	9.2E+04	3.9E+04	24.9	22.2
-3.200	3.34E+07	3388.2	4.313E+03	3.85E-02	7.01E-03	2.04E-08	2360.5	9.2E+04	3.8E+04	24.9	22.2
-3.100	3.24E+07	3406.7	4.920E+03	4.42E-02	7.76E-03	2.32E-08	2356.1	9.2E+04	3.8E+04	24.9	22.2
-3.000	3.14E+07	3425.2	5.609E+03	5.07E-02	8.61E-03	2.63E-08	2351.7	9.2E+04	3.7E+04	24.9	22.2
-2.900	3.03E+07	3443.6	6.393E+03	5.81E-02	9.54E-03	2.98E-08	2347.4	9.2E+04	3.6E+04	24.9	22.2
-2.800	2.93E+07	3461.8	7.282E+03	6.65E-02	1.06E-02	3.38E-08	2343.1	9.2E+04	3.5E+04	24.9	22.2
-2.700	2.83E+07	3479.8	8.293E+03	7.60E-02	1.17E-02	3.83E-08	2338.9	9.2E+04	3.4E+04	24.9	22.2
-2.600	2.72E+07	3497.7	9.442E+03	8.69E-02	1.30E-02	4.34E-08	2334.8	9.2E+04	3.3E+04	24.9	22.2
-2.500	2.62E+07	3515.2	1.075E+04	9.91E-02	1.43E-02	4.92E-08	2330.7	9.2E+04	3.3E+04	24.9	22.2
-2.400	2.51E+07	3532.5	1.223E+04	1.13E-01	1.59E-02	5.58E-08	2326.9	9.2E+04	3.2E+04	24.9	22.2
-2.300	2.41E+07	3549.5	1.393E+04	1.29E-01	1.76E-02	6.33E-08	2323.1	9.2E+04	3.1E+04	24.9	22.2
-2.200	2.30E+07	3566.5	1.585E+04	1.46E-01	1.94E-02	7.18E-08	2319.3	9.2E+04	3.0E+04	24.9	22.2
-2.100	2.20E+07	3583.7	1.804E+04	1.67E-01	2.15E-02	8.14E-08	2315.6	9.2E+04	3.0E+04	24.9	22.2
-2.000	2.09E+07	3601.1	2.053E+04	1.90E-01	2.38E-02	9.23E-08	2311.9	9.2E+04	2.9E+04	24.9	22.2
-1.900	1.98E+07	3619.0	2.336E+04	2.17E-01	2.64E-02	1.05E-07	2308.1	9.2E+04	2.8E+04	24.9	22.2
-1.800	1.88E+07	3637.7	2.659E+04	2.48E-01	2.92E-02	1.19E-07	2304.3	9.2E+04	2.7E+04	24.9	22.2
-1.700	1.77E+07	3657.3	3.025E+04	2.84E-01	3.24E-02	1.35E-07	2300.4	9.2E+04	2.7E+04	24.9	22.2
-1.600	1.66E+07	3678.1	3.441E+04	3.26E-01	3.60E-02	1.52E-07	2296.3	9.2E+04	2.6E+04	24.9	22.2
-1.500	1.56E+07	3700.7	3.912E+04	3.76E-01	4.00E-02	1.73E-07	2292.0	9.2E+04	2.5E+04	24.9	22.2
-1.400	1.45E+07	3725.4	4.445E+04	4.35E-01	4.46E-02	1.95E-07	2287.4	9.2E+04	2.4E+04	24.9	22.2
-1.300	1.34E+07	3753.0	5.048E+04	5.05E-01	4.98E-02	2.20E-07	2282.4	9.2E+04	2.3E+04	24.9	22.2
-1.200	1.24E+07	3784.2	5.726E+04	5.91E-01	5.59E-02	2.48E-07	2277.0	9.2E+04	2.2E+04	24.9	22.2
-1.100	1.13E+07	3820.1	6.485E+04	6.98E-01	6.29E-02	2.78E-07	2270.9	9.2E+04	2.1E+04	24.9	22.2
-1.000	1.02E+07	3862.1	7.332E+04	8.31E-01	7.13E-02	3.11E-07	2264.1	9.2E+04	2.0E+04	24.9	22.2
-0.900	9.21E+06	3911.2	8.270E+04	1.00E+00	8.13E-02	3.46E-07	2256.3	9.2E+04	1.8E+04	24.9	22.2
-0.800	8.17E+06	3966.2	9.302E+04	1.22E+00	9.31E-02	3.83E-07	2247.7	9.2E+04	1.7E+04	24.9	22.2
-0.700	7.15E+06	4025.7	1.043E+05	1.50E+00	1.07E-01	4.22E-07	2238.5	9.2E+04	1.5E+04	24.9	22.2
-0.600	6.13E+06	4088.4	1.167E+05	1.84E+00	1.23E-01	4.63E-07	2228.9	9.2E+04	1.3E+04	24.9	22.2
-0.500	5.11E+06	4153.4	1.303E+05	2.25E+00	1.41E-01	5.08E-07	2219.0	9.2E+04	1.2E+04	24.9	22.2
-0.400	4.10E+06	4219.7	1.452E+05	2.76E+00	1.62E-01	5.56E-07	2208.9	9.2E+04	1.0E+04	24.9	22.2
-0.300	3.08E+06	4286.8	1.616E+05	3.37E+00	1.85E-01	6.07E-07	2198.8	9.2E+04	8.2E+03	24.9	22.2
-0.200	2.06E+06	4353.7	1.796E+05	4.10E+00	2.10E-01	6.63E-07	2188.6	9.2E+04	6.4E+03	24.9	22.2
-0.100	1.04E+06	4419.8	1.996E+05	4.96E+00	2.39E-01	7.25E-07	2178.6	9.2E+04	4.7E+03	24.9	22.2
0.000	0.00E+00	4484.4	2.219E+05	5.95E+00	2.69E-01	7.93E-07	2168.7	9.2E+04	2.9E+03	24.9	22.2
0.099	-1.04E+06	4559.1	2.462E+05	7.20E+00	3.04E-01	8.59E-07	2158.2	9.2E+04	1.2E+03	24.9	22.2
0.196	-2.08E+06	4643.3	2.725E+05	8.81E+00	3.45E-01	9.32E-07	2148.1	9.2E+04	-4.4E+02	24.9	22.2
0.293	-3.12E+06	4735.9	3.010E+05	1.08E+01	3.90E-01	1.01E-06	2138.2	9.2E+04	-1.9E+03	24.9	22.2
0.390	-4.15E+06	4836.4	3.318E+05	1.33E+01	4.41E-01	1.09E-06	2128.6	9.2E+04	-3.3E+03	24.9	22.2
0.486	-5.19E+06	4943.9	3.649E+05	1.63E+01	4.96E-01	1.17E-06	2119.3	9.2E+04	-4.6E+03	24.9	22.2
0.580	-6.23E+06	5057.8	4.004E+05	2.00E+01	5.54E-01	1.25E-06	2110.2	9.2E+04	-5.8E+03	24.9	22.2
0.673	-7.27E+06	5177.6	4.383E+05	2.43E+01	6.17E-01	1.33E-06	2101.4	9.2E+04	-6.9E+03	24.9	22.2
0.763	-8.31E+06	5302.8	4.787E+05	2.96E+01	6.82E-01	1.42E-06	2093.0	9.2E+04	-7.9E+03	24.9	22.2
0.851	-9.35E+06	5432.8	5.218E+05	3.60E+01	7.54E-01	1.51E-06	2084.8	9.2E+04	-8.8E+03	24.9	22.2
0.936	-1.04E+07	5567.2	5.675E+05	4.40E+01	8.37E-01	1.60E-06	2076.8	9.2E+04	-9.8E+03	24.9	22.2
1.017	-1.14E+07	5705.7	6.160E+05	5.44E+01	9.40E-01	1.69E-06	2068.9	9.2E+04	-1.1E+04	24.9	22.2

Tab. F.8 Average model atmosphere of the peripheral umbral dots (PUD) of sunspot umbra S2 (NOAA 10933).

log $\tau_{5000}$	height [cm]	T [K]	$P_{gas}$ [g cm <sup>-1</sup> s <sup>-2</sup> ]	$P_{electr.}$ [g cm <sup>-1</sup> s <sup>-2</sup> ]	$\kappa$ [g <sup>-1</sup> ]	$\rho$ [cm <sup>-3</sup> ]	B [G]	$\zeta_{\mu}$ [cm s <sup>-1</sup> ]	$v_{LOS}$ [cm s <sup>-1</sup> ]	$\gamma_B$ [deg]	$X_B$
-4.000	4.46E+07	3281.5	1.422E+03	1.36E-02	3.19E-03	6.92E-09	2354.9	9.3E+04	3.5E+04	32.3	37.5
-3.900	4.34E+07	3301.2	1.634E+03	1.58E-02	3.54E-03	7.90E-09	2348.3	9.3E+04	3.5E+04	32.3	37.5
-3.800	4.23E+07	3320.7	1.874E+03	1.83E-02	3.92E-03	9.01E-09	2341.7	9.3E+04	3.4E+04	32.3	37.5
-3.700	4.12E+07	3340.3	2.147E+03	2.12E-02	4.34E-03	1.03E-08	2335.0	9.3E+04	3.3E+04	32.3	37.5
-3.600	4.00E+07	3359.9	2.457E+03	2.44E-02	4.82E-03	1.17E-08	2328.4	9.3E+04	3.2E+04	32.3	37.5
-3.500	3.89E+07	3379.5	2.809E+03	2.82E-02	5.34E-03	1.33E-08	2321.8	9.3E+04	3.2E+04	32.3	37.5
-3.400	3.78E+07	3399.0	3.208E+03	3.25E-02	5.93E-03	1.51E-08	2315.1	9.3E+04	3.1E+04	32.3	37.5
-3.300	3.67E+07	3418.6	3.661E+03	3.74E-02	6.58E-03	1.71E-08	2308.5	9.3E+04	3.0E+04	32.3	37.5
-3.200	3.55E+07	3438.1	4.175E+03	4.31E-02	7.30E-03	1.94E-08	2301.9	9.3E+04	2.9E+04	32.3	37.5
-3.100	3.44E+07	3457.6	4.759E+03	4.95E-02	8.09E-03	2.20E-08	2295.3	9.3E+04	2.9E+04	32.3	37.5
-3.000	3.33E+07	3477.0	5.421E+03	5.69E-02	8.98E-03	2.50E-08	2288.7	9.3E+04	2.8E+04	32.3	37.5
-2.900	3.22E+07	3496.4	6.172E+03	6.52E-02	9.96E-03	2.83E-08	2282.1	9.3E+04	2.7E+04	32.3	37.5
-2.800	3.11E+07	3515.7	7.024E+03	7.48E-02	1.10E-02	3.20E-08	2275.5	9.3E+04	2.6E+04	32.3	37.5
-2.700	2.99E+07	3535.0	7.992E+03	8.56E-02	1.23E-02	3.62E-08	2269.0	9.3E+04	2.6E+04	32.3	37.5
-2.600	2.88E+07	3554.1	9.091E+03	9.80E-02	1.36E-02	4.10E-08	2262.4	9.3E+04	2.5E+04	32.3	37.5
-2.500	2.77E+07	3573.1	1.034E+04	1.12E-01	1.51E-02	4.64E-08	2255.9	9.3E+04	2.4E+04	32.3	37.5
-2.400	2.66E+07	3592.0	1.176E+04	1.28E-01	1.67E-02	5.25E-08	2249.5	9.3E+04	2.4E+04	32.3	37.5
-2.300	2.54E+07	3610.8	1.337E+04	1.46E-01	1.85E-02	5.94E-08	2243.1	9.3E+04	2.3E+04	32.3	37.5
-2.200	2.43E+07	3629.7	1.520E+04	1.67E-01	2.05E-02	6.73E-08	2236.7	9.3E+04	2.2E+04	32.3	37.5
-2.100	2.31E+07	3648.7	1.727E+04	1.91E-01	2.27E-02	7.62E-08	2230.3	9.3E+04	2.1E+04	32.3	37.5
-2.000	2.20E+07	3668.1	1.964E+04	2.18E-01	2.52E-02	8.62E-08	2223.9	9.3E+04	2.1E+04	32.3	37.5
-1.900	2.08E+07	3688.0	2.232E+04	2.50E-01	2.79E-02	9.76E-08	2217.5	9.3E+04	2.0E+04	32.3	37.5
-1.800	1.97E+07	3708.5	2.537E+04	2.87E-01	3.10E-02	1.10E-07	2211.1	9.3E+04	1.9E+04	32.3	37.5
-1.700	1.86E+07	3729.8	2.883E+04	3.29E-01	3.45E-02	1.25E-07	2204.6	9.3E+04	1.9E+04	32.3	37.5
-1.600	1.74E+07	3752.4	3.275E+04	3.79E-01	3.83E-02	1.41E-07	2198.1	9.3E+04	1.8E+04	32.3	37.5
-1.500	1.63E+07	3776.4	3.719E+04	4.38E-01	4.27E-02	1.60E-07	2191.5	9.3E+04	1.7E+04	32.3	37.5
-1.400	1.51E+07	3802.4	4.222E+04	5.07E-01	4.76E-02	1.80E-07	2184.8	9.3E+04	1.6E+04	32.3	37.5
-1.300	1.40E+07	3830.9	4.790E+04	5.90E-01	5.32E-02	2.03E-07	2178.1	9.3E+04	1.6E+04	32.3	37.5
-1.200	1.29E+07	3862.6	5.429E+04	6.90E-01	5.96E-02	2.29E-07	2171.1	9.3E+04	1.5E+04	32.3	37.5
-1.100	1.18E+07	3898.5	6.146E+04	8.12E-01	6.70E-02	2.57E-07	2164.0	9.3E+04	1.4E+04	32.3	37.5
-1.000	1.06E+07	3939.7	6.947E+04	9.64E-01	7.57E-02	2.87E-07	2156.6	9.3E+04	1.3E+04	32.3	37.5
-0.900	9.56E+06	3987.3	7.836E+04	1.16E+00	8.60E-02	3.20E-07	2148.9	9.3E+04	1.2E+04	32.3	37.5
-0.800	8.47E+06	4040.1	8.819E+04	1.39E+00	9.80E-02	3.55E-07	2141.0	9.3E+04	1.1E+04	32.3	37.5
-0.700	7.40E+06	4096.8	9.901E+04	1.69E+00	1.12E-01	3.92E-07	2132.9	9.3E+04	9.9E+03	32.3	37.5
-0.600	6.34E+06	4156.4	1.109E+05	2.05E+00	1.28E-01	4.32E-07	2124.6	9.3E+04	8.7E+03	32.3	37.5
-0.500	5.29E+06	4218.0	1.240E+05	2.49E+00	1.46E-01	4.75E-07	2116.2	9.3E+04	7.6E+03	32.3	37.5
-0.400	4.24E+06	4280.9	1.385E+05	3.02E+00	1.66E-01	5.21E-07	2107.8	9.3E+04	6.4E+03	32.3	37.5
-0.300	3.19E+06	4344.3	1.545E+05	3.65E+00	1.89E-01	5.72E-07	2099.4	9.3E+04	5.3E+03	32.3	37.5
-0.200	2.13E+06	4407.6	1.722E+05	4.40E+00	2.14E-01	6.27E-07	2090.9	9.3E+04	4.1E+03	32.3	37.5
-0.100	1.07E+06	4470.3	1.919E+05	5.27E+00	2.42E-01	6.88E-07	2082.5	9.3E+04	3.0E+03	32.3	37.5
0.000	0.00E+00	4531.5	2.138E+05	6.28E+00	2.72E-01	7.56E-07	2074.2	9.3E+04	1.8E+03	32.3	37.5
0.099	-1.07E+06	4603.9	2.379E+05	7.55E+00	3.06E-01	8.21E-07	2065.3	9.3E+04	6.6E+02	32.3	37.5
0.196	-2.15E+06	4686.4	2.641E+05	9.19E+00	3.46E-01	8.94E-07	2056.7	9.3E+04	-3.9E+02	32.3	37.5
0.293	-3.22E+06	4778.3	2.926E+05	1.13E+01	3.92E-01	9.70E-07	2048.4	9.3E+04	-1.4E+03	32.3	37.5
0.390	-4.29E+06	4878.6	3.235E+05	1.38E+01	4.42E-01	1.05E-06	2040.3	9.3E+04	-2.3E+03	32.3	37.5
0.485	-5.36E+06	4986.7	3.568E+05	1.69E+01	4.96E-01	1.13E-06	2032.4	9.3E+04	-3.2E+03	32.3	37.5
0.579	-6.44E+06	5101.7	3.926E+05	2.07E+01	5.55E-01	1.21E-06	2024.7	9.3E+04	-4.0E+03	32.3	37.5
0.671	-7.51E+06	5223.2	4.309E+05	2.53E+01	6.18E-01	1.30E-06	2017.3	9.3E+04	-4.8E+03	32.3	37.5
0.761	-8.58E+06	5350.5	4.720E+05	3.09E+01	6.86E-01	1.38E-06	2010.1	9.3E+04	-5.5E+03	32.3	37.5
0.849	-9.66E+06	5483.1	5.158E+05	3.79E+01	7.62E-01	1.48E-06	2003.1	9.3E+04	-6.3E+03	32.3	37.5
0.933	-1.07E+07	5620.6	5.624E+05	4.69E+01	8.54E-01	1.57E-06	1996.2	9.3E+04	-6.9E+03	32.3	37.5
1.015	-1.18E+07	5762.6	6.120E+05	5.88E+01	9.71E-01	1.67E-06	1989.3	9.3E+04	-7.6E+03	32.3	37.5

Tab. F.9 Average model atmosphere of the core umbra region (CU) of sunspot umbra S3 (NOAA 10 944).

$\log \tau_{5000}$	height [cm]	T [K]	$P_{gas}$ [g cm <sup>-1</sup> s <sup>-2</sup> ]	$P_{electr.}$ [g <sup>-1</sup> s <sup>-2</sup> ]	$\kappa$ [g <sup>-1</sup> ]	$\rho$ [cm <sup>-3</sup> ]	B [G]	$\zeta_{\mu}$ [cm s <sup>-1</sup> ]	$v_{LOS}$ [cm s <sup>-1</sup> ]	$\gamma_B$ [deg]	$\chi_B$
-4.000	4.30E+07	3336.0	1.347E+03	1.50E-02	3.27E-03	6.41E-09	4014.1	7.0E+04	2.5E+04	26.3	5.9
-3.900	4.20E+07	3348.4	1.553E+03	1.71E-02	3.61E-03	7.36E-09	3967.2	7.0E+04	2.5E+04	26.3	5.9
-3.800	4.09E+07	3360.7	1.789E+03	1.94E-02	3.97E-03	8.45E-09	3920.2	7.0E+04	2.5E+04	26.3	5.9
-3.700	3.98E+07	3373.1	2.058E+03	2.21E-02	4.38E-03	9.70E-09	3873.3	7.0E+04	2.5E+04	26.3	5.9
-3.600	3.87E+07	3385.4	2.365E+03	2.51E-02	4.83E-03	1.11E-08	3826.3	7.0E+04	2.5E+04	26.3	5.9
-3.500	3.76E+07	3397.6	2.716E+03	2.85E-02	5.33E-03	1.27E-08	3779.3	7.0E+04	2.5E+04	26.3	5.9
-3.400	3.66E+07	3409.8	3.117E+03	3.23E-02	5.87E-03	1.46E-08	3732.2	7.0E+04	2.5E+04	26.3	5.9
-3.300	3.55E+07	3422.0	3.574E+03	3.66E-02	6.48E-03	1.66E-08	3685.0	7.0E+04	2.5E+04	26.3	5.9
-3.200	3.44E+07	3434.1	4.096E+03	4.15E-02	7.15E-03	1.90E-08	3637.7	7.0E+04	2.5E+04	26.3	5.9
-3.100	3.33E+07	3446.1	4.692E+03	4.70E-02	7.88E-03	2.17E-08	3590.3	7.0E+04	2.5E+04	26.3	5.9
-3.000	3.23E+07	3457.9	5.372E+03	5.31E-02	8.69E-03	2.48E-08	3542.7	7.0E+04	2.5E+04	26.3	5.9
-2.900	3.12E+07	3469.6	6.149E+03	6.00E-02	9.58E-03	2.83E-08	3494.9	7.0E+04	2.5E+04	26.3	5.9
-2.800	3.01E+07	3481.0	7.036E+03	6.77E-02	1.06E-02	3.24E-08	3446.8	7.0E+04	2.5E+04	26.3	5.9
-2.700	2.90E+07	3492.2	8.048E+03	7.64E-02	1.16E-02	3.70E-08	3398.3	7.0E+04	2.6E+04	26.3	5.9
-2.600	2.80E+07	3503.1	9.206E+03	8.60E-02	1.28E-02	4.22E-08	3349.3	7.0E+04	2.6E+04	26.3	5.9
-2.500	2.69E+07	3513.4	1.053E+04	9.68E-02	1.41E-02	4.82E-08	3299.8	7.0E+04	2.6E+04	26.3	5.9
-2.400	2.58E+07	3523.3	1.204E+04	1.09E-01	1.55E-02	5.51E-08	3249.5	7.0E+04	2.6E+04	26.3	5.9
-2.300	2.48E+07	3532.8	1.377E+04	1.22E-01	1.71E-02	6.29E-08	3198.6	7.0E+04	2.6E+04	26.3	5.9
-2.200	2.37E+07	3542.0	1.576E+04	1.37E-01	1.88E-02	7.19E-08	3147.1	7.0E+04	2.6E+04	26.3	5.9
-2.100	2.26E+07	3551.1	1.803E+04	1.54E-01	2.06E-02	8.23E-08	3095.2	7.0E+04	2.7E+04	26.3	5.9
-2.000	2.15E+07	3560.2	2.063E+04	1.72E-01	2.27E-02	9.42E-08	3042.9	7.0E+04	2.7E+04	26.3	5.9
-1.900	2.04E+07	3569.5	2.361E+04	1.94E-01	2.49E-02	1.08E-07	2990.3	7.0E+04	2.7E+04	26.3	5.9
-1.800	1.93E+07	3579.1	2.702E+04	2.18E-01	2.74E-02	1.23E-07	2937.2	7.0E+04	2.7E+04	26.3	5.9
-1.700	1.82E+07	3589.1	3.092E+04	2.45E-01	3.02E-02	1.41E-07	2883.8	7.0E+04	2.7E+04	26.3	5.9
-1.600	1.72E+07	3599.8	3.539E+04	2.76E-01	3.32E-02	1.62E-07	2829.9	7.0E+04	2.8E+04	26.3	5.9
-1.500	1.61E+07	3611.3	4.050E+04	3.11E-01	3.65E-02	1.85E-07	2775.5	7.0E+04	2.8E+04	26.3	5.9
-1.400	1.50E+07	3624.1	4.635E+04	3.52E-01	4.03E-02	2.12E-07	2720.5	7.0E+04	2.8E+04	26.3	5.9
-1.300	1.39E+07	3638.3	5.302E+04	3.99E-01	4.44E-02	2.42E-07	2664.8	7.0E+04	2.8E+04	26.3	5.9
-1.200	1.28E+07	3654.6	6.062E+04	4.55E-01	4.91E-02	2.76E-07	2608.0	7.0E+04	2.8E+04	26.3	5.9
-1.100	1.17E+07	3673.4	6.927E+04	5.20E-01	5.44E-02	3.15E-07	2550.1	7.0E+04	2.7E+04	26.3	5.9
-1.000	1.07E+07	3695.5	7.909E+04	5.99E-01	6.04E-02	3.58E-07	2490.6	7.0E+04	2.7E+04	26.3	5.9
-0.900	9.59E+06	3721.5	9.019E+04	6.94E-01	6.74E-02	4.06E-07	2429.3	7.0E+04	2.6E+04	26.3	5.9
-0.800	8.52E+06	3750.7	1.027E+05	8.08E-01	7.54E-02	4.59E-07	2366.5	7.0E+04	2.6E+04	26.3	5.9
-0.700	7.45E+06	3782.4	1.167E+05	9.44E-01	8.46E-02	5.18E-07	2302.5	7.0E+04	2.5E+04	26.3	5.9
-0.600	6.39E+06	3815.8	1.325E+05	1.10E+00	9.49E-02	5.83E-07	2237.8	7.0E+04	2.4E+04	26.3	5.9
-0.500	5.33E+06	3850.5	1.502E+05	1.29E+00	1.07E-01	6.54E-07	2172.4	7.0E+04	2.3E+04	26.3	5.9
-0.400	4.27E+06	3885.9	1.701E+05	1.52E+00	1.20E-01	7.34E-07	2106.7	7.0E+04	2.2E+04	26.3	5.9
-0.300	3.21E+06	3921.7	1.923E+05	1.78E+00	1.34E-01	8.22E-07	2040.8	7.0E+04	2.1E+04	26.3	5.9
-0.200	2.14E+06	3957.5	2.173E+05	2.08E+00	1.50E-01	9.20E-07	1975.0	7.0E+04	2.0E+04	26.3	5.9
-0.100	1.08E+06	3992.8	2.454E+05	2.42E+00	1.68E-01	1.03E-06	1909.3	7.0E+04	1.9E+04	26.3	5.9
0.000	0.00E+00	4027.2	2.770E+05	2.82E+00	1.88E-01	1.15E-06	1844.1	7.0E+04	1.9E+04	26.3	5.9
0.099	-1.08E+06	4074.7	3.123E+05	3.35E+00	2.13E-01	1.27E-06	1773.3	7.0E+04	1.8E+04	26.3	5.9
0.199	-2.15E+06	4134.2	3.511E+05	4.08E+00	2.44E-01	1.40E-06	1703.7	7.0E+04	1.7E+04	26.3	5.9
0.299	-3.23E+06	4204.6	3.940E+05	5.06E+00	2.84E-01	1.54E-06	1634.5	7.0E+04	1.6E+04	26.3	5.9
0.401	-4.30E+06	4285.0	4.408E+05	6.37E+00	3.32E-01	1.68E-06	1565.2	7.0E+04	1.5E+04	26.3	5.9
0.504	-5.38E+06	4374.3	4.919E+05	8.11E+00	3.90E-01	1.83E-06	1496.0	7.0E+04	1.4E+04	26.3	5.9
0.607	-6.45E+06	4471.9	5.472E+05	1.04E+01	4.60E-01	1.98E-06	1426.7	7.0E+04	1.3E+04	26.3	5.9
0.710	-7.53E+06	4577.0	6.071E+05	1.34E+01	5.40E-01	2.13E-06	1357.7	7.0E+04	1.2E+04	26.3	5.9
0.813	-8.61E+06	4688.7	6.714E+05	1.72E+01	6.33E-01	2.29E-06	1289.4	7.0E+04	1.2E+04	26.3	5.9
0.915	-9.68E+06	4806.6	7.406E+05	2.21E+01	7.35E-01	2.46E-06	1222.0	7.0E+04	1.1E+04	26.3	5.9
1.015	-1.08E+07	4930.0	8.146E+05	2.82E+01	8.47E-01	2.63E-06	1156.0	7.0E+04	1.0E+04	26.3	5.9
1.113	-1.18E+07	5058.3	8.930E+05	3.53E+01	9.86E-01	2.76E-06	1091.7	7.0E+04	9.9E+03	26.3	5.9

Tab. F.10 Average model atmosphere of the diffuse background region (DB) of sunspot umbra S3 (NOAA 10944).

log $\tau_{5000}$	height [cm]	T [K]	$P_{gas}$ [g cm $^{-1}$ s $^{-2}$ ]	$P_{electr.}$ [g cm $^{-1}$ s $^{-2}$ ]	$\kappa$ [g $^{-1}$ ]	$\rho$ [cm $^{-3}$ ]	B [G]	$\zeta_{\mu}$ [cm s $^{-1}$ ]	$v_{LOS}$ [cm s $^{-1}$ ]	$\gamma_B$ [deg]	$\chi_B$
-4.000	4.71E+07	3379.9	1.315E+03	1.72E-02	3.43E-03	6.20E-09	2459.5	6.1E+04	1.8E+04	24.1	38.5
-3.900	4.59E+07	3395.9	1.513E+03	1.97E-02	3.79E-03	7.09E-09	2452.3	6.1E+04	1.8E+04	24.1	38.5
-3.800	4.47E+07	3411.9	1.738E+03	2.25E-02	4.19E-03	8.11E-09	2445.1	6.1E+04	1.8E+04	24.1	38.5
-3.700	4.35E+07	3427.8	1.994E+03	2.58E-02	4.63E-03	9.27E-09	2437.9	6.1E+04	1.8E+04	24.1	38.5
-3.600	4.24E+07	3443.7	2.286E+03	2.94E-02	5.12E-03	1.06E-08	2430.7	6.1E+04	1.8E+04	24.1	38.5
-3.500	4.12E+07	3459.5	2.618E+03	3.36E-02	5.66E-03	1.21E-08	2423.6	6.1E+04	1.8E+04	24.1	38.5
-3.400	4.00E+07	3475.3	2.997E+03	3.83E-02	6.25E-03	1.37E-08	2416.4	6.1E+04	1.8E+04	24.1	38.5
-3.300	3.89E+07	3490.9	3.427E+03	4.36E-02	6.91E-03	1.57E-08	2409.3	6.1E+04	1.8E+04	24.1	38.5
-3.200	3.77E+07	3506.4	3.918E+03	4.96E-02	7.64E-03	1.78E-08	2402.2	6.1E+04	1.8E+04	24.1	38.5
-3.100	3.65E+07	3521.8	4.476E+03	5.64E-02	8.45E-03	2.03E-08	2395.1	6.1E+04	1.8E+04	24.1	38.5
-3.000	3.54E+07	3536.9	5.112E+03	6.40E-02	9.33E-03	2.31E-08	2388.0	6.1E+04	1.8E+04	24.1	38.5
-2.900	3.42E+07	3551.8	5.836E+03	7.26E-02	1.03E-02	2.62E-08	2381.0	6.1E+04	1.8E+04	24.1	38.5
-2.800	3.30E+07	3566.2	6.662E+03	8.22E-02	1.14E-02	2.98E-08	2374.1	6.1E+04	1.8E+04	24.1	38.5
-2.700	3.19E+07	3580.3	7.603E+03	9.29E-02	1.26E-02	3.39E-08	2367.2	6.1E+04	1.8E+04	24.1	38.5
-2.600	3.07E+07	3593.7	8.676E+03	1.05E-01	1.39E-02	3.86E-08	2360.4	6.1E+04	1.8E+04	24.1	38.5
-2.500	2.95E+07	3606.4	9.902E+03	1.18E-01	1.53E-02	4.39E-08	2353.8	6.1E+04	1.8E+04	24.1	38.5
-2.400	2.83E+07	3618.1	1.130E+04	1.33E-01	1.68E-02	5.00E-08	2347.3	6.1E+04	1.8E+04	24.1	38.5
-2.300	2.72E+07	3629.3	1.290E+04	1.49E-01	1.85E-02	5.70E-08	2340.9	6.1E+04	1.8E+04	24.1	38.5
-2.200	2.60E+07	3640.0	1.474E+04	1.67E-01	2.03E-02	6.50E-08	2334.6	6.1E+04	1.8E+04	24.1	38.5
-2.100	2.48E+07	3650.5	1.684E+04	1.87E-01	2.24E-02	7.41E-08	2328.3	6.1E+04	1.8E+04	24.1	38.5
-2.000	2.36E+07	3661.2	1.924E+04	2.10E-01	2.46E-02	8.45E-08	2322.0	6.1E+04	1.8E+04	24.1	38.5
-1.900	2.24E+07	3672.1	2.199E+04	2.36E-01	2.71E-02	9.65E-08	2315.7	6.1E+04	1.8E+04	24.1	38.5
-1.800	2.12E+07	3683.6	2.513E+04	2.65E-01	2.98E-02	1.10E-07	2309.3	6.1E+04	1.8E+04	24.1	38.5
-1.700	2.00E+07	3695.9	2.872E+04	2.99E-01	3.29E-02	1.26E-07	2302.8	6.1E+04	1.8E+04	24.1	38.5
-1.600	1.88E+07	3709.5	3.282E+04	3.37E-01	3.63E-02	1.43E-07	2296.0	6.1E+04	1.8E+04	24.1	38.5
-1.500	1.76E+07	3724.7	3.750E+04	3.82E-01	4.01E-02	1.63E-07	2289.1	6.1E+04	1.8E+04	24.1	38.5
-1.400	1.64E+07	3742.0	4.282E+04	4.35E-01	4.44E-02	1.86E-07	2281.8	6.1E+04	1.8E+04	24.1	38.5
-1.300	1.52E+07	3762.2	4.886E+04	4.98E-01	4.93E-02	2.12E-07	2274.0	6.1E+04	1.8E+04	24.1	38.5
-1.200	1.40E+07	3786.0	5.569E+04	5.74E-01	5.49E-02	2.40E-07	2265.8	6.1E+04	1.8E+04	24.1	38.5
-1.100	1.28E+07	3814.5	6.339E+04	6.68E-01	6.15E-02	2.71E-07	2256.8	6.1E+04	1.8E+04	24.1	38.5
-1.000	1.16E+07	3849.0	7.202E+04	7.86E-01	6.93E-02	3.05E-07	2246.8	6.1E+04	1.7E+04	24.1	38.5
-0.900	1.04E+07	3890.7	8.163E+04	9.37E-01	7.86E-02	3.42E-07	2235.8	6.1E+04	1.7E+04	24.1	38.5
-0.800	9.28E+06	3938.4	9.226E+04	1.13E+00	8.97E-02	3.82E-07	2223.9	6.1E+04	1.6E+04	24.1	38.5
-0.700	8.11E+06	3990.5	1.040E+05	1.37E+00	1.03E-01	4.24E-07	2211.3	6.1E+04	1.6E+04	24.1	38.5
-0.600	6.96E+06	4045.9	1.169E+05	1.66E+00	1.17E-01	4.69E-07	2198.1	6.1E+04	1.5E+04	24.1	38.5
-0.500	5.80E+06	4103.5	1.310E+05	2.02E+00	1.34E-01	5.17E-07	2184.7	6.1E+04	1.4E+04	24.1	38.5
-0.400	4.65E+06	4162.6	1.466E+05	2.46E+00	1.54E-01	5.69E-07	2171.0	6.1E+04	1.3E+04	24.1	38.5
-0.300	3.50E+06	4222.3	1.638E+05	2.98E+00	1.75E-01	6.26E-07	2157.2	6.1E+04	1.3E+04	24.1	38.5
-0.200	2.34E+06	4281.9	1.828E+05	3.61E+00	1.99E-01	6.87E-07	2143.5	6.1E+04	1.2E+04	24.1	38.5
-0.100	1.17E+06	4340.6	2.039E+05	4.34E+00	2.26E-01	7.55E-07	2129.8	6.1E+04	1.1E+04	24.1	38.5
0.000	0.00E+00	4397.8	2.274E+05	5.18E+00	2.55E-01	8.30E-07	2116.4	6.1E+04	1.1E+04	24.1	38.5
0.099	-1.17E+06	4466.0	2.532E+05	6.26E+00	2.88E-01	9.03E-07	2102.0	6.1E+04	9.8E+03	24.1	38.5
0.198	-2.35E+06	4544.3	2.812E+05	7.68E+00	3.29E-01	9.84E-07	2088.1	6.1E+04	9.2E+03	24.1	38.5
0.297	-3.52E+06	4631.8	3.116E+05	9.48E+00	3.75E-01	1.07E-06	2074.4	6.1E+04	8.6E+03	24.1	38.5
0.396	-4.70E+06	4727.7	3.447E+05	1.18E+01	4.27E-01	1.16E-06	2061.0	6.1E+04	8.2E+03	24.1	38.5
0.495	-5.87E+06	4831.2	3.803E+05	1.46E+01	4.85E-01	1.25E-06	2048.0	6.1E+04	7.8E+03	24.1	38.5
0.593	-7.04E+06	4941.6	4.187E+05	1.80E+01	5.48E-01	1.34E-06	2035.2	6.1E+04	7.4E+03	24.1	38.5
0.690	-8.22E+06	5058.3	4.598E+05	2.21E+01	6.17E-01	1.43E-06	2022.8	6.1E+04	7.1E+03	24.1	38.5
0.785	-9.39E+06	5180.7	5.036E+05	2.71E+01	6.87E-01	1.52E-06	2010.7	6.1E+04	6.8E+03	24.1	38.5
0.878	-1.06E+07	5308.4	5.504E+05	3.30E+01	7.59E-01	1.62E-06	1999.1	6.1E+04	6.5E+03	24.1	38.5
0.968	-1.17E+07	5440.9	6.003E+05	4.02E+01	8.38E-01	1.73E-06	1987.9	6.1E+04	6.3E+03	24.1	38.5
1.055	-1.29E+07	5577.7	6.533E+05	4.90E+01	9.28E-01	1.84E-06	1977.0	6.1E+04	6.1E+03	24.1	38.5

Tab. F.11 Average model atmosphere of the core umbral dots (CUD) of sunspot umbra S3 (NOAA 10 944).

$\log \tau_{5000}$	height [cm]	T [K]	$P_{gas}$ [g cm <sup>-1</sup> s <sup>-2</sup> ]	$P_{electr.}$ [g <sup>-1</sup> s <sup>-2</sup> ]	$\kappa$ [g <sup>-1</sup> ]	$\rho$ [cm <sup>-3</sup> ]	B [G]	$\zeta_{\mu}$ [cm s <sup>-1</sup> ]	$v_{LOS}$ [cm s <sup>-1</sup> ]	$\gamma_B$ [deg]	$\chi_B$
-4.000	4.36E+07	3261.4	1.436E+03	1.30E-02	3.14E-03	7.03E-09	2343.8	8.6E+04	2.2E+04	21.6	42.4
-3.900	4.25E+07	3280.0	1.651E+03	1.50E-02	3.48E-03	8.04E-09	2340.0	8.6E+04	2.2E+04	21.6	42.4
-3.800	4.14E+07	3298.6	1.896E+03	1.74E-02	3.85E-03	9.18E-09	2336.2	8.6E+04	2.1E+04	21.6	42.4
-3.700	4.03E+07	3317.2	2.174E+03	2.00E-02	4.26E-03	1.05E-08	2332.3	8.6E+04	2.1E+04	21.6	42.4
-3.600	3.92E+07	3335.8	2.490E+03	2.31E-02	4.72E-03	1.19E-08	2328.5	8.6E+04	2.1E+04	21.6	42.4
-3.500	3.81E+07	3354.3	2.849E+03	2.66E-02	5.23E-03	1.36E-08	2324.7	8.6E+04	2.0E+04	21.6	42.4
-3.400	3.70E+07	3372.8	3.256E+03	3.06E-02	5.80E-03	1.55E-08	2321.0	8.6E+04	2.0E+04	21.6	42.4
-3.300	3.59E+07	3391.2	3.720E+03	3.52E-02	6.42E-03	1.76E-08	2317.2	8.6E+04	2.0E+04	21.6	42.4
-3.200	3.48E+07	3409.6	4.246E+03	4.04E-02	7.12E-03	1.99E-08	2313.5	8.6E+04	1.9E+04	21.6	42.4
-3.100	3.38E+07	3427.9	4.844E+03	4.63E-02	7.89E-03	2.26E-08	2309.8	8.6E+04	1.9E+04	21.6	42.4
-3.000	3.27E+07	3446.0	5.523E+03	5.30E-02	8.74E-03	2.57E-08	2306.2	8.6E+04	1.9E+04	21.6	42.4
-2.900	3.16E+07	3464.1	6.294E+03	6.07E-02	9.68E-03	2.91E-08	2302.6	8.6E+04	1.8E+04	21.6	42.4
-2.800	3.05E+07	3481.9	7.171E+03	6.93E-02	1.07E-02	3.31E-08	2299.2	8.6E+04	1.8E+04	21.6	42.4
-2.700	2.94E+07	3499.5	8.167E+03	7.91E-02	1.19E-02	3.75E-08	2295.8	8.6E+04	1.8E+04	21.6	42.4
-2.600	2.83E+07	3516.8	9.301E+03	9.02E-02	1.31E-02	4.25E-08	2292.6	8.6E+04	1.8E+04	21.6	42.4
-2.500	2.72E+07	3533.7	1.059E+04	1.03E-01	1.45E-02	4.82E-08	2289.6	8.6E+04	1.7E+04	21.6	42.4
-2.400	2.60E+07	3550.1	1.206E+04	1.17E-01	1.61E-02	5.46E-08	2286.8	8.6E+04	1.7E+04	21.6	42.4
-2.300	2.49E+07	3566.3	1.373E+04	1.32E-01	1.78E-02	6.20E-08	2284.1	8.6E+04	1.7E+04	21.6	42.4
-2.200	2.38E+07	3582.3	1.563E+04	1.50E-01	1.96E-02	7.03E-08	2281.6	8.6E+04	1.6E+04	21.6	42.4
-2.100	2.27E+07	3598.4	1.780E+04	1.71E-01	2.17E-02	7.98E-08	2279.1	8.6E+04	1.6E+04	21.6	42.4
-2.000	2.16E+07	3614.8	2.027E+04	1.94E-01	2.40E-02	9.06E-08	2276.5	8.6E+04	1.6E+04	21.6	42.4
-1.900	2.04E+07	3631.6	2.308E+04	2.21E-01	2.65E-02	1.03E-07	2274.0	8.6E+04	1.6E+04	21.6	42.4
-1.800	1.93E+07	3649.1	2.627E+04	2.51E-01	2.94E-02	1.17E-07	2271.3	8.6E+04	1.5E+04	21.6	42.4
-1.700	1.82E+07	3667.6	2.991E+04	2.87E-01	3.25E-02	1.32E-07	2268.4	8.6E+04	1.5E+04	21.6	42.4
-1.600	1.70E+07	3687.4	3.404E+04	3.28E-01	3.61E-02	1.50E-07	2265.2	8.6E+04	1.5E+04	21.6	42.4
-1.500	1.59E+07	3708.9	3.873E+04	3.77E-01	4.01E-02	1.70E-07	2261.7	8.6E+04	1.5E+04	21.6	42.4
-1.400	1.48E+07	3732.6	4.404E+04	4.35E-01	4.47E-02	1.92E-07	2257.7	8.6E+04	1.4E+04	21.6	42.4
-1.300	1.37E+07	3759.2	5.003E+04	5.04E-01	4.99E-02	2.17E-07	2253.1	8.6E+04	1.4E+04	21.6	42.4
-1.200	1.26E+07	3789.6	5.678E+04	5.89E-01	5.59E-02	2.45E-07	2247.7	8.6E+04	1.3E+04	21.6	42.4
-1.100	1.15E+07	3824.7	6.434E+04	6.94E-01	6.29E-02	2.75E-07	2241.3	8.6E+04	1.3E+04	21.6	42.4
-1.000	1.04E+07	3866.1	7.277E+04	8.26E-01	7.13E-02	3.07E-07	2233.5	8.6E+04	1.2E+04	21.6	42.4
-0.900	9.32E+06	3914.8	8.211E+04	9.97E-01	8.13E-02	3.42E-07	2224.1	8.6E+04	1.2E+04	21.6	42.4
-0.800	8.26E+06	3969.5	9.238E+04	1.21E+00	9.32E-02	3.78E-07	2213.3	8.6E+04	1.1E+04	21.6	42.4
-0.700	7.22E+06	4028.9	1.036E+05	1.49E+00	1.07E-01	4.17E-07	2201.6	8.6E+04	1.0E+04	21.6	42.4
-0.600	6.18E+06	4091.5	1.160E+05	1.83E+00	1.23E-01	4.59E-07	2189.2	8.6E+04	9.8E+03	21.6	42.4
-0.500	5.16E+06	4156.5	1.295E+05	2.25E+00	1.42E-01	5.03E-07	2176.3	8.6E+04	9.0E+03	21.6	42.4
-0.400	4.14E+06	4222.9	1.443E+05	2.76E+00	1.62E-01	5.50E-07	2163.0	8.6E+04	8.2E+03	21.6	42.4
-0.300	3.12E+06	4289.9	1.605E+05	3.37E+00	1.86E-01	6.01E-07	2149.6	8.6E+04	7.4E+03	21.6	42.4
-0.200	2.09E+06	4356.9	1.785E+05	4.10E+00	2.11E-01	6.57E-07	2136.3	8.6E+04	6.6E+03	21.6	42.4
-0.100	1.05E+06	4423.1	1.983E+05	4.96E+00	2.40E-01	7.18E-07	2123.1	8.6E+04	5.9E+03	21.6	42.4
0.000	0.00E+00	4487.6	2.205E+05	5.95E+00	2.71E-01	7.85E-07	2110.2	8.6E+04	5.1E+03	21.6	42.4
0.098	-1.05E+06	4562.3	2.446E+05	7.21E+00	3.05E-01	8.50E-07	2096.5	8.6E+04	4.3E+03	21.6	42.4
0.194	-2.11E+06	4646.5	2.707E+05	8.82E+00	3.46E-01	9.23E-07	2083.3	8.6E+04	3.6E+03	21.6	42.4
0.289	-3.16E+06	4739.1	2.991E+05	1.08E+01	3.92E-01	9.98E-07	2070.4	8.6E+04	3.0E+03	21.6	42.4
0.383	-4.22E+06	4839.6	3.297E+05	1.33E+01	4.42E-01	1.08E-06	2057.9	8.6E+04	2.4E+03	21.6	42.4
0.474	-5.27E+06	4947.2	3.626E+05	1.64E+01	4.97E-01	1.15E-06	2045.8	8.6E+04	1.8E+03	21.6	42.4
0.563	-6.32E+06	5061.1	3.979E+05	2.00E+01	5.57E-01	1.23E-06	2034.0	8.6E+04	1.3E+03	21.6	42.4
0.650	-7.38E+06	5180.9	4.355E+05	2.43E+01	6.18E-01	1.32E-06	2022.6	8.6E+04	8.8E+02	21.6	42.4
0.734	-8.43E+06	5306.1	4.757E+05	2.95E+01	6.81E-01	1.40E-06	2011.6	8.6E+04	4.5E+02	21.6	42.4
0.815	-9.48E+06	5436.2	5.185E+05	3.58E+01	7.50E-01	1.49E-06	2001.0	8.6E+04	5.7E+01	21.6	42.4
0.894	-1.05E+07	5570.7	5.639E+05	4.36E+01	8.30E-01	1.59E-06	1990.7	8.6E+04	-3.1E+02	21.6	42.4
0.971	-1.16E+07	5709.3	6.121E+05	5.37E+01	9.29E-01	1.68E-06	1980.5	8.6E+04	-6.7E+02	21.6	42.4

Tab. F.12 Average model atmosphere of the peripheral umbral dots (PUD) of sunspot umbra S3 (NOAA 10944).

log $\tau_{5000}$	height [cm]	T [K]	$P_{gas}$ [g cm <sup>-1</sup> s <sup>-2</sup> ]	$P_{electr.}$ [g <sup>-1</sup> s <sup>-2</sup> ]	$\kappa$ [g <sup>-1</sup> ]	$\rho$ [cm <sup>-3</sup> ]	B [G]	$\zeta_{\mu}$ [cm s <sup>-1</sup> ]	$v_{LOS}$ [cm s <sup>-1</sup> ]	$\gamma_B$ [deg]	$X_B$
-4.000	4.54E+07	3317.5	1.384E+03	1.49E-02	3.28E-03	6.66E-09	2355.3	8.5E+04	2.7E+04	30.1	50.6
-3.900	4.43E+07	3336.2	1.590E+03	1.72E-02	3.63E-03	7.61E-09	2347.0	8.5E+04	2.6E+04	30.1	50.6
-3.800	4.31E+07	3354.8	1.825E+03	1.99E-02	4.02E-03	8.68E-09	2338.8	8.5E+04	2.5E+04	30.1	50.6
-3.700	4.19E+07	3373.4	2.091E+03	2.29E-02	4.46E-03	9.90E-09	2330.5	8.5E+04	2.5E+04	30.1	50.6
-3.600	4.08E+07	3392.0	2.394E+03	2.64E-02	4.94E-03	1.13E-08	2322.3	8.5E+04	2.4E+04	30.1	50.6
-3.500	3.96E+07	3410.6	2.738E+03	3.03E-02	5.47E-03	1.28E-08	2314.1	8.5E+04	2.3E+04	30.1	50.6
-3.400	3.84E+07	3429.1	3.129E+03	3.48E-02	6.06E-03	1.46E-08	2305.8	8.5E+04	2.3E+04	30.1	50.6
-3.300	3.73E+07	3447.6	3.573E+03	3.99E-02	6.72E-03	1.66E-08	2297.6	8.5E+04	2.2E+04	30.1	50.6
-3.200	3.62E+07	3466.1	4.077E+03	4.58E-02	7.44E-03	1.88E-08	2289.4	8.5E+04	2.1E+04	30.1	50.6
-3.100	3.50E+07	3484.5	4.649E+03	5.24E-02	8.25E-03	2.13E-08	2281.2	8.5E+04	2.0E+04	30.1	50.6
-3.000	3.38E+07	3502.8	5.299E+03	6.00E-02	9.14E-03	2.42E-08	2273.0	8.5E+04	2.0E+04	30.1	50.6
-2.900	3.27E+07	3521.0	6.037E+03	6.85E-02	1.01E-02	2.74E-08	2264.8	8.5E+04	1.9E+04	30.1	50.6
-2.800	3.15E+07	3539.1	6.876E+03	7.82E-02	1.12E-02	3.11E-08	2256.7	8.5E+04	1.8E+04	30.1	50.6
-2.700	3.04E+07	3557.1	7.829E+03	8.92E-02	1.24E-02	3.52E-08	2248.6	8.5E+04	1.7E+04	30.1	50.6
-2.600	2.92E+07	3574.8	8.912E+03	1.02E-01	1.38E-02	3.99E-08	2240.5	8.5E+04	1.7E+04	30.1	50.6
-2.500	2.80E+07	3592.2	1.014E+04	1.16E-01	1.52E-02	4.52E-08	2232.5	8.5E+04	1.6E+04	30.1	50.6
-2.400	2.69E+07	3609.4	1.154E+04	1.32E-01	1.69E-02	5.12E-08	2224.5	8.5E+04	1.5E+04	30.1	50.6
-2.300	2.57E+07	3626.4	1.314E+04	1.49E-01	1.86E-02	5.81E-08	2216.6	8.5E+04	1.5E+04	30.1	50.6
-2.200	2.45E+07	3643.3	1.495E+04	1.70E-01	2.06E-02	6.58E-08	2208.8	8.5E+04	1.4E+04	30.1	50.6
-2.100	2.34E+07	3660.4	1.702E+04	1.93E-01	2.28E-02	7.46E-08	2200.9	8.5E+04	1.3E+04	30.1	50.6
-2.000	2.22E+07	3677.7	1.937E+04	2.20E-01	2.53E-02	8.46E-08	2193.0	8.5E+04	1.3E+04	30.1	50.6
-1.900	2.10E+07	3695.5	2.204E+04	2.50E-01	2.80E-02	9.59E-08	2185.1	8.5E+04	1.2E+04	30.1	50.6
-1.800	1.98E+07	3714.0	2.508E+04	2.86E-01	3.10E-02	1.09E-07	2177.2	8.5E+04	1.1E+04	30.1	50.6
-1.700	1.86E+07	3733.4	2.853E+04	3.27E-01	3.44E-02	1.23E-07	2169.2	8.5E+04	1.1E+04	30.1	50.6
-1.600	1.74E+07	3754.0	3.246E+04	3.75E-01	3.82E-02	1.40E-07	2161.2	8.5E+04	9.9E+03	30.1	50.6
-1.500	1.63E+07	3776.3	3.690E+04	4.31E-01	4.24E-02	1.58E-07	2153.0	8.5E+04	9.2E+03	30.1	50.6
-1.400	1.51E+07	3800.6	4.194E+04	4.98E-01	4.73E-02	1.79E-07	2144.7	8.5E+04	8.5E+03	30.1	50.6
-1.300	1.40E+07	3827.7	4.763E+04	5.78E-01	5.28E-02	2.02E-07	2136.3	8.5E+04	7.7E+03	30.1	50.6
-1.200	1.28E+07	3858.2	5.404E+04	6.74E-01	5.92E-02	2.27E-07	2127.5	8.5E+04	6.9E+03	30.1	50.6
-1.100	1.17E+07	3893.3	6.124E+04	7.93E-01	6.65E-02	2.55E-07	2118.5	8.5E+04	6.0E+03	30.1	50.6
-1.000	1.06E+07	3934.2	6.927E+04	9.42E-01	7.52E-02	2.86E-07	2109.1	8.5E+04	5.0E+03	30.1	50.6
-0.900	9.45E+06	3981.8	7.817E+04	1.13E+00	8.56E-02	3.19E-07	2099.2	8.5E+04	4.0E+03	30.1	50.6
-0.800	8.37E+06	4035.2	8.800E+04	1.37E+00	9.77E-02	3.53E-07	2088.9	8.5E+04	2.9E+03	30.1	50.6
-0.700	7.31E+06	4092.8	9.880E+04	1.66E+00	1.12E-01	3.90E-07	2078.4	8.5E+04	1.8E+03	30.1	50.6
-0.600	6.26E+06	4153.6	1.107E+05	2.03E+00	1.28E-01	4.30E-07	2067.6	8.5E+04	6.1E+02	30.1	50.6
-0.500	5.22E+06	4216.5	1.237E+05	2.47E+00	1.46E-01	4.72E-07	2056.6	8.5E+04	-5.9E+02	30.1	50.6
-0.400	4.19E+06	4280.7	1.381E+05	3.01E+00	1.67E-01	5.18E-07	2045.6	8.5E+04	-1.8E+03	30.1	50.6
-0.300	3.16E+06	4345.6	1.539E+05	3.65E+00	1.90E-01	5.68E-07	2034.5	8.5E+04	-3.0E+03	30.1	50.6
-0.200	2.12E+06	4410.4	1.715E+05	4.40E+00	2.16E-01	6.23E-07	2023.5	8.5E+04	-4.3E+03	30.1	50.6
-0.100	1.07E+06	4474.4	1.910E+05	5.29E+00	2.44E-01	6.82E-07	2012.5	8.5E+04	-5.5E+03	30.1	50.6
0.000	0.00E+00	4536.9	2.128E+05	6.32E+00	2.74E-01	7.49E-07	2001.6	8.5E+04	-6.7E+03	30.1	50.6
0.098	-1.07E+06	4610.4	2.366E+05	7.60E+00	3.09E-01	8.13E-07	1989.9	8.5E+04	-7.9E+03	30.1	50.6
0.194	-2.14E+06	4693.8	2.625E+05	9.27E+00	3.49E-01	8.85E-07	1978.7	8.5E+04	-8.9E+03	30.1	50.6
0.288	-3.20E+06	4786.4	2.906E+05	1.14E+01	3.95E-01	9.60E-07	1967.7	8.5E+04	-9.9E+03	30.1	50.6
0.380	-4.27E+06	4887.4	3.211E+05	1.39E+01	4.44E-01	1.04E-06	1957.1	8.5E+04	-1.1E+04	30.1	50.6
0.471	-5.34E+06	4995.9	3.540E+05	1.70E+01	4.98E-01	1.12E-06	1946.8	8.5E+04	-1.2E+04	30.1	50.6
0.559	-6.40E+06	5111.3	3.892E+05	2.08E+01	5.57E-01	1.19E-06	1936.8	8.5E+04	-1.3E+04	30.1	50.6
0.644	-7.47E+06	5233.1	4.270E+05	2.53E+01	6.17E-01	1.28E-06	1927.1	8.5E+04	-1.4E+04	30.1	50.6
0.726	-8.54E+06	5360.5	4.674E+05	3.08E+01	6.81E-01	1.37E-06	1917.8	8.5E+04	-1.4E+04	30.1	50.6
0.806	-9.61E+06	5493.3	5.106E+05	3.75E+01	7.54E-01	1.46E-06	1908.7	8.5E+04	-1.5E+04	30.1	50.6
0.884	-1.07E+07	5630.8	5.565E+05	4.61E+01	8.41E-01	1.55E-06	1899.9	8.5E+04	-1.6E+04	30.1	50.6
0.961	-1.17E+07	5772.6	6.053E+05	5.75E+01	9.52E-01	1.64E-06	1891.1	8.5E+04	-1.7E+04	30.1	50.6



---

# Picture credits

---

Except for the figures listed below all figures in this thesis were made by the author, Richard Wenzel.

1. Fig. 2.1 compiled by RW using a photograph of Miloslav Druckmüller with kind permission
2. Fig. 2.2 taken from Vernazza et al. (1981)
3. Fig. 2.3 made with PStricks
4. Fig. 2.4 taken from Rempel et al. (2009) with kind permission
5. Fig. 2.5 compiled by RW using a sunspot image by V. Zakharov with kind permission
6. Fig. 2.8 taken from Berdyugina & Solanki (2002) with kind permission
7. Fig. 2.9 taken from Berdyugina & Solanki (2002) with kind permission
8. Fig. D.0 taken from (Frutiger, 2000)



---

# List of publications

---

## Peer-reviewed publications

- "Sunspot umbra model atmospheres"  
Wenzel, R., Berdyugina, S.V., Fluri, D.M., Arnaud, J., Sainz Dalda, A.,  
2010, A&A, in review
- "Sunspot umbrae: from small to large"  
Wenzel, R., Fluri, D.M., Berdyugina, S.V.,  
2011, A&A, in review

## Contribution to conference proceedings & posters

- "Umbra model atmosphere from Full Stokes inversions"  
Wenzel, R., Berdyugina, S.V., Fluri, D.M., Arnaud, J., Sainz Dalda, A.,  
2010 in Astronomical Society of the Pacific Conference Series, Vol.  
428, SOHO-23, ed. S. R. Cranmer, J. T. Hoeksema, & J. L. Kohl,  
117-+
- "Sunspot Model Atmosphere from Inversion of Stokes Profiles",  
ESPM-12, Freiburg i.B., Germany, Sep 8 – 12 2008
- "Sunspot model atmosphere from Full Stokes inversions",  
SOHO-23 conference, Maine, USA, Sep 21 – 25 2009

- "Sunspot model atmosphere from Full Stokes inversions", EAST-AST conference, Freiburg i. B., Germany, Oct 13 – 16 2009
- "Sunspot umbra model atmospheres from Full Stokes inversions", SPW6, Maui/Hawai, USA, May 30 – June 4 2010



---

# Curriculum Vitæ

---

Name	Richard Wenzel
Date of birth	December 24, 1982
Place of birth	Leipzig, Germany
1995 - 2001	Thomasschule zu Leipzig - Gymnasium, Germany Abitur (A levels in Chemistry and Math)
2001 - 2002	german civil service
2002 - 2004 2004	Studies of Physics at the University of Leipzig "Vordiplom"
2004 - 2007 2007	Studies of Physics at the ETH Zürich Dipl. Phys. ETH Diploma Thesis: <i>Doppler Imaging of IM Pegasi</i>
2007 - 2011	Research assistant in the Solar Physics Group and the Star and Planet Formation Research Group, Institute for Astronomy, ETH Zürich
2011	Doctoral Thesis <i>Sunspot umbra atmospheres</i> Supervisors: Prof. Dr. Svetlana V. Berdyugina and Prof. Dr. Michael R. Meyer

Member of the Swiss Society of Astrophysics and Astronomy (SGAA)

---

# Acknowledgements

---

I consider myself very lucky having seen so many aspects of astrophysical research during the last years.

With a PhD in solar physics I was given the opportunity to work in a field that combines many of my interests and fosters a lot of skills I appreciate. I analyzed unique datasets, went for observations on my own and traveled far for conferences to meet a lot of most interesting people. Talking to them and being regarded as a member of their community right from the start impressed me. They often made time available for personal discussions as soon as I was able to phrase my questions.

Thank you, everybody. Especially thank you, Sveta, for making that possible.

At the start my official supervisor was Prof. Jan Stenflo who retired when the extragalactic and stellar-solar parts of the Institute for Astronomy were united at the Höggerberg campus, creating a milestone in the history of solar physics.

At the end of this journey, I am most grateful to have two very ener-

getic scientists as my *Doktormutter* and *Doktorvater*, respectively: Prof. Svetlana Berdyugina at the Kiepenheuer-Institut (KIS) in Freiburg and Prof. Michael Meyer here in Zurich. To them and to my co-examiners PD Hans-Martin Schmid and Dr. Bruce Lites I extend my gratitude for reading and commenting on the thesis.

In the former group of Sveta, I am indoubted to Dr. Dominique Fluri, who was my strongest and most valuable critic helping me debugging Fortran code and checking my logic. Together with him and my office mate Dr. Chrigi Sennhauser I had a most fruitful and fun time. At the KIS I got the most helpful and constructive feedback on inversions and sunspots from Dr. Reza Rezai and Dr. Rolf Schlichenmaier. Thank you!

Apart from the big moments the pain of the plains was severly facilitated if not erased in many cases by the most knowledgeable and sympathetic members of the institutes in Zurich and Freiburg who helped me in numerous situations with personal and professional advice and often were splendid partners for thoughtful discussions or rude table soccer games:

A big "Merci!" goes to: Dr. Nadine Afram, Dr. Adam Amara, Henning Avenhaus, Andrea Banzatti, Dr. Marina Battaglia, Andreas Bazon, Axel Beckert, Dr. Christian Behtge, Dr. Martin Bernet, Prof. Dr. Arnold Benz, Rongmon Bordoloi, Dr. JuanMa Borrero, Dr. Jo Bruls, Thomas Bschorr, Esther Bünzli, Dr. Peter Caligari, Marianne Chiesi, Barbara Codoni, Dr. Bartosz Dabrowski, Dr. Carolin Dedes, Catharina Diener, Hans-Peter Doerr, Dr. Robert Feldmann, Morton Franz, Dr. Vincent Geers, Dr. Daniel Gisler, Dr. Nazaret Bello Gonzalez, Dr. Oliver Hahn, Dr. Reiner Hammer, Eveline Hardmeier, Dr. Kevin Heng, Dr. Christian Herzog, Dr. René Holzreuter, Dr. Pawel Kampczyk, Tobias Kaufmann, Dr. Lucia Kleint, Dr. Christian Knobel, Prof. Dr. Jeff Kuhn, Monika Leimgruber, Tanja Leist, Prof. Dr. Oskar von der Lühe, Dr. Francesco Miniati, Christian Monstein, Dr. Christian Nutto, Dr. Yingjie Peng, Dr. Craig Rudick, PD Dr. Wolfgang Schmidt, Micha Scholl, Dr. Alexander Shapiro and his wife Anna, Gürkan Sengün, Pascal Steger, Prof. Dr. Oskar Steiner, Peter Steiner, Dr. Christian Thalmann,

Dr. Sascha Quanz, Dr. Susanne Wampfler, Oliver Wiloth, and Dr. Pia Zacharias.

Outside the institute but still on campus my fellow board members of the AMP (representatives of the academic staff) not only helped in keeping the mental health but also fostered the communication and exchange among PhDs from all institutes of the department organizing events like the tradition-to-be soccer tournament Boltzmann-Cup.

For leisure activities and the necessary bit of distraction I extend my gratitude to my friends with whom I had the pleasure forming the improvisational theater company *fearlesfanz*. For their constant hospitality and readiness to barbeque or having a coffee anytime I shall invite the members of the *nanomat group* on a next occasion. For their ever smiling support I do thank my typo hunter Franziska Fricke and the catalan chef Dr. Vidal Salvador Pané.

Special thanks go to my parents and my family in Germany for their encouragement and infinite support. Danke für alles.

And to my love, Tessa, thanks for being with me.